Prediction of Damage to Cement-Based Structures Subject to Tunnelling-Induced Settlements

By

Gerardo Cirillo

Thesis presented in partial fulfillment of the requirements for the degree of Master of Engineering (Civil) at the University of Stellenbosch.

Study leaders: Prof G.P.A.G van Zijl, H. Netzel.

December 2003

Declaration

I, the undersigned, hereby declare that the work contained in this thesis is my own original work and that I have not previously in its entirety or in part submitted it at any university for a degree.

Abstract

Tunneling in busy urban areas is becoming a common practice, caused by the ever-increasing number of commuters. This causes a decline in the service level that the surface transportation systems provide in cities. Tunneling induces movement of the soil directly surrounding the tunnel. These movements are translated into surface movements, which are translated into structural displacements of the surrounding surface infrastructure. These displacements, for which the infrastructure may not have been designed, put a question mark on the infrastructure aesthetics, serviceability, as well as structural stability.

Burland and Wroth (1974) proposed a simple analytical damage assessment approach (Limiting tensile strain method (**LTS**)) to aid in the design of tunnels with respect to the structural integrity of the affected surface infrastructure. This study is concerned with the accuracy of this approach applied to the damage assessment of laterally unconfined, solid masonry walls, subject to a sagging mode of settlement deformation with no soil to wall friction. It is also concerned with the proposal of modifications to the approach, where deemed necessary.

Finite element models of solid masonry walls are built and analysed in order to determine the accuracy of the simple analytical damage assessment approach with regard to the prediction of strains in solid masonry walls subject to tunneling-induced displacements. The predictions are found to be accurate for walls of **L/H** ratio equal to 2 and larger. For walls of **L/H** ratio smaller than 2, the predictions are found to be underestimates.

The simple analytical damage assessment approach is unable to account for the stiffness of the soil directly under the foundation of the wall. The stiffness of the soil plays a major role in the stress and strain distributions in the wall. It is therefore deemed necessary to modify the simple analytical damage assessment approach by accounting for the soil to wall interaction and the effect it has on the settlement damage to solid masonry walls. The soil to wall interaction is found to reduce the number of mitigating measures originally recommended for the walls, by the simple

analytical damage assessment approach, as it accounts for the bedding of the wall into the soil previously unaccounted for.

This study has reached the point where it is able to accurately predict whether a laterally unconfined, solid masonry wall, subject to a sagging mode of settlement deformation with no soil to wall friction will experience magnitudes of strain surpassing the yielding strain of the material. This was fundamentally achieved by developing a better representation of the strains in solid masonry walls as well as accounting for the inherent soil to wall interaction

This study is intended to pioneer the proliferation of similar studies for various other structures. A methodology, applicable for similar investigations envisaged for other structures, is hereby developed.

Abstrak

Tonnels in besige stedelike gebiede is besig om 'n allerdaagse verskynsel te raak a.g.v. die skerp toename in pendelaars. Die rede hiervoor is die afname in die kwaliteit van bogrondse vervoerdienste. Tonnels veroorsaak beweging van grond direk in aanraking met die tonnel. Hierdie bewegings versprei na die oppervlak wat strukturele verplasings veroorsaak. Vir n' struktuur wat nie vir hierdie verplasings ontwerp is nie, ontstaan vrae oor die estetika, diensbaarheid asook die stabiliteit van die struktuur.

Burland en Wroth (1974) het 'n eenvoudige analitiese skade-assesseringsmetode voorgestel (Limiting tensile strain method (**LTS**)) vir die ontwerp van tonnels m.b.t. die strukturele integriteit van die geaffekteerde oppervlak se infrastruktuur. Hierdie studie handel oor die akkuraatheid van dié benadering, toegepas op die assessering van skade op lateraal onbeperkte, soliede messelwerkmure, onderhewig aan die deurbuigings mode van versakkingsdeformasie, met geen grond tot muur wrywing.

Eindige element modelle van messelwerkmure is gebou en geanaliseer om die akkuraatheid van die eenvoudige analitiese skade-assesseringsmetode te bepaal, m.b.t. die voorspelling van die vervormings in messelwerkmure onderhewig aan grondverplasings veroorsaak deur tonnels. Die voorspellings is akkuraat in mure met lengte tot hoogte (**L/H**) verhoudings van 2 en hoër. Vir mure met L/H verhoudings van minder as 2, word daar gevind dat die voorspellings onkonserwatief is.

By die eenvoudige analitiese skade-assesseringsmetode word die styfheid van grond direk onder die fondasies van die muur nie in ag geneem nie. Die grondstyfheid speel 'n kardinale rol by die spannings- en vervormingsverdelings in die muur. Dit is daarvoor nodig om die eenvoudige analitiese skade-assesseringsmetode aan te pas om die grond tot muur interaksie in ag te neem. Die interaksie tussen die grond en die muur veroorsaak 'dat a minder of geen skade voorkomende maatreëls getref hoef te word as wat oorspronklik deur die envoudige analitiese skade-assesseringsmetode voorgestel sou word. Dit neem die inbedding van die muur in die grond in ag, wat voorheen geïgnoreer is.

Die studie het 'n punt bereik waar dit akkuraat kan voorspel of 'n lateraal onbeperkte, soliede messelwerkmuur, onderhewig aan die deurbuiging mode van versakkingsdeformasie en met ĝeen grond tot muur wrywing, vervormings hoër as die swigvervorming van die material sal ondervind. Dit is bereik deur 'n beter voorstelling van die vervormings in soliede messelwerkmure asook die in agneming van inhirente grond tot muur interaksie.

Die studie is veronderstel om die voorganger te wees vir soortgelyke studies toegepas op verskeie ander struktuurklasse. Die sistematiese metode wat hier ontwikkel is kan toegepas word op die ander struktuurklasse.

Acknowledgments

The undertaking of my master's thesis at the Technical University of Delft (TUDelft) in the Netherlands, from the period September 2002 - September 2003, was an unforgettable and enriching experience for which I am most grateful.

I would like to thank the following people:

Prof G.P.A.G van Zijl for the supervision of my thesis. Prof van Zijl's contribution has been invaluable to this thesis's successful completion. I really appreciate the effort Prof. van Zijl put into my obtaining a Delta scholarship from the Dutch government, which partly contributed toward the financing of my stay in the Netherlands. I also appreciate the trust Prof van Zijl afforded me by using his goodwill with the Structural Mechanics Group (SMG), at the Faculty of Architecture (TUDelft) lead by Prof J.Rots, who contributed to the remainder of the financial support, which I needed for my stay in the Netherlands. I appreciate the use of Prof van Zijl's laptop as well as for his understanding with regard to the difficulties and frustrations attached to the completion of any thesis.

Prof J.Rots for all he did to make my stay in the Netherlands enjoyable, from lending me a television to watch the European football qualification matches to introducing me to a local football club in Delft where I eventually became a member. I appreciate all the trouble Prof Rots went through in organizing me accommodation at short notice in Delft as well as for providing me with financial support via the SMG. I would also like to thank the *members* of the SMG for all there help and for their friendship. I would particularly like to thank *Maetee Boonpichetvong* for helping me with all my computer problems and *Stefano Invernizzi* for picking me up at six in the morning from the airport when I arrived in the Netherlands as well as helping me with any technical questions I had.

Holger Netzel for the supervision of my thesis in the Netherlands. I thank him for his contribution to the successful completion of the thesis and for sharing his vast

practical experience in the field of structural damage assessment. I also look forward to collaborating with Holger and Crux engineering of Amsterdam in the near future.

Grinaker/LTA for their financial support during my career at Stellenbosch and for allowing me to take this opportunity when it came about.

My parents, Giovanni and Lesley Cirillo, and brothers, Giovanni and Domenico Cirillo, for their continual support throughout. The contribution you played toward the successful completion of my master's thesis and my career at the University of Stellenbosch is invaluable. I must especially thank my *mother* for all her emails filled with news and support from home.

My grandparents for all their support.

Ilaria Martini for the wonderful person and special friend that she is. Ti ringrazio tanto per tutto quello che sei stata per me. Sei stata veramente importante e non solo per quanto riguarda la mia tesi. Non ti posso spiegare quanto penso che sia valsa la pena di venire in Olanda solo per il fatto di averti conosciuto. Ti porterò nel mio cuore per sempre

Francesco Serafino and Alessio Nicoli for an incredible friendship and for the enjoyable time we spent at the Sebastian's Brug together. Vi voglio ringraziare tanto per la vostra amicizia. Il periodo che ho passato insieme a voi lo ricorderò per sempre. Spero che qualche giorno nel futuro realizzeremo ciò di cui abbiamo parlato.

Gerardo Ceccacci for all his help and advice while I was in Italy. *Giulio Ceccacci* for going out of his way to come and visit me in Delft while he was working on a contract in Belgium. Grazie tanto cugini, vi stimo tanto.

Zia Chiara, zio Cesare, zia Margherita, zio Virginio and cousins for having me in their homes during the Christmas holidays and during the summer. Vi ringrazio tanto per tutto e vi voglio tanto bene.

Storm and Scarlett Hiten, my cousins, for taking the time to visit me in the Netherlands from South Africa. I thank you both so much for how you supported me in that week.

Bjorn Thompson and Vicky Holford for the great time in Spain.

Francesco Ratti and Bernadette Peeters for their friendship and support.

Peeters family for welcoming me into their home at Den Bos on numerous occasions. I particularly thank them for the Carnival and Easter weekends.

Friends from Leiden and Amsterdam.

Stefano Invernizzi, Uberto Visconti, Julia Schoenwaelder, Konca Saher, Monica Rychtarikova, Andrew and Pearl Barendse at the TUDelft for their friendship.

E. De Ruiter and C.M Ravesloot for the friendly atmosphere in out office.

M. Lotter and M. Kaarsdorp for all the administrative work.

Robert Alfonsi for his friendship and for accompanying me to the airport with all my luggage when I left for home.

Daniel and Wolhuter Theron for the Afrikaans translation of the abstract.

Everyone else who I was not able to mention, but who also contributed to this thesis.

Thank you.

Dedication

I dedicate this thesis to my parents.

Table of Contents

Chapter 1

Introduction

Underground metropolitan transportation systems are found in all major cities of the world. They perform an important role in the service a city provides in terms of transportation. Underground metropolitan systems help maintain sanity above the ground even with the high traffic demands of large cities.

Ground movements induced by tunneling are transferred in the form of differential settlements to the surface infrastructure. Differential settlements cause the redistribution of the infrastructure's existing loads, causing critical stresses and strains to develop in areas for which the infrastructure initially may not have been designed. These redistributed loads put a question mark on the infrastructure's ability to continue performing one or both of their ultimate limit and serviceability limit state functions. The investigation into the ability of the infrastructure to withstand the ensuing displacements forms a major part of the design process in a large tunneling project.

There are many types of different structures on a tunnel route. Some of these structures constitute large and very complicated indeterminate structural systems. In order to investigate their ability to withstand these displacements, powerful software tools are necessary, such as finite element analysis programs. The problem is that in performing a complete investigation into the structural behaviour of these structures, finite element analyses will be required for each structure on the tunnel route. Time and economical constraints render this solution practically impossible.

Burland and Wroth (1974) and Burland *et al* (1977) developed a simple analytical damage assessment approach referred to as the limiting tensile strain approach **(LTS)**, using simply supported weightless elastic beams (Timoshenko 1931), which mimic the real structure undergoing displacements similar to those as induced by tunnels. These simply supported weightless elastic beams are used in order to judge the ability of the real structure to withstand the tunneling-induced displacements. According to the strains **(ε)** calculated in the simply supported elastic beams, the structures are

categorised into different damage categories (Boscarding and Cording 1989). The ensuing mitigating measures for the real structure are then based on the damage category as assigned to the structure.

The purpose of this study is to verify the accuracy of the **LTS** with regard to the prediction of the resulting strain levels in real structures subject to tunneling-induced ground settlements. The strain levels predicted by the **LTS** will be compared to the strain levels calculated from finite element analyses on models of the real structures. The diversity of structures in a city makes it very difficult for any study to make a general remark on the accuracy of using the **LTS** for this purpose. Nevertheless, structures can be categorised into general structural classes, whereby the accuracy of using the **LTS** on a specific class of structure can be studied. The structure considered in this study is a laterally unconfined, solid masonry wall, symmetrically positioned over the sagging zone of a green field settlement trough with no soil to wall friction, also otherwise referred to as a deep masonry beam.

This study focuses on the influence of differential vertical settlements on possible damage in solid masonry walls without foundations. A methodology, applicable for similar investigations envisaged for other structural classes, is hereby developed.

The mechanism of ground movements induced by tunnels is studied in chapter 2. This includes a definition of all the concerned variables (Burland and Wroth 1974) as well as a mathematical approach for the prediction of the settlement profile (green field settlement trough) induced by tunnels (Peck 1969, O'Reilly and New 1982 and extended by New and O'Reilly 1991). A means of predicting the ensuing displacements is very important to the engineer and therefore a mathematical description of the displacements is very practical in the damage assessment process. **LTS** is studied in chapter 4 and the divisions of the various damage categories discussed in chapter 3, even though there is no intention to justify them. In chapter 5, without changing the approach, **LTS** is analytically manipulated to render it specifically applicable to a laterally unconfined, solid masonry wall, symmetrically positioned over the sagging zone of a green field settlement trough with no soil to wall friction. Strain calculations, using the **LTS**, are performed for various wall length to height **(L/H)** ratios and undergoing predicted tunneling-induced displacements.

In chapter 6, the applicability of using the finite element method as an accurate solution to the differential equation, which describes the structural behaviour of deep beams, is verified. Bares and Bauverlag's (1969) analytical solution to the above differential equation is used to compare to the finite element method solution. In chapter 7, finite element models of solid masonry walls are built with **L/H** ratios corresponding to the **L/H** ratios of the simply supported elastic beams implemented by the **LTS** in the strain calculations. These models, under linear elastic conditions, are forced to mimic the relative maximum deflection (Δ_{mr}) of the settlement trough's sagging zone. The strain results obtained from the linear elastic finite element calculations are plotted against the corresponding deflection ratios (Δ/L) of the solid masonry walls. These plots are compared to similar plots constructed by the **LTS**, corresponding to the simply supported elastic beams. The Δ/L ratio is calculated by dividing the mid-span deflection (Δ) of the solid masonry wall by its span length (**L**). In using the **LTS**, the magnitude of Δ is equated to Δ_{mr}. The Δ/L ratio is therefore dependent on the properties of the settlement trough. The strain plot comparisons will provide an initial indication with regard to the accuracy of using the **LTS** in predicting the development of strain levels in solid masonry walls.

In chapter 8, the boundary conditions of the above models are changed to determine what influence the soil properties, directly under the wall, have on the wall Δ/L ratio. The investigation with regard to the soil to wall interaction leads to the definition of a vertical soil to wall stiffness ratio (K_{soil}/K_{wall}). As stated previously, the **LTS** assumes that Δ conforms exactly to Δ_{mr}. A nonlinear structural interface is, however, implemented between the wall and the pseudo soil, to model the influence of the soil interaction, with respect to the K_{soil}/K_{wall} ratio, without actually modeling the soil itself. The interface is forced to deform independently from the wall according to the shape of the predicted green field settlement trough. The properties of the wall remain linear elastic during these calculations, which are referred to as the semi-nonlinear analyses. These semi-nonlinear analyses are intended to facilitate the construction of graphs, which plot the predicted Δ/L ratios versus the "real" Δ/L ratios developed in the wall as a result of the soil interaction. The intention is to use the "real" Δ/L ratio to read off the corresponding strains from the respective ε:Δ/L relationships. These

relationships are plotted firstly by the **LTS** in chapter 5 as well as with the results of the linear elastic finite element analyses conducted in chapter 7.

In Chapter 9, both the **LTS** and the modified simple analytical damage assessment approach referred to as the modified limiting tensile strain method **(MLTS)** are applied in performing damage classifications on different solid masonry walls subject to tunneling-induced displacements. This highlights the difference in the damage categorisation, calculated by the respective analytical approaches. The author's modified version, the **MLTS** of the **LTS**, constitutes using the **ε:Δ/L** relationships obtained from the results of the linear elastic models in chapter 7 in conjunction with the reduced wall **Δ/L** ratios investigated in chapter 8.

In chapter 10 the semi-nonlinear models of the walls used in chapter 9 are modified into full nonlinear models by assigning nonlinear constitutive behaviour to the masonry constituting the wall. The resulting strain levels as well as induced damage, calculated with the full nonlinear wall models, are compared to the strain levels and damage predictions, calculated with both the **MLTS** and the **LTS** in chapter 9. The conservatism of the **LTS** with regard to categorising solid masonry walls into the different damage categories is judged. The ability of the **MLTS** in undertaking the same task is also judged.

This study is intended to pioneer the proliferation of similar studies for various structural classes, undergoing various modes of settlement deformation. If this can be achieved for different structural classes, it will be possible to develop a program to categorise different structures, subject to different modes of settlement deformation, into the respective tabulated damage categories. The ensuing mitigating measures can then be recommended based on the damage category assigned to the structure.

Chapter 2

Tunnelling in urban areas

2.1 Introduction

Our cities are under increased pressure to grow in size as the numbers of inhabitants increase continuously. In this day and age most of the cities in the world have exhausted their ability to grow in the horizontal direction, as there is no more land available for development. The only way for these cities to grow and accommodate the ever-growing population is to extend upwards in terms of sky rise buildings and to descend downwards in terms of tunnels.

Positive population growth exerts increased pressure on the cities' already pressured transportation system, which in turn has negative economic and environmental effects for society. Negative economic effects, to name a few, are the reduced life span of the cities' road networks, which is induced by the higher traffic demands, as well as the damage that the time lost in traffic jams has on the countries' economy. Negative environmental effects are increased noise and air pollution, which combine to negatively effect the health of the cities' citizens and this in itself is a negative economical effect as health insurances rise.

Although tunnels constructed in urban areas have many long-term environmental benefits, they also create significant environmental problems. Such problems induced during the construction process are construction traffic, vibrations, dust, noise pollution as well as temporary restrictions on access to certain roads and other public areas. Long-term problems induced by the presence of tunnels can include land and building acquisition, traffic and ventilation noise, vibration levels, ground water changes, pollution and damaging effects on the ecology.

The environmental impact that is concerned with the subsidence of the cities' infrastructure due to ground movements induced by tunneling has become of great concern to the cities' authorities. Construction of tunnels and deep excavations is accompanied by ground movements, which cause the redistribution of the surrounding

infrastructure's loads. This infrastructure, when initially designed may not have been designed to resist such redistribution of loads and therefore in the design of underground constructions, the potential for settlement damage on the existing surrounding infrastructure forms an essential boundary condition in the design stage. The settlement risk assessment studies therefore play an important role in the feasibility of underground works in urban surroundings.

The development of rational procedures is necessary for assessing the risks of damage to surrounding infrastructure. These procedures need to be coupled with effective protective measures, which may be implemented when predicted levels of damage are judged to be unacceptable from either serviceability or ultimate limit state points of view.

This chapter is devoted to the subject of ground movements induced by tunnels. Definitions of ground and foundation movements (Burland and Wroth 1974) are presented. Mathematical equations (Peck 1969, O'Reilly and New 1982 and extended by New and O'Reilly 1991) used to model the vertical and horizontal ground movements induced by tunnels, are elaborated. The fundamental purpose of this chapter is to assist the reader in developing a good idea of the mechanisms involved with regard to ground movements induced primarily by tunnels.

2.2 Ground movement due to tunneling and excavation

The construction of tunnels and surface excavations inevitably causes movements in the soil directly surrounding the tunnel or excavation. At the ground's surface, these soil movements form a settlement trough. Figure 2.1 schematically represents the transverse and longitudinal surface settlement trough above an advancing tunnel with its axis at depth (z_0) below ground level. It should be noted that in addition to this transverse settlement trough, which forms as a result of the presence of a completed tunnel directly below it, the construction of tunnels causes ground movements with a settlement trough developing above and ahead of the tunnel. This developing settlement trough can be seen as the longitudinal settlement trough, which is only present during the construction process.

Initially, the case of a single tunnel in "green field" conditions, without surface structures, will be considered. It has been accepted that irrespective of the type and size of the structures founded above the tunnel, the same settlement trough will develop. The method implemented follows that as outlined by Peck (1969), O'Reilly and New (1982) and extended by New and O'Reilly (1991).

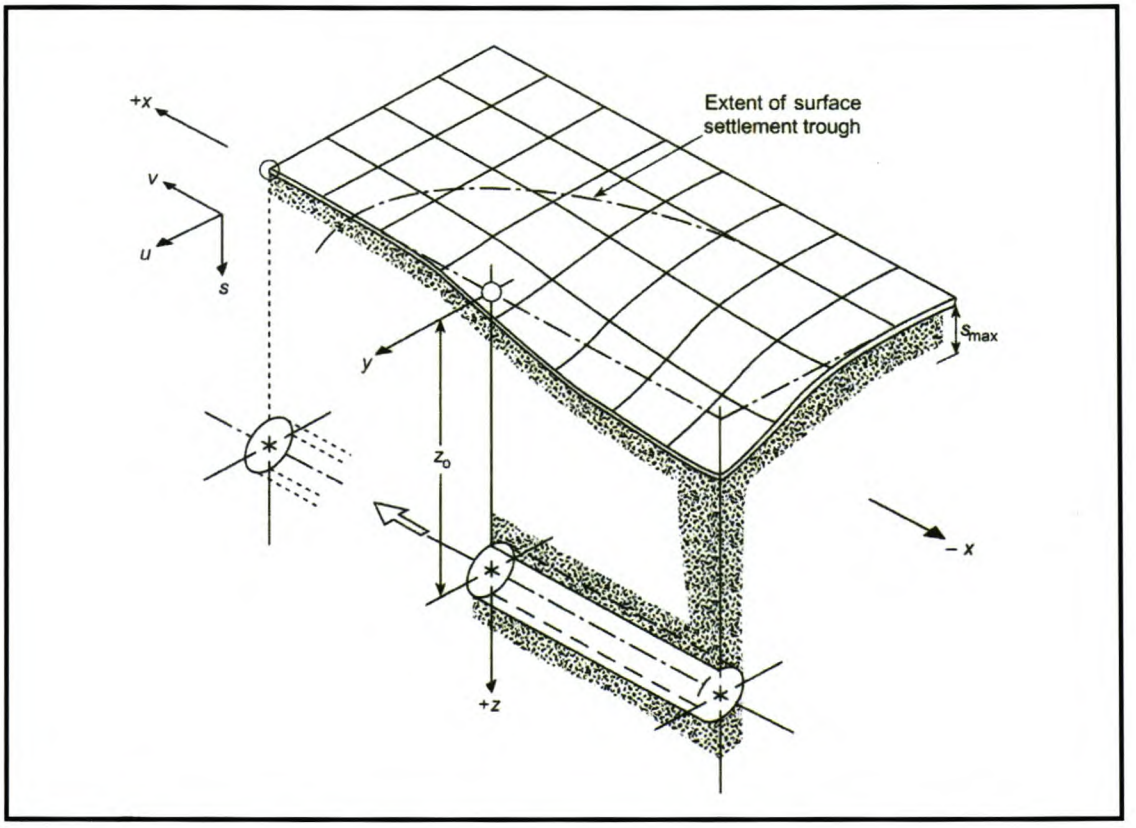

Figure 2.1 Ground settlements above an advancing tunnel (Burland and Wroth 1974).

Analysis of a considerable number of case records has demonstrated that the resulting transverse settlement trough, as presented in Figure 2.2, immediately after a tunnel has been constructed, is well described by a Gaussian distribution curve as follows:

$$S_v = S_{max} e^{\left(-\left(\frac{y^2}{2i^2}\right)\right)} \qquad (2.1)$$

Where:

- S_v is the vertical settlement.

- $\mathbf{S_{max}}$ is the maximum settlement on the tunnel centre line.
- **y** is the horizontal distance from the tunnel centre line.
- ***i*** is the horizontal distance from the tunnel centre line to the point of inflection on the settlement trough.

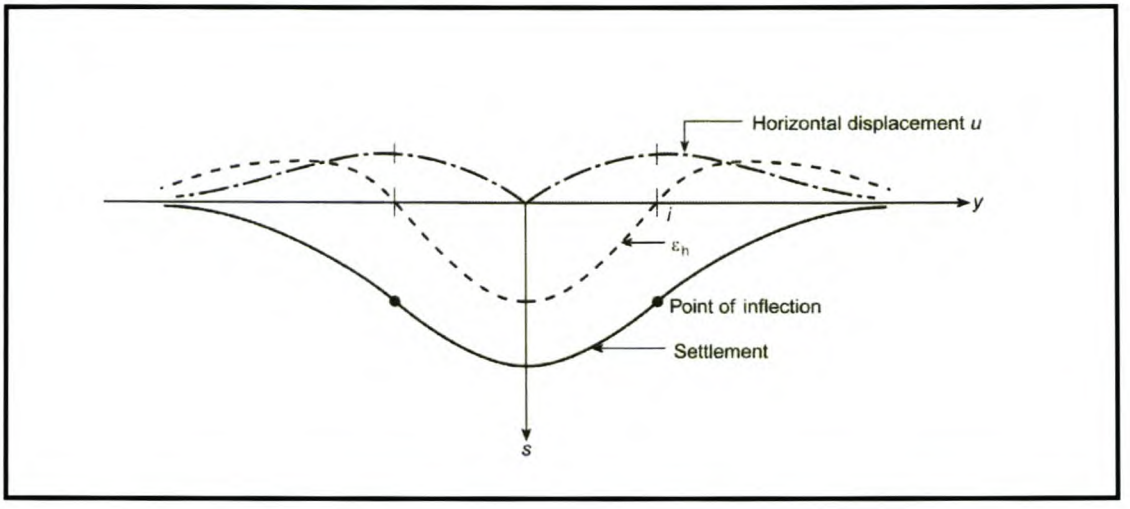

Figure 2.2 Transverse green field settlement trough (Burland and Wroth 1974).

For near surface settlements O'Reilly and New (1982) showed that the dimension ***i*** in Figure 2.2 is approximately a linear function of the depth $\mathbf{z_0}$ and independent of the method in which the tunnel was constructed. This was later confirmed by Rankin (1988). The simple approximate solution was assumed:

$$i = Kz_o \tag{2.2}$$

Values of the trough width parameter **(K)** for tunnels in clay and sands or gravels may be taken as approximately 0.5 and 0.25 respectively. The value of **K** is dependent on whether the ground is primarily cohesive or granular, and in the latter case on whether or not the tunnel is above or below the water table. The value of **K** for *surface* settlements is reasonably constant for tunnels at different depths in the same ground.

The volume of the settlement trough (per metre length of tunnel), $\mathbf{(V_s)}$, can be obtained by integrating equation (2.1) to give:

$$V_s = \sqrt{(2\pi)}iS_{max} \tag{2.3}$$

The volume loss **(V_l)** of V_s is defined by the following equation:

$$V_l = {}^{V_s}\!/_{V_t} \tag{2.4}$$

The V_l is defined as V_s divided by the volume per unit length of the excavated tunnel V_t. The V_l is a fundamental parameter and its magnitude is primarily dependent on the type of ground and on the tunneling method. V_l is mainly dependent on the workmanship, represented by the pressure control (tail void pressures and front pressures) in the tunneling boring machine **(TBM)**. A V_l of (0.005) 0.5% relates to very good performance and that of (0.02 and larger) 2% and larger relates to bad performance.

Note that for a tunnel with a circular cross-section of diameter **D**, V_s can be expressed in terms of V_l by the following equation:

$$V_s = V_l\left(\frac{\pi}{4}D^2\right) \tag{2.5}$$

For tunnels with non-circular cross-sections the term **($\pi D^2/4$)** in equation (2.5) can be replaced with the tunnels cross-sectional area. Equations (2.2) to (2.5) can be manipulated to derive the following equation, which calculates S_{max}, as:

$$S_{max} = \frac{0.31V_lD^2}{Kz_o} \tag{2.6}$$

Combining equations (2.1) and (2.6) helps derive the equation, which represents the mathematical description of the resulting transverse green field settlement trough immediately after a tunnel has been constructed:

$$S_v = \frac{0.31V_lD^2}{Kz_o}e^{\left(-\left(\frac{y^2}{2i^2}\right)\right)} \tag{2.7}$$

Until now, only vertical ground settlements have been discussed. There is very little measured data relating to the horizontal movements of buildings caused by horizontal ground movements induced by tunneling. The data that does exist seems to show that the assumption of O'Reilly and New (1982) is generally conservative, but reasonable. Their assumption is that the resultant vectors of ground movement are directed towards the tunnel axis. The vector of ground movement has vertical and horizontal components $\mathbf{S_v}$ and $\mathbf{S_h}$ respectively. If it is assumed that the vector is directed towards the tunnel axis, then the horizontal settlement of the settlement trough is calculated with the following equation.

$$S_h = \left(\frac{y}{z_o}\right) S_v \tag{2.8}$$

This allows for a simple assessment of horizontal movement, which may contribute to horizontal tensile strains, potentially causing structural damage. Figure 2.3 depicts the relation between the vertical settlement trough, horizontal movements and horizontal strains occurring at ground level for a single tunnel. The horizontal ground strains, (ε_h), can be calculated by differentiating equation (2.8) with respect to **y**, remembering that $\mathbf{S_v}$, as in equation (2.7), is a function of **y**. Therefore ε_h at a certain position along the settlement trough is:

$$\frac{dS_h}{dy} = \varepsilon_h = f(y) \tag{2.9}$$

The maximum horizontal movements along the settlement trough take place at the positions of the inflection points. The horizontal strain at these positions is therefore equal to zero. The horizontal strains in the sagging zone **(- i < y < i)** of the settlement trough are compressive and those in the hogging zone **(- i > y > i)** of the settlement trough are tensile.

In some cases the temporary longitudinal settlement trough, which is present only during the construction of the tunnel, can have a larger effect on the settlement damage to a building than that of the transverse settlement trough. The ground

movements and associated building strains should then be determined from the longitudinal settlement trough, which can be assumed to have the form of a cumulative probability curve as described by Attewell and Woodman (1982) and summarised by New and Bowers (1994). A result of this assumption is that settlement directly above the tunnel face corresponds to $\mathbf{0.5S_{max}}$.

When multiple tunnels are to be constructed, it is generally accepted that the ground deformations of the respective tunnels can be superimposed onto one another. In the case of multiple tunnels where the clear distance between the two tunnels is smaller than the tunnel width, this assumption is seen to be unconservative. Assuming a larger $\mathbf{V_l}$ for the second tunnel and then superimposing both tunnels ground movements can solve this problem. It should be noted that in some cases a single tunnel could have a more adverse damaging effect on a building than multiple tunnels will. This is due to the fact that relative displacements cause the settlement damage to buildings and not the absolute displacements.

2.3 Definitions of ground and foundation movements

Burland and Wroth (1974) proposed a consistent set of definitions based on the displacements (either measured or calculated) of a number of discrete points on the foundations of a building. It was deemed important not to use terms, which would prejudice any conclusions about the distortions of the superstructure itself, because these depend on many additional factors. The definitions are represented in Figure 2.3.

The following are a few important points:

a) *Rotation or slope* θ is the change in gradient of a line joining two reference points (e.g. AB in Figure 2.3 (a)).

b) The *angular strain* α is defined in Figure 2.3 (a). It is positive for upward concavity (sagging) and negative for downward concavity (hogging).

c) *Relative deflection* Δ is the displacement of a point relative to the line connecting two reference points on either side (See Figure 2.3 (b)). The sign convention is as for (b).

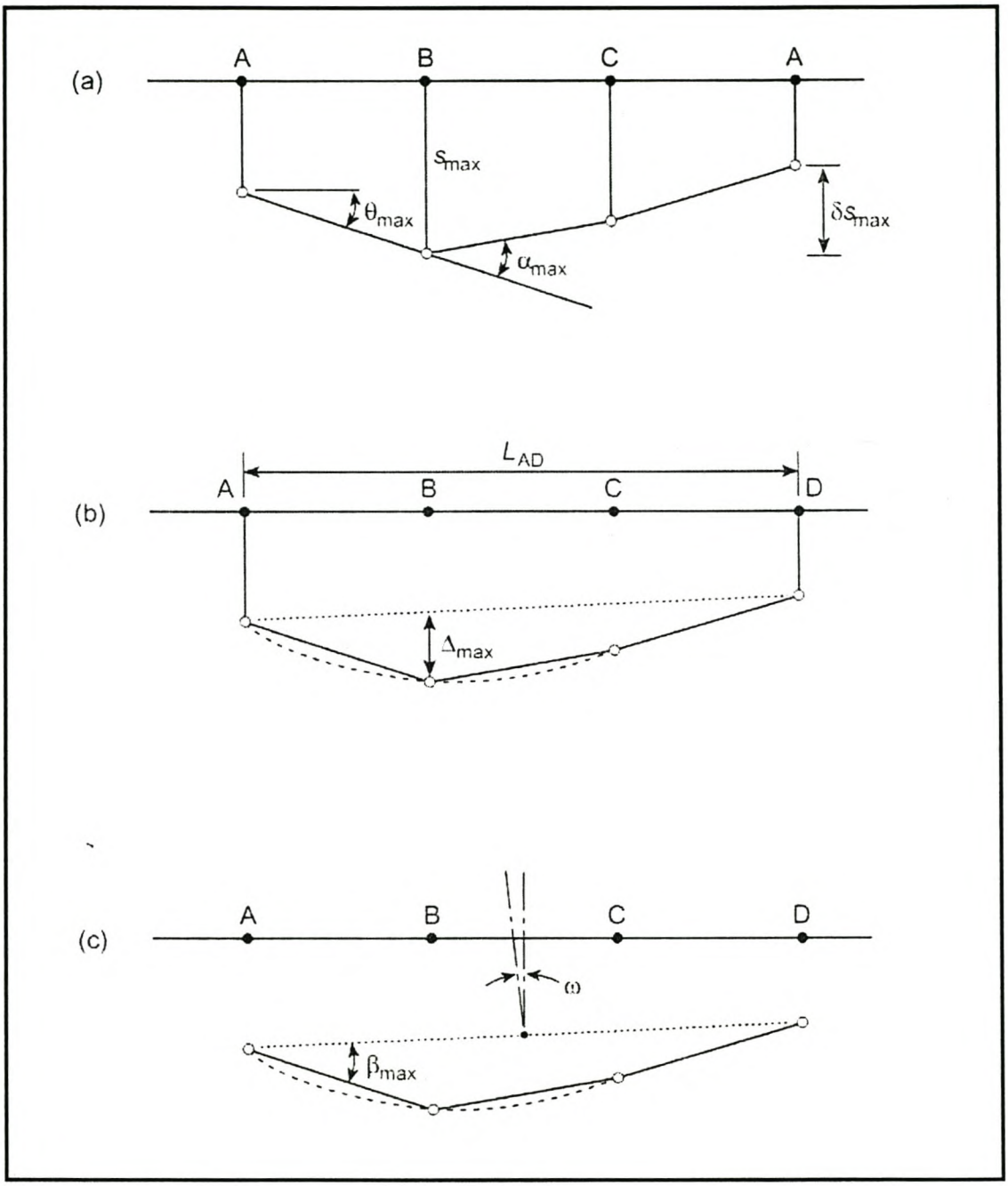

Figure 2.3 Ground and foundation movements (Burland and Wroth 1974).

(a) Settlement **s**, relative settlement **δs**, rotation **θ**, and angular strain **α**:

(b) Relative deflection **Δ** and deflection ratio **Δ/L**

(c) Tilt **ω** and relative rotation (angular distortion) **β**

d) *Deflection ratio* (sagging ratio or hogging ratio) is denoted by Δ/L where **L** is the distance between the two reference points defining Δ. The sign convention is as for (b) and (c).

e) *Tilt* ω describes the rigid body rotation of the structure or a well-defined part of it (See Figure 2.3 (c)).

f) *Relative rotation* (angular distortion) β is the rotation of the line joining two points, relative to the tilt ω (See Figure 2.3 (c)). It is not always straightforward to identify the tilt and the evaluation of β with angular strain α. For these reasons Burland and Wroth preferred the use of Δ/L as a measure of building distortion.

g) *Average horizontal strain* ε_h is defined as the change of length δL over the length **L**. In soil mechanics it is customary to take a reduction of length (compression) as positive. In this study, the walls' are modeled to exhibit no soil to wall friction. This results in no horizontal strains being transferred from the soil to the wall.

The above definitions have been formulated with the intention only to apply to in-plane deformations. It is important to understand that no attempt has been made to define three-dimensional behaviour.

2.4 Summary

In the introduction to this chapter, the needs as well as the difficulties associated with tunneling in urban areas were presented. A short description of the mechanisms controlling the need for tunnels as well as both the short and long-term negative environmental effects of tunneling were discussed. It was explained how the subsidence of the cities' infrastructure due to ground movements induced by tunneling is a serious environmental impact that needs to be taken into account during the design of a tunnel. The need for a simple procedure, the **LTS,** to perform this function was highlighted. Section 2.2 discussed the actual ground movements as induced by

tunneling and excavations. A mathematical model used to describe these movements was also presented. Section 2.3 discussed the definitions of ground and foundation movements as proposed by Burland and Wroth (1974)

The next chapter presents the approach as implemented by the **LTS** in classifying structures in terms of expected damage as induced by ground movements. The concept of the limiting tensile strain (ε_{lim}) is presented and it is shown how this strain is associated with the damage classification of structures.

Chapter 3

Damage classification related to the limiting tensile strain

3.1 Introduction

The assessment of the degree of building damage can be a very subjective matter. It may be determined by factors such as the function of the building, the caution of the professional engineer concerned about litigation, local experience, market value and saleability of the property. In the absence of objective guidelines for the assessment of the degree of building damage, unrealistic expectations towards building performance can develop. For the assessment of the risk of damage to buildings experiencing ground movements, the classification of damage is clearly an important consideration. It has been found in the UK that the development of an objective classification of damage, is helping to create realistic attitudes towards building damage, as well as providing logical and objective criteria for the design of buildings and other structures subject to ground movements.

Firstly in this chapter, the method as proposed by Burland *et al* (1977) for the classification of damage is presented. Secondly, the idea by Burland and Wroth (1974) that tensile strain might be a fundamental parameter in determining the onset of cracking is explored. Lastly, the concept of the limiting tensile strain ε_{lim} (Burland *et al* 1977) is defined and its application as proposed by Boscardin and Cording (1989) in the damage classification of structures, discussed.

3.2 Categories of damage

Categories of damage for buildings can be considered with regard to the effect on the aesthetics, serviceability and stability of the building. As the movements of the building foundation increase, damage to a building will gradually progress from affecting its aesthetics, then its serviceability and finally its stability. Table 3.1 defines six categories of damage, numbered 0 to 5 in increasing order of severity. It is taken that categories 0, 1 and 2 relate to aesthetical damage, 3 and 4 to serviceability damage and 5 relates to damage affecting the stability of the building. It was first put

forward by Burland *et al* (1977), who drew on the work by Jennings and Kerrich (1962), the UK National Coal Board (1975) and MacLeod and Littlejohn (1974). Since then it has been adopted with only slight modifications by BRE (1981 and 1990), the Institution of Structural Engineers London (1978, 1989, 1994 and 2000) and by the Institution of Civil Engineers and BRE again in Freeman *et al* (1994).

Category of damage	Normal degree of severity	**Description of typical damage** (ease of repair in bold type). Note: Crack width is only one factor in assessing category of damage and should not be used on its own as a direct measure of it.
0	Negligible	Hairline cracks less than about 0.1mm wide.
1	Very slight	**Fine cracks that are easily treated during normal decoration.** Damage generally restricted to internal wall finishes. Close inspection may reveal some cracks in external brickwork or masonry. Typical crack widths up to 1mm.
2	Slight	**Cracks easily filled. Redecoration probably required. Recurrent cracks can be masked by suitable linings.** Cracks may be visible externally and **some repainting may be required to ensure weather-tightness.** Doors and windows may stick slightly. Typical crack widths up to 5mm.
3	Moderate	**The cracks require some opening up and can be patched by a mason. Repainting of external brickwork and possibly a small amount of brickwork to be replaced.** Doors and windows sticking. Service pipes may fracture. Weather-tightness often impaired. Typical crack widths are 5-15mm or several > 3mm.
4	Severe	**Extensive repair work involving breaking-out and replacing sections of walls, especially over doors and windows.** Windows and doorframes distorted, floor sloping noticeably[1]. Walls leaning[1] or bulging noticeably, some loss of bearing in beams. Service pipes disrupted. Typical crack widths are 15-25mm, but also depends on the number of cracks.
5	Very severe	**This requires a major repair job involving partial or complete rebuilding.** Beams lose bearing; walls lean badly and require shoring. Windows broken with distortion. Danger of instability. Typical crack widths are greater than 25mm, but depend on the number of cracks.

[1] Note: Local deviation of slope, from the horizontal or vertical, of more than 1/100 will normally be clearly visible. Overall deviations in excess of 1/150 are undesirable.

Table 3.1 Classification of visible damage to walls with particular reference to ease of repair of plaster and brickwork or masonry (Burland *et al* 1977).

The system of classification in Table 3.1 is based on the ease of repair of the visible damage. Important points to be noted when considering the classification are:

a) The classification relates only to the visible damage at a given time and not to its cause or possible progression, which are separate issues.

b) Classification of damage solely on crack width must be resisted. It is the ease of repair that is the critical factor in determining the category of damage.

c) The classification was developed for brickwork or block work and stone masonry. It can be adopted for other forms of cladding, but is not intended to apply to reinforced concrete structural elements.

d) More stringent criteria may be necessary where damage may lead to corrosion, penetration or leakage of harmful liquids and gases or structural failure.

Table 3.1 also lists the "normal degree of severity" associated with each category. These degrees of severity relate to standard domestic and office buildings and serve as a guide to building owners and occupiers. In special circumstances, such as for buildings with valuable or sensitive finishes, this ranking of severity of damage may not be appropriate.

The dividing line between damage categories 2 and 3 is very important as case records show that damage up to category 2 can result from a variety of causes, either from within the structure itself (e.g. shrinkage or thermal effects), or damage associated with ground movements. Identification of the cause of damage is usually very difficult and it normally results from a combination of causes. If the damage exceeds category 2 the cause is usually much easier to identify and it is frequently associated with ground movements only. The division between damage category 2 and 3 therefore represents an important threshold.

3.3 Onset of visible cracking

Tensile strain usually, but not always causes cracking in masonry walls. Following the work of Polshin and Tolkar (1957), Burland and Wroth (1974) explored the idea that tensile strain might be a fundamental parameter in determining the onset of cracking. They showed that for a given material, the onset of visible cracking is associated with a well-defined value of average tensile strain that is not sensitive to the mode of deformation. They defined this as a critical tensile strain (ε_{crit}), which is measured over a gauge length of a metre or more.

Burland and Wroth 1974 made the following important observations.

(a) The average values of ε_{crit} at which visible cracking occurs are very similar for a variety of types of brickwork and block work and are in the range 0.05 to 0.1 %.

(b) For reinforced concrete beams the onset of visible cracking occurs at lower values of tensile strain in the range 0.03 to 0.05 %.

(c) The above values of ε_{crit} are much larger than the local tensile strains corresponding to tensile failure.

(d) The onset of visible cracking does not necessarily represent a limit of serviceability. Provided the cracking is controlled, it may be acceptable to allow deformations well beyond the initiation of visible cracking.

3.4 Limiting tensile strain – serviceability parameter

Burland *et al* (1977) replaced the concept of "critical tensile strain" ε_{crit} with that of "limiting tensile strain" (ε_{lim}). The importance of this is that ε_{lim} can be used as a serviceability parameter that can be varied to take into account differing materials and serviceability limit states.

Boscardin and Cording (1989) developed a concept of differing levels of tensile strain. They showed that the categories of damage given in Table 3.1 could be broadly related to ranges of ε_{lim}. These ranges are tabulated in Table 3.2 and it is important as it provides a link between estimated building deformations and the possible severity of damage.

Category of damage	Normal degree of severity	Limiting tensile strain (ε_{lim}) (%)
0	Negligible	0-0.05
1	Very slight	0.05-0.075
2	Slight	0.075-0.15
3	Moderate*	0.15-0.3
4 to 5	Severe to very severe	>0.3

*Note: Boscardin and Cording (1989) describe the damage corresponding to ε_{lim} in the range 0.15-0.3 % as "moderate to severe". However, none of the cases quoted by them exhibits severe damage for this range of strains. There is therefore no evidence to suggest that tensile strains up to 0.3 per cent will result in severe damage.

Table 3.2 Relationship between category of damage and ε_{lim} (Boscardin and Cording 1989).

3.5 Summary

This chapter has provided a short introduction into the classification of damage as proposed by Burland *et al* (1977) and as implemented in the **LTS** (Burland and Wroth 1974).

It also presented a means of performing this damage categorisation with regards to the development of strain levels ε_{lim} (Boscardin and Cording 1989).

The next chapter presents an overview pertaining to the **LTS** (Burland and Wroth 1974).

Chapter 4

Simple Analytical Damage Assessment Approach: Limiting tensile strain method (LTS)

Burland and Wroth (1974) and Burland *et al* (1977) used the concept of limiting tensile strain ε_{lim} to study the onset of cracking in simply supported weightless elastic beams undergoing sagging and hogging modes of deformation.

This chapter firstly investigates the respective deflection calculations with respect to two different simply supported elastic beam models. The first model is of a simply supported elastic beam under the influence of a point load **(P)** at mid-span and the second of a simply supported elastic beam under the influence of a uniformly distributed load **(q)**. Secondly, the sagging and hogging modes of settlement deformation are discussed and then the general **LTS** equations, used to calculate the strains in the simply supported elastic beams, derived. Thirdly, it is shown how the **LTS** accounts for horizontal strains associated with horizontal ground movements. Lastly, a short description with regard to how the **LTS** determines the relevant building dimensions is presented.

4.1 Deflection: simply supported elastic beam (central point load)

In deflection calculations of simply supported elastic beams exhibiting **L/H** ratios larger than 10, only the influence of bending is taken into account, as the influence of shear is negligibly small. In the case of deep beams however, the influence of shear on its deflections may be significant. Deep beams are usually associated with **L/H** ratios of magnitude 3 and smaller, which is considerably lower than 10. An additional deflection caused by the shearing force will be produced in the form of a mutual sliding of adjacent cross sections along each other.

The deflection of a simply supported beam under the influence of a point load **P** applied at mid-span, Figure 4.1, due to both bending and shearing modes of deformation can be derived from the principle of virtual work as (Timoshenko 1931):

$$\Delta = \frac{PL^3}{48EI}\left(1+\left(\alpha\frac{12r^2}{L^2}\right)\left(\frac{E}{G}\right)\right) \tag{4.1}$$

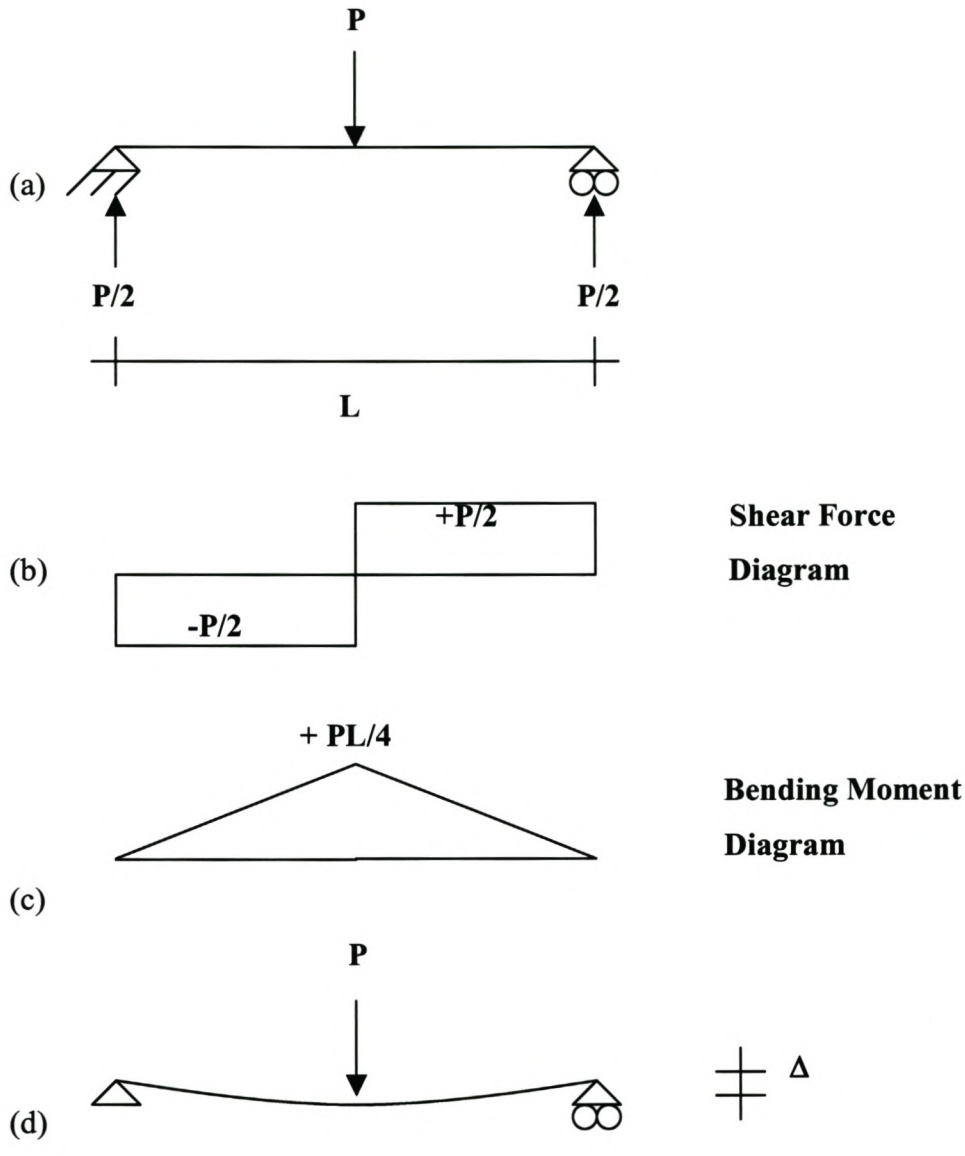

Figure 4.1 Simply supported beam under the influence of a centrally applied point load.

(a) Model of the beam geometry and load.

(b) Shear force diagram of the beam in (a).

(c) Bending moment diagram of the beam in (a).

(d) Deflected shape of the beam in (a).

Young's modulus of elasticity is denoted by **(E)**, the shearing modulus of elasticity is denoted by **(G)** and the cross-sections inertial moment by **(I)**. The shear form factor taking into account the parabolic shear stress distribution of a rectangular beam to the contribution of shear effects to the overall deflection **(α)** and the radius of gyration of the cross-section by **(r)**.

The radius of gyration of a cross section is represented by the following equation:

$$r = \sqrt{\frac{I}{A}} \tag{4.2}$$

Where **(A)** is the area of the beam cross-section.

The value of α for a circular cross-section is α = 10/9 and for a rectangular cross section α = 6/5. Netzel (ITA 2003) corrected the **LTS** as proposed by Burland and Wroth (1974) with reference to using the correct value of the shear form factor for a rectangular cross-section.

Combining equations (4.1) and (4.2), the deflection of a simply supported beam under the influence of **P** applied at mid-span, due to both bending and shearing modes of deformation can be expressed as follows:

$$\Delta = \frac{PL^3}{48EI}\left(1+\left(\alpha\frac{12I}{AL^2}\right)\left(\frac{E}{G}\right)\right) \tag{4.3}$$

4.2 Deflection: simply supported elastic beam (uniform load)

The deflection of a simply supported beam under the influence of **q**, Figure 4.2, due to both bending and shearing modes of deformation can be derived from energy principles to be (Timoshenko 1931):

$$\Delta = \frac{5qL^4}{384EI}\left(1+\left(\alpha\frac{48r^2}{5L^2}\right)\left(\frac{E}{G}\right)\right) \tag{4.4}$$

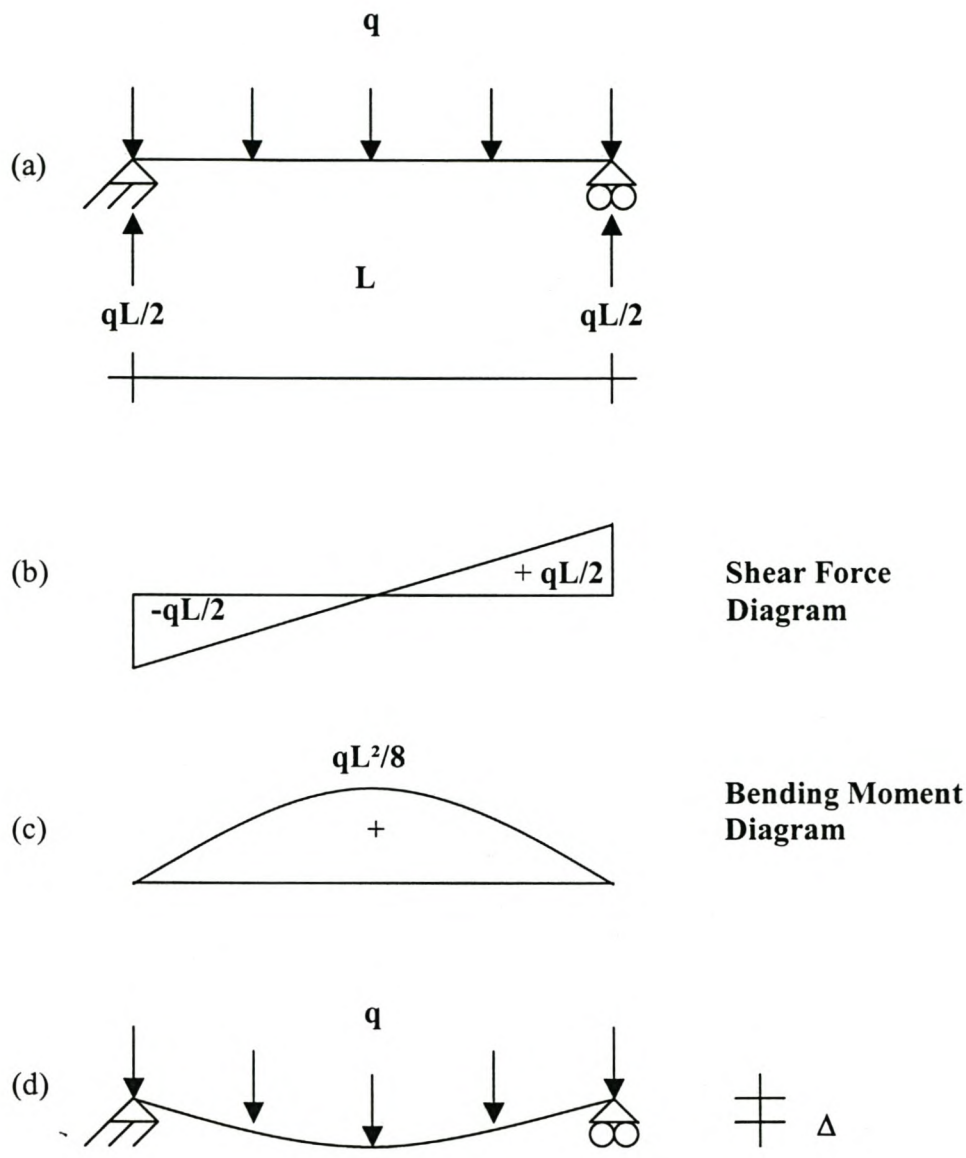

Figure 4.2 Simply supported beam under the influence of a uniformly distributed load.

(a) Model of the beam geometry and load.

(b) Shear force diagram for the beam in (a).

(c) Bending moment diagram for the beam in (a).

(d) Deflected shape of the beam in (a).

The variables in equation (4.4) are as those in equation (4.1), with **q** the uniformly distributed load expressed in N/mm replacing the point load **P** expressed in N.

Combining equations (4.2) and (4.4), the deflection of a simply supported beam under the influence of a uniformly distributed load, due to both bending and shearing modes of deformation can be expressed as:

$$\Delta = \frac{5qL^4}{384EI}\left(1+\left(\alpha\frac{48I}{5AL^2}\right)\left(\frac{E}{G}\right)\right) \tag{4.5}$$

4.3 Sagging and Hogging Modes of Deformation

This section describes how the **LTS** predicts the development of strains in structures subjected to tunnel-induced displacements. The equations involved in the respective strain calculations are derived from equations (4.3) and (4.5). Figure 4.3 illustrates the approach adopted by Burland and Wroth (1974), where a rectangular simply supported elastic beam of span length **L** and height **H** represents the building.

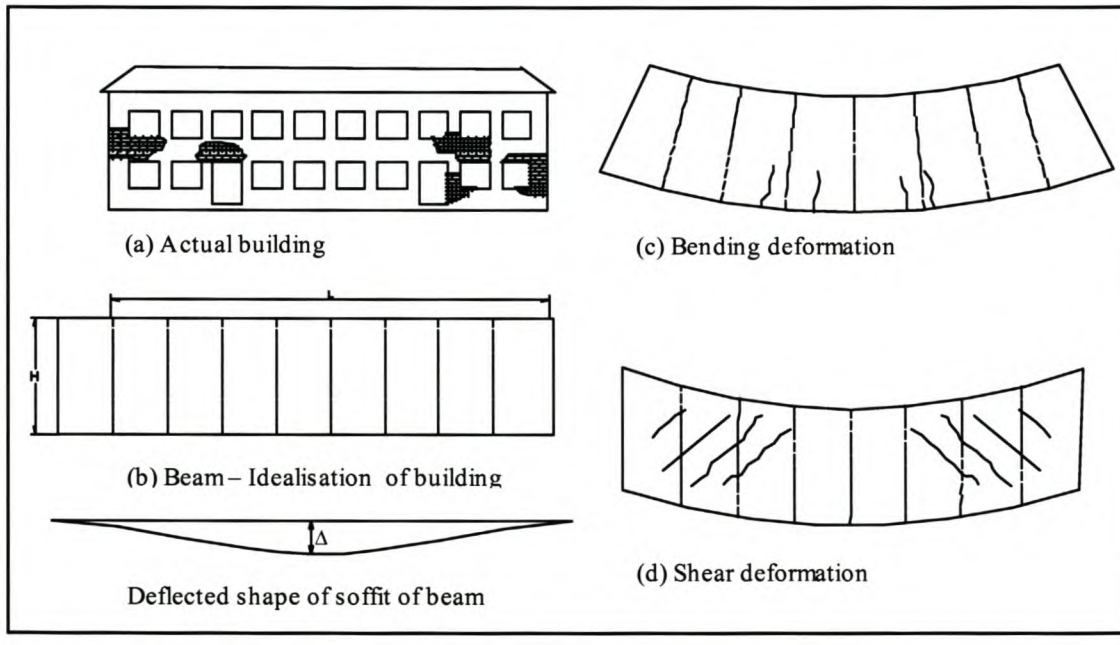

Figure 4.3 Cracking of a simply supported beam in bending and in shear.

For a given deflected building shape, tensile strains are calculated to determine at which **Δ/L** ratio cracking will initiate for both hogging and sagging modes of deformation. The strain distribution within the beam is dependent on the beam's mode of deformation. Two extreme modes are bending only about a neutral axis at the

center (Figure 4.3 (c)) and shearing only (Figure 4.3 (d)). For the bending mode of failure, cracking will occur at the bottom extreme fiber, which is where the tensile strains are a maximum. Diagonal cracking will initiate due to the shearing mode of failure, as the maximum tensile strains are inclined at 45°. The above modes of deformation occur simultaneously and it is therefore necessary to calculate both bending and diagonal tensile strains to ascertain which mode is limiting. The dominant characteristic strain is dependent on the **L/H** ratio of the building.

The mid-span deflection of a simply supported beam under the influence of **P** due to both bending and shearing modes of deformation is as equation (4.3):

$$\Delta = \frac{PL^3}{48EI}\left(1+\left(\alpha\frac{12I}{AL^2}\right)\left(\frac{E}{G}\right)\right) \tag{4.6}$$

and that of a simply supported beam under the influence of **q** due to both bending and shearing modes of deformation is as equation (4.5):

$$\Delta = \frac{5qL^4}{384EI}\left(1+\left(\alpha\frac{48I}{5AL^2}\right)\left(\frac{E}{G}\right)\right) \tag{4.7}$$

The beam displacements are a function of the beam load as can be seen in equations (4.6) and (4.7). The stresses, at different positions within the body of the beam, are also functions of the beam load. Stresses can be related to strains with the aid of Young's modulus of elasticity **E** and the shear modulus of elasticity **G**. In this case, when it is decided at which positions within the body of the beam the strains are desired, the stresses sampled at those positions can be related to the strains, which in turn are related to the mid-span deflections **Δ**, as calculated with equations (4.6) and (4.7). Then, for various mid-span deflections **Δ** the magnitudes of the strains at these respective positions within the body of the beam can be calculated. Burland and Wroth (1974) decided to calculate the maximum bending strain (ε_{bmax}), on the beam's bottom fiber at mid-span and the diagonal tensile strain (ε_d), on the neutral axis at quarter span.

The relationship between ε_{bmax} and Δ of a simply supported beam, loaded with either a point load at mid-span or a uniformly distributed load, can be derived as follows:

Figure 4.4 represents the bending stress distribution for a rectangular section under the influence of a bending moment **M**. As stated previously, ε_{bmax} is sampled on the bottom fibre at mid-span due to it being the position at which the maximum strain develops, resulting from bending under the influence of the above stated loads.

Bending stress in a beam is calculated with the following equation:

$$\sigma = \frac{Mt}{I} \tag{4.8}$$

Where in this case **(M)** is the bending moment at mid-span of the beam.

The distance from the cross-section's neutral axis to the fibre at which the stress is calculated is denoted by **(t)** and **(I)** represents the moment of inertia resisting bending.

The bending moment at mid-span of a simply supported beam under the influence of **P** is:

$$M = \frac{PL}{4} \tag{4.9}$$

The bending moment at mid-span of a simply supported beam under the influence of **q** is:

$$M = \frac{qL^2}{8} \tag{4.10}$$

The following relation uses Young's modulus of elasticity to relate the stress to the strain for the case of linear elasticity:

$$\sigma = E\varepsilon \tag{4.11}$$

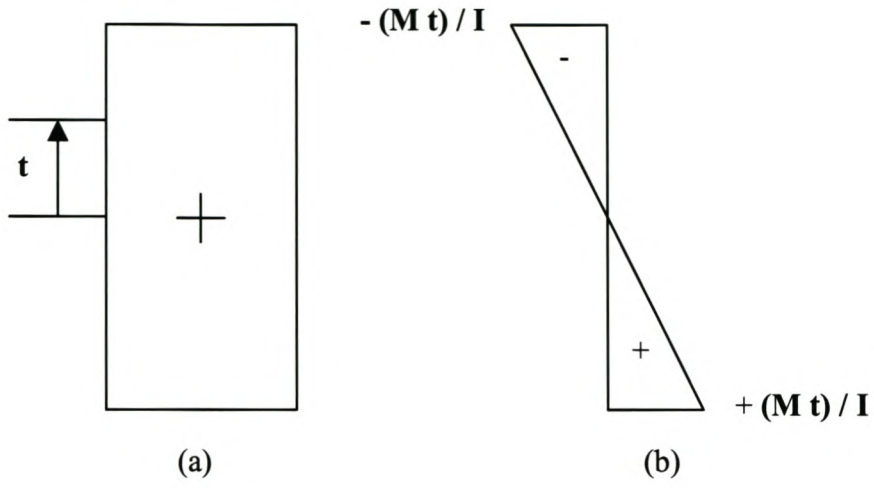

Figure 4.4 Flexural bending: rectangular cross-section.

(a) Rectangular cross-section transmitting a bending moment **M**.

(b) Linear bending stress distribution.

The combination of equations (4.8), (4.9) and (4.11) results in the following equation expressing ε_{bmax} for a simply supported beam under the influence of **P**:

$$\varepsilon_{b\max} = \frac{PLt}{4EI} \tag{4.12}$$

The combination of equations (4.8), (4.10) and (4.11) result in the following equation expressing ε_{bmax} for a simply supported beam under the influence of **q**:

$$\varepsilon_{b\max} = \frac{qL^2t}{8EI} \tag{4.13}$$

Making **P** the dependent variable of equation (4.12) results in the following equation:

$$P = \left(\frac{4EI}{Lt}\right)\varepsilon_{b\max} \tag{4.14}$$

Making **q** the dependent variable of equation (4.13) results in the following equation:

$$q = \left(\frac{8EI}{L^2 t}\right)\varepsilon_{b\max} \tag{4.15}$$

Substituting equation (4.14) into equation (4.6) provides the relation between **Δ** and ε_{bmax} of a simply supported beam under the influence of **P**:

$$\Delta = \left(\left(\frac{L^2}{12t}\right) + \left(\left(\frac{I\alpha}{At}\right)\left(\frac{E}{G}\right)\right)\right)\varepsilon_{b\max} \tag{4.16}$$

Substituting equation (4.15) into equation (4.7) provides the relation between **Δ** and ε_{bmax} of a simply supported beam under the influence of **q**:

$$\Delta = \left(\left(\frac{5L^2}{48t}\right) + \left(\left(\frac{I\alpha}{At}\right)\left(\frac{E}{G}\right)\right)\right)\varepsilon_{b\max} \tag{4.17}$$

The relationship between ε_d and Δ of a simply supported beam loaded with either a point load at mid-span or with a uniformly distributed load, can be derived as follows:

The diagonal tensile strain ε_d, as proposed by Burland and Wroth (1974) is to be sampled at the neutral axis of the beam's cross-section at quarter span. The shear stress distribution varies parabolically over the depth of the cross-section as is represented in Figure 4.5.

The average shear stress (τ_{avg}) over the entire cross-section is calculated as follows:

$$\tau_{avg} = \frac{V}{A} \tag{4.18}$$

The value of the shear stress on the neutral axis is calculated as follows:

$$\tau = k\tau_{avg} \tag{4.19}$$

The numerical factor **(k)** is multiplied with the average shear stress on the cross-section to obtain the maximum shear stress at the position of the neutral axis. The value of **k** for a rectangular section is **k** = 3/2.

For a state of pure shear the absolute values of the principle stresses **(σ_1)**, **(σ_2)** are equal to the absolute value of the shear stress **(τ)**. This is a result that is derived from the study of stress transformations and it is graphically demonstrated in Figure 4.6.

Thus:

$$\sigma_1 = |\sigma_2| = |\tau| \tag{4.20}$$

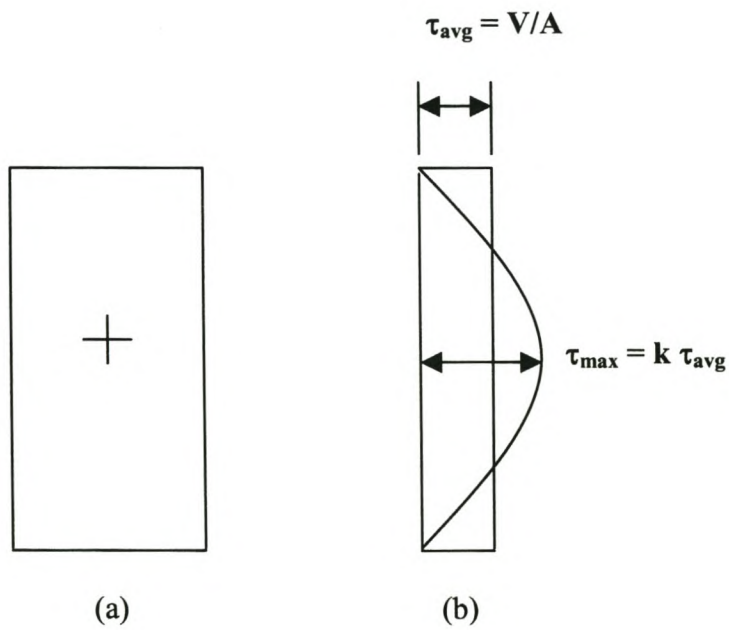

Figure 4.5 Shearing: Rectangular cross-section.

(a) Rectangular cross-section transmitting a vertical shear force **V**.

(b) Real parabolic and average shear stress distributions.

This is if:

$$-\sigma_1 = \sigma_2 \tag{4.21}$$

The strain ε_d is calculated with the following equation:

$$\varepsilon_d = \varepsilon_1 = \frac{\sigma_1}{E} - \nu\frac{\sigma_2}{E} \tag{4.22}$$

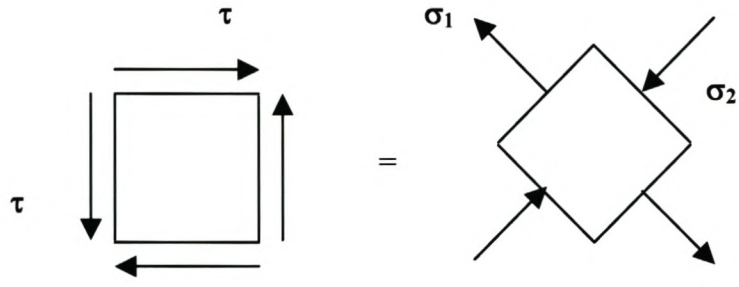

Figure 4.6 Stress transformations from a state of pure shear to a state of principal stresses.

By substituting equations (4.20) and (4.21) into equation (4.22), the following equation is obtained:

$$\varepsilon_d = \left(\frac{\tau}{E}\right)(1+\nu) \tag{4.23}$$

The expression for the shear modulus in terms of Young's modulus of elasticity is:

$$G = \frac{E}{2(1+\nu)} \tag{4.24}$$

By substituting equation (4.24) into equation (4.23), the following equation for ε_d is obtained:

$$\varepsilon_d = \frac{\tau}{2G} \tag{4.25}$$

Equations (4.18) and (4.19) substituted into equation (4.25) yields the following expression for ε_d:

$$\varepsilon_d = \frac{kV}{2AG} \tag{4.26}$$

The value of the shear force **(V)** at quarter span of the beam loaded with **P** is:

$$V = \frac{P}{2} \tag{4.27}$$

In the case of the beam loaded with **q**:

$$V = \frac{qL}{4} \tag{4.28}$$

By substituting equations (4.27) into equation (4.26), ε_d of the beam loaded with **P** can be expressed in terms of **P** as follows:

$$\varepsilon_d = \frac{kP}{4AG} \tag{4.29}$$

By substituting equation (4.28) into equation (4.26), ε_d of the beam loaded with **q** can be expressed in terms of **q** as follows:

$$\varepsilon_d = \frac{kqL}{8AG} \tag{4.30}$$

Making **P** the dependent variable of equation (4.29) results in the following expression for **P** in terms of ε_d of the beam loaded with **P**:

$$P = \left(\frac{4AG}{k}\right)\varepsilon_d \tag{4.31}$$

Making **q** the dependent variable of equation (4.30) results in the following expression for **q** in terms of ε_d of the beam loaded with **q**:

$$q = \left(\frac{8AG}{kL}\right)\varepsilon_d \tag{4.32}$$

Substituting equation (4.31) into equation (4.6) provides the relation between Δ and ε_d at quarter span of a simply supported beam loaded with **P**:

$$\Delta = \left(\left(\frac{AGL^3}{12kEI}\right) + \left(\frac{L\alpha}{k}\right)\right)\varepsilon_d \tag{4.33}$$

Substituting equation (4.32) into equation (4.7) provides the relation between Δ and ε_d of a simply supported beam loaded with **q**:

$$\Delta = \left(\left(\frac{5AGL^3}{48kEI}\right) + \left(\frac{L\alpha}{k}\right)\right)\varepsilon_d \tag{4.34}$$

Now that the mid-span deflection's Δ have been related to the various forms of strains in equations (4.16), (4.17), (4.33) and (4.34), it is possible to mathematically manipulate these equations so as to find a relation between the Δ/L ratio and these various forms of strains.

The relationships between ε_{bmax}:Δ/L and ε_d:Δ/L for the simply supported beam loaded with **P** are represented with the following equations:

$$\frac{\Delta}{L} = \left(\left(\frac{L}{12t}\right) + \left(\left(\frac{I\alpha}{AtL}\right)\left(\frac{E}{G}\right)\right)\right)\varepsilon_{b\max} \tag{4.35}$$

$$\frac{\Delta}{L} = \left(\frac{AGL^2}{12kEI} + \left(\frac{\alpha}{k} \right) \right) \varepsilon_d \tag{4.36}$$

The relationships between ε_{bmax}:**Δ/L** and ε_d:**Δ/L** for the simply supported beam loaded with **q** are represented with the following equations:

$$\frac{\Delta}{L} = \left(\frac{5L}{48t} + \left(\left(\frac{I\alpha}{AtL} \right) \left(\frac{E}{G} \right) \right) \right) \varepsilon_{b\max} \tag{4.37}$$

$$\frac{\Delta}{L} = \left(\frac{5AGL^2}{48kEI} + \left(\frac{\alpha}{k} \right) \right) \varepsilon_d \tag{4.38}$$

By setting ε_{bmax} and ε_d, in equations (4.35-4.38) equal to ε_{lim}, the limiting values of **Δ/L** for the deflection of simply supported beams can be calculated. For a given value of ε_{lim}, the limiting value of **Δ/L** depends on **L/H**, **E/G** and the position of the neutral axis. If the model used is the simply supported beam with a point load **P** at mid-span, then the limiting value of **Δ/L** is the lowest as calculated with equations (4.35) and (4.36). On the other hand, if the simply supported beam loaded with a uniformly distributed load **q** is the model implemented then the limiting value of **Δ/L** is the lowest as calculated with equations (4.37) and (4.38). Burland and Wroth (1974) propose that the position of a building's cross-section neutral axis when under the influence of hogging deformation be taken at the bottom fibre – a result that is borne out in practice. In the case of sagging deformation the position of the building's cross-section neutral axis is to be taken at its middle fiber.

4.4 The influence of horizontal strain

The purpose of this section is to point out that the **LTS** expresses horizontal ground movements caused by tunneling-induced settlement in terms of horizontal strains. Strain transformation equations, which are used to add the horizontal strains to ε_{bmax} and ε_d, calculated from the vertical ground movements, are presented.

It was shown that ground surface movements associated with tunneling do not only include vertical movements, but also horizontal movements. If horizontal movements are translated from the ground into the structure, the development of horizontal strains in the structure are therefore imminent. It is thought that the horizontal tensile strain (ε_h) can be included in the analysis using simple superposition, i.e. it is assumed that the soil's horizontal strain under the building's foundation can be averaged out. The deflected beam is then subjected to a uniform tensile or compressive strain over its full length, which is equal to the calculated average horizontal soil strain.

The resultant total bending strain (ε_{br}) as a result of the extra horizontal strain can be calculated with the following equation:

$$\varepsilon_{br} = \varepsilon_{b\max} + \varepsilon_h \tag{4.39}$$

The resultant total diagonal strain (ε_{dr}) as a result of the extra horizontal strain can be calculated with the following equation:

$$\varepsilon_{dr} = \left(\varepsilon_h \left(\frac{1-\nu}{2} \right) + \sqrt{\left((\varepsilon_h)^2 \left(\frac{1+\nu}{2} \right)^2 + (\varepsilon_d)^2 \right)} \right) \tag{4.40}$$

Where (ν) is Poisson's ratio. The strain ε_{lim} therefore is the greater of ε_{br} and ε_{dr}. Thus for a beam of length **L** and height **H**, it is a straightforward matter to calculate the value of ε_{lim} for a given value of Δ/L and ε_h, in terms of **t**, **E/G** and ν. This value of ε_{lim} can then be used to classify which damage category the structure falls into and then in this way, assess the potential associated damage.

4.5 Relevant building dimensions

It is important to correctly define the relevant height and length of the building. This section clearly explains how the length and height components of buildings subject to tunnel-induced displacements are calculated. A typical case of a building affected by a single tunnel's settlement trough is shown in Figure 4.7.

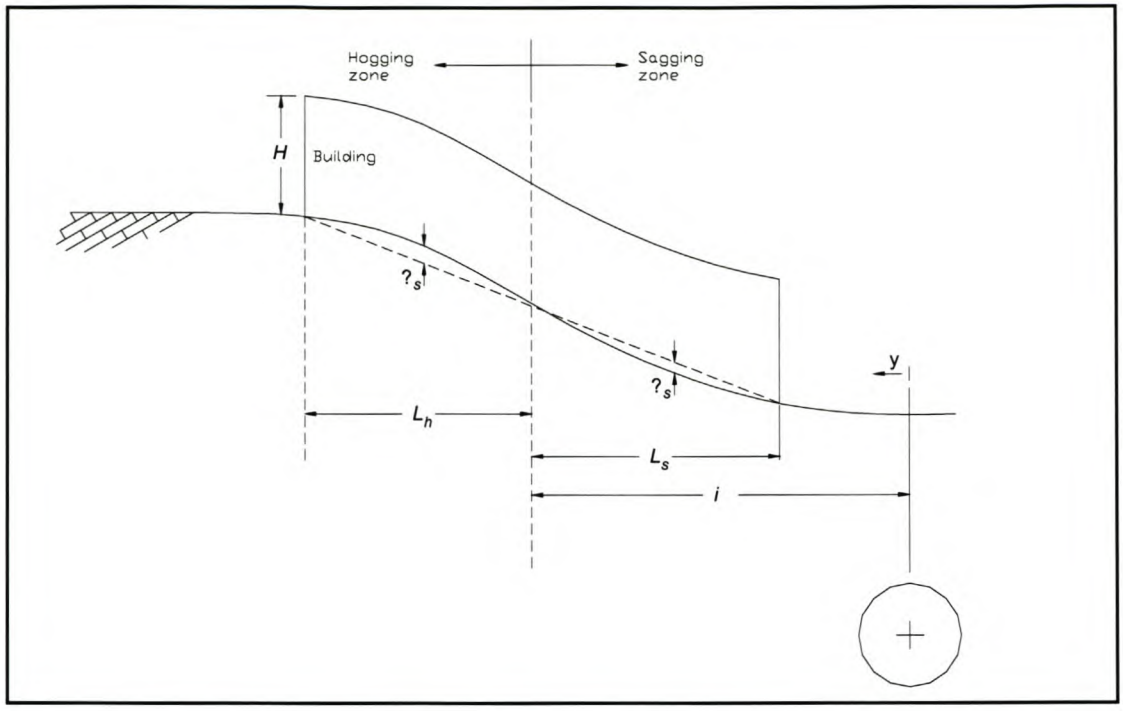

Figure 4.7 Building deformation.

The height **H** is taken as the height from foundation level to the eaves. The roof is usually ignored. It is assumed that a building can be considered separately either side of a point of inflection, i.e. points of inflection of the settlement trough (at foundation level) will be used to partition a building. The length of building is not considered beyond the practical limit of the settlement trough, which for a single tunnel can be taken as **2.5*i*** (2.5 times the distance, on either side of the settlement trough's axis, to the settlement trough's point of inflection), where the ratio of $\mathbf{S_v/S_{max}}$ equals 0.044. In the calculation of building strain, the building span length **L** is required and is defined as the length of building in the hogging or sagging zone (shown as $\mathbf{L_h}$ or $\mathbf{L_s}$ in Figure 4.7) and limited by a point of inflection or extent of settlement trough.

4.6 Summary

The equations used by the **LTS**, which relate strains to **Δ/L** ratios of simply supported elastic beams, as a consequence of vertical ground movements were derived. A means of accounting for horizontal ground movements in terms of horizontal strains was presented and, finally, the relevant dimensions of buildings discussed.

The following chapter analytically manipulates the **LTS** to be specifically applicable to laterally unconfined, solid masonry walls, symmetrically positioned over the sagging zone of green field settlement troughs and with no soil to wall friction. Various analytical relationships pertaining to the fundamental variables are developed, which broaden the scope of the method with respect to the analysis of the above structure.

Chapter 5

Development of the limiting tensile strain method (LTS)

5.1 Buildings symmetrically positioned over the sagging zone

This chapter presents the simple analytical damage assessment approach **LTS** as proposed by Burland and Wroth (1974), developed to predict the structural response for one type of structure subject to one mode of settlement deformation. The type of structure considered is that of laterally unconfined, solid masonry walls, symmetrically positioned over the sagging zone of a green field settlement trough and with no soil to wall friction. Only the sagging mode of settlement deformation is considered with no horizontal soil displacements transferred to the walls.

A certain settlement trough can be mathematically defined with a Gaussian distribution depending on the tunnel type, position, dimensions as well as the surrounding soil properties. The settlement trough parameters, **which will be used throughout this study**, are as follows:

- Depth of the tunnels axis: $\mathbf{z_o}$ = 22000 mm.
- Diameter of the tunnel: **D** = 9500 mm.
- Point of inflection: **i** = 9900 mm.
- Trough width parameter: **K** = 0.45.
- Volume loss: $\mathbf{V_l}$ = (0.03) 3%.

Combining equations (2.1), (2.2) and (2.6) from chapter 2 results in the Gaussian distribution curve defining the transverse settlement trough immediately after a tunnel has been constructed:

$$S_v = \frac{0.31 V_l D^2}{K z_o} e^{\left(-\left(\frac{y^2}{2(Kz_o)^2}\right)\right)} \qquad (5.1)$$

Figure 5.1 graphically displays plots of half the settlement trough used in this study for three different cases of volume loss $\mathbf{V_l}$. Volume losses of 1%, 2% and 3% were implemented in Figure 5.1. The troughs are plotted with equation (5.1). Only half of each trough is plotted due to their symmetrical shape. Variation of the volume loss $\mathbf{V_l}$ only serves to increase the displacements, but has no effect on changing the horizontal position of the trough's points of inflection. Note that the settlement trough with a volume loss $\mathbf{V_l}$ of 3% **will be used in all calculations throughout the rest of this study** and will be referred to as the settlement trough implemented in this study. It can be seen to represent the upper limit of volume loss due to tunnelling in soft soils (Shirlaw and Doran 1988).

When settlement damage to surrounding structures is investigated, all the above variables are available to the engineer. The ground movements experienced by the structures on the tunnel route can therefore be predicted with the help of the simple Gaussian distribution defined by equation (5.1). The ensuing displacements experienced by the structures depend heavily on their position on the surface above the tunnel as well as on their structural dimensions.

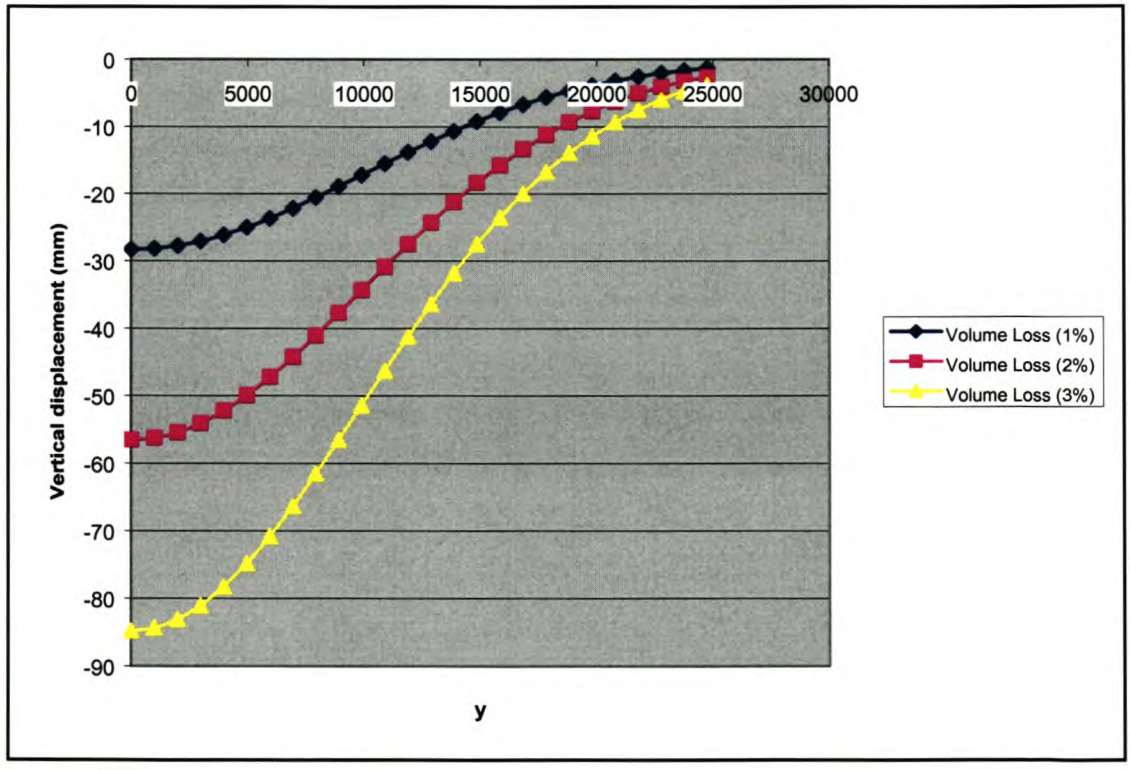

Figure 5.1 Same settlement trough for three different volume losses $\mathbf{V_l}$, equation (5.1).

5.2 Relationship between L and Δ in the sagging zone

Figure 5.2 represents the relationship $\Delta = \mathbf{f(L)}$ between the span length **L** of a beam and its mid-span deflection Δ as induced by the sagging zone of the settlement trough. It can be proven that Δ experienced by a beam, symmetrically positioned over the sagging zone of a green field settlement trough, is dependent on the beam's span length **L**. This is assuming that Δ equals the maximum relative deflection Δ_{mr} of the sagging zone. The mid-span position of a beam symmetrically positioned over the sagging zone of a green field settlement trough is directly above the position of Δ_{mr}.

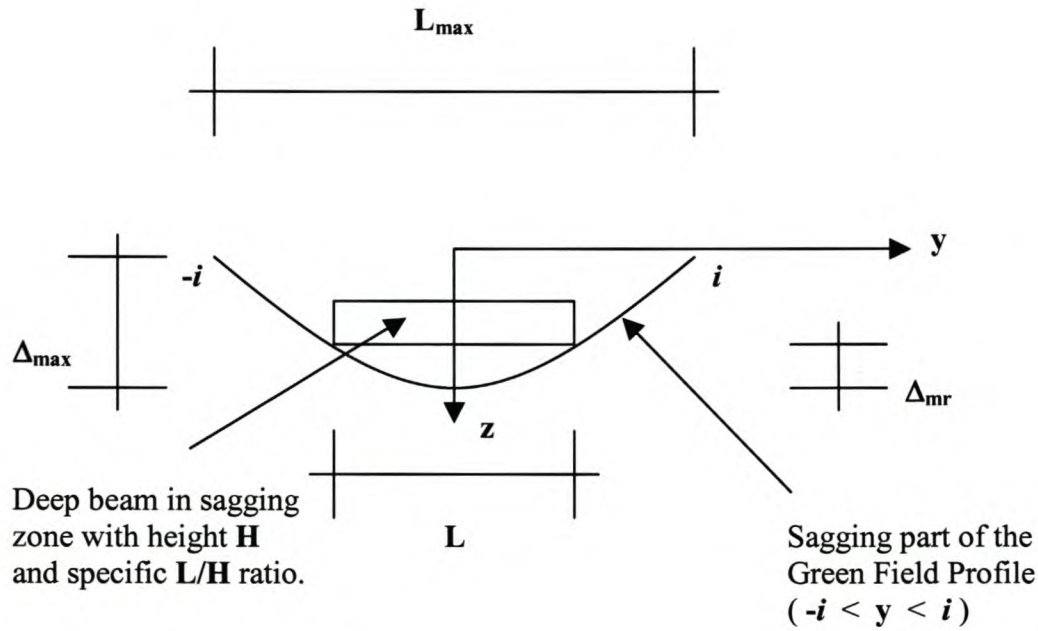

Figure 5.2 Relationship between **L** and Δ for a beam symmetrically positioned over the sagging zone of a green field settlement trough.

A unique relationship $\Delta = \mathbf{f(L)}$, between the beam's span length **L** and its mid-span deflection Δ can be derived for the case of beams symmetrically positioned over the sagging zone of a green field settlement trough. As the beam span length **L** changes, the magnitude of Δ changes. This is assuming that Δ is equal to Δ_{mr} calculated from the beam position on the sagging zone, which is a function of the span length **L**. For a green field settlement trough it can be proven that the relationship between these two variables is non-linear. This will be elaborated next.

The vertical settlement according to a green field profile is:

$$S_v = S_{\max} e^{\left(-\left(\frac{y^2}{2i^2}\right)\right)} \tag{5.2}$$

Where $\mathbf{S_{max}}$, from equation (2.6), is:

$$S_{\max} = \frac{0.31 V_l D^2}{K z_o} \tag{5.3}$$

The following relationship between **L** and **y** is derived from Figure 5.2:

$$L = 2y \tag{5.4}$$

It is seen that when only considering beams symmetrically positioned over the sagging zone of a green field settlement trough, **y** is a variable ranging from 0 to ***i***. Therefore, the relationship between **L** and **Δ**, as being derived, is valid for all values of **L** ranging from 0 to 2***i***.

Rewriting equation (5.4) in another form yields:

$$y = \frac{L}{2} \tag{5.5}$$

Rewriting equation (2.2), (O'Reilly and New 1982):

$$i = K z_o \tag{5.6}$$

The beam mid-span deflection **Δ** is calculated by subtracting the deflection at the building foundation level ($\mathbf{S_v}$ @ **y** = **L**/2) from the settlement trough's maximum deflection ($\mathbf{S_{max}} = \mathbf{S_v}$ @ **y** = 0):

$$\Delta = S_{max} - S_v\left(\frac{L}{2}\right) \tag{5.7}$$

Substituting equations (5.5) and (5.6) into equation (5.2) results in the following equation:

$$S_v = S_{max} e^{\left(-\left(\frac{(L/2)^2}{2(Kz_o)^2}\right)\right)} \tag{5.8}$$

Substituting equation (5.8) into equation (5.7) results in the following equation:

$$\Delta = S_{max} - S_{max} e^{\left(-\left(\frac{(L/2)^2}{2(Kz_o)^2}\right)\right)} \tag{5.9}$$

Rewriting equation (5.9) results in the following equation:

$$\Delta = S_{max}\left(1 - e^{\left(-\left(\frac{(L/2)^2}{2(Kz_o)^2}\right)\right)}\right) \tag{5.10}$$

Substituting equation (5.3) into equation (5.10), results in the equation expressing the relationship between **Δ** and **L** for a beam symmetrically positioned over the sagging zone of a green field settlement trough:

$$\Delta = \frac{0.31 V_l D^2}{Kz_o}\left(1 - e^{\left(-\left(\frac{(L/2)^2}{2(Kz_o)^2}\right)\right)}\right) \tag{5.11}$$

Figure 5.3 represents the non-linear relationship between **L** and **Δ**, for beams symmetrically positioned over the sagging zone of the green field settlement trough implemented in this study. Note that this relationship will be different for all other

green field settlement troughs, but can easily be generated by simply changing the concerned variables in equation (5.11).

The assumption made here is that Δ of the beam mimics that as calculated with equation (5.11). In reality, however, the mid-span deflection Δ of the wall is not expected to be equal to Δ_{mr}. This is as a result of the beam's inherent bending stiffness as well as the complicated soil to wall interaction. This therefore signifies that Δ may be smaller than that predicted by the settlement trough, (equation (5.11)). The assumption that Δ equals the deflection as calculated with equation (5.11), is seen to be a conservative approach.

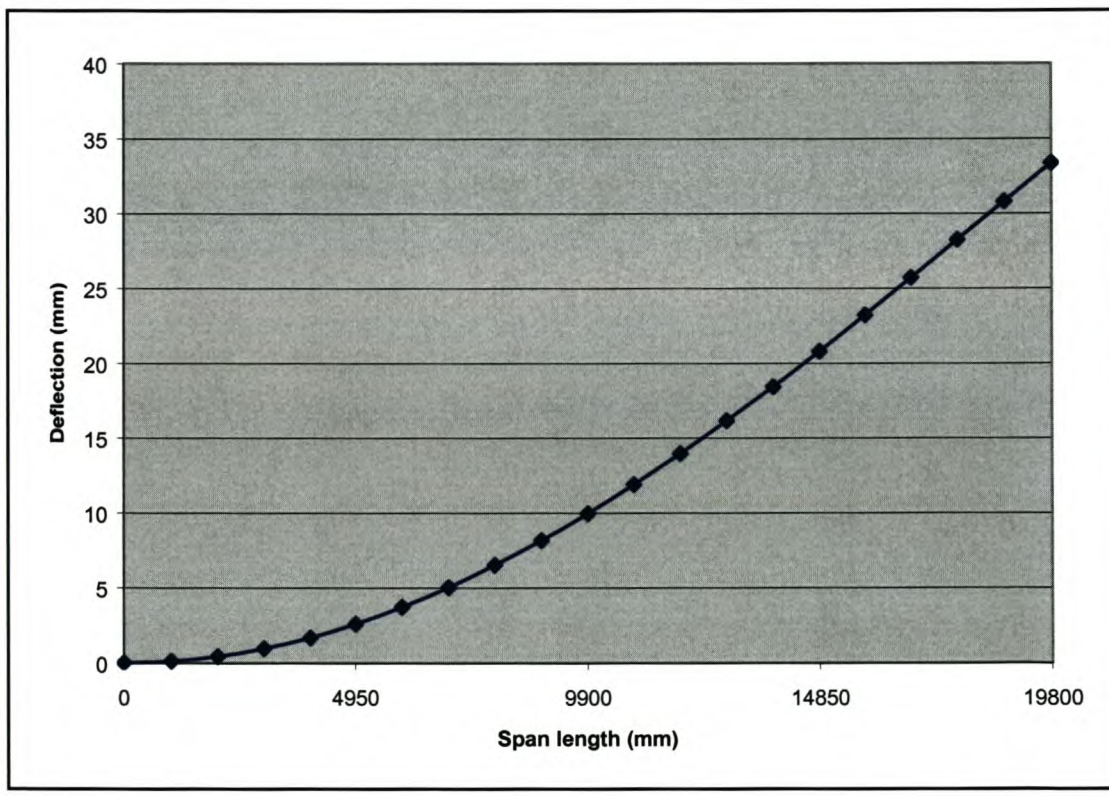

Figure 5.3 Nonlinear relationship between **L** and Δ for beams symmetrically positioned over the sagging zone of the settlement trough implemented in this study. $\mathbf{V_l} = 0.03$ (3%).

5.3 Relationships between the deflection ratio and the respective maximum bending and diagonal tensile strains

This section presents the derivation of the relationships $\Delta/L:\varepsilon_{bmax}$ and $\Delta/L:\varepsilon_d$ for a simply supported elastic beam under the influence of a point load **P** at mid-span (**P** model) and for a simply supported elastic beam under the influence of a uniformly distributed load **q** (**q** model). Equations (4.35) to (4.38) are manipulated for the application of simulating the structural behaviour of laterally unconfined, solid masonry walls, symmetrically positioned over the sagging zone of a green field settlement trough and with no soil to wall friction.

The inertial moment **I** of a rectangular cross section is:

$$I = \frac{1}{12} bH^3 \tag{5.12}$$

The distance from the neutral axis of a beam to its outer fiber **t** in the sagging zone is:

$$t = \frac{H}{2} \tag{5.13}$$

The area of the beam rectangular cross-section is:

$$A = bH \tag{5.14}$$

The values of **k** and α for a rectangular cross-section are:

$$k = \frac{3}{2} and \alpha = \frac{6}{5} \tag{5.15}$$

Equations (5.12) to (5.15) are used to convert equations (4.35) to (4.38) into equations (5.16), (5.17), (5.24) and (5.25), which simulate the relationships $\Delta/L:\varepsilon_{bmax}$ and $\Delta/L:\varepsilon_d$ for both the **P** and **q** models of varying **L/H** ratios:

a) The simply supported elastic beam is manipulated to simulate the structural behaviour of a laterally unconfined, solid masonry wall, symmetrically positioned over the sagging zone of a green field settlement trough with no soil to wall friction.

b) The properties of the settlement trough used in the derivation of the relationships are those **used throughout this study**.

c) The material properties assigned to the simply supported elastic beams will be in accordance with the masonry used in the solid masonry wall models. These properties will be presented later in this section and will be **used throughout this study**.

P model: Derivation of the relationship $\Delta/L:\varepsilon_{bmax}$ and $\Delta/L:\varepsilon_{d}$.

$$\frac{\Delta}{L}=\left(\left(\frac{1}{6}\right)\left(\frac{L}{H}\right)+\left(\frac{1}{5}\right)\left(\frac{H}{L}\right)\left(\frac{E}{G}\right)\right)\varepsilon_{b\max} \tag{5.16}$$

$$\frac{\Delta}{L}=\left(\left(\frac{2}{3}\right)\left(\frac{L}{H}\right)^{2}\left(\frac{G}{E}\right)+\left(\frac{4}{5}\right)\right)\varepsilon_{d} \tag{5.17}$$

P model ε_{bmax}**:** From equation (5.16), Figure 5.4 presents the relationship between $\Delta/L:\varepsilon_{bmax}$ as developed due to the induced displacements. It is important to note that the magnitude of **L** is bound by the settlement trough's two inflection points. Therefore, the maximum value of **L** is $2i$ and its minimum value is zero.

The bounds of **L** for a beam symmetrically positioned over the sagging zone of a green field settlement trough are:

$$0 < L < 2i \tag{5.18}$$

Thus each point on the respective **L/H** curves presented in Figure 5.4, represent a different magnitude of **L** within the bounds of equation (5.18). The magnitude of Δ is

calculated with equation (5.11), according to the specific magnitude of **L**, which then enables the calculation of the **Δ/L** ratio for the specific point. Each of the curves in Figure 5.4 represent a different **L/H** ratio. This is controlled by continuously varying the magnitude of **H** for each point on the curve in accordance with the specific **L/H** ratio and magnitude of **L**.

If **f** is the magnitude of the **L/H** ratio, then the magnitude of **H** is calculated as follows:

$$H = \frac{L}{f} \tag{5.19}$$

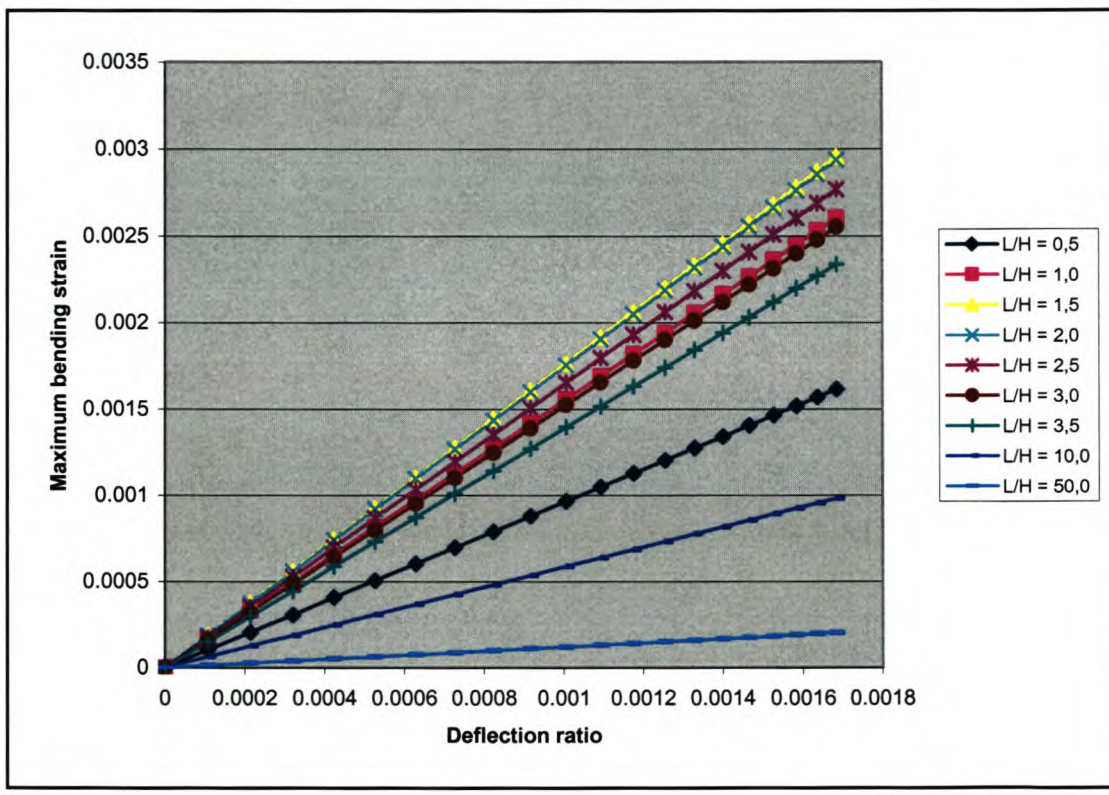

Figure 5.4 Relationship between **Δ/L:ε_{bmax}**, (**P** model), equation (5.16).

It is seen that the factor **(ε_{bmax}/(Δ/L))**, which is the gradient of the curves presented in Figure 5.4, displays no proportionality to the **L/H** ratio for a given **Δ/L** ratio. This is seen by noting that the gradient of the curve representing an **L/H** ratio of 2.0 is larger than that of the curve representing an **L/H** ratio of 0.5. On the other hand the gradient

of the curve representing an **L/H** ratio of 10.0 is smaller than that of the curve representing an **L/H** ratio of 0.5. There is a critical **L/H** ratio, which causes the maximum gradient, **(ε_{bmax}/(Δ/L))** and for the parameters as represented by Figure 5.4, it lies between the **L/H** ratios of 1.5 and 2.0.

The reason for this non-proportional relationship is due to the fact that the magnitude of **L** is bound by equation (5.18). This means that for a specific magnitude of **L**, the **L/H** ratio can only increase by enforcing the magnitude of **H** to decrease. In Figure 5.4 it is seen that beyond the critical **L/H** ratio ε_{bmax} decreases as the **L/H** ratio increases. This phenomenon is explained next:

Making ε_{bmax} the dependent variable of equation (5.16) results in equation (5.20):

$$\varepsilon_{b\max} = \frac{30HG\Delta}{5L^2G + 6H^2E} \tag{5.20}$$

The limit of equation (5.20) as the magnitude of **H** strives to zero and thus the **L/H** ratio to infinity is:

$$\lim_{H\to 0}\left(\frac{30HG\Delta}{5L^2G + 6H^2E}\right) = \frac{0}{5L^2G} = 0 \tag{5.21}$$

Therefore, as the **L/H** ratio strives to infinity, **H** strives to zero, which results in ε_{bmax} striving to zero. This is verified in Figure 5.4 and the result is specific to the case where the magnitude of **L** is bound by certain limits.

P model ε_d**:** From equation (5.17), Figure 5.5 presents the relationship between **Δ/L:ε_d** as developed due to the induced displacements. The respective **L/H** curves were developed in the same way as in Figure 5.4. Note that the factor **(ε_d/(Δ/L))**, which is the gradient of the curves presented in Figure 5.5, has a non-linear inverse proportionality to the **L/H** ratio for a given **Δ/L** ratio. In Figure 5.5 it is seen that as the **L/H** ratio increases ε_d decreases in magnitude for a given **Δ/L** ratio. This is also a noteworthy result, which is explained next:

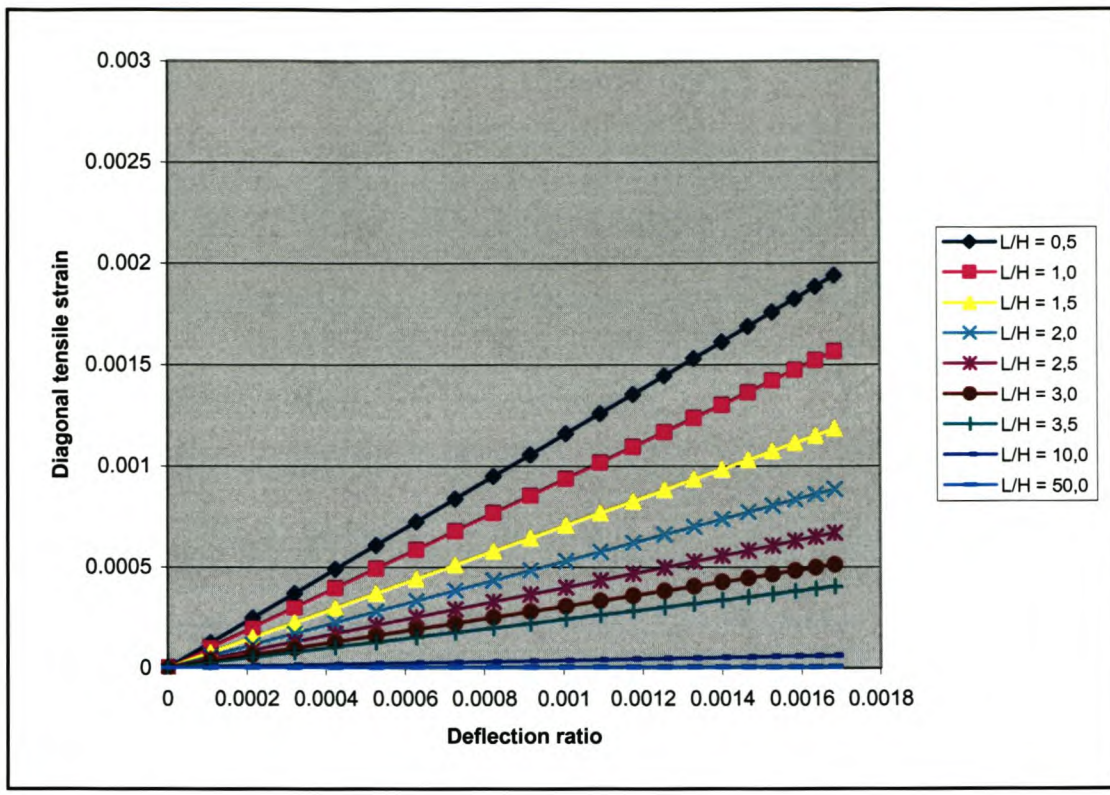

Figure 5.5 Relationship between $\Delta/L:\varepsilon_d$, (**P** model), equation (5.17).

Equation (5.22) expresses ε_d as the dependent variable of equation (5.17):

$$\varepsilon_d = \frac{15H^2E\Delta}{10L^3G+12H^2LE} \tag{5.22}$$

It must again be remembered that **L** is bound by equation (5.18), which signifies that for the magnitude of the **L/H** ratio to increase, the magnitude of **H** needs to decrease. Therefore, as the **L/H** ratio strives to infinity, the magnitude of **H** strives to zero.

The limit of equation (5.22) as **H** strives to zero and thus the **L/H** ratio to infinity is:

$$\lim_{H\to 0}\left(\frac{15H^2E\Delta}{10L^3G+12H^2LE}\right)=\frac{0}{10L^3G}=0 \tag{5.23}$$

This explains why the magnitude of ε_d decreases as the **L/H** ratio increases. This result is specific to the case where the magnitude of **L** is bound by certain limits. The

non-linearity is a result of the fact that the **L/H** ratio in equation (5.17) is squared. It can however be concluded that the smaller the magnitude of the **L/H** ratio the larger the magnitude of ε_d.

Ɋ model: Derivation of the relationship between $\Delta/L:\varepsilon_{bmax}$ and $\Delta/L:\varepsilon_d$:

$$\frac{\Delta}{L} = \left(\left(\frac{5}{24}\right)\left(\frac{L}{H}\right) + \left(\frac{1}{5}\right)\left(\frac{H}{L}\right)\left(\frac{E}{G}\right)\right)\varepsilon_{b\max} \tag{5.24}$$

$$\frac{\Delta}{L} = \left(\left(\frac{5}{6}\right)\left(\frac{L}{H}\right)^2\left(\frac{G}{E}\right) + \left(\frac{4}{5}\right)\right)\varepsilon_d \tag{5.25}$$

q model ε_{bmax}: From equation (5.24), Figure 5.6 presents the relationship between $\Delta/L:\varepsilon_{bmax}$ as developed due to the induced displacements.

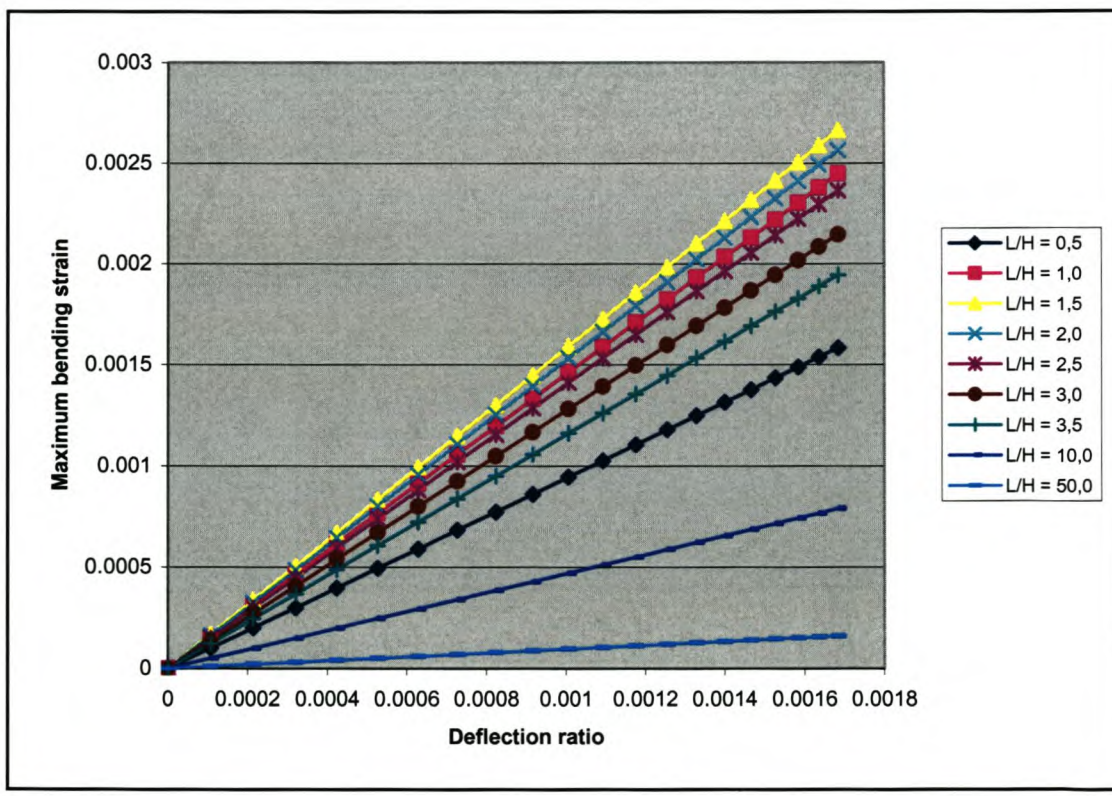

Figure 5.6 Relationship between ε_{bmax} and **Δ/L**, (**q** model), equation (5.24).

The respective **L/H** curves were developed in the same way as in Figure 5.4. Figure 5.6 displays the same phenomenon as was seen in Figure 5.4. The reason behind the phenomenon in Figure 5.6 is as that described for Figure 5.4.

q model ε_d**:** From equation (5.25), Figure 5.7 presents the relationship between Δ/L:ε_d as developed due to the induced displacements.

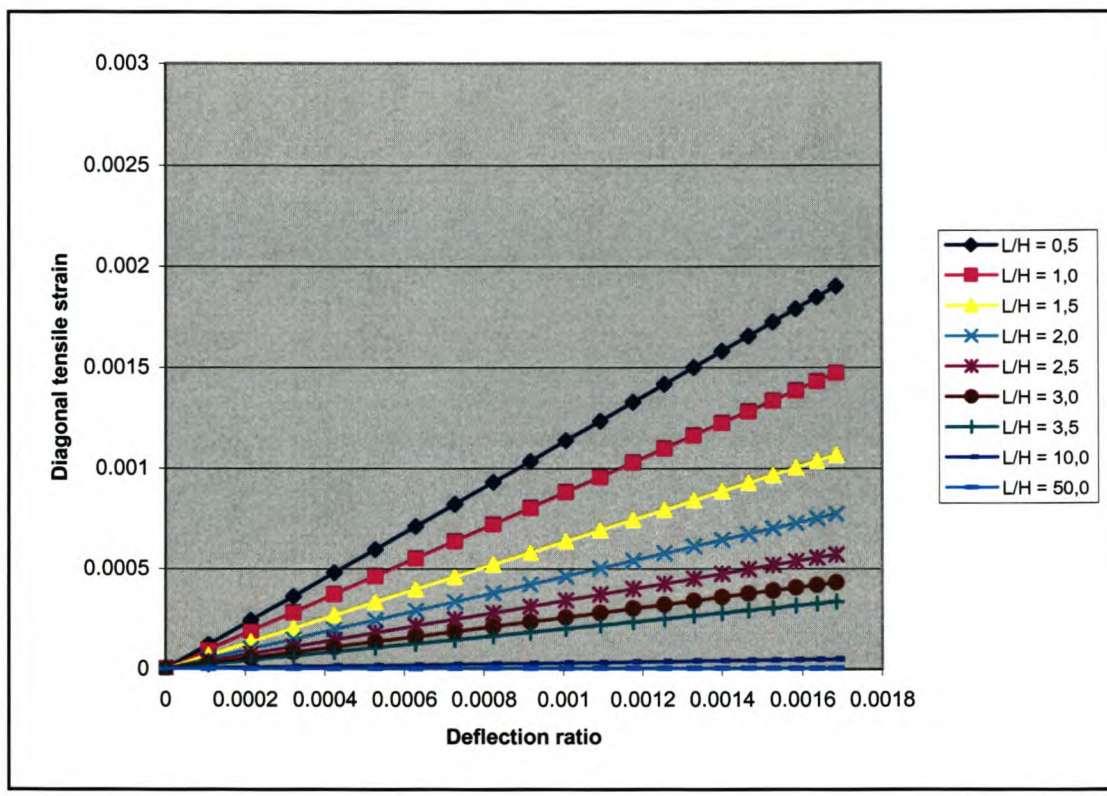

Figure 5.7 Relationship between ε_d and Δ/L, (**q** model), equation (5.25).

The respective **L/H** curves were developed in the same way as in Figure 5.4. Figure 5.6 displays the same phenomenon as was seen in Figure 5.5. The reason behind the phenomenon in Figure 5.7 is as that described for Figure 5.5.

From Figures 5.4 to 5.7 it is concluded that for the simply supported elastic beams modeled as being symmetrically positioned over the sagging zone of a green field settlement trough:

a) There is a critical **L/H** ratio, which will result in the largest magnitude of ε_{bmax}.

b) As the **L/H** ratio strives to infinity, the magnitude of ε_{bmax} strives to zero.

c) The lower the magnitude of the **L/H** ratio, the larger the magnitude of ε_d.

d) As the **L/H** ratio strives to infinity, the magnitude of ε_d strives to zero.

e) For a given **L/H** ratio, there exists a linear relationship between both $\Delta/L:\varepsilon_{bmax}$ and $\Delta/L:\varepsilon_d$.

f) For a given **Δ/L** and **L/H** ratio, the equations associated with the **P** model calculate larger magnitudes of strains compared to those calculated by the equations associated with the **q** model.

In investigating the factors that relate ε_{bmax} and ε_d to the **Δ/L** ratio in equations (5.16) and (5.17) (**P** model) to those in equations (5.24) and (5.25) (**q** model), it is seen that the factors associated to the **P** model are smaller than those associated to the **q** model. It is therefore obvious that, for the same **Δ/L** ratio, the **P** model will predict larger magnitudes of strain than the **q** model.

Note that the **Δ/L** ratios of the respective beams are dependent on the magnitudes of **P** and **q**, which can be compared in terms of a total load on the beam. This, however, is irrelevant as the respective loads are only used to enforce the **Δ/L** ratios, which in reality are enforced by the tunnel's settlement trough. It should be understood as two different models, the **P** and the **q** model, used to model the same problem. The only comparison that should be drawn between the two is related to which model is able to calculate the more suitable solution. In practical engineering problems there are always various models proposed for the solution to a certain problem or class of problem. One model is normally never better than another in terms of a global solution to the problem or class of problem. However, a certain model always solves a

part of the problem better than the other models and therefore a satisfactory global solution is normally obtained by the implementation of various models.

The masonry properties **used throughout this study** are as follows:

- Young's modulus of elasticity: **E** = 4000 **MPa**
- Shear modulus of elasticity: **G** = 1667 **MPa**
- Poisson's ratio: ν = 0.2
- Density: ρ = 1800 **kg/m^3**

5.4 Critical L/H ratio with regard to the maximum bending strain

In the previous section it was seen that for a certain critical **L/H** ratio the maximum magnitude of ε_{bmax}, for a given **Δ/L** ratio, can be obtained using equations (5.16) and (5.24). The purpose of this section is to determine what these respective critical **L/H** ratios are and what variables they are dependent upon.

The following equation is obtained by setting ε_{bmax} as the dependent variable of equation (5.16):

$$\varepsilon_{b\max} = \frac{30H^2G\Delta}{5L^2G + 6H^2E} \tag{5.26}$$

For a given magnitude of **L**, ε_{bmax} in equation (5.26) is differentiated with regard to **H** and set equal to zero:

$$\frac{d\varepsilon_{b\max}}{dH} = \frac{\left(\left(5L^2G + 6H^2E\right)30G\Delta - 30HG\Delta(12HE)\right)}{\left(5L^2G + 6H^2E\right)^2} = 0$$

$$\left(5L^2G + 6H^2E\right)30G\Delta = 30HG\Delta(12HE)$$

$$5L^2G + 6H^2E = 12H^2E$$

$$\left(\frac{L}{H}\right)^2 = \left(\frac{6E}{5G}\right)$$

$$\frac{L}{H} = \sqrt{\frac{6E}{5G}} \tag{5.27}$$

The critical **L/H** ratio with regard to ε_{bmax} for the **P** model is calculated by equation (5.27). Equation (5.27) relates to the **P** model simulating the structural behaviour of laterally unconfined, solid masonry walls, symmetrically positioned over the sagging zone of a green field settlement trough and with no soil to wall friction. It is noted that this critical **L/H** ratio is only dependent on the material properties implemented in the model. For the material properties presented in section 5.3, the critical **L/H** ratio is 1.697, as calculated by equation (5.27).

The following equation is obtained by setting ε_{bmax} as the dependent variable of equation (5.24):

$$\varepsilon_{b\max} = \frac{120HG\Delta}{25L^2G + 24H^2E} \tag{5.28}$$

In the same way as equation (5.26) was used as basis to obtain equation (5.27), equation (5.28) can be used to obtain equation (5.29), which calculates the critical **L/H** ratio with regard to ε_{bmax} for the **q** model. Equation (5.28) relates to the **q** model simulating the structural behaviour of laterally unconfined, solid masonry walls, symmetrically positioned over the sagging zone of a green field settlement trough and with no soil to wall friction.

$$\frac{L}{H} = \sqrt{\frac{24E}{25G}} \tag{5.29}$$

Again, the critical **L/H** ratio calculated by equation (5.29) is only dependent on the material properties implemented in the model. For the material properties presented in section 5.3, the critical **L/H** ratio is 1.517 as calculated by equation (5.29).

As stated earlier, these critical **L/H** ratios were determined for a given magnitude of **L**. The magnitude of **L**, within the bounds of equation (5.18), must now be determined at which the largest magnitude of ε_{bmax} will develop for the respective critical **L/H** ratios.

Equation (5.26) can be expressed in terms of its critical **L/H** ratio as follows:

$$\varepsilon_{b\max} = \frac{30(L/1.697)G\Delta}{5L^2G + 6(L/1.697)^2 E} \tag{5.30}$$

Similarly equation (5.28) can be expressed in terms of its critical **L/H** ratio as follows:

$$\varepsilon_{b\max} = \frac{120(L/1.517)G\Delta}{25L^2G + 24(L/1.517)^2 E} \tag{5.31}$$

Figure 5.8 presents ε_{bmax} versus **L**, equations (5.30) and (5.31) respectively. It must be remembered that the span length of the beam **L** is bound by the limits of equation (5.18) and that as the magnitude of **L** changes the magnitude of Δ also changes. Equation (5.11) was substituted into equations (5.30) and (5.31) to aid in the construction of Figure 5.8. Figure 5.8 clearly displays that ε_{bmax}, at the critical **L/H** ratios, is a maximum at the maximum magnitude of **L** within the bounds of equation (5.18). Therefore, equations (5.26) and (5.28) plotted over the domain of the various **L/H** ratios implementing the maximum magnitude of **L** within the bounds of equation (5.18) will calculate the largest magnitude of ε_{bmax}. For a fixed magnitude of **L**, the **L/H** ratio can only be varied by varying the magnitude of **H**. This leads to the conclusion that the development of ε_{bmax} in simply supported elastic beams modeled as being symmetrically positioned over the sagging zone of a green field settlement trough is not only dependent on the **L/H** ratio, but also on the magnitude of **L** as it determines the magnitude of Δ. Therefore, two beams of different span length **L**, but of equal **L/H** ratio symmetrically positioned over the sagging zone of a green field settlement trough, experience different magnitudes of ε_{bmax}.

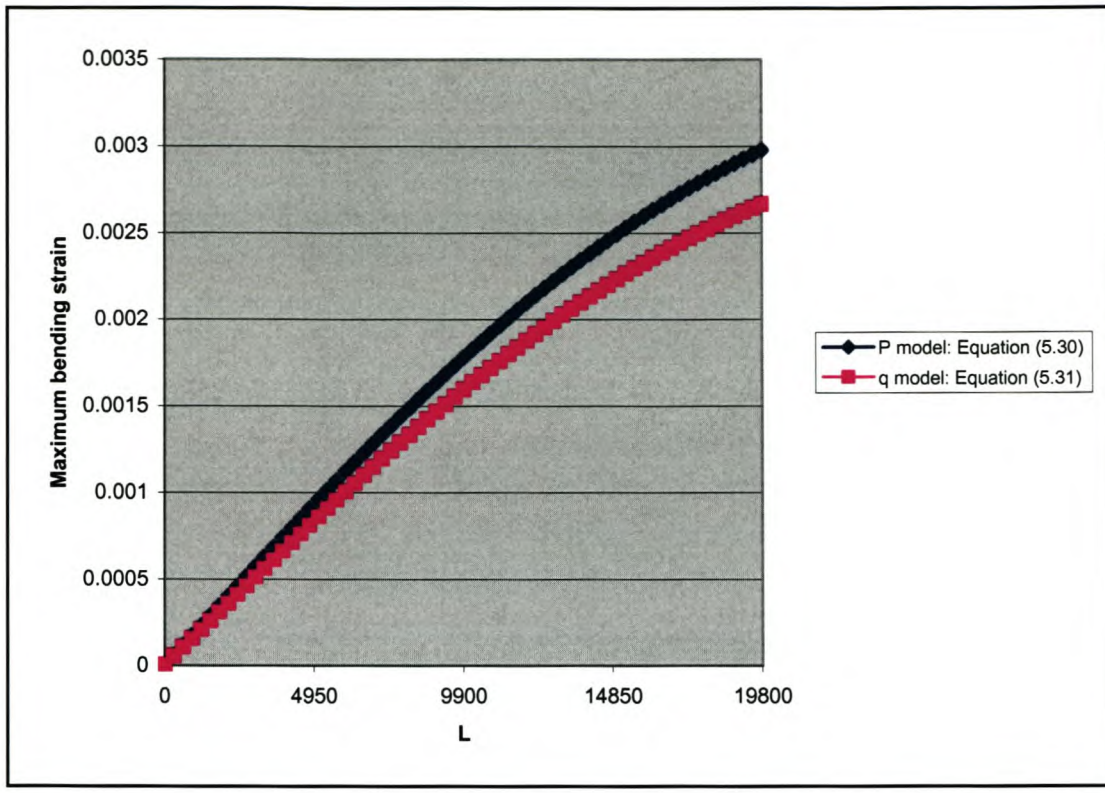

Figure 5.8 Relationship between ε_{bmax} and **L**, equations (5.30) and (5.31). (Critical **L/H** ratios, $V_l = 0.03$ (3%)).

Figure 5.9 presents the relationship of ε_{bmax} versus the **L/H** ratios, for both the **P** and **q** models, at the maximum magnitude of **L**, $L_{max} = 2i$ and at $L_{max}/2 = i$.

The following points are noted from the investigation of Figure 5.9:

a) The strain ε_{bmax} calculated by the **P** model for a given magnitude of **L** is larger than that calculated by the **q** model for the same magnitude of **L**, at **L/H** ratios larger than unity. For **L/H** ratios smaller than unity both models calculate the same values of ε_{bmax} for a given span length **L**.

b) The critical **L/H** ratios are those which correspond to the summit of each curve and they correspond to the values calculated by equations (5.27) and (5.29).

c) It is also seen that as the **L/H** ratio strives to infinity, the magnitude of ε_{bmax} strives to zero, as calculated with the limit equation (5.21).

d) It is seen that the first derivative of ε_{bmax} with regards to **H** of equations (5.26) and (5.28) at the critical **L/H** ratios are absolute maxima. This can be proven mathematically with the theory of differential calculus.

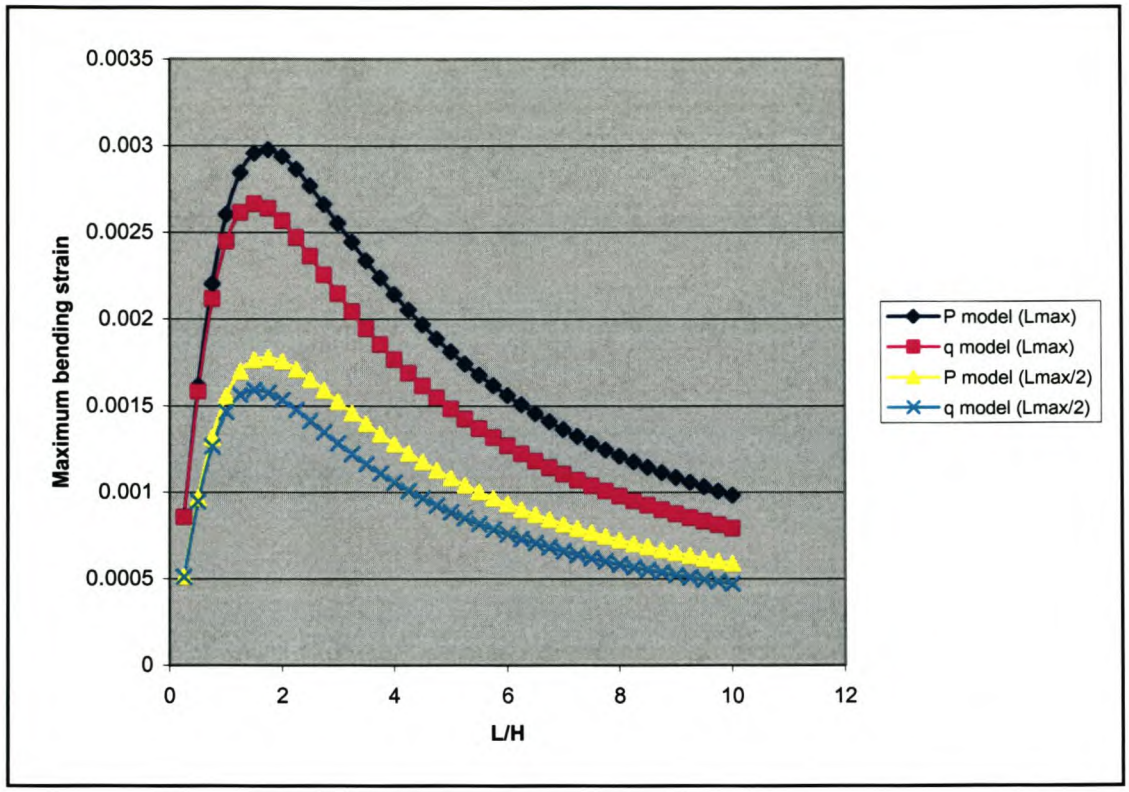

Figure 5.9 Maximum bending strain ε_{bmax} versus the **L/H** ratio for both **P** and **q** models. $\mathbf{V_l} = 0.03$ (3%).

5.5 Maximum bending strain equated to the diagonal tensile strain

This section is dedicated to determining at which **L/H** ratio ε_{bmax} and ε_d have equal magnitudes. The limiting tensile strain ε_{lim} is accepted to be the maximum of either ε_{bmax} or ε_d. It is practical to determine which **L/H** ratio represents the boundary between either ε_{bmax} and ε_d being accepted as the limiting tensile strain ε_{lim}, for both the **P** and **q** models.

Equation (5.22) is obtained by making ε_d the dependent variable of equation (5.17) and is rewritten as equation (5.32):

$$\varepsilon_d = \frac{15H^2E\Delta}{10L^3G + 12H^2LE} \tag{5.32}$$

Equations (5.32) and (5.26) respectively calculate the magnitudes of ε_d and ε_{bmax} for the **P** model, which simulates the structural behaviour of laterally unconfined, solid masonry walls, symmetrically positioned over the sagging zone of a green field settlement trough and with no soil to wall friction. Equating ε_d of equation (5.32) to ε_{bmax} of equation (5.26) results in equation (5.33), which calculates the **L/H** ratio at which $\varepsilon_{bmax} = \varepsilon_d$ for the **P** model.

$$\frac{L}{H} = \frac{E}{4G} \tag{5.33}$$

It is noted that this **L/H** ratio is dependent only on the material properties implemented in the model. For the material properties presented in section 5.3, the **L/H** ratio at which $\varepsilon_{bmax} = \varepsilon_d$ is 0.6 as calculated by equation (5.33).

Equation (5.34) is obtained by making ε_d the dependent variable of equation (5.25):

$$\varepsilon_d = \frac{30H^2E\Delta}{25L^3G + 24H^2LE} \tag{5.34}$$

Equations (5.34) and (5.28) respectively calculate the magnitudes of ε_d and ε_{bmax} for the **q** model, which simulates the structural behaviour of laterally unconfined, solid masonry walls, symmetrically positioned over the sagging zone of a green field settlement trough and with no soil to wall friction. Equating ε_d of equation (5.34) to ε_{bmax} of equation (5.28) results in the same equation as equation (5.33), which calculates the **L/H** ratio at which $\varepsilon_{bmax} = \varepsilon_d$ for the **q** model. It has therefore been determined that for both the **P** and the **q** models, the equation that calculates the **L/H** ratio which results in $\varepsilon_{bmax} = \varepsilon_d$ is that of equation (5.33).

5.6 The effect of L and L/H on the diagonal tensile strain

This section is dedicated to determining what affect the span length **L** and the **L/H** ratio have on the magnitude of ε_d. As in the case of ε_{bmax}, the magnitude of ε_d is dependent on the **L/H** ratio for a certain magnitude of **L**. It was also determined that over and above the **L/H** ratio, ε_{bmax} is dependent on the span length **L** for a specific **L/H** ratio. The reason for this is that two beams of equal **L/H** ratio, but with different span lengths **L**, will experience different mid-span deflections Δ if symmetrically positioned over the sagging zone of a green field settlement trough and if $\Delta = \Delta_{mr}$.

Equations (5.32) and (5.34) calculate the magnitude of ε_d for the **P** and **q** models respectively, simulating the structural behaviour of laterally unconfined, solid masonry walls, symmetrically positioned over the sagging zone of a green field settlement trough and with no soil to wall friction. Figure 5.10 presents the relationship of ε_d versus the **L/H** ratios, for both the **P** and **q** models, at the maximum magnitude of **L**, $L_{max} = 2i$ and at $L_{max}/2 = i$. It clearly displays that simply supported elastic beams with equal **L/H** ratios, but with different span lengths **L**, symmetrically positioned over the sagging zone of a green field settlement trough experience different magnitudes of ε_d. The reason being that the magnitude of Δ is dependent on the magnitude of **L**, according to equation (5.11).

The following points are noted from the investigation of Figure 5.10:

a) The strains ε_d calculated by the **P** model for a given magnitude of **L** are larger than those calculated by the **q** model for the same magnitude of **L**, at the majority of **L/H** ratios.

b) As the **L/H** ratio strives to zero, both the **P** and **q** models calculate equal magnitudes of ε_d. The magnitude of ε_d is undefined for an **L/H** ratio equal to zero.

c) As the **L/H** ratio strives to infinity, ε_d strives to zero as was expressed with the limit equation (5.23).

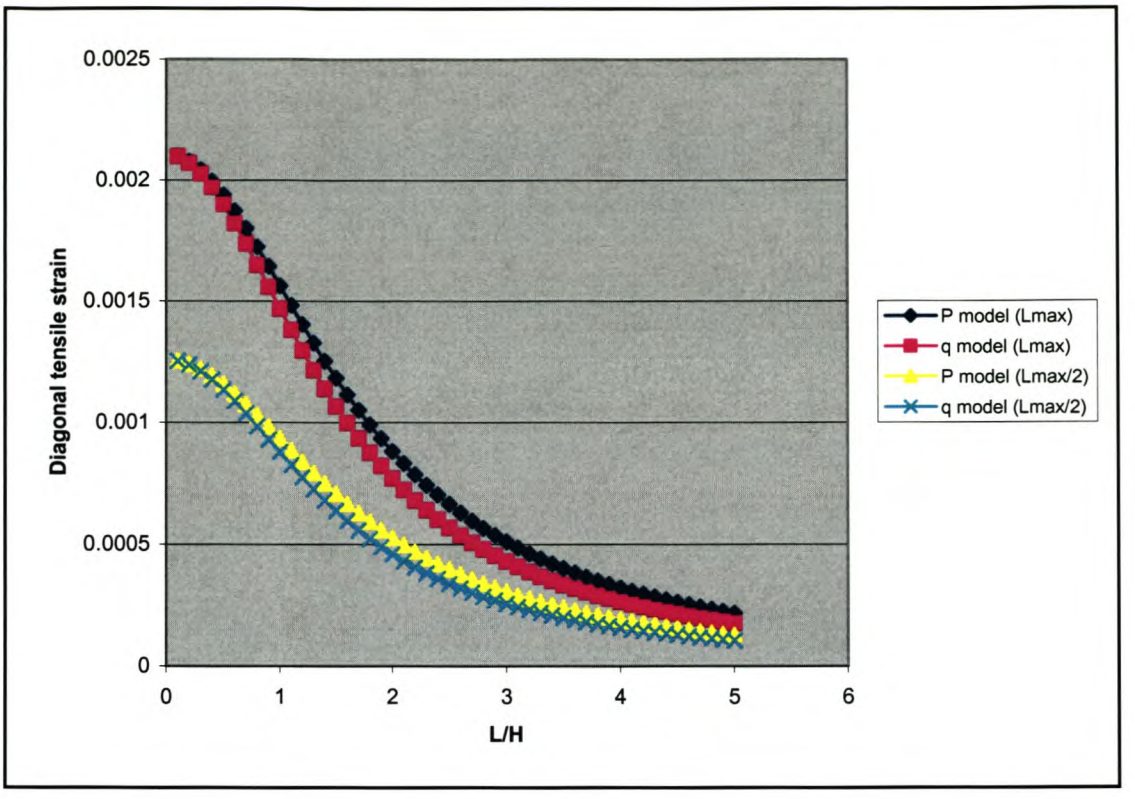

Figure 5.10 Diagonal tensile strain ε_d versus the **L/H** ratio for both **P** and **q** models. $\mathbf{V_l}$ = 0.03 (3%).

In order to determine at which magnitude of **L** the maximum magnitude of ε_d will develop, equations (5.32) and (5.34) will be expressed in terms of a fixed **L/H** ratio and then ε_d will be plotted over the domain of **L** in Figure 5.11.

Equation (5.32) expressed in terms of an **L/H** ratio of 0.5 is presented as:

$$\varepsilon_d = \frac{15(2L)^2 E\Delta}{10L^3 G + 12(2L)^2 LE} \tag{5.35}$$

Equation (5.34) expressed in terms of an **L/H** ratio of 0.5 is presented as:

$$\varepsilon_d = \frac{30(2L)^2 E\Delta}{25L^3 G + 24(2L)^2 LE} \tag{5.36}$$

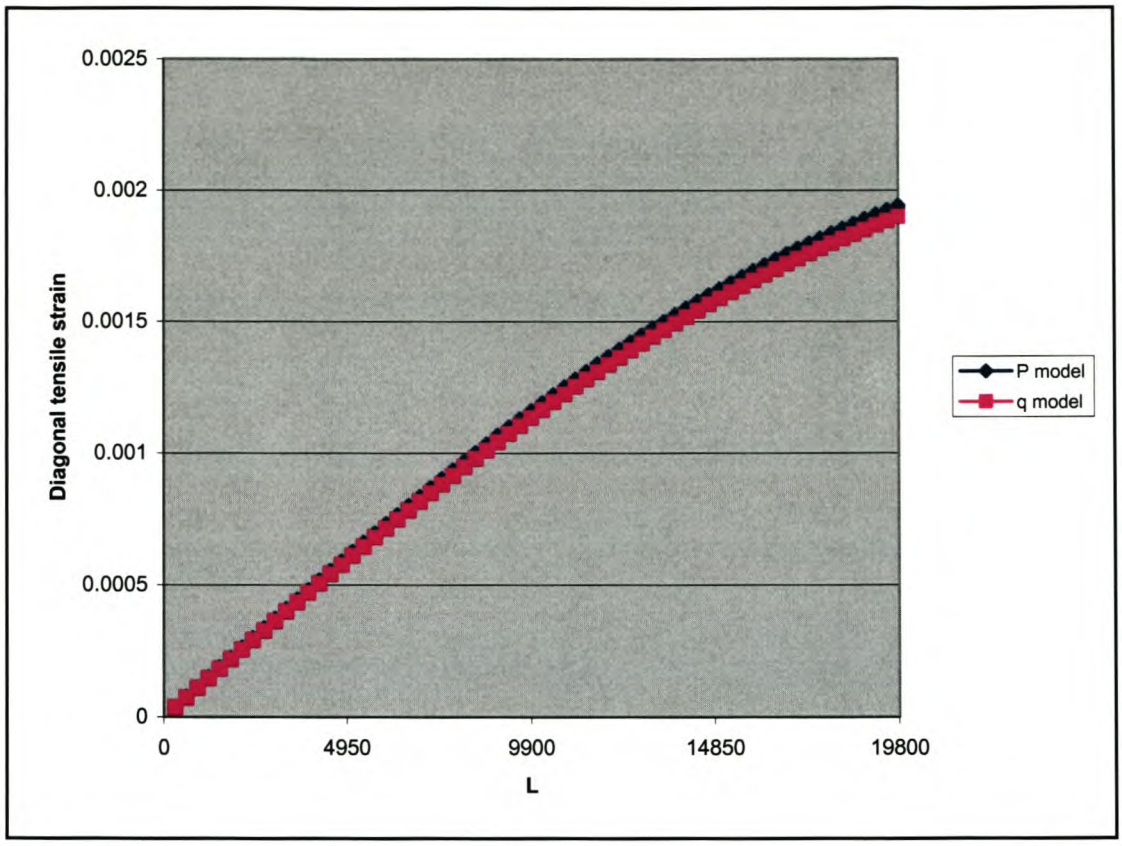

Figure 5.11 Relationship between ε_d and **L** from equations (5.35) and (5.36). (**L/H** = 0.5, $\mathbf{V_l} = 0.03$ (3%)).

From Figure 5.11 it is noted that the magnitude of ε_d in simply supported elastic beams, symmetrically positioned over the sagging zone of a green field settlement trough is not only dependent on the magnitude of the **L/H** ratio, but also on the magnitude of **L** as the magnitude of Δ is dependent on **L**. It is also noted that the maximum magnitude of ε_d develops at the maximum magnitude of **L**, $\mathbf{L_{max}} = 2i$. It has been determined that two beams of equal **L/H** ratio, but with different span length **L** symmetrically positioned over the sagging zone of a green field settlement trough develop different magnitudes of ε_d.

5.7 Limiting tensile strain versus the L/H ratio

Burland and Wroth (1974) based the **LTS** on the principal of the limiting tensile strain ε_{lim} in the structure under investigation. The magnitude of ε_{lim} is taken to be largest of ε_{bmax} and ε_d. From the previous sections it is obvious that the magnitude of ε_{lim} is

dependent on the **L/H** ratio, the span length **L**, the material properties as well as the characteristics of the settlement trough.

Figure 5.12 presents the relationship between ε_{lim} versus the **L/H** ratio for two possible span lengths **L**. The maximum possible span length within the bounds of equation (5.18), $L_{max} = 2i$, and $L_{max}/2 = i$, which corresponds to half the maximum span length L_{max}.

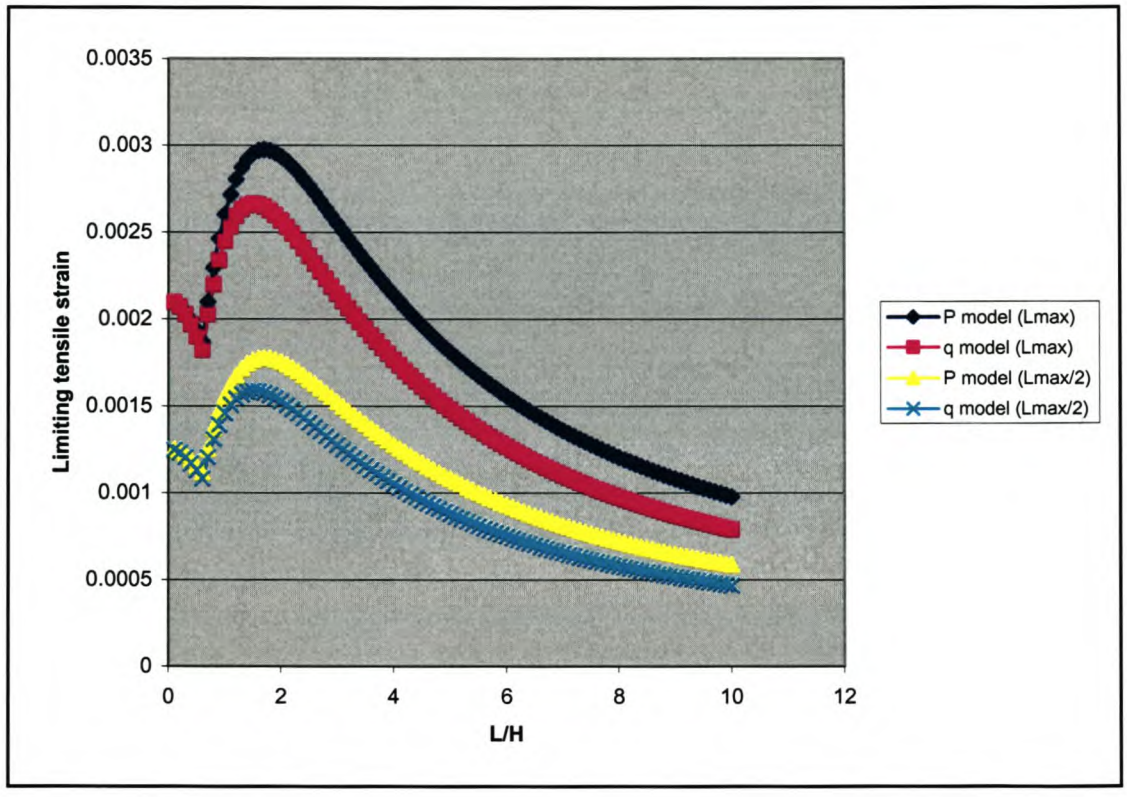

Figure 5.12 Envelopes of ε_{lim} versus the **L/H** ratio for both the **P** and **q** models. (Settlement trough parameters as in section 5.1, $V_l = 0.03$ (3%)).

The curves represent the envelopes of strains ε_{lim} as computed from equations (5.16) and (5.17) for the **P** model, and equations (5.24) and (5.25) for the **q** model. For the material properties implemented in this study, ε_{lim} is equal to ε_d for **L/H** ratios smaller and equal to 0.6, and equal to ε_{bmax} for **L/H** ratios larger and equal to 0.6.

In the construction of Figure 5.12 it is important to understand how the **L/H** ratio affects both ε_{bmax} and ε_d. For a fixed span length **L**, both strains vary as the **L/H** ratio

varies. Furthermore, for a fixed **L/H** ratio, both strains vary as the span length **L** varies. In order to plot the envelope curves in Figure 5.12 with constant span lengths **L** and at the same time vary the magnitude of the **L/H** ratio, the magnitude of the beams height **H** is varied in tandem with that of the **L/H** ratio in accordance with the magnitude of **L**.

5.8 Settlement trough independent relationships

Up to now, through sections 5.1 to 5.7, all the calculations have been based on beams symmetrically positioned over the sagging zone of the green field settlement trough implemented in this study. Therefore, all calculations implemented and relationships derived in the previous sections have conformed to the relationship between **L** and **Δ**, as defined by equation (5.11) and graphically displayed in Figure 5.3. This section is dedicated to the investigation of the relationships between $\Delta/L:\varepsilon_{bmax}$ and $\Delta/L:\varepsilon_{d}$, independent of a fixed relationship between the beams span length **L** and the mid-span deflection **Δ**. This section will therefore investigate the above relationships where the magnitude of **Δ** is not dependent on the magnitude of **L**.

The objectives of this section are to study:

a) How the relationships between $\Delta/L:\varepsilon_{bmax}$ and $\Delta/L:\varepsilon_{d}$ differ for two simply supported elastic beams of different span length **L**, but equal **L/H** ratio, undergoing the same range of **Δ/L** ratios. Both beams are composed of the same material.

b) How the relationships between $\Delta/L:\varepsilon_{bmax}$ and $\Delta/L:\varepsilon_{d}$ differ for two simply supported elastic beams of different span length **L**, but equal **L/H** ratio, undergoing the same range of mid-span deflections **Δ**. Both beams are composed of the same material.

Equations (5.16) and (5.17) respectively describe the relationship between $\Delta/L:\varepsilon_{bmax}$ and $\Delta/L:\varepsilon_{d}$ for the **P** model, whereas equations (5.24) and (5.25) respectively describe the relationship between $\Delta/L:\varepsilon_{bmax}$ and $\Delta/L:\varepsilon_{d}$ for the **q** model. Each of the above

equations relate the **Δ/L** ratio to a respective strain with a certain factor. The variables within each of the factors are the **L/H** and **E/G** ratios. In the above objectives the simply supported elastic beams being compared are of the same material. This therefore signifies that the only variable within the factors relating the **Δ/L** ratio to the respective strains is the **L/H** ratio.

The answer to objective a) therefore, is that the relationships between **Δ/L:ε_{bmax}** and **Δ/L:ε_d** for the two different beams are exactly the same. This can be deduced by taking a closer look at the above-mentioned equations. Equation (5.37) is a copy of equation (5.16):

$$\frac{\Delta}{L} = \left(\left(\frac{1}{6}\right)\left(\frac{L}{H}\right) + \left(\frac{1}{5}\right)\left(\frac{H}{L}\right)\left(\frac{E}{G}\right)\right)\varepsilon_{b\max} \qquad (5.37)$$

For two simply supported elastic beams composed of the same material and of equal **L/H** ratio, the factors relating the **Δ/L** ratio to ε_{bmax} in equation (5.37) are equal for both beams irrespective of their respective span lengths **L**. Therefore, both the beams in objective a) will have equal factors relating the **Δ/L** ratio to the respective strains, even though both display different span lengths **L**. Therefore, from equation (5.37) it is seen that if both these beams experience the same **Δ/L** ratio, they will both experience the same magnitude of ε_{bmax}. It must however be noted that both these beams will experience different magnitudes of **Δ** in order to display equal **Δ/L** ratios. Similarly, equations (5.17), (5.24) and (5.25) can be investigated and the same conclusion drawn.

The answer to objective b) is that the relationships between **Δ/L:ε_{bmax}** and **Δ/L:ε_d** for the two different beams do differ from one another. This again can be deduced by taking a closer look at the above-mentioned equations. Due to the fact that both beams are composed of the same material, the factors relating the **Δ/L** ratio to the respective strains are equal for both beams, even though they display different span lengths **L**. The fact that they both experience equal magnitudes of **Δ** and that they display different span lengths **L** results in different **Δ/L** ratios for both beams. The magnitudes of the respective strains therefore differ for each beam.

Therefore, in conclusion, simply supported elastic beams composed of the same material, of equal **L/H** ratio, but displaying different span lengths **L** will develop equal magnitudes of ε_{bmax} and ε_d if they experience equal Δ/L ratios. The same cannot be said if they experience equal magnitudes of Δ.

5.9 Summary

This chapter was fundamentally concerned with deriving relationships between Δ/L ratios and strains for both the **P** and **q** models. The reason for this is that these calculated strains are intended to be used as predictions for the development of strains in solid masonry walls subject to similar Δ/L ratios as induced by tunneling.

Only the sagging mode of settlement deformation is considered in this study. The **P** and **q** models were developed in such a way that they could closely model the case of a laterally unconfined, solid masonry wall, symmetrically positioned over the sagging zone of a green field settlement trough and with no soil to wall friction. The **P** and **q** models were developed in such a way that they could handle walls displaying different **L/H** ratios and span lengths **L**. The magnitude of **L** is bound as indicated in equation (5.18), which relates to the settlement trough implemented in this study.

A unique relationship between **L** and Δ was derived for simply supported elastic beams modeled as being symmetrically positioned over the sagging zone of a green field settlement trough, assuming that Δ equals Δ_{mr}.

Figures 5.4 to 5.7 presented the relationships between Δ/L:ε_{bmax} and Δ/L:ε_d for both the **P** and **q** models displaying various **L/H** ratios. These curves are intended to predict the development of strains in solid masonry walls, symmetrically positioned over the sagging zone of a green field settlement trough.

Critical **L/H** ratios with respect to ε_{bmax} in both the **P** and **q** models were determined to be dependent only on the material properties implemented in the models. Equations (5.27) and (5.29) express these critical **L/H** ratios for the respective models.

It was determined that for the simply supported elastic beams implemented in the **P** and **q** models, the magnitude of their ε_{bmax} was directly proportional to the magnitude of their span lengths **L** (Figure 5.9), irrespective of their **L/H** ratios. It is therefore practical to express ε_{bmax} in terms of Δ**/L**, as a single curve represents a single **L/H** ratio irrespective of **L**.

The **L/H** ratio, which equates ε_{bmax} and ε_d in the simply supported elastic beams implemented in both the **P** and **q** models, is calculated with equation (5.33). This unique **L/H** ratio was also determined to be dependent only on the material properties implemented in the respective models.

It was determined that for the simply supported elastic beams implemented in the **P** and **q** models, the magnitude of their ε_d was directly proportional to the magnitude of their span lengths **L** (Figure 5.10), irrespective of their **L/H** ratios. It is therefore practical to express ε_d in terms of Δ**/L**, as a single curve represents a single **L/H** ratio irrespective of **L**.

Envelopes presenting the relationship between ε_{lim}**:L/H** for simply supported elastic beams of a given span length **L** can be constructed. Figure 5.12 represents such a relationship. If the strains in the simply supported elastic beams are proven to be good predictions for the development of strains in solid masonry walls, an engineer will be able to plot such a relationship for an upper and a lower limit with regard to the span length **L** of a solid masonry wall symmetrically positioned over the sagging zone of a green field settlement trough. In this way, an initial idea can be obtained with respect to which solid masonry walls, according to their **L/H** ratios, will need mitigating measures as predicted by their damage category. The magnitude of ε_{lim} determines into which damage category the solid masonry walls are to be categorised.

Finally, it was determined that simply supported elastic beams composed of the same material, of equal **L/H** ratio, but displaying different span lengths **L** will develop equal magnitudes of ε_{bmax} and ε_d if they experience equal Δ**/L** ratios. The same cannot be said if they experience equal magnitudes of Δ.

The next chapter is dedicated to determining the applicability of using the finite element method as an accurate solution to the differential equation, which describes the structural behaviour of deep beams. Once this is verified, an investigation into the most suitable way of simply supporting a solid masonry wall in a finite element model is undertaken.

Chapter 6

Verification of the finite element method: Deep beam analysis

6.1 Introduction

This chapter is concerned with verifying that the finite element method is an accurate solution to the differential equation, which describes the structural behaviour of deep beams. This is undertaken in section 6.2. The chapter also investigates the most suitable method of simply supporting a solid masonry wall in a finite element model, sections 6.3 to 6.5. This is necessary, as simply supported linear elastic finite element models of solid masonry walls are to be built in order to determine the accuracy of using the **LTS** for the calculation of strains in these walls.

As mentioned earlier, Burland and Wroth (1974) based the **LTS** on the calculation of strains in simply supported elastic beams. Here, finite element analyses of deep beams are performed to verify the accuracy of implementing the **LTS** for the prediction of strains in deep beams. Similar conditions are modelled as in the **LTS**, i.e. simple supports and the application of a load to enforce a particular **Δ/L** ratio.

The analyses of deep beams pose many more difficulties to a structural analyst than slender beams (simply supported elastic beams). This is mainly due to the fact that the fundamental hypothesis of the flexure theory: *Plane sections through a slender beam taken normal to its axis remain plane after the beam is subjected to bending*, does not stand true for deep beams.

The fundamental hypothesis for simply supported elastic rectangular beams is exact for the case of pure bending. If shear also exists, a small error is introduced. Practically, however, this assumption is generally applicable with a high degree of accuracy (whether the material behaves elastically or plastically), providing the height of the beam **H** is small in relation to the span length **L**. This is not the case for deep beams and this therefore further enforces the fact that the strains calculated with equations (5.16), (5.17), (5.24) and (5.25), using the dimensions of deep beams for **L** and **H**, need verifying by the finite element method.

Due to the fact that the strains obtained from the numerical linear elastic finite element analyses are to be compared to those calculated analytically with the **LTS**, their accuracy must be verified. For this purpose semi-analytical solutions in the literature are used. Bares and Bauverlag (1969) published semi-analytically determined stress distributions in deep beams for certain **L/H** ratios, load configurations, boundary conditions and combinations thereof. It is decided to investigate the stress results pertaining to a deep beam structure, for a certain boundary value problem as defined in the publication by Bares and Bauverlag (1969). A finite element model conforming to the chosen boundary value problem is built and used for the verification process. The stress results from the finite element analyses are then compared to the analytical stress results. A good correspondence between the results of the analytical and numerical methods will prove that the finite element method is an accurate solution of the fundamental differential equation, as derived for the deep beam problem.

Once the verification of the finite element method is complete, it is possible to build the same model of the deep beam with different boundary constraints. The results of all the numerical models are then compared to one another to investigate the influence of the boundary conditions on the results. From these different models, a suitable model to be used in the linear elastic analyses, can be made to finally compare its results to those obtained with the **LTS**.

6.2 The Bares and Bauverlag's (1969) model versus the finite element method

When a thin plate is loaded with forces along its middle plane, the out of plane stresses σ_z, τ_{xz}, τ_{yz} may be neglected and the other stresses, σ_x, σ_y, $\tau_{xy} = \tau_{yx}$ working parallel to the middle plane can be assumed to be uniformly distributed over the thickness of the plate. This condition is known as the condition of plane stress.

Consider, in Figure 6.1, a finite element of the thin plate with dimensions **dx**, **dy** and **t**. The forces, which are exerted on this finite element by the adjacent material, are normal and tangential forces. A gravitational body force is also exerted on the element by the self-weight of the material. These normal and tangential forces that are exerted

on the finite element by the adjacent material are expressed in terms of average stresses in Figure 6.1.

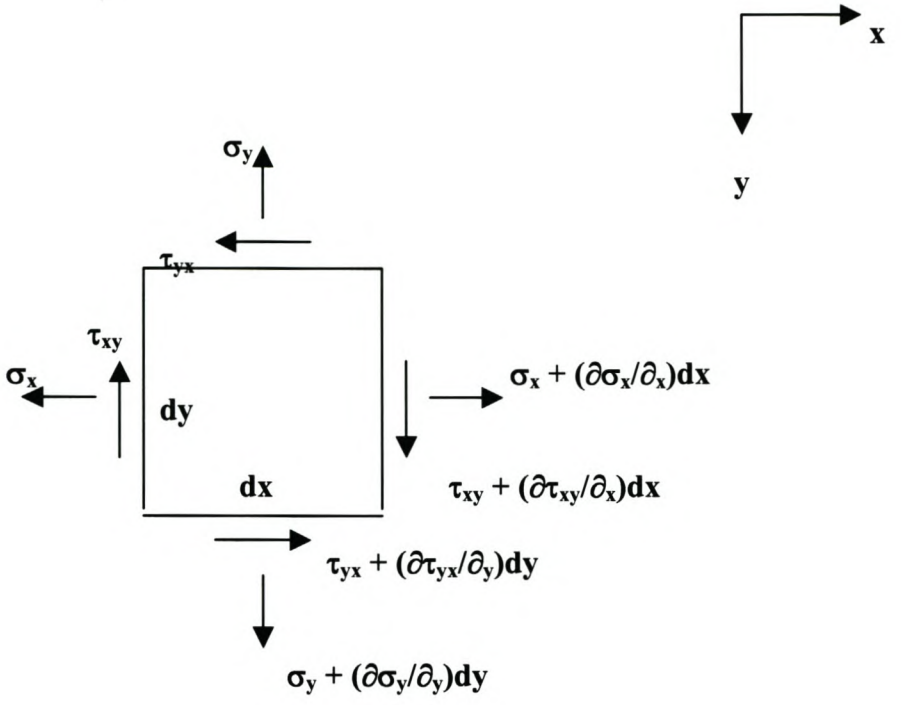

Figure 6.1 Finite element of a thin plate with thickness **t**.

The following stress equilibrium equations are derived from Figure 6.1:

$$\frac{\partial \sigma_x}{\partial x} + \frac{\partial \tau_{yx}}{\partial y} = 0 \qquad \frac{\partial \sigma_y}{\partial y} + \frac{\partial \tau_{xy}}{\partial x} + \gamma_1 = 0 \tag{6.1}$$

The variable (γ_1) is the contribution of gravity.

The infinitesimal strains in the directions of the co-ordinate axes are represented by the relations:

$$\varepsilon_x = \frac{\partial u}{\partial x} \qquad \varepsilon_y = \frac{\partial v}{\partial y} \tag{6.2}$$

The infinitesimal change of angle is given by:

$$\gamma_{xy} = \frac{\partial v}{\partial x} + \frac{\partial u}{\partial y} \tag{6.3}$$

The constitutative law, here chosen as linear elasticity, links the stresses and strains by the expressions:

$$\varepsilon_x = \frac{1}{E}\left(\sigma_x - \nu\sigma_y\right) \qquad \varepsilon_y = \frac{1}{E}\left(\sigma_y - \nu\sigma_x\right) \tag{6.4}$$

$$\gamma_{xy} = \frac{\tau_{xy}}{G} = \left(\frac{2(1+\nu)}{E}\right)\tau_{xy} \tag{6.5}$$

The manipulation of equations (6.1-6.5) results in the following differential equation:

$$2(1+\nu)\left(\frac{\partial^2\tau_{xy}}{\partial x\partial y}\right) = \frac{\partial^2\sigma_x}{\partial y^2} - \nu\left(\frac{\partial^2\sigma_y}{\partial y^2}\right) + \frac{\partial^2\sigma_y}{\partial x^2} - \nu\left(\frac{\partial^2\sigma_x}{\partial x^2}\right) \tag{6.6}$$

In order to solve this differential equation analytically, a suitable choice of Airy stress functions, **(F)**, needs to be undertaken to produce the following differential equation:

$$\frac{\partial^4 F}{\partial x^4} + 2\frac{\partial^4 F}{\partial x^2\partial y^2} + \frac{\partial^4 F}{\partial y^4} = 0 \tag{6.7}$$

Where,

$$\frac{\partial^2 F}{\partial y^2} = \sigma_x \tag{6.8}$$

$$\frac{\partial^2 F}{\partial x^2} = \sigma_y \tag{6.9}$$

$$\frac{\partial^2 F}{\partial x\partial y} = -\tau_{xy} \tag{6.10}$$

This differential equation is solved analytically by considering appropriate boundary values of stress and displacement. Bares and Bauverlag (1969) published analytical

solutions for such deep beam boundary value problems. The choice of these Airy functions is beyond the scope of this study.

A deep beam boundary value problem is chosen from Bares and Bauverlag's (1969) publication as a reference solution to verify that the finite element method accurately models and solves the boundary value problem. Figure 6.2 represents the finite element model of the Bares and Bauverlag's (1969) boundary value problem.

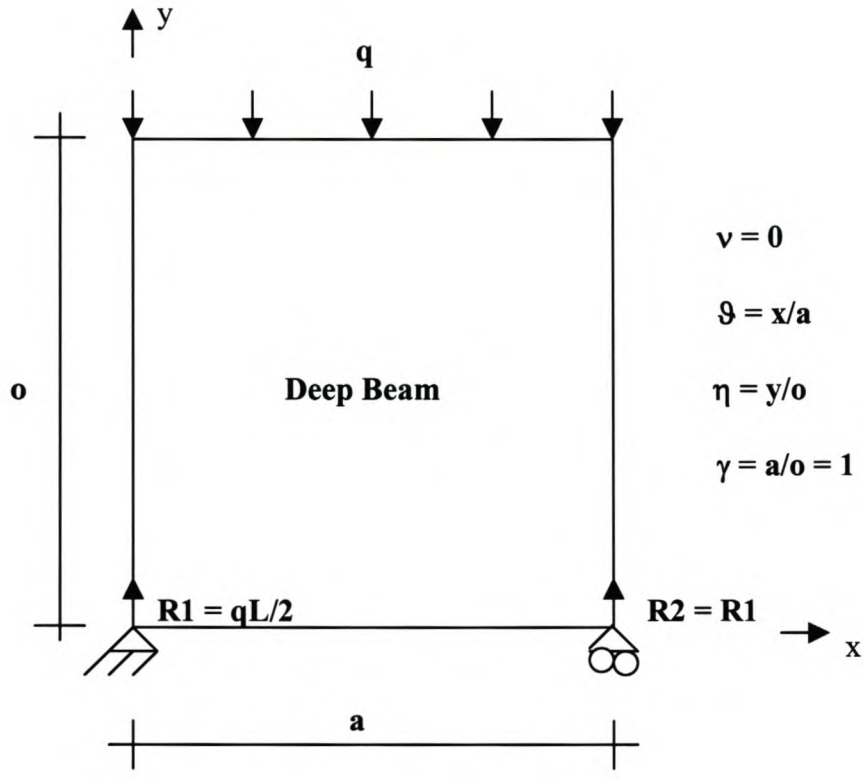

Figure 6.2 The finite element model of Bares and Bauverlag's (1969) deep beam boundary value problem. (Model 1).

The boundary value problem chosen had an **L/H** ratio equal to 1. A uniformly distributed load acted along the top edge of the deep beam. Both lower corners where constrained by single point constraints. The bottom left constraint was implemented as a hinge, which restrained translation in the horizontal and vertical directions. The

bottom right constraint was that of a roller, which restrained translation in the vertical direction only.

The following magnitudes were assigned to the respective variables in the construction of the finite element model, referred to as Model 1 hereafter:

- Span length **a** = 19500 mm
- Height **o** = 19500 mm
- Uniform load **q** = 1 N/mm
- Thickness **b** = 300 mm

Table 6.1 is used to analytically calculate the horizontal stresses (σ_{xx}) at certain points on the body of Bares and Bauverlag's (1969) boundary value problem of a deep beam with an **L/H** or **a/o** ratio equal to unity.

η \ ϑ	0.5	0.9
1.0	-0.267	-0.038
0.75	-0.280	-0.045
0.5	-0.458	-0.089
0.25	-0.013	-0.369
0	2.191	6.865
M.F	**q/b**	

Table 6.1 Analytical horizontal stresses σ_{xx} at certain points on the body of Bares and Bauverlag's (1969) boundary value problem of a deep beam.

The factors corresponding to the normalised coordinates, (ϑ) and (η), in Table 6.1 are multiplied with the multiplication factor (**M.F**) to obtain the horizontal stresses σ_{xx} at the respective positions on the body of the deep beam.

Figure 6.3 represents a comparison between the σ_{xx} distributions, along a vertical section at mid-span, corresponding to the analytical Bares and Bauverlag's (1969) method and the numerical finite element method.

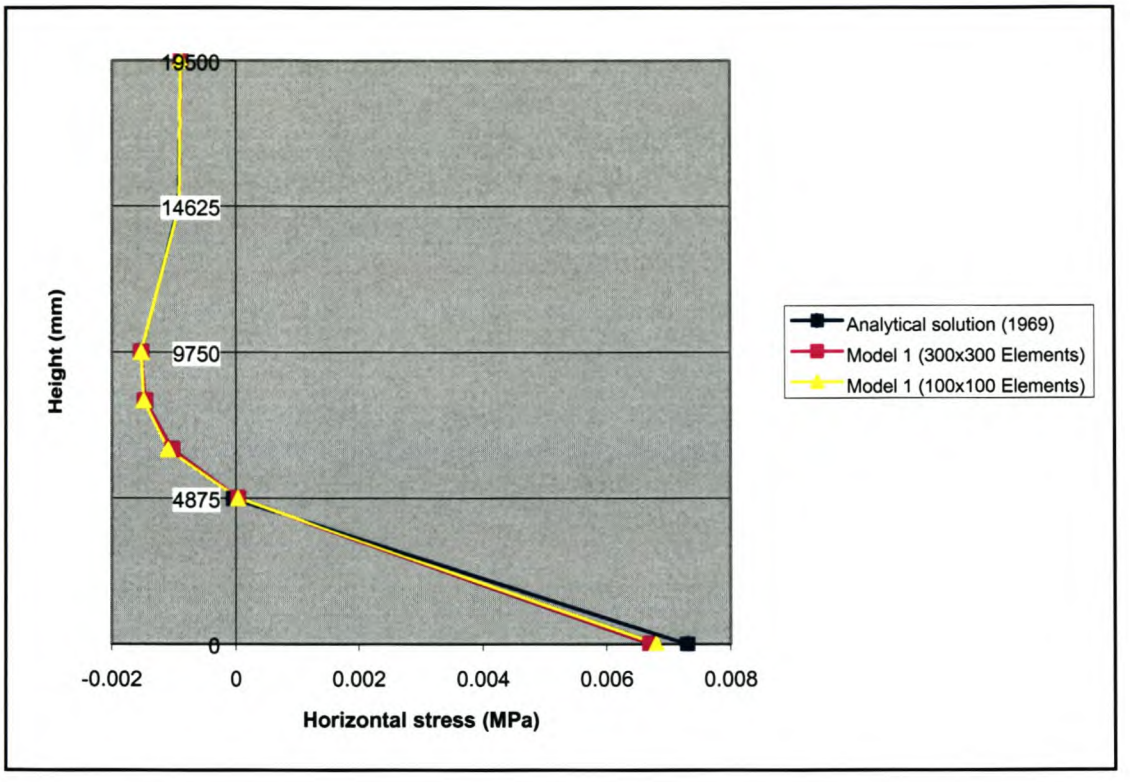

Figure 6.3 σ_{xx} distribution at $\vartheta = 0.5$ (mid-span) over the height of the deep beam.

As seen in Figure 6.3, the analytical and numerical solutions of the σ_{xx} distributions correspond closely at mid-span plotted over the height **H** of the deep beam. Quadratic, linear, plane stress membrane elements are used in the meshing of the deep beam. Two different mesh sizes are implemented and analysed to ensure that the solution has converged with regard to mesh size. As is seen, the results obtained with the 300x300 mm elements closely matched those obtained with the 100x100 mm elements. This confirms that the solution has already converged with the coarser 300x300 mm mesh. Stresses in the finite element model are also sampled at the positions, $\eta = 0.333$ and 0.416 over and above the positions in Table 6.1, as there is concern about the shape of the curve in this critical region. As can be seen, however, the curve follows the expected path nicely.

Figure 6.4 represents a comparison of the σ_{xx} distributions, along a vertical section close to the support, corresponding to the analytical Bares and Bauverlag's (1969) method and the numerical finite element method.

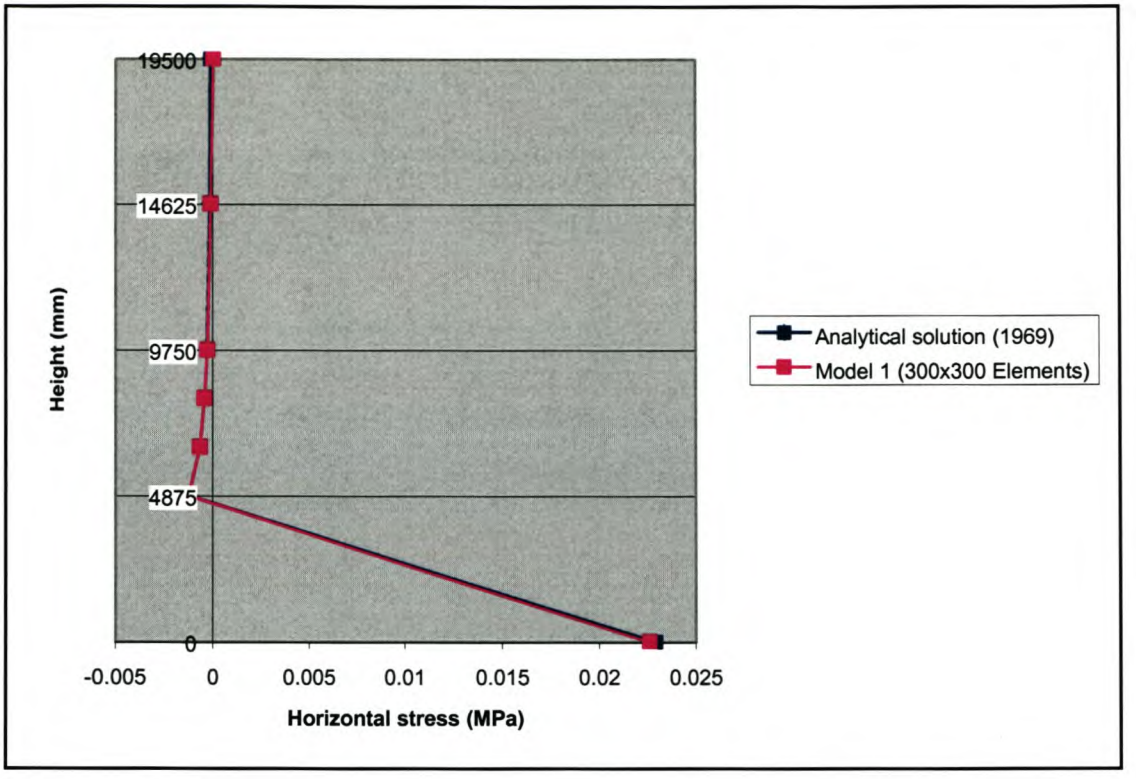

Figure 6.4 σ_{xx} distribution at $\vartheta = 0.9$ over the height of the deep beam.

Figure 6.4 enhances the fact that the analytical and numerical solutions conform closely to one another. It is concluded that the modelling of deep beams with the finite element method, is an accurate solution to the differential equation (6.6), describing the structural behaviour of deep beams. In the following section, alternative finite element models of simply supported deep beams are investigated.

6.3 Variations of model 1

Having verified that using the finite element method in the modelling of deep beams is an accurate solution to the differential equation (6.6), the influence of various boundary constraints applied to model 1 is investigated. The investigation will aid in the definition of a suitable boundary value problem for the finite element modelling of simply supported deep beams. Once again it is important to remember that, in order to

verify the accuracy of implementing the **LTS** for predicting strains in solid masonry walls, the chosen boundary value problem must simulate similar conditions as were implemented for the simply supported elastic beams used in the **LTS**.

Initially, simply supporting the deep beam seems possible by simply restraining single nodes against translation, near the position of the supports. The problem with this approach is that it inevitably causes stress concentrations at these restraints. The concern is not these stress concentrations themselves, but more their influence on the stress and strain distributions throughout the rest of the model. Another problem with this approach is that the elements near these constraints become so seriously deformed under loading, that the deflection profile of the model's bottom edge does not simulate that of a simply supported beam's deflection profile under similar loading conditions. This creates problems with respect to the displacements of the deep beam. The mid-span deflection Δ is exaggerated by the large local displacements at the deep beam's point constraints. The exaggeration of Δ makes it practically impossible to obtain Δ/L ratios, which match those of the simply supported elastic beams used in the **LTS**. If matching Δ/L ratios cannot be obtained, then any comparisons attempted are considered meaningless.

The following models are thus investigated to study different boundary conditions:

1. **Model 2:** Figure 6.5.

   - Model 1's bottom edge is lengthened to overlap the pin supports by a distance **(e)**, without changing the magnitude of the span length **L**.
   - The uniformly distributed load **q** is applied on the deep beams top edge from directly above the left support to directly above the right support.
   - The span length **L** is measured from the left pin support to its right roller support.
   - The magnitudes of Model 2's variables are as those for Model 1, with **e** = 300 mm.

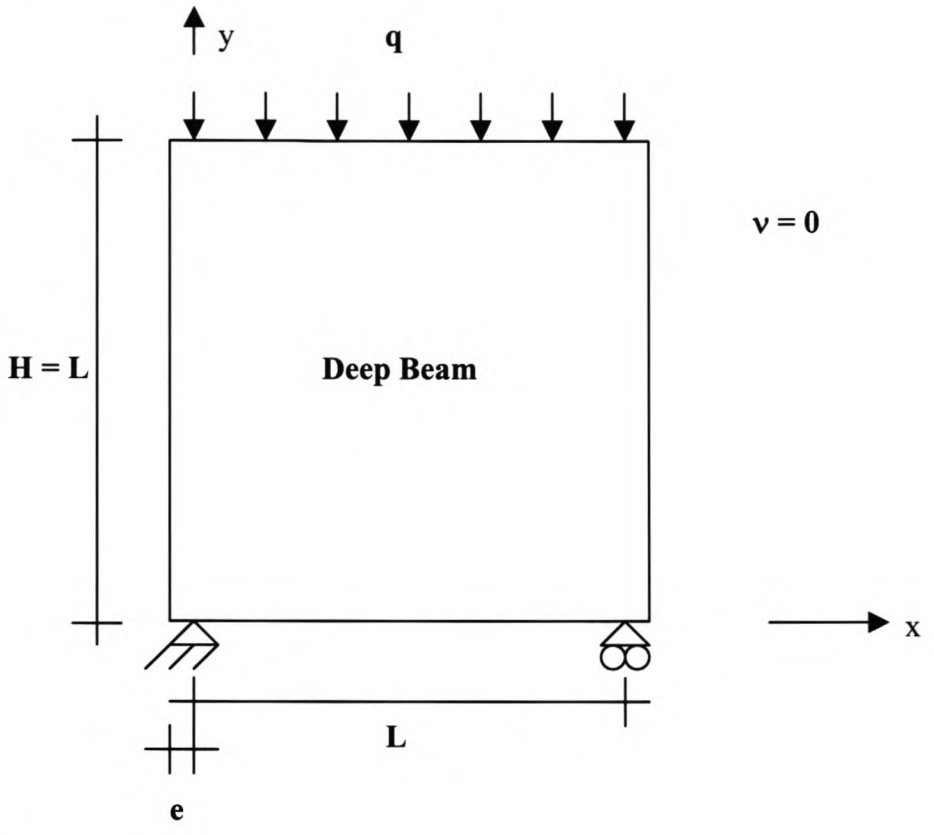

Figure 6.5 (Model 2)

2. **Model 3:** Figure 6.6

- Replacing the point restraints with small column supports can solve the problem pertaining to the deflection profile.
- The columns distribute the loads over a few elements instead of concentrating the loads on a single node. This approach solves the problem with respect to the exaggerated deflections.
- The columns are assigned a bending stiffness significantly smaller than that of the deep beam so that the rotation at the top of the columns is governed by the bending stiffness of the deep beam.
- The uniformly distributed load **q** is applied to the beams top edge extending from the centre of the left column to the centre of the right column.
- The span length **L** is measured from the centre of the left column to the centre of the right column.
- The magnitudes of Model 3's variables are as those for Model's 1 and 2.

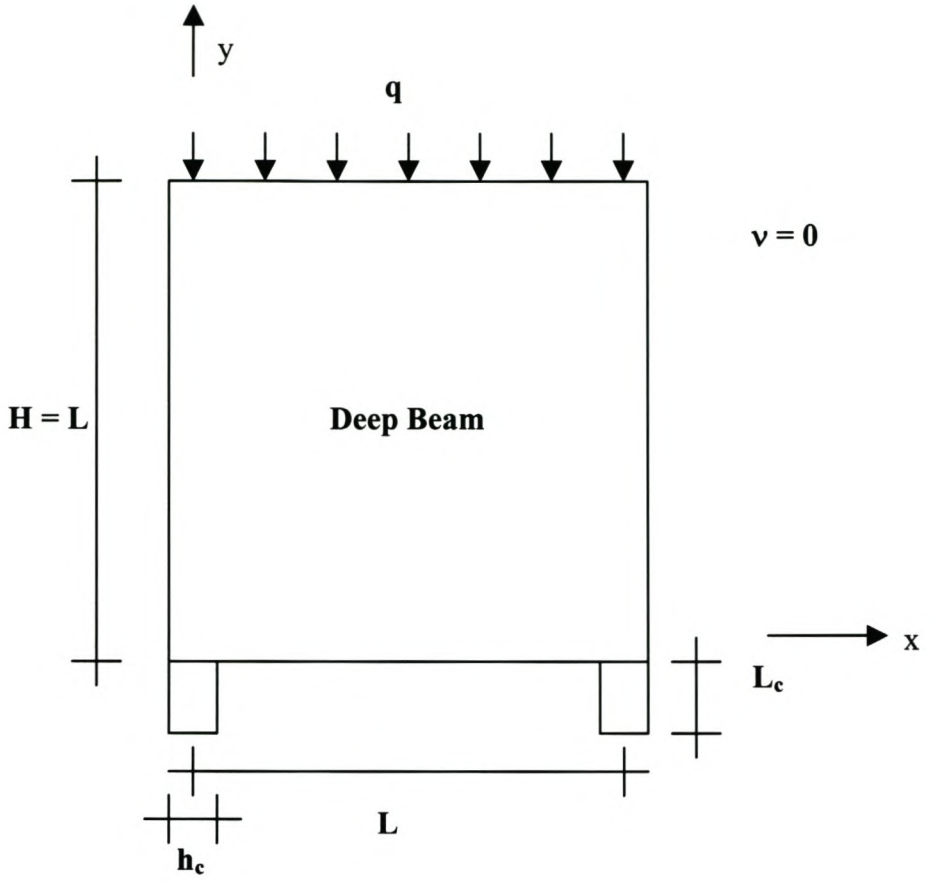

Figure 6.6 (Model 3)

The bending stiffness of the columns implemented in Model 3 must not govern the rotation and shape of the model's deflection profile under loading, but must serve to satisfactorily distribute the loads without seriously deforming the elements near the supports. A column of length, **(L_c)** = 1500 mm is chosen. The cross-section chosen is 600x300 mm. The thickness of the column, **(s)** = 300 mm is chosen to match the deep beam thickness, **b** = 300mm. The depth of the column's cross-section is denoted by **(h_c)** = 600mm.

From the theory of structural mechanics, the bending stiffness $\mathbf{K_b}$ of a structural element is represented by:

$$K_b = \frac{E_i I_i}{L_i} \tag{6.11}$$

The length of the structural member is denoted by $\mathbf{L}_i$, its Young's modulus of elasticity denoted by $\mathbf{E}_i$ and its inertial moment by $\mathbf{I}_i$.

The inertial moment of the column, denoted by the variable $(\mathbf{I_c})$, is calculated with the following equation:

$$I_c = \frac{1}{12} s(h_c)^3 \tag{6.12}$$

The inertial moment of the deep beam is calculated with the following equation:

$$I = \frac{1}{12} b(H)^3 \tag{6.13}$$

Therefore, noting that **s** = **b** in Model 3, the bending stiffness ratio of the deep beam versus the column is denoted by the following equation:

$$\frac{K_{b,beam}}{K_{b,column}} = \left(\frac{H}{h_c}\right)^3 \left(\frac{L_c}{L}\right) \tag{6.14}$$

The height of the deep beam resisting bending is, $\mathbf{H}$ = 19500 mm. That of the column resisting bending is, $\mathbf{h_c}$ = 600 mm. The span length of the deep beam is, $\mathbf{L}$ = 19500 mm and that of the column is, $\mathbf{L_c}$ = 1500 mm. From equation (6.14), the bending stiffness ratio of the deep beam versus the column is equal to 2640. This signifies that the bending stiffness of the deep beam is 2640 times larger than that of the column's bending stiffness. From this, it is clear that the rotation of the columns will be governed by the bending stiffness of the deep beam and not by the columns.

3. **Model 4:** Figure 6.7

- The span length **L** is measured from the centre of the supports.
- An extreme support condition with a large bearing width and infinite stiffness is created. The left corner is pinned and rollers placed along the bottom edge over a distance of $\mathbf{h_c}$ = (**L** /10).

- The uniformly distributed load **q** is applied to the beam top edge extending from the centre of the left support to the centre of the right support.
- The magnitudes of Model 4's variables are as those for Model 1, with $\mathbf{h_c}$ = 1950mm.

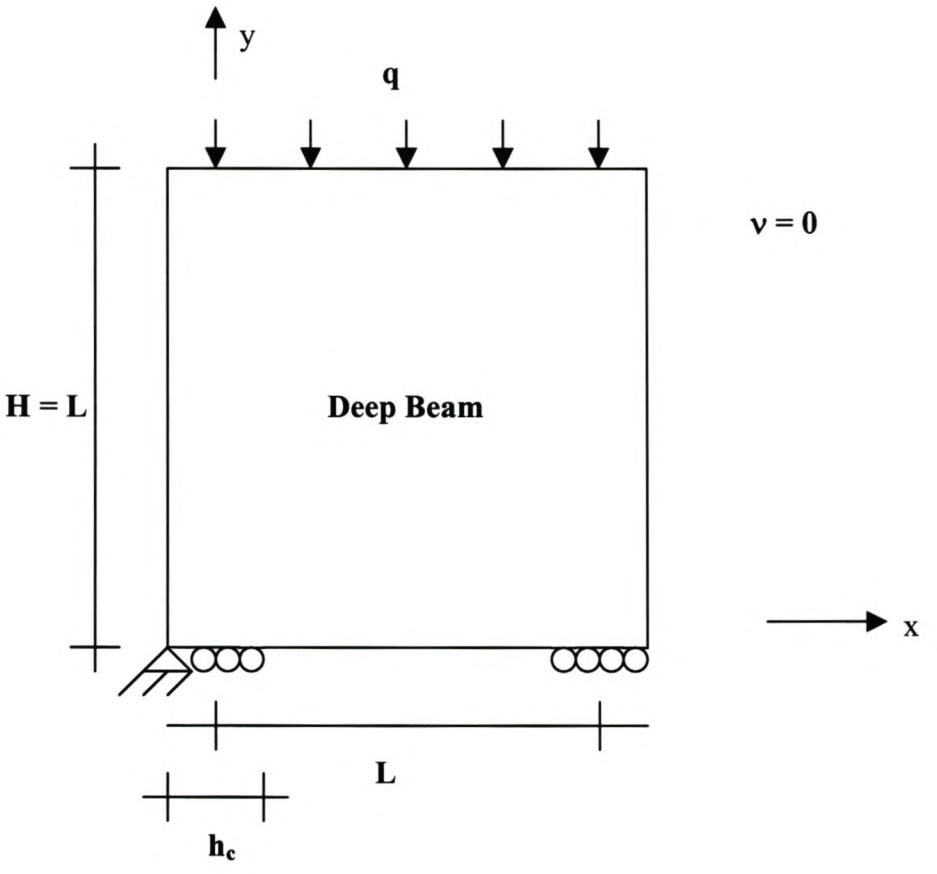

Figure 6.7 (Model 4)

4. Model 5: Figure 6.8

- Model 5 is created to simulate Model 3, with the only difference being that the columns are assigned an infinite bending stiffness. The columns are removed from the model and rollers used to create the infinite stiffness of the support.

- Model 4 implemented the same method of including columns of infinite stiffness. Model 4, however, implemented columns with a larger cross-sectional depth.
- A hinge is implemented at the bottom left corner of the deep beam.

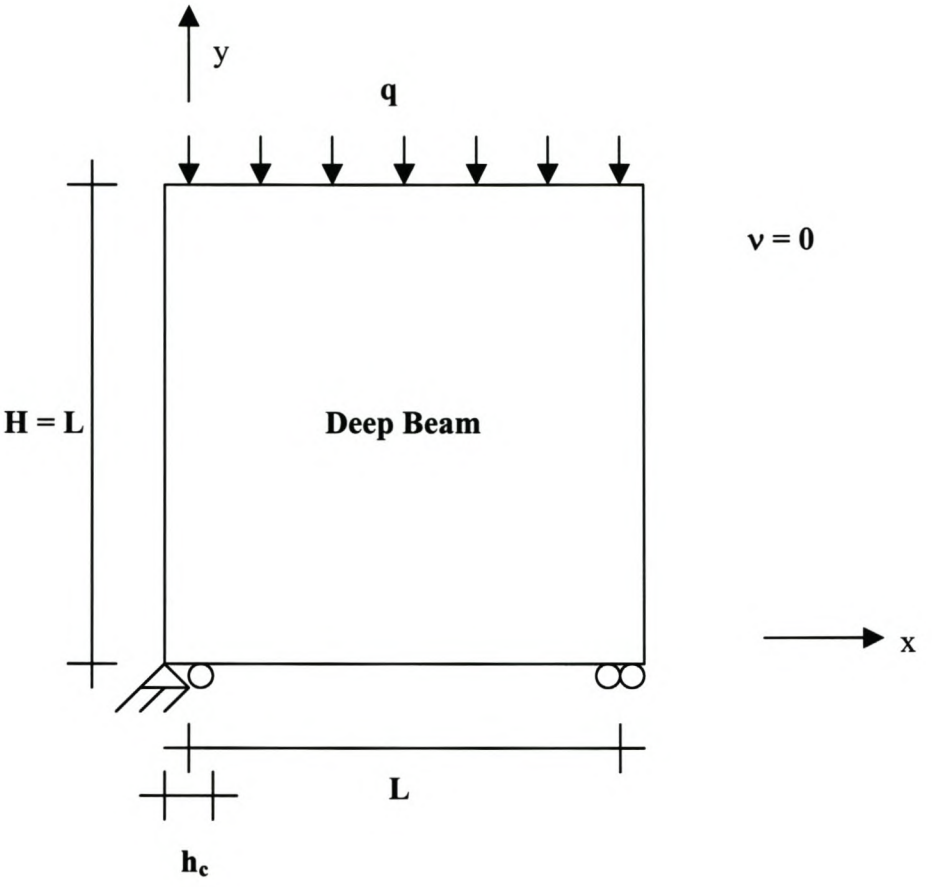

Figure 6.8 (Model 5)

- The span length **L** of the deep beam is measured from the centre of the left support to the centre of the right support.
- The uniformly distributed load **q** is applied to the top edge of the beam extending from the centre of the left support to the centre of the right support.
- The magnitudes of the variables in Model 5 are those as implemented in Model 1, with $\mathbf{h_c}$ = 600mm.

6.4 Variations in the horizontal stress distributions for the various models

This section compares the horizontal stress σ_{xx} distributions for Models 1 to 5 plotted over the height of the deep beam **H** at various vertical sections. Finite element analyses of Models 1 to 5 produced the stress results presented in Figures 6.9 to 6.11.

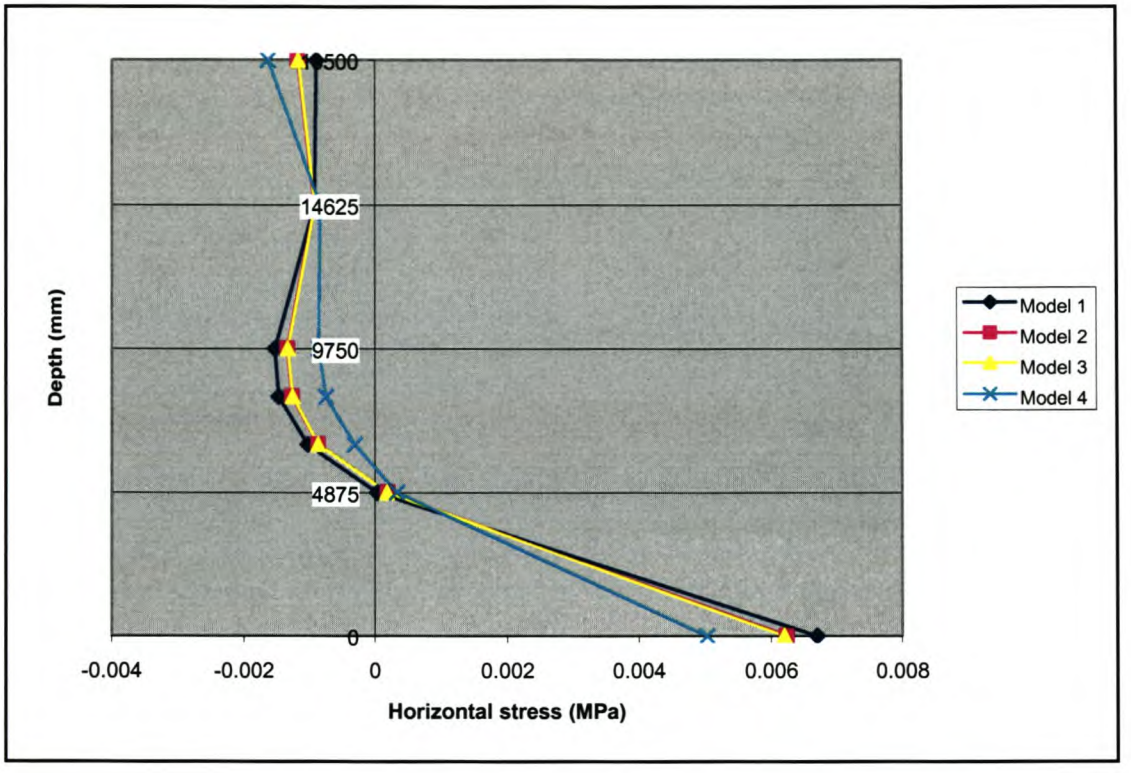

Figure 6.9 Variations in the σ_{xx} distributions at mid-span for Models 1-4.

It is clear from Figures 6.9 and 6.10 that the σ_{xx} distributions pertaining to Models 2 and 3 correspond closely to one another both at mid-span and quarter span, which are the positions at which the strains are sampled in the simply supported elastic beams. There are basically two similarities, which cause the similar behaviour of Models 2 and 3. The first is that the rotations of the beam at the pin supports, in Model 2, as well as the rotation of the columns, in Model 3, are governed by the bending stiffness of the deep beam itself. The second is that the pin support, in Model 2, is located on a common node, shared by two elements. This enables the pin support to distribute the load over two elements. Likewise, in Model 3, the column extends over the same two elements and therefore Model 3 distributes the load in the same way as Model 2 does.

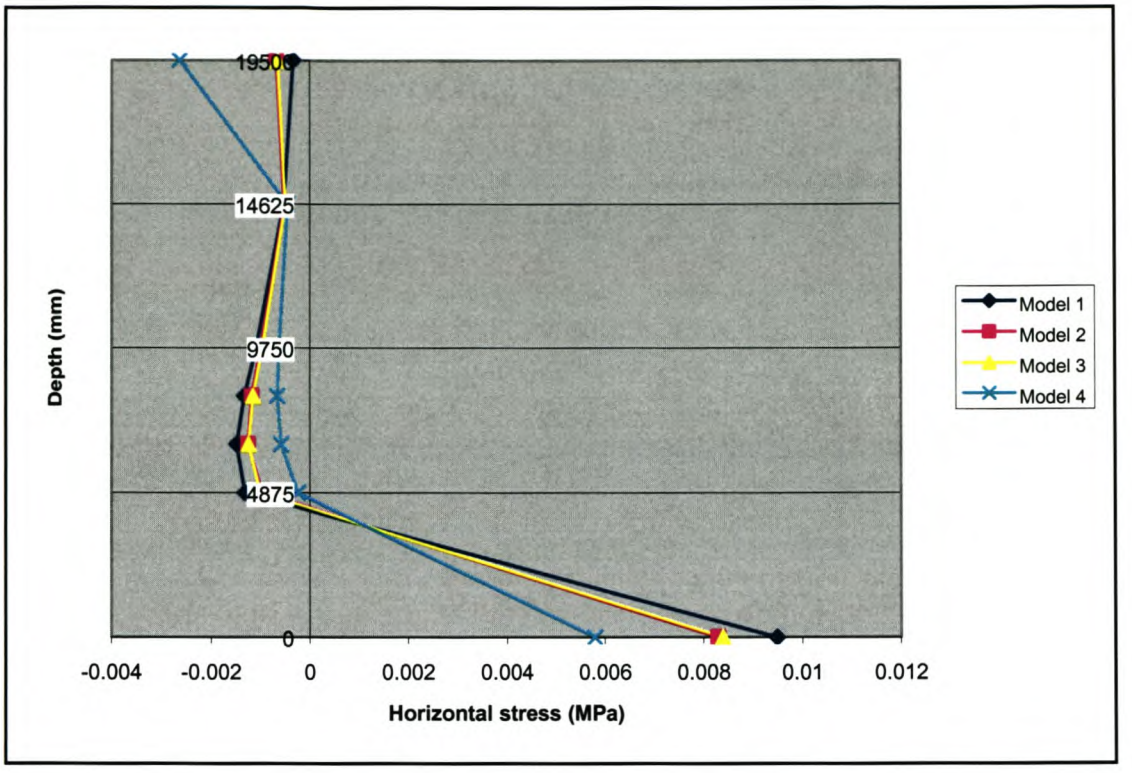

Figure 6.10 Variations in the σ_{xx} distributions at quarter span for Models 1-4.

The response of Models 2 and 3 vary slightly from the response of Model 1 in both Figures 6.9 and 6.10. Four clear differences noted, while investigating the σ_{xx} distributions of Model 1 are that:

a) *A higher tensile stress is developed on the bottom fibre of each vertical section.*

b) *The neutral axis is located lower down on the deep beam for each vertical section.*

c) *Higher compressive stresses develop near the middle fibre for each vertical section.*

d) *A lower compressive stress is developed on the top fibre of each vertical section.*

These differences can be attributed to the fact that the supports in Models 2 and 3 are able to distribute the load over a larger area and therefore seem to slightly clamp the corners of the deep beam. Any type of support that creates a type of clamping effect will have a larger effect in terms of working against the effect of the uniformly distributed load than a support, which does not create clamping at all. This clamping effect will clearly reduce σ_{xx} on the bottom fibre for Models 2 to 3.

Supports, as those implemented in Model 4, serve to significantly clamp the corners of the deep beam. Model 4's supports therefore create a significantly larger clamping effect than those of Model's 2 and 3. From Figures 6.9 to 6.10 it is seen that the same pattern of differences exist between the response of Model 4 versus Model's 2 and 3 as those presented above between Model 1 versus Model's 2 and 3.

Model 5 is created to investigate what effect increasing the stiffness of the columns in Model 3 has on the σ_{xx} distribution at quarter and mid-span. The stiffness of the columns is increased to have an infinite stiffness. As seen in Figure 6.11, the change in the σ_{xx} distribution at quarter span is negligible. This signifies that, already at quarter span, the effect of the clamping has been damped out. Therefore, the stress distributions at quarter and mid-span of Model 3 are independent of the column stiffness.

It is important to note that the same cannot be said for larger columns, as their effect on the σ_{xx} distributions might only be damped out somewhere between quarter and mid-span. For large enough columns the effect might never be damped out. However, Figure 6.11 has proven that assigning the columns in Model 3 with an infinitive stiffness will have a negligible effect on the original σ_{xx} distributions as calculated without the infinitively stiff columns. It signifies that the effect of the stiff columns has been damped out before quarter span.

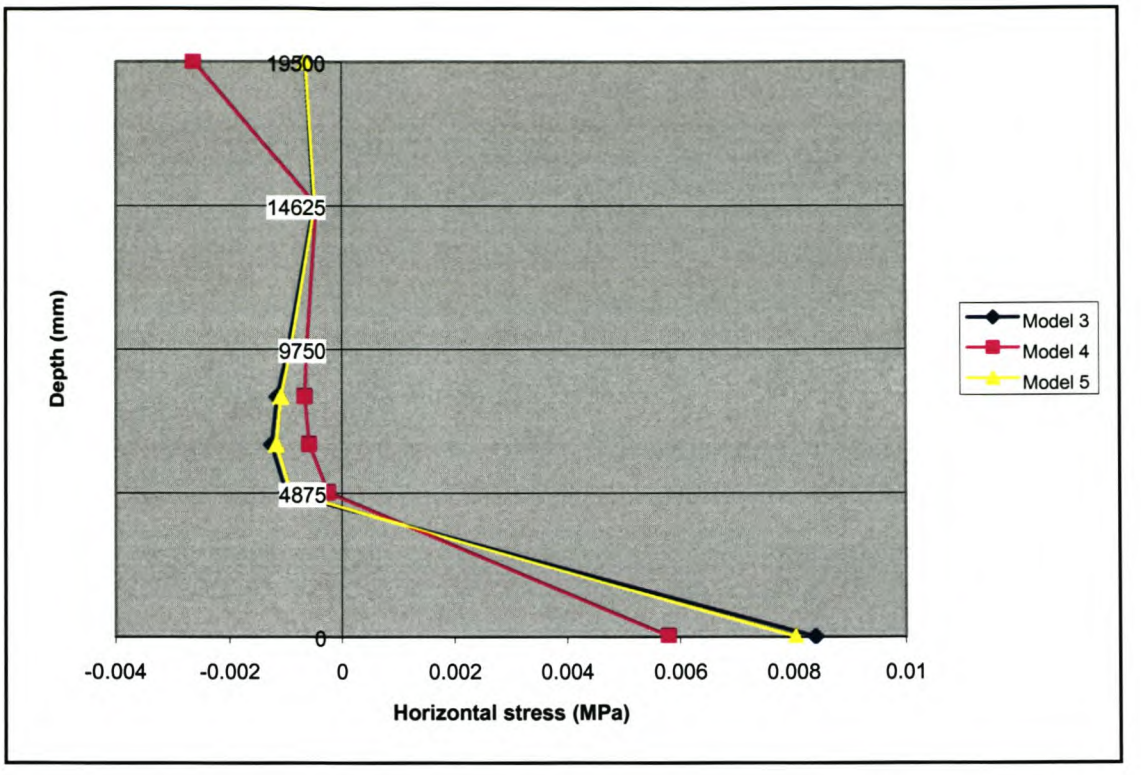

Figure 6.11 Variations in the σ_{xx} distributions at quarter span for Models 3, 4 and 5

From an economical point of view, for practicing engineers, it can be seen that a deep beam structure is a very uneconomical structure with regard to the amount of material used versus the amount needed to resist the load. The stresses near the middle fibres are lower than those on the extreme fibres. This is due to the arched path that the loads follow through the deep beam and finally into the foundation.

From a practical design point of view, it is more conservative to simply support the deep beam when designing for the σ_{xx} tensile stresses on the bottom fibre and to clamp the corners when designing for the σ_{xx} compressive stresses on the top fibre.

6.5 Variations in the deflection profiles for the various models

This section compares the differences between the various Model deflection profiles in Figures 6.12 to 6.17.

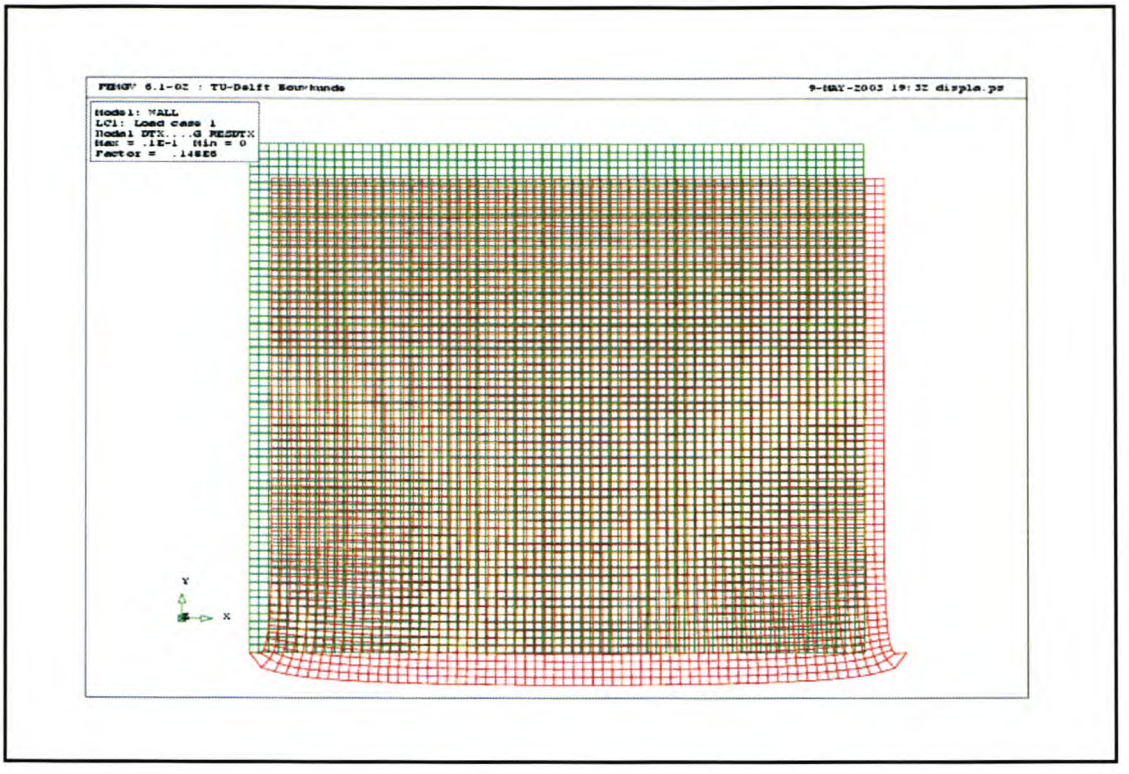

Figure 6.12 Deflected shape of Model 1.

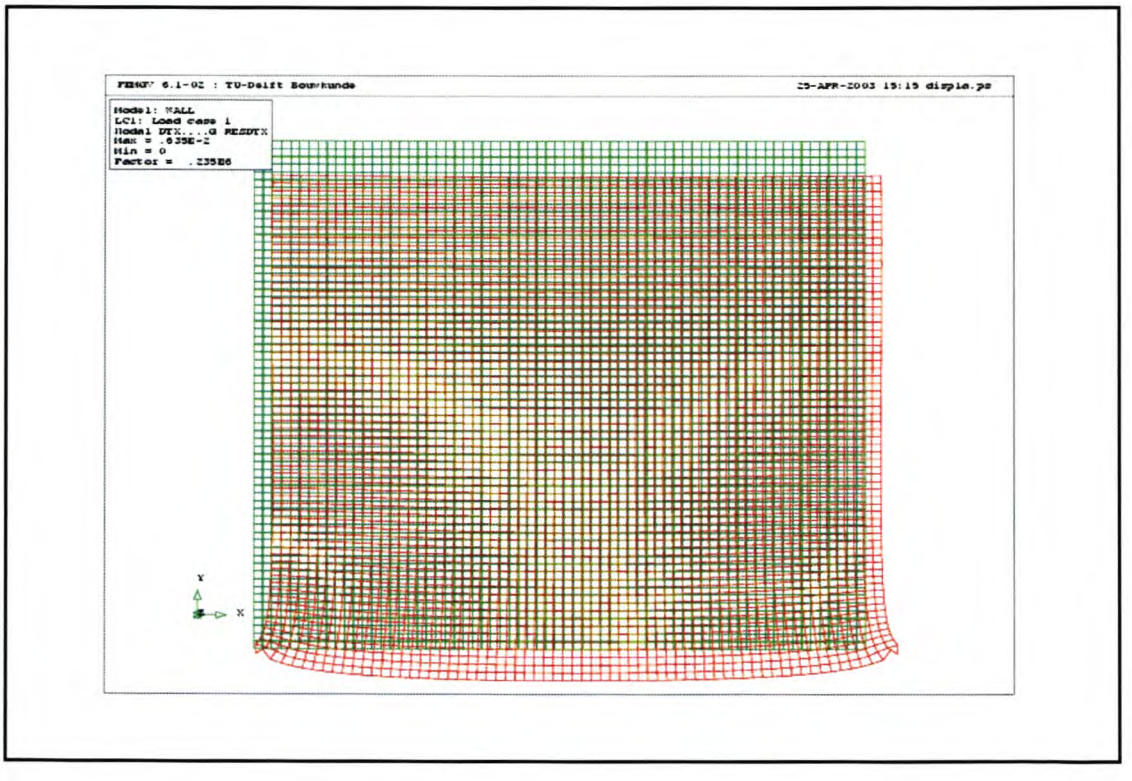

Figure 6.13 Deflected shape of Model 2.

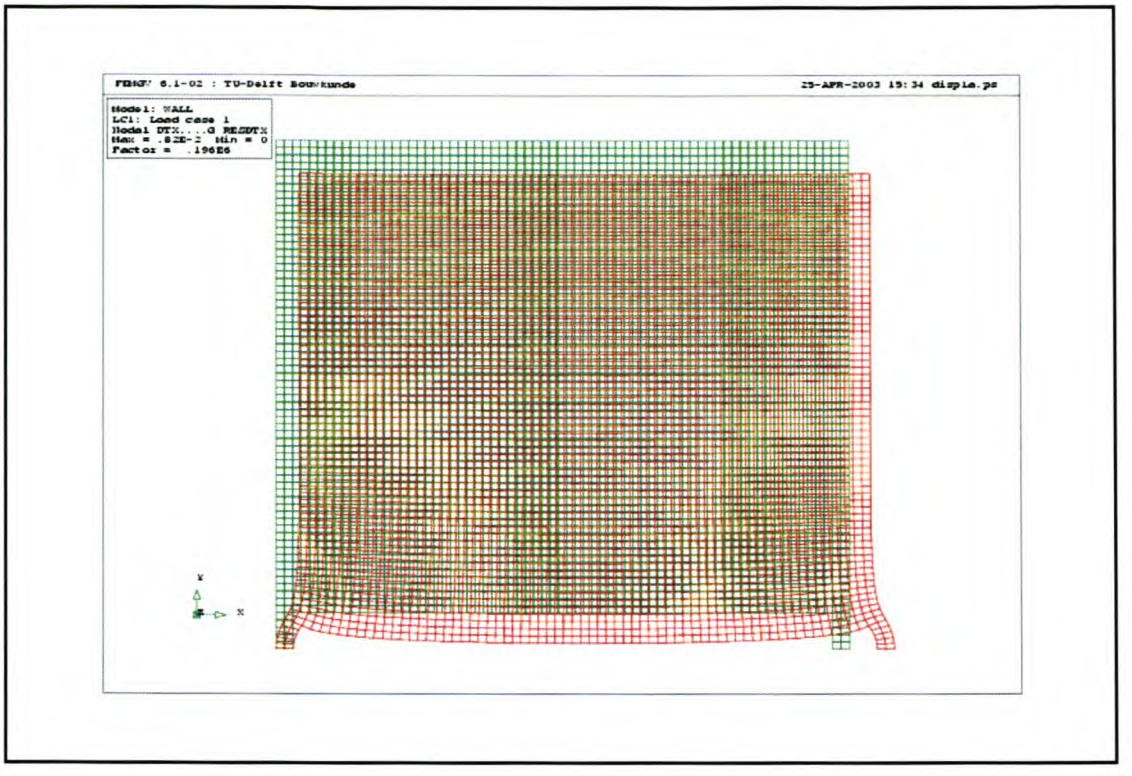

Figure 6.14 Deflected shape of Model 3.

In Figures 6.12 and 6.13 it is seen how the pinned supports cause serious local deformations of the elements to which they are connected. This causes stress concentrations to develop in the region near the supports, which are a direct result of these exaggerated displacements. Figure 14, however, presents how the implementation of the small columns in Model 3 prevents the exaggerated displacements.

Figure 6.15 plots the displacements of the bottom edge of the deep beams as obtained in the analyses of Models 1 to 3. At first it does not seem to make sense that the σ_{xx} distributions at quarter and mid-span match so closely whilst their displacements in Figure 6.15 are so different from one another. The reason for the large difference in displacements between these respective models is due to the fact that the elements closest to the supports in the models, supported by pins, are so badly deformed. These excessive, local displacements near the supports influence the displacements of all the other nodes along the bottom edge of the deep beam. These local displacements are more severe in Model 1 than they are in Model 2, which is due to Model 2's ability to

distribute the load over two elements, as opposed to one element in Model 1. This effect is clearly seen in Figure 6.15, where the mid-span deflection Δ for Model 1 is a factor 2 times that of Model 3.

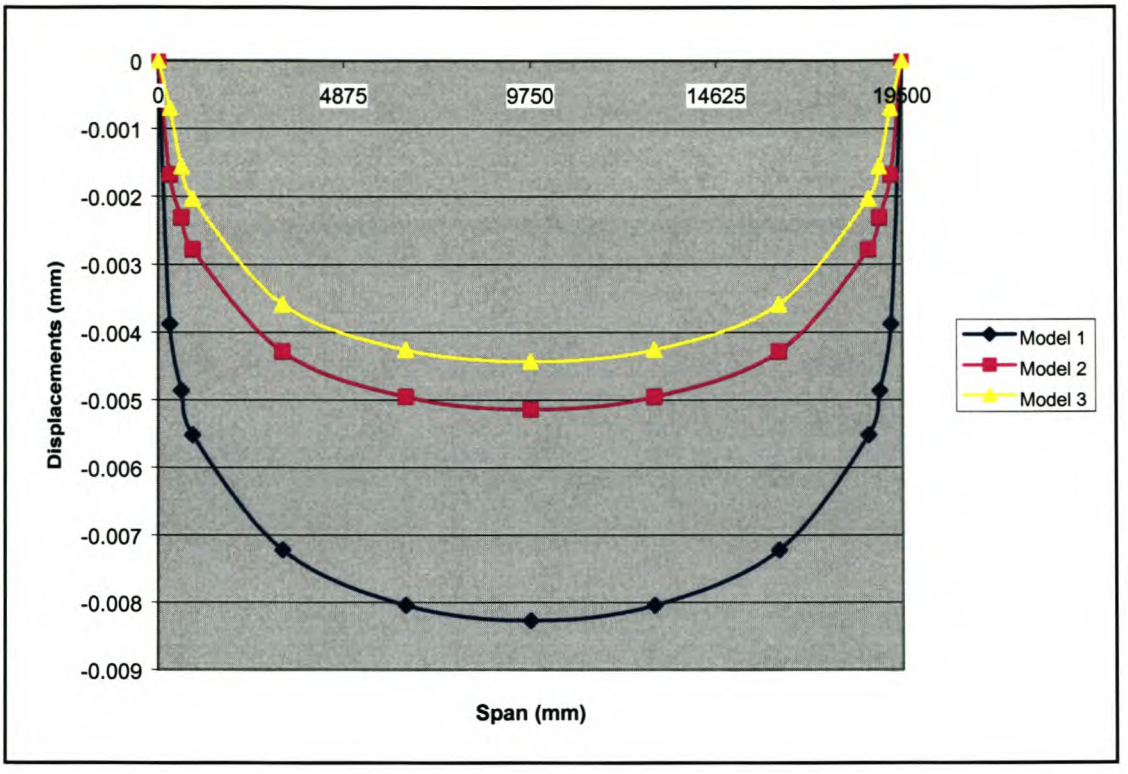

Figure 6.15 Deflection profiles for the bottom edge of the Models 1 to 3.

The stresses, however, are calculated from the relative displacements in the finite element method. Due to the close correspondence between the stress distributions of Models 1 to 3, the relative displacements should also correspond closely. In order to compare the relative displacements of Models 1 to 3, the deformations of the elements closest to the supports were disregarded completely. These results are presented in Figures 6.16 to 6.17. These Figures demonstrate how the relative displacements correspond more closely to one another.

The **Δ/L** ratios form the basis for the comparisons between the strain results of the simply supported elastic beams and the strain results of the simply supported finite element models of the deep beams. Only when the **Δ/L** ratios match one another can the respective strain results be compared. It is therefore important that the respective **Δ/L** ratios match one another.

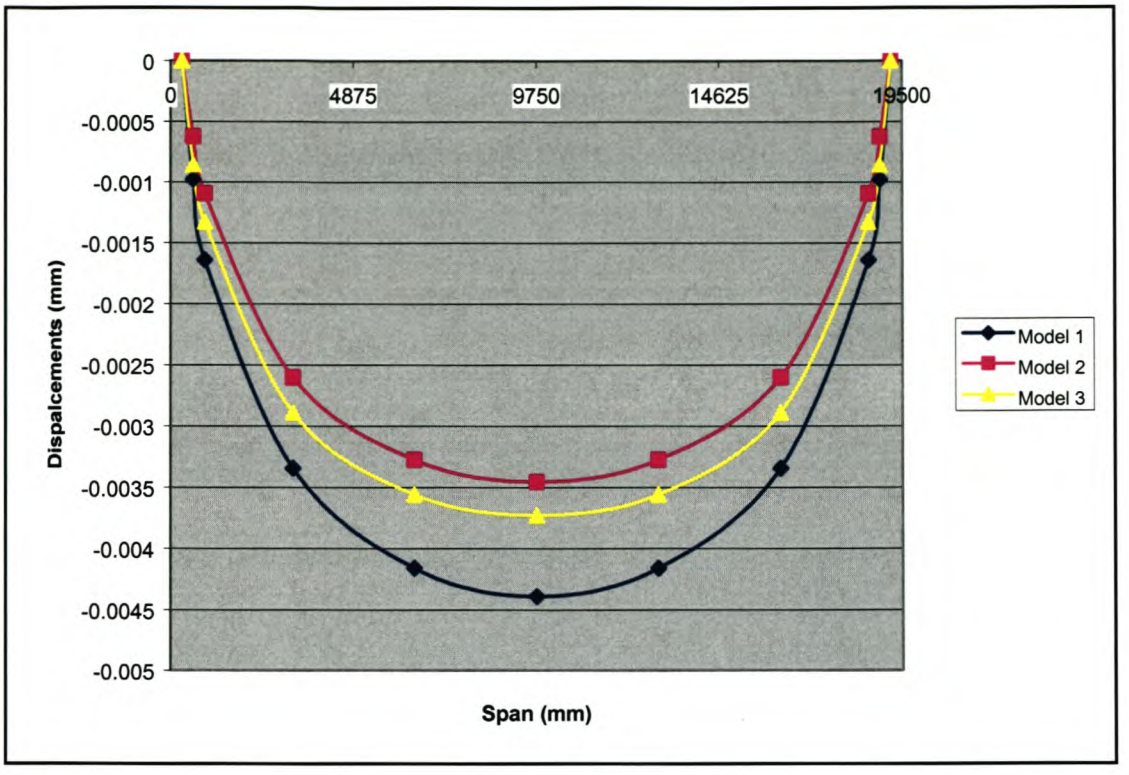

Figure 6.16 Relative displacements (First element alongside support disregarded).

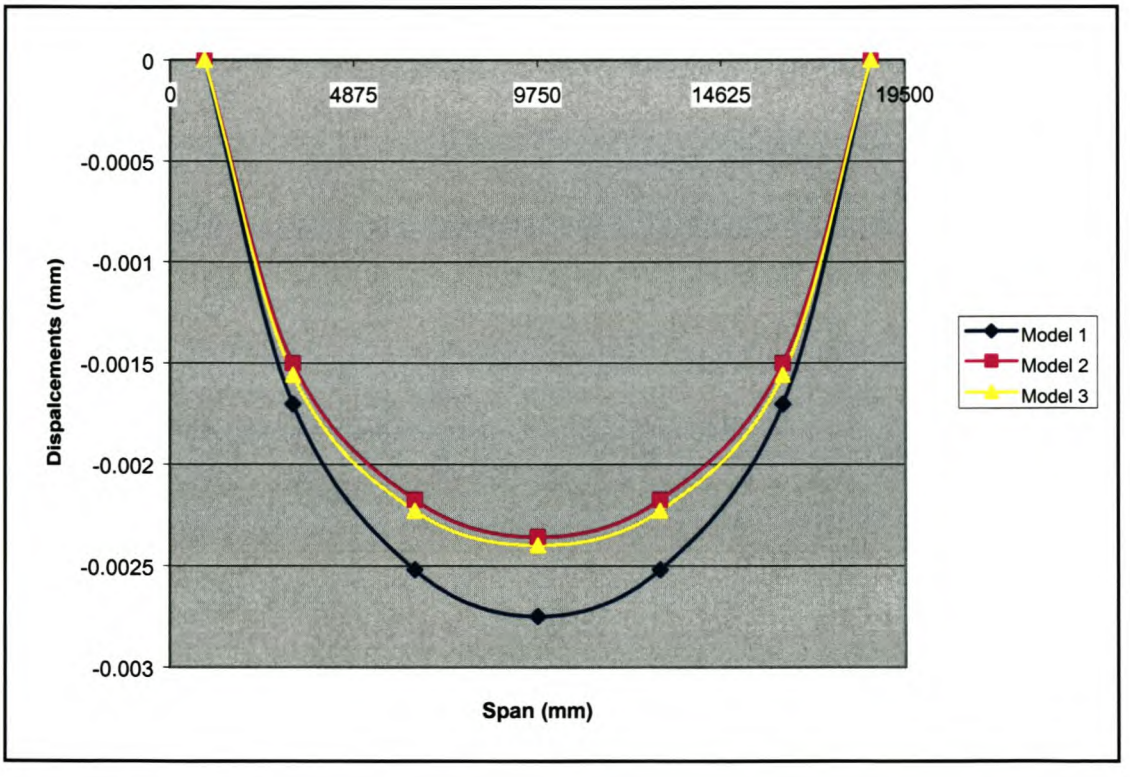

Figure 6.17 Relative displacements (First three elements alongside support disregarded).

Figures 6.16 to 6.17 have demonstrated that the **Δ/L** ratios of Models 1 to 3 closely match one another when taking the relative displacements into account. The calculation of the **Δ/L** ratio is made easier in Model 3 as the local displacements experienced at its columns are small and of a uniform nature. The magnitude of the mid-span deflection **Δ** is calculated by subtracting the shortening of the columns from the vertical deflection of the node on the bottom edge of the deep beam at mid-span. The **Δ/L** ratio is then easily obtainable by dividing **Δ** by the deep beam span length **L**. Therefore, Model 3 is deemed the more suitable model for the comparison with the simply supported elastic beams used in the **LTS** (Burland and Wroth 1974).

6.6 Summary

Firstly this chapter demonstrated that the finite element method used in the modelling of deep beams is an accurate solution to the fundamental differential equation (6.6), pertaining to the structural analysis of the deep beams.

Secondly, various simply supported finite element models of deep beams, simulating the simply supported elastic beams used in the **LTS** (Burland and Wroth 1974), were investigated. After investigations into their stress distributions and bottom edge deflection profiles, Model 3 was chosen as the most suitable model. This was due to the ability of Model 3's column supports in solving the problem of irregular bottom edge deflection profiles, which resulted from local exaggerated displacements at nodal pin supports. Regular deflection profiles are desired in order for the correct determination of the **Δ/L** ratios.

The following chapter is dedicated to building linear elastic finite element models of simply supported solid masonry walls of various span lengths **L** and **L/H** ratios, implementing the boundary value problem of Model 3. The linear elastic models are then subjected to **Δ/L** ratios similar to those implemented in the **LTS** on beams of equal span length **L** and **L/H** ratio. The strain results obtained from the finite element analyses are then compared to the strain results obtained from the **P** and **q** models for similar **L/H** and **Δ/L** ratios.

Chapter 7

Linear elastic strain results: (Simply supported deep beams)

7.1 Introduction

The fundamental purpose of this chapter is to justify the ability of the **P** and **q** models to accurately calculate the relationships between $\Delta/L:\varepsilon_{bmax}$ and $\Delta/L:\varepsilon_d$ pertaining to solid masonry walls. Linear elastic finite element models of simply supported solid masonry walls (deep beams) are subjected to the same Δ/L ratios as those enforced on the simply supported elastic beams implemented for the **P** and **q** models. The above relationships corresponding to the **P** and **q** models are then directly compared to those of the solid masonry walls. The model dimensions ensure compatibility with the sagging zone of the settlement trough implemented in this study. This relates to the bounds of the wall's span length **L**, represented by equation (5.18). The models are also representative of walls found in practical structures today.

Points a) to e) relate to the structural behaviour of the simply supported elastic beams implemented in the **P** and **q** models subject to a sagging mode of deformation. This chapter investigates the validity of the following points for the case of deep beam structural behaviour.

a) For a given **L/H** ratio, $\Delta/L:\varepsilon_{bmax}$ and $\Delta/L:\varepsilon_d$ represent linear relationships, irrespective of the magnitude of the span length **L**.

b) An **L/H** ratio close to 2 is calculated to be the critical ratio with respect to the magnitude of ε_{bmax} in both the **P** and **q** models for the given material properties (section 5.3).

c) At an **L/H** ratio equal to 0.6, ε_{bmax} and ε_d are calculated to have equal magnitudes in both the **P** and **q** models.

d) For **L/H** ratios smaller than 0.6, ε_d is calculated to govern cracking in the simply supported elastic beams.

e) For **L/H** ratios larger than 0.6, ε_{bmax} is calculated to govern cracking in the simply supported elastic beams.

The material properties of the simply supported elastic beams used for the **P** and **q** models are the same as those implemented in the construction of the linear elastic solid masonry wall models. These material properties are presented in section 5.3 of this study. A uniformly distributed load applied to the model's top edge (Model 3, chapter 6) is used to enforce the respective **Δ/L** ratios, which corresponds only to the **q** model. Nevertheless, the results pertaining to both the **P** and **q** models are used in this chapter.

7.2 Properties of the deep beam models

Table 7.1 tabulates the dimensions and material properties of the deep beam models to be analysed in this chapter.

Models A to C employ the maximum possible span length **L** of 19800mm, to maintain compatibility with the sagging zone of the settlement trough implemented in this study. They are assigned **L/H** ratios of 1 to 3 respectively.

Model D employs a span length **L** of 9900mm. Its results are compared with those of Model B in order to investigate the effect of a change in **L** on the respective strains for a wall of **L/H** ratio equal to 2.

Model E employs a span length **L** of 9000mm and an **L/H** ratio of 0.5.

Model F employs a span length **L** of 12000mm. Its results are compared with those of Model E in order to investigate the effect of a change in **L** on the respective strains for a wall of **L/H** ratio equal to 0.5.

Model G employs a span length **L** of 9000mm and an **L/H** ratio of 0.6. It is used to investigate whether the magnitudes of ε_{bmax} and ε_d are equal. This will determine whether an **L/H** ratio of 0.6 is the boundary at which the governing strain changes from ε_d to ε_{bmax} for solid masonry walls with the given masonry properties (section 5.3).

Model	L (mm)	L/H	Δ/L	Material	E (MPa)	G (MPa)
A	19800	1	0.001685	Masonry	4000	1667
B	19800	2	0.001685	Masonry	4000	1667
C	19800	3	0.001685	Masonry	4000	1667
D	9900	2	0.001006	Masonry	4000	1667
E	9000	0.5	0.000924	Masonry	4000	1667
F	12000	0.5	0.001185	Masonry	4000	1667
G	9000	0.6	0.000924	Masonry	4000	1667

Table 7.1 Dimensions and material properties of the linear elastic deep beam models.

All models tabulated in Table 7.1 are built in accordance with the boundary value example of Model 3 in chapter 6. Therefore, in order to enforce the respective models to deform with the corresponding **Δ/L** ratios, a uniformly distributed load **q** is applied to the top edge of the respective models. Note that the maximum possible **Δ/L** ratio corresponding to the shape of the sagging zone implemented in this study is equal to that enforced on Models A to C. In order to calculate the **Δ/L** ratios of the respective models, each model's mid-span deflection **Δ** is calculated with equation (5.11). The magnitude of **Δ** is dependent on the model span length **L** and on the properties of the settlement trough. Dividing the **Δ** by **L** is the definition of the **Δ/L** ratio. Initially a uniformly distributed load with a unit magnitude $\mathbf{q_{unit}}$ is applied to the top edge of each model. The mid-span deflection Δ_q resulting from the application of $\mathbf{q_{unit}}$ is calculated and used to determine the magnitude of **q** which results in enforcing the **Δ/L** ratios tabulated in Table 7.1 for each of the respective models.

The uniformly distributed load **q**, required to enforce the **Δ/L** ratio tabulated in Table 7.1 for each of the respective models, is calculated with the following equation:

$$q = q_{unit}\left(\frac{\Delta}{\Delta_q}\right) \tag{7.1}$$

It must be remembered that Δ is the mid-span deflection as calculated with equation (5.11).

7.3 Methodology: Extraction of strains in the deep beam models

This section describes the methodology employed in the extraction of strains from the body of the deep beam models. The strain results are represented along different lines on the body of the deep beam models. Due to symmetry, only half of each deep beam is modelled. Figure 7.1 shows the positions of the lines along which the strain results are presented.

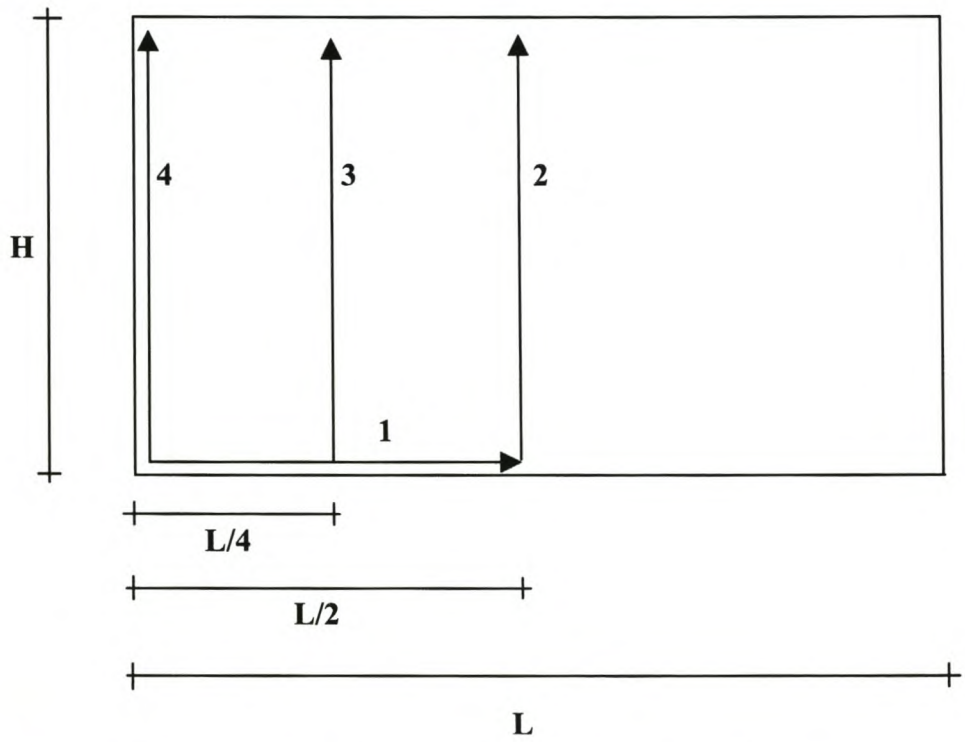

Figure 7.1 Deep beam with the positions of the four lines along which the strain results are represented.

The strain results are represented along three vertical and one horizontal line on the body of the deep beam. The vertical lines start from the bottom edge of the deep beam and propagate to its top edge. The vertical lines are at the positions of mid-span (2),

quarter span (3) and just off set from the simple column support (4). The horizontal line starts at the bottom left corner and propagates along the bottom fibre to mid-span (1). Figure 7.1 represents the entire deep beam, whereas only half the deep beam is modelled. Results represented on lines in the same positions on the other half of the deep beam will be identical due to the structural symmetry of the problem.

The positions on the respective lines, along which ε_{bmax} and ε_d are sampled, are as follows:

a) At the same relative geometrical positions at which they were sampled on the simply supported elastic beams, denoted by the abbreviation **SBP** (Simple Beam Position). Note that this strain is calculated as an average of all the strains at the respective integration points of a single element.

b) The positions on the respective lines at which the maximum strains develop in the deep beam, denoted by the abbreviation **MAXP** (Maximum Position). Note that this strain is calculated as an average of all the strains at the respective integration points of a single element.

c) The position on the deep beam body where the maximum tensile strain develops, irrespective if it falls on one of the lines or not. This strain is denoted by the abbreviation **AMAX** (Absolute Maximum). Note that this strain is calculated at a single integration point of a certain element, which most likely is a peak strain.

The strain ε_{bmax} is sampled from the results of ε_{xx} as obtained from the analyses of the models presented in Table 7.1. This is justified by the fact that the results of ε_{xx}, at the positions of sampling, are identical to the results of the maximum principal tensile strains ε_1. In the development of the **LTS**, presented in chapter 4, ε_d is calculated from a state of pure shear only, as represented in Figure 4.6. The stresses σ_{yy} and therefore strains ε_{yy} are not taken into account in the formulation of ε_d. This is conservative as ε_{yy} decreases the magnitude of ε_d. If it were considered here, the resulting ε_d would not be conservative, as the uniformly distributed load is excessive to enforce the

deformation of the deep beam in terms of a **Δ/L** ratio. The sampling of ε_d will therefore be performed with the help of equation (7.4).

Equation (7.2) is a copy of equation (4.25):

$$\varepsilon_d = \frac{\tau}{2G} \tag{7.2}$$

The variable τ is the absolute value of the shear stress corresponding to the absolute value of the shear strains γ sampled along the lines presented earlier. The variable **G** is the shear modulus of the masonry used in the construction of the deep beam models.

The shear stress τ is related to the shear strain γ with the following equation:

$$\tau = g\gamma \tag{7.3}$$

Substituting equation (7.3) into equation (7.2) results in the following equation for ε_d:

$$\varepsilon_d = \frac{\gamma}{2} \tag{7.4}$$

The strain results presented along the respective lines for each of the models are included in digital format on a CD, which is an Appendix to this study.

7.4 Principal strain contours

This section graphically presents colour contour plots in Figures 7.2 to 7.8 of the maximum principal strains ε_1 for models A to G under the influence of the **Δ/L** ratios tabulated in Table 7.1. The different contour levels correspond to the damage categories tabulated in Tables 3.1 and 3.2.

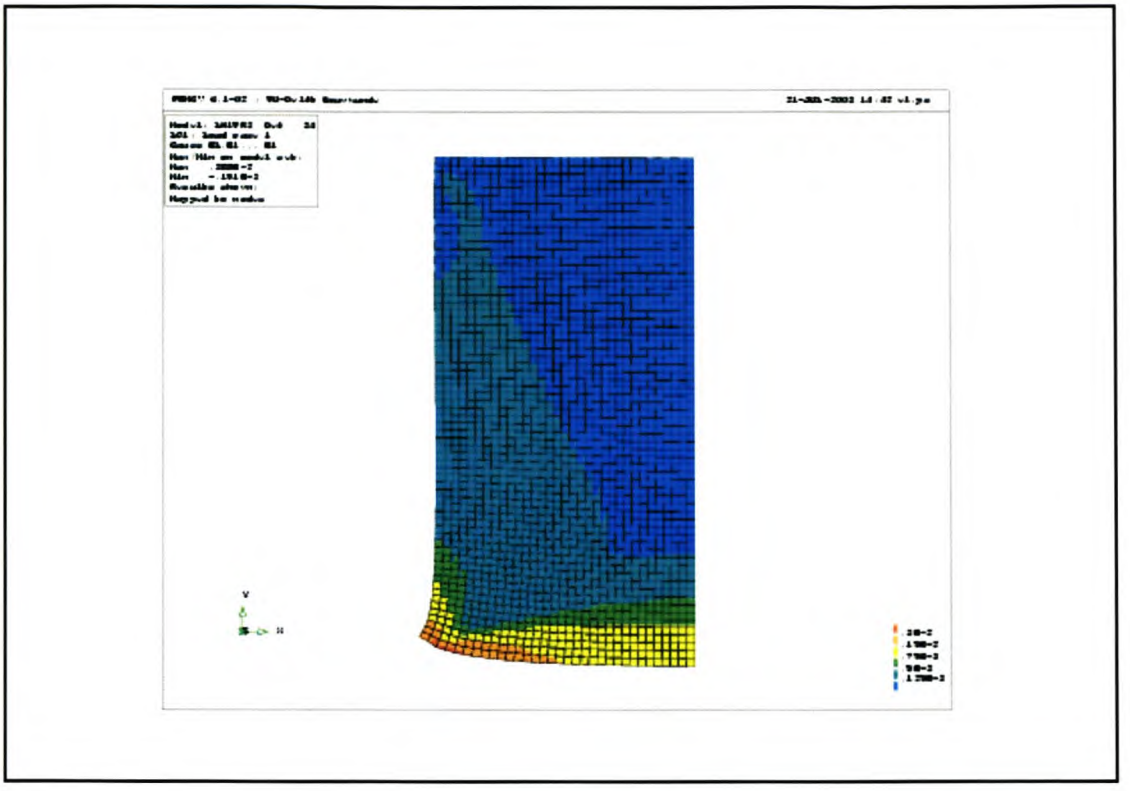

Figure 7.2 Maximum principal strains ε_1, Model A. (**L/H** = 1, **L** = 19800mm).

The dark blue contour corresponds to the region of the wall that has not experienced tensile strains above the yielding tensile strain ε_{yield} of the masonry. The magnitude of ε_{yield} for the masonry implemented in this study is 0.000125, using a horizontal tensile strength of 0.25 MPa. The light blue contour corresponds to that region of the wall experiencing initial cracking. The tensile strains have therefore surpassed ε_{yield} in this region of the wall. The two blue contours, correspond to damage category 0 according to Table 3.1, which is concerned with a *negligible* degree of severity. Strain levels causing cracking of the masonry, associated with a negligible degree of severity is an initial indication that Tables 3.1 to 3.2 are designed to serve a broad range of structural classes. The green contour corresponds to damage category 1, which is concerned with a *very slight* degree of severity. The yellow contour corresponds to damage category 2, which is concerned with a *slight* degree of severity. The brown contour corresponds to damage category 3, which is concerned with a *moderate* degree of severity. The red contour corresponds to damage category 4-5, which is concerned with a *severe to very severe* degree of severity.

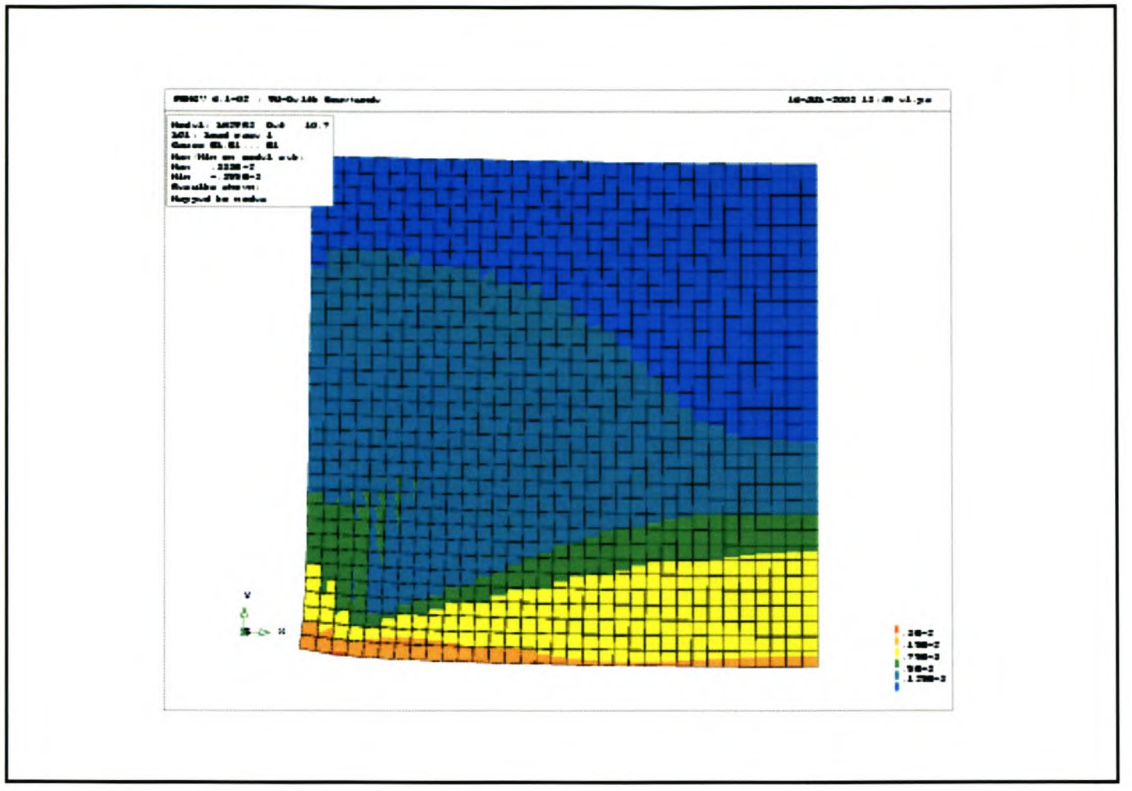

Figure 7.3 Maximum principal strains ε_1, Model B. (**L/H** = 2, **L** = 19800mm).

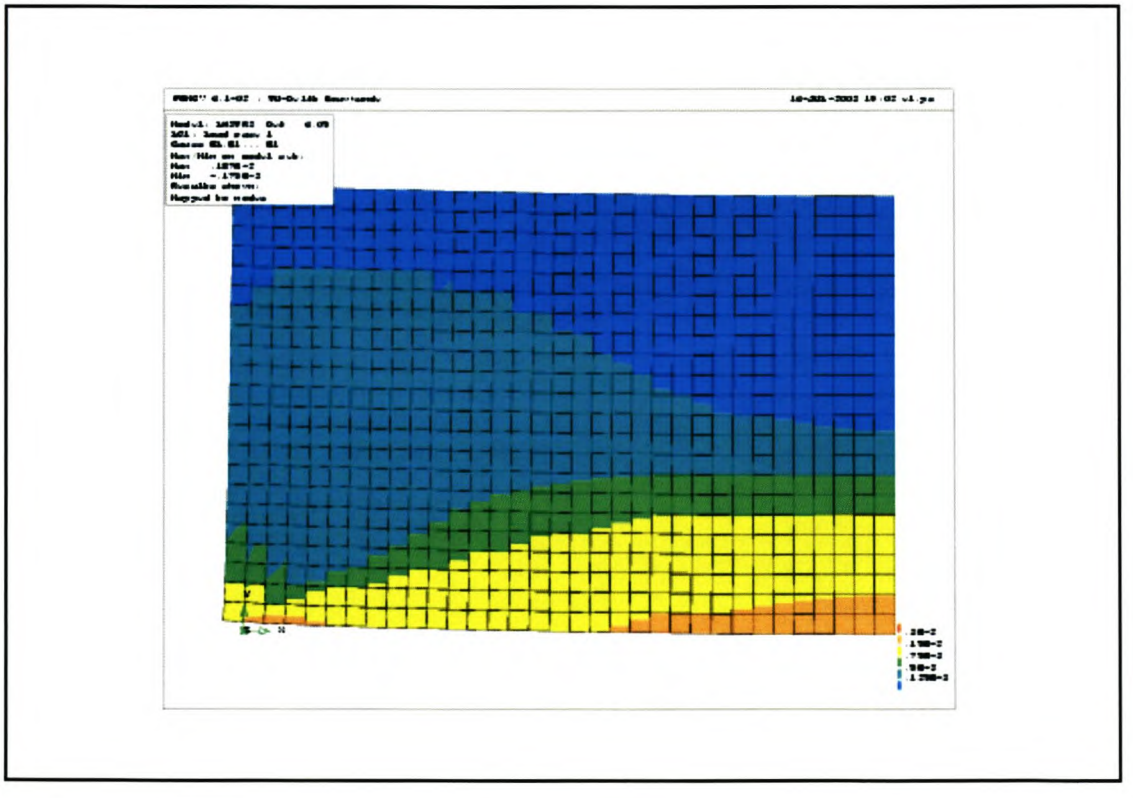

Figure 7.4 Maximum principal strains ε_1, Model C. (**L/H** = 3, **L** = 19800mm).

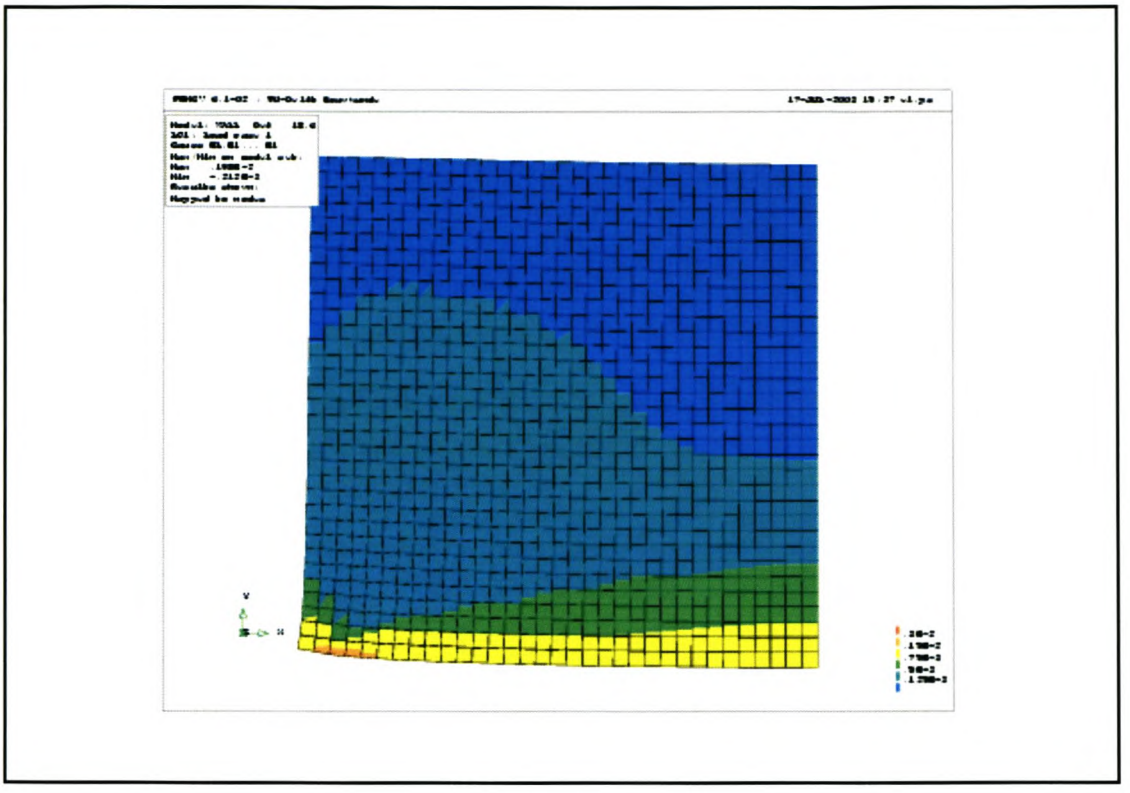

Figure 7.5 Maximum principal strains ε_1, Model D. (**L/H** = 2, **L** = 9900mm).

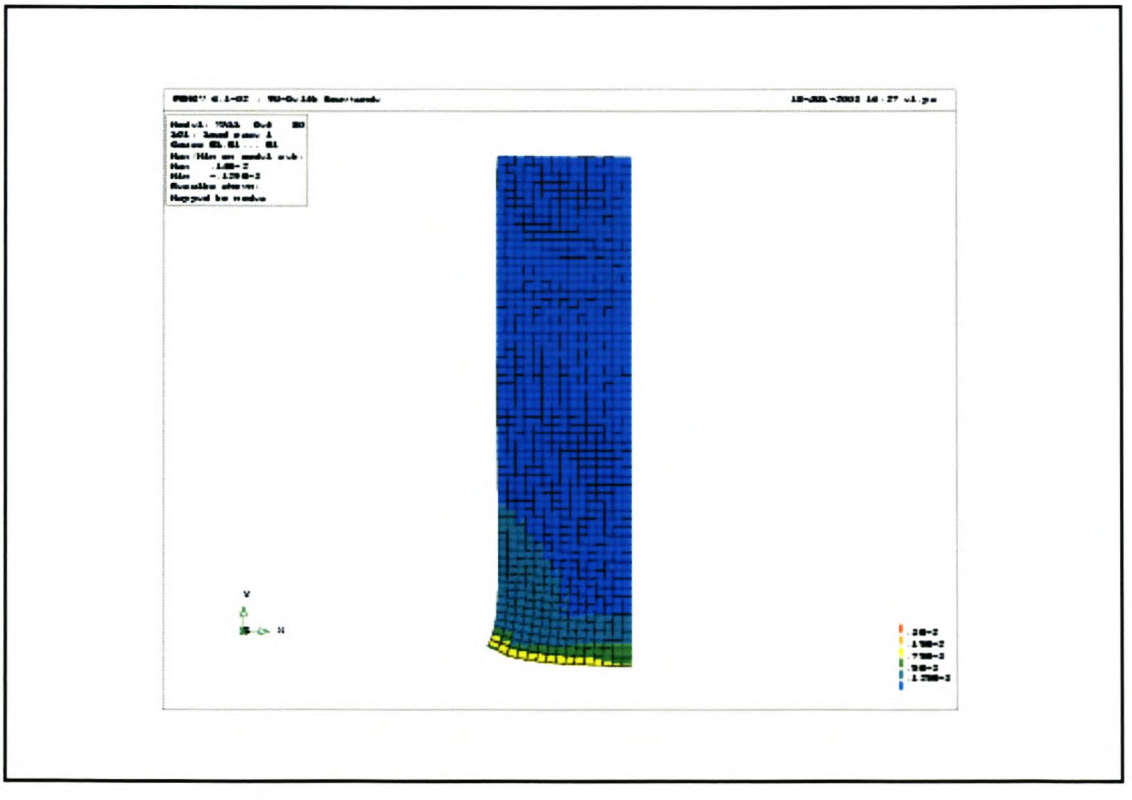

Figure 7.6 Maximum principal strains ε_1, Model E. (**L/H** = 0.5, **L** = 9000mm).

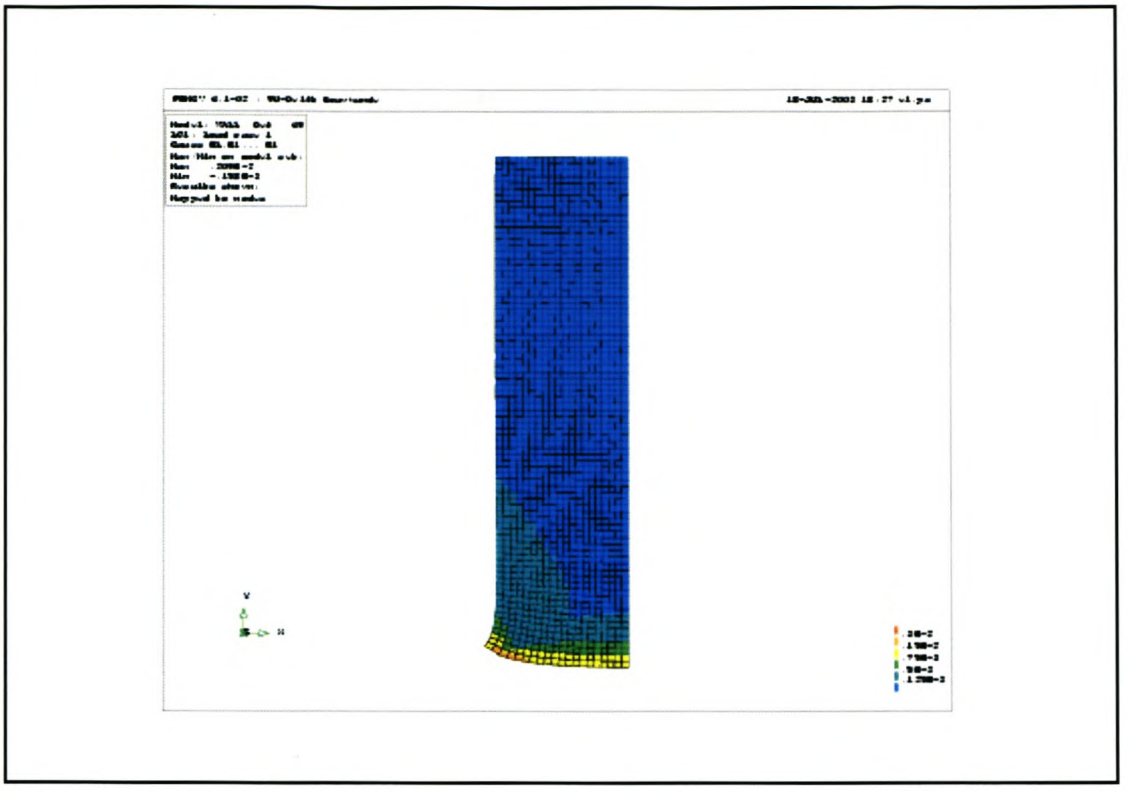

Figure 7.7 Maximum principal strains ε_1, Model F. (**L/H** = 0.5, **L** = 12000mm).

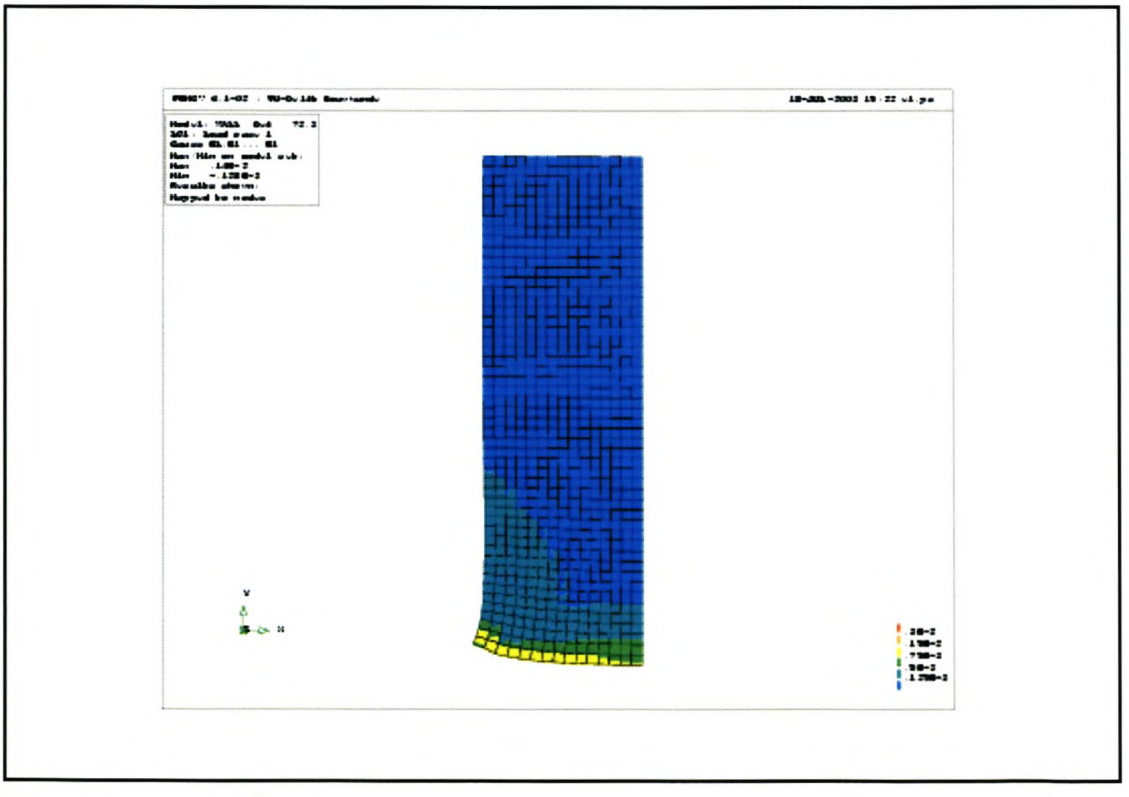

Figure 7.8 Maximum principal strains ε_1, Model G. (**L/H** = 0.6, **L** = 9000mm).

Damage categories 4-5 do not develop at the supports in Model C, but develop strongly in Model A and to a lesser degree in Model B. Therefore, as the **L/H** ratio of the deep beam increases, and thus as the beam becomes more slender, it becomes more difficult for the larger damage categories to develop at the deep beam's supports. The opposite occurs with regard to the development of the larger damage categories on the bottom fibre at mid-span. Damage category 3 does not develop at mid-span in Model A, but develops strongly in Model C and to a lesser degree in Model B. Therefore, as the **L/H** ratio of the deep beam increases, and thus as the beam becomes more slender, it is easier for the larger damage categories to develop at mid-span on the bottom fibre.

Model B and D both have **L/H** ratios equal to 2, but their maximum principal strain ε_1 distributions differ. This is due to their differing **Δ/L** ratios.

Damage categories 3 to 5 do not develop in Model E and G as their **Δ/L** ratios are smaller than the maximum **Δ/L** ratio corresponding to the settlement trough implemented in this study, as enforced on Models A to C.

Damage categories 4 to 5 do not develop in Model F as its **Δ/L** ratio is smaller than that of the maximum **Δ/L** ratio corresponding to the settlement trough implemented in this study, as enforced on Models A to C.

7.5 Extraction of strains

Table 7.2 tabulates the magnitudes of ε_{bmax} and γ. These are the strains extracted at positions **SBP** and **MAXP** along the respective lines presented in Figure 7.1. Table 7.2 also tabulates the magnitudes of ε_d, as are calculated from equation (7.4). The strains marked with stars are those sampled from the same positions on the body of the deep beam, but on different lines. Table 7.3 tabulates the magnitudes of the maximum tensile strains extracted at the position of **AMAX** irrespective of whether they fall on one of the lines presented in Figure 7.1 or not.

Mode 1	Line	ε_{bmax} (10^{-3})		γ (10^{-3})		ε_d (10^{-3})		Δ/L (10^{-3})
		SBP	MAXP	SBP	MAXP	SBP	MAXP	
A L/H=1	1	*1.125	3	N.A	*5.25	N.A	*2.625	1.685
	2	*1.125	*1.125	N.A	0	N.A	0	
	3	N.A	1.5	0.667	0.875	0.3335	0.4375	
	4	N.A	2	N.A	*5.25	N.A	*2.625	
B L/H=2	1	*1.5	2.5	N.A	*2.8	N.A	*1.4	1.685
	2	*1.5	*1.5	N.A	0	N.A	0	
	3	N.A	1.5	**1.094	**1.094	**0.547	**0.547	
	4	N.A	2.056	N.A	*2.8	N.A	*1.4	
C L/H=3	1	*1.9167	*1.9167	N.A	1.4167	N.A	0.70835	1.685
	2	*1.9167	*1.9167	N.A	0	N.A	0	
	3	N.A	1.375	*0.806	*0.806	*0.403	*0.403	
	4	N.A	1.1875	N.A	1.6	N.A	0.8	
D L/H=2	1	*0.9(1.5)	1.5(2.5)	N.A	*1.6875	N.A	*0.844(1.4)	1.006
	2	*0.9(1.5)	*0.9	N.A	0	N.A	0	
	3	N.A	0.9	**0.655	**0.655	*0.33(0.547)	0.32725	
	4	N.A	1.25	N.A	*1.6875	N.A	*0.844(1.4)	
E L/H=0.5	1	*0.73(1.3)	1.09(2)	N.A	*1.6	N.A	*0.8(1.46)	0.924
	2	*0.73(1.3)	*0.731	N.A	0	N.A	0	
	3	N.A	0.93	0.6	0.67	0.3(0.5472)	0.335	
	4	N.A	0.78	N.A	*1.6	N.A	*0.8(1.459)	
F L/H=0.5	1	*0.9(1.25)	1.615(2.3)	N.A	*2.43	N.A	*1.22(1.73)	1.185
	2	*0.9(1.25)	*0.857	N.A	0	N.A	0	
	3	N.A	1.13	0.0769	0.66	0.038(0.055)	0.33	
	4	N.A	1.167	N.A	*2.43	N.A	*1.215(1.7)	
G L/H=0.6	1	*0.73(1.3)	1.1(2.01)	N.A	*1.6	N.A	0.8	0.924
	2	*0.73(1.3)	*0.73	N.A	0	N.A	0	
	3	N.A	0.93	0.6	0.17	0.3(0.547)	0.085(0.16)	
	4	N.A	0.78	N.A	*1.6	N.A	0.0008	

Note: Models A-C have span lengths equal to 19800mm, Model D a span length equal to 9900mm, Models E and G a span length equal to 9000mm and Model F a span length equal to 12000mm.

Table 7.2 Extracted strains at positions of **SBP** and **MAXP**.

Model A	ε_{bmax} (10^{-3})	γ (10^{-3})	ε_d (10^{-3})
	AMAX	AMAX	AMAX
A (L/H =1)	0.00388	0.00521	0.00261
B (L/H=2)	0.00333	0.00295	0.00148
C (L/H=3)	0.00187	0.00164	0.00082
D (L/H=2)	0.00198 (0.0033)	0.00176 (0.00295)	0.00088 (0.00148)
E (L/H=0.5)	0.0014 (0.0025536)	0.0016 (0.0029184)	0.0008 (0.0014592)
F (L/H=0.5)	0.00209 (0.002972)	0.00242 (0.003441)	0.00121 (0.001721)
G (L/H=0.6)	0.0014 (0.0025536)	0.0016 (0.0029184)	0.0008 (0.0014592)

Note: Models A-C have span lengths equal to 19800mm, Model D a span length equal to 9900mm, Models E and G a span length equal to 9000mm and Model F a span length equal to 12000mm.

Table 7.3 Extracted strains at positions **AMAX**.

The strains presented in brackets correspond to those, which would develop at the maximum **Δ/L** ratio for the given model. These strains are linearly interpolated from those sampled in relation to the change in the mid-span deflection **Δ**. The change in the mid-span deflection is calculated in accordance with the maximum **Δ/L** ratio. Linear interpolation of the strain results is possible due to the fact that the results are obtained from linear elastic analyses.

The strain results in brackets corresponding to Model D match the sampled strain results corresponding to Model B. Both Model B and D have **L/H** ratios equal to 2. The difference between Model B and D is their different span lengths **L**. This leads to the conclusion that there is a single linear relationship between $\Delta/L:\varepsilon_{bmax}$ and $\Delta/L:\varepsilon_d$ corresponding to deep beams of **L/H** ratio equal to 2, irrespective of the magnitude of its span length **L**.

The strains in brackets corresponding to Models E and F do not have the same magnitudes. This therefore leads to the conclusion that there is no single linear relationship between $\Delta/L:\varepsilon_{bmax}$ and $\Delta/L:\varepsilon_d$ corresponding to deep beams of **L/H** ratio equal to 0.5 representing all magnitudes of the span length **L**.

Model G (**L/H** = 0.6) does not exhibit equal magnitudes of ε_{bmax} and ε_d. Therefore the **L/H** ratio at which the governing strain changes from ε_{bmax} to ε_d in deep beams is not equal to 0.6 as was the case for the simply supported elastic beams.

7.6 Discussion of results

From a first glance of the results the most notable discovery is that in the difference of the relationships between $\Delta/L:\varepsilon_{bmax}$ and $\Delta/L:\varepsilon_d$ for deep beams of **L/H** ratios equal to 2 and 0.5. The relationships corresponding to the deep beam with an **L/H** ratio equal to 2 conforms to the relationships depicted in the simply supported elastic beams, whereas the relationships corresponding to the deep beam with an **L/H** ratio equal to 0.5 do not. This result is due to the fact that the structural behaviour of the deep beam

with an **L/H** ratio equal to 2 simulates that of the simply supported elastic beam's structural behaviour closer than the deep beam with an **L/H** ratio equal to 0.5.

Figure 7.9 represents Model B's horizontal ε_{xx}, vertical ε_{yy} and shear γ strains along line (2) on its body.

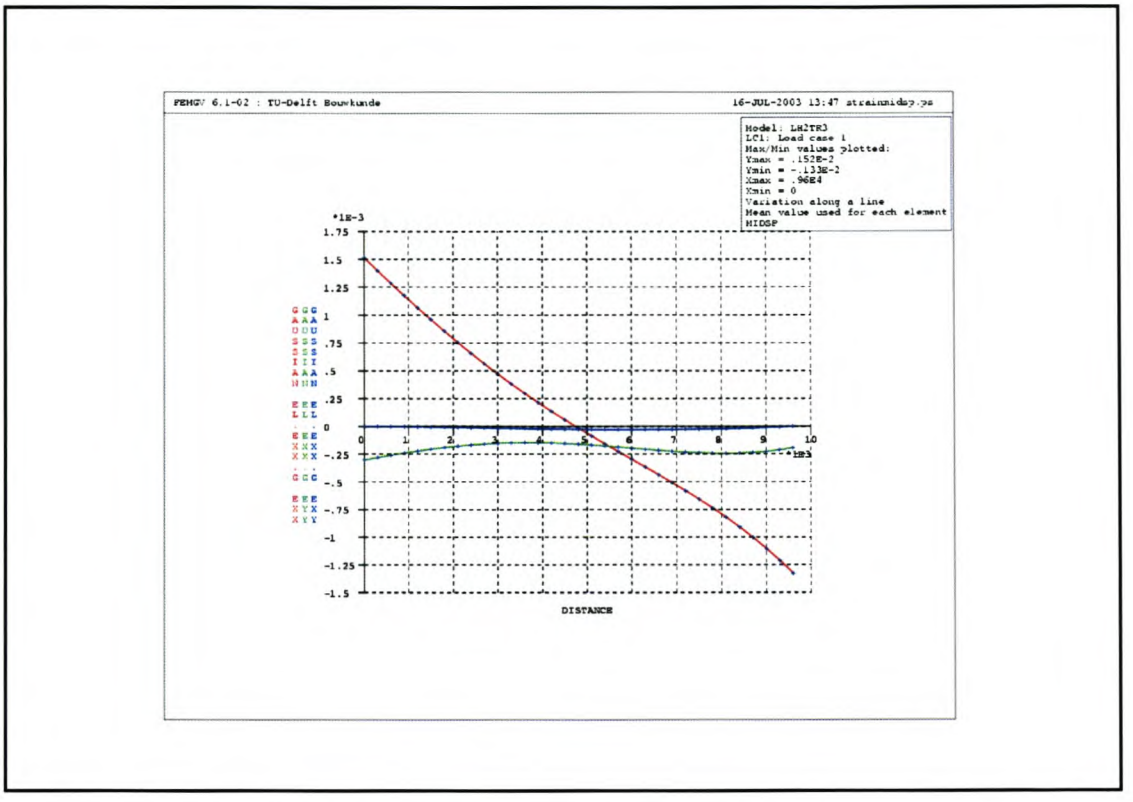

Figure 7.9 Model B horizontal ε_{xx}, vertical ε_{yy} and shear γ strains represented along line (2) on its body. (**L/H** = 2, **L** = 19800mm).

Model B has an **L/H** ratio equal to 2. It is seen that the ε_{xx} distribution (colour coded red) is approximately linear, which is consistent with that of the ε_{xx} distribution in simply supported elastic beams.

Figure 7.10 presents Model E's horizontal ε_{xx}, vertical ε_{yy} and shear γ strains along line (2) on its body.

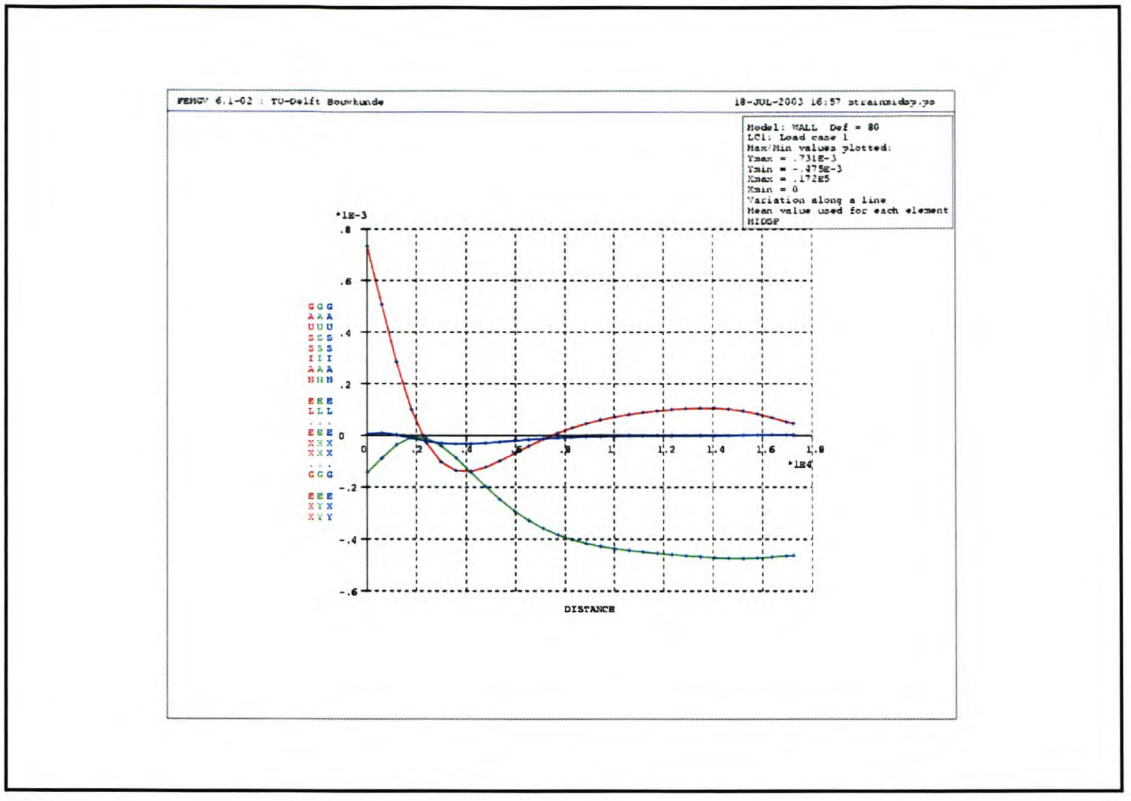

Figure 7.10 Model E horizontal ε_{xx}, vertical ε_{yy} and shear γ strains represented along line (2) on its body. (**L/H** = 0.5, **L** = 9900mm).

Model E has an **L/H** ratio equal to 0.5. It is seen that the ε_{xx} distribution (colour coded red) is not linear, which is inconsistent with that of a simply supported elastic beam.

A further deep beam is modelled with an **L/H** ratio equal to 0.5 and span length **L** equal to 19800mm in order to investigate the effect of the span length **L** on the relationships between $\Delta/L:\varepsilon_{bmax}$ and $\Delta/L:\varepsilon_{d}$.

Due to the fact that the structural behaviour of the deep beam with an **L/H** ratio equal to 2 closely simulates the structural behaviour of the simply supported elastic beam under similar conditions, it is safely assumed that the deep beam with an **L/H** ratio equal to 3 will exhibit a similar structural behaviour. This, however, cannot be assumed for a deep beam with an **L/H** ratio equal to 1. It is therefore necessary to investigate Model A's (**L/H** = 1) ε_{xx} distribution along line (2) on its body.

Figure 7.11 presents Model A's horizontal ε_{xx}, vertical ε_{yy} and shear γ strains along line (2) on its body.

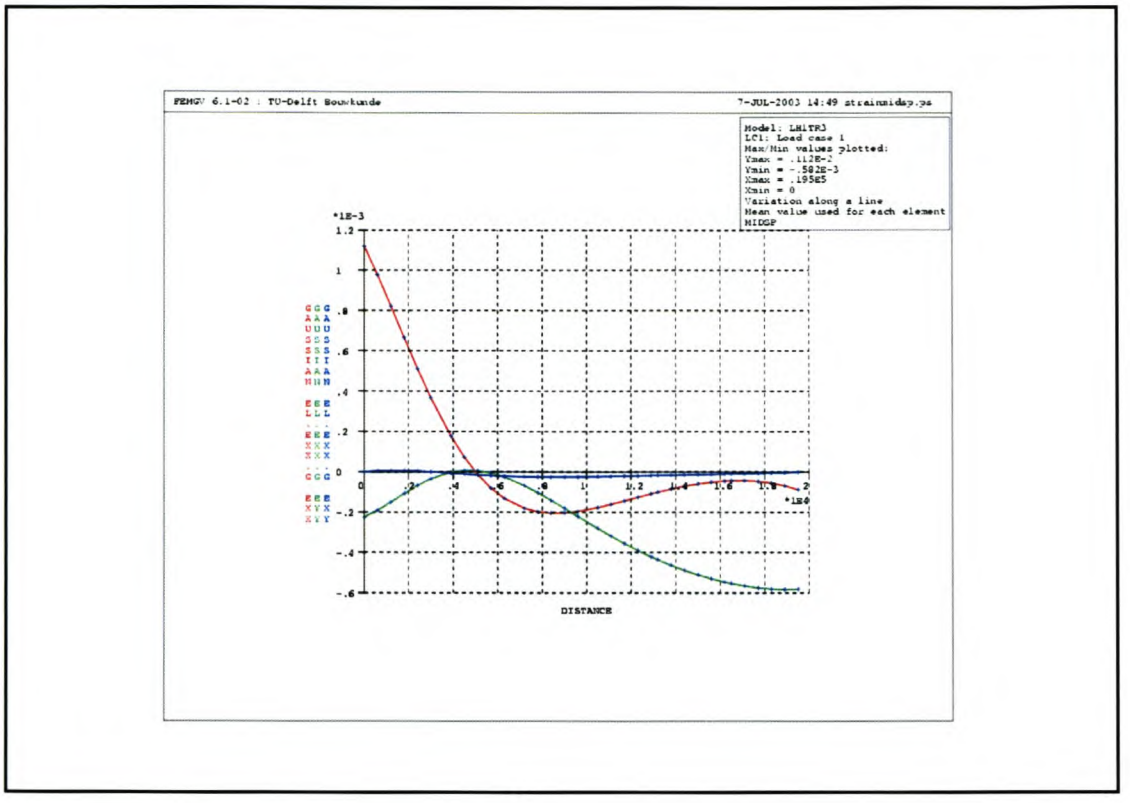

Figure 7.11 Horizontal ε_{xx}, vertical ε_{yy} and shear γ strains plotted on line (2) for Model A. (**L/H** = 1, **L** = 19800mm).

Model A has an **L/H** ratio equal to 1. It is seen that the ε_{xx} distribution (colour coded red) is also not linear, which again is not consistent with that of a simply supported elastic beam's ε_{xx} distribution. This is the same phenomenon seen in deep beams of **L/H** ratio equal to 0.5, which does not exhibit a single linear relationship between $\Delta/L:\varepsilon_{bmax}$ and $\Delta/L:\varepsilon_{d}$ for all magnitudes of **L**.

Further deep beams are modelled with **L/H** ratios equal to 1 and varying span lengths **L** in order to investigate the effect of the span length **L** on the relationships between $\Delta/L:\varepsilon_{bmax}$ and $\Delta/L:\varepsilon_{d}$. Two extra beams are modelled, one with a span length **L** equal to 12000mm and the other with a span length **L** equal to 9900mm.

The relationships between $\Delta/L:\varepsilon_{bmax}$ and $\Delta/L:\varepsilon_d$ corresponding to different **L/H** ratios are presented in section 7.7. These relationships will be superimposed onto the same relationships calculated for the simply supported elastic beams of corresponding **L/H** ratio.

7.7 Δ/L versus ε_{bmax} and ε_d

7.7.1 L/H = 1

From the results of the linear elastic models of **L/H** ratio 1, it is concluded that there is no single linear relationship between both $\Delta/L:\varepsilon_{bmax}$ and $\Delta/L:\varepsilon_d$ for solid masonry walls of **L/H** ratio equal to 1, that is representative of all span lengths **L**. Linear relationships representing various span lengths **L**, can however be presented.

Figure 7.12 presents the relationship between $\Delta/L:\varepsilon_{bmax}$ sampled at positions **SBP**, **MAXP** and **AMAX**, for deep beams of **L/H** ratio equal to 1.

Conclusions pertaining to Figure 7.12 are:

a) Strains ε_{bmax} sampled at position **SBP** are overestimated by the **LTS** for a given Δ/L ratio at all the respective span lengths **L**.

b) Strains ε_{bmax} sampled at position **MAXP** are underestimated by the **LTS** for a given Δ/L ratio at a span length **L** equal to 19800mm. Strains ε_{bmax} sampled at position **MAXP** are slightly overestimated by the **LTS** for a given Δ/L ratio at span lengths **L** smaller than 12000mm.

c) Strains ε_{bmax} sampled at position **AMAX** are underestimated by the **LTS** for a given Δ/L ratio at all the respective span lengths **L**. It is brought to the reader's attention that these can be local peak stresses.

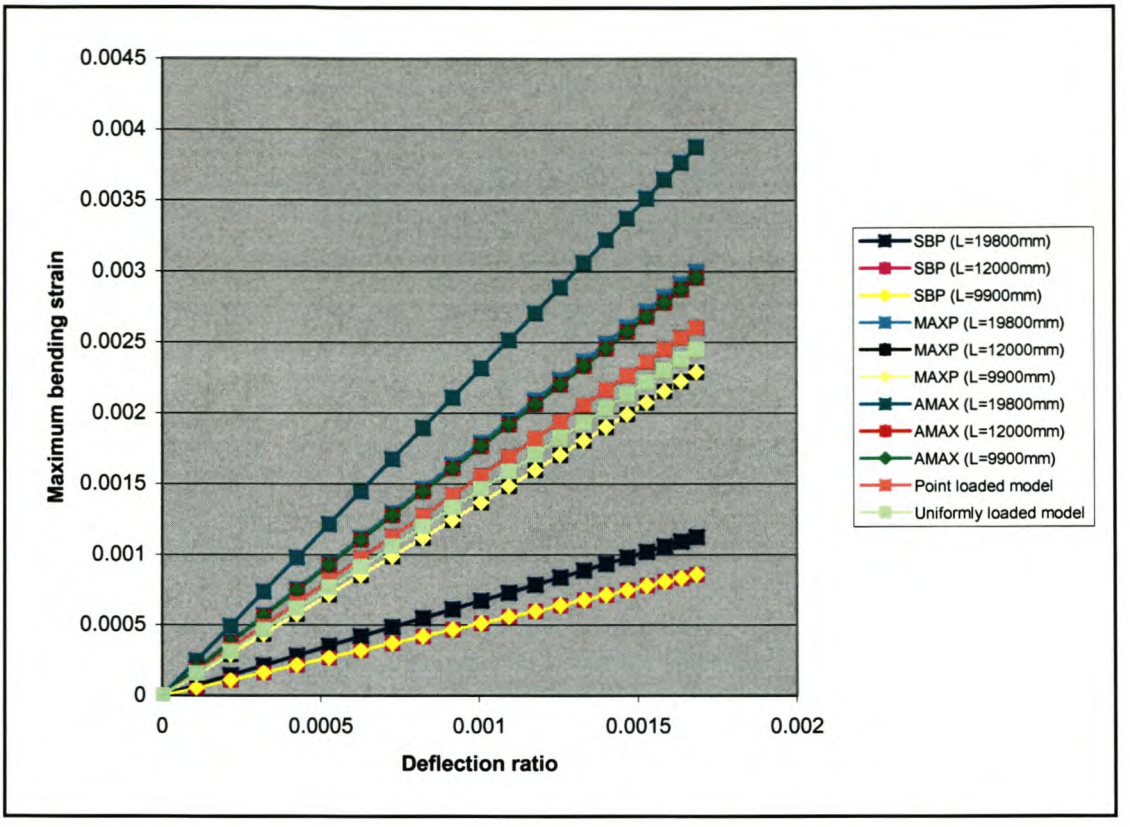

Figure 7.12 Relationship between $\Delta/L:\varepsilon_{bmax}$ for different span lengths **L**. (**L/H** = 1).

Figure 7.13 presents the relationship between $\Delta/L:\varepsilon_d$ sampled at positions **SBP**, **MAXP** and **AMAX**, for deep beams of **L/H** ratio equal to 1.

Conclusions pertaining to Figure 7.13 are:

a) Strains ε_d sampled at position **SBP** are overestimated by the **LTS** for a given **Δ/L** ratio at all the respective span lengths **L**.

b) Strains ε_d sampled at positions **MAXP** and **AMAX** are underestimated by the **LTS** for a given **Δ/L** ratio at all the respective span lengths **L**.

c) Strains ε_d sampled at position **AMAX** are slightly smaller than those sampled at **MAXP** for a given **Δ/L** ratio. This is due to the fact that the average value **MAXP** of all the strains at each respective integration point of a certain

element is larger than the peak strain **AMAX** at a single integration point of a certain element.

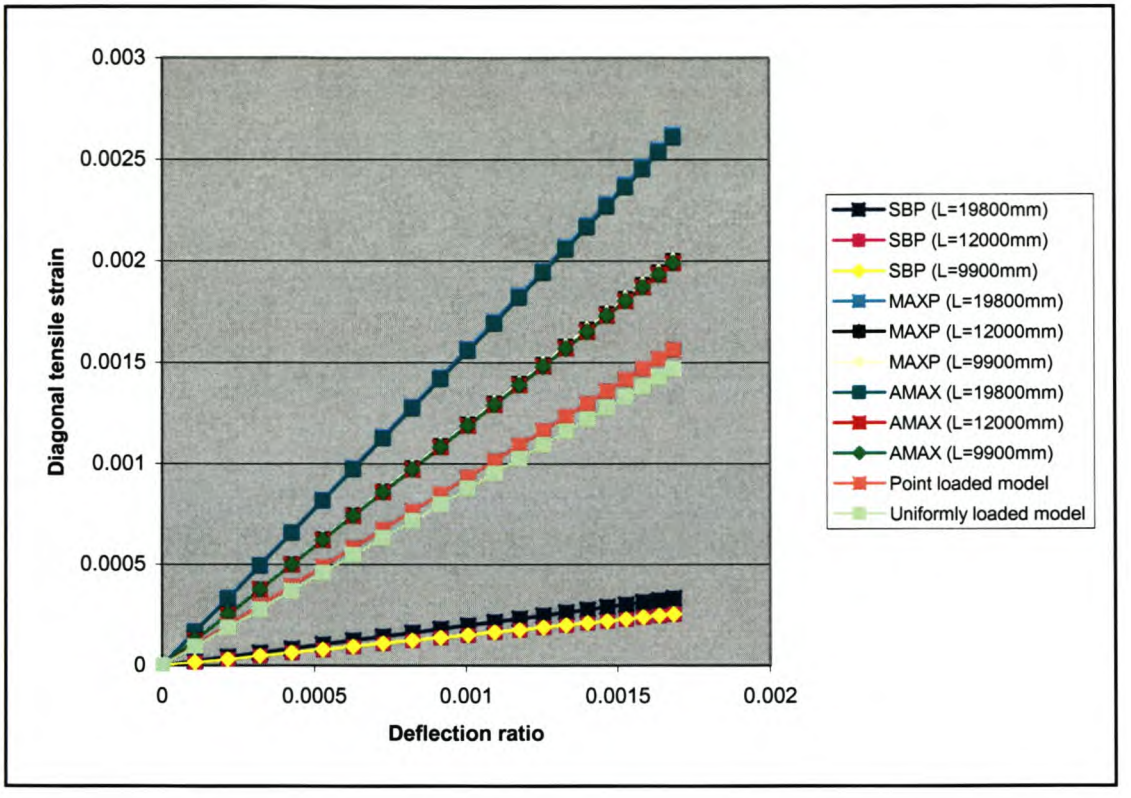

Figure 7.13 relationship between $\Delta/L:\varepsilon_d$ for different span lengths **L**. (**L/H** = 1).

From Figures 7.12 to 7.13, it is concluded that ε_{bmax} is the limiting tensile strain ε_{lim} affecting a deep beam with an **L/H** ratio equal to 1, irrespective of the deep beams span length **L**. Figures 7.14 to 7.16 present the results of Figures 7.12 and 7.13 in a format to assist engineers in categorising solid masonry walls of **L/H** ratio equal to 1 into the different damage categories. It is clear that up to now the dependent variables concerning this categorisation for solid masonry walls are the **L/H** ratio, the **Δ/L** ratio and the material properties of the wall.

Figures 7.14 to 7.16 assist the engineer in categorising solid masonry walls, symmetrically positioned over the sagging zone of a green field settlement trough, into their respective damage categories as defined in Tables 3.1 and 3.2. Firstly the span length **L** of the solid masonry wall is determined. Once the span length **L** has been determined, it is substituted into equation (5.11) together with the properties of

the settlement trough in order to calculate its mid-span deflection Δ. This Δ is divided by the span length **L** to calculate the magnitude of the **Δ/L** ratio. Each curve in Figures 7.14 to 7.16 represents a certain **Δ/L** ratio. The engineer therefore starts on the horizontal axis at the position defined by the specific span length **L** and moves vertically upwards to the position defined by the magnitude of the calculated **Δ/L** ratio. The engineer can interpolate between the respective **Δ/L** ratio curves to represent intermediate magnitudes of the **Δ/L** ratio. At the position of the applicable **Δ/L** ratio, the engineer then moves horizontally to the left to read off the respective limiting tensile strains ε_{lim}. These ε_{lim} strains are then used to categorise the solid masonry wall into its specific damage category. Due to the fact that ε_{bmax} was determined to be ε_{lim} for a solid masonry wall of **L/H** ratio equal to 1, Figures 7.14 to 7.16 are constructed with the results pertaining to ε_{bmax}.

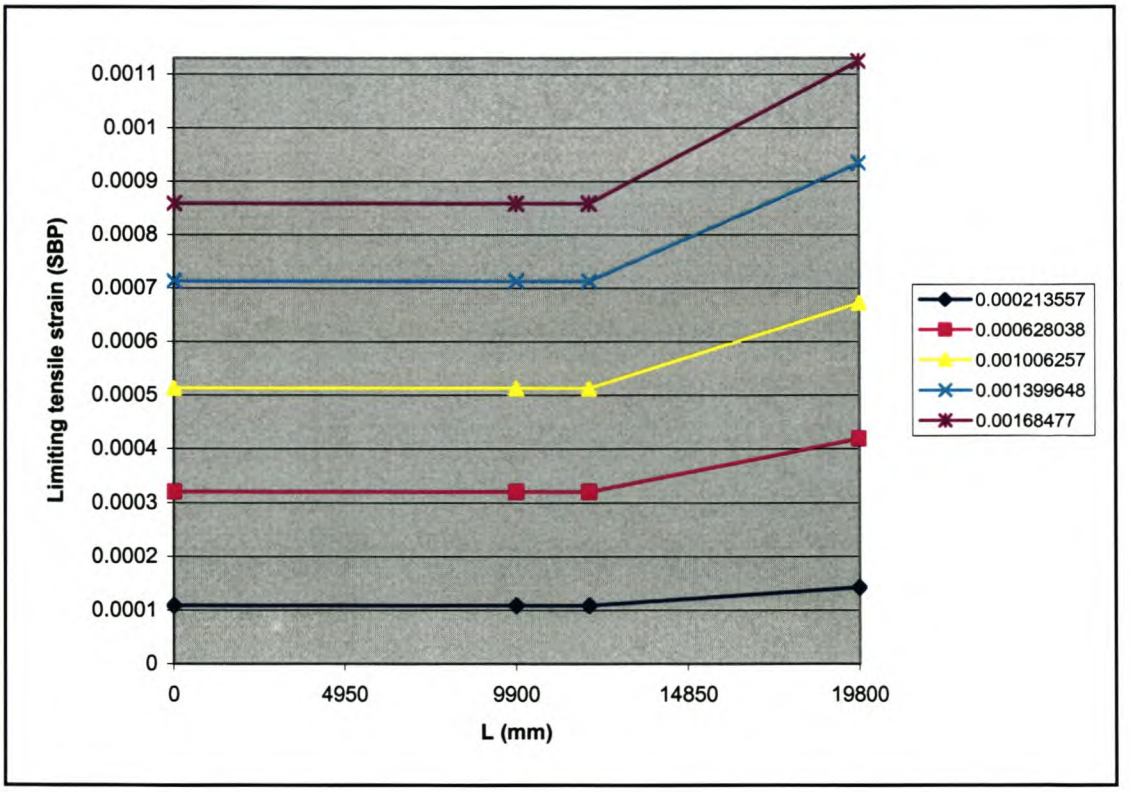

Figure 7.14 Strain ε_{lim} **(SBP)** versus **L** for various **Δ/L** ratios. (**L/H** = 1).

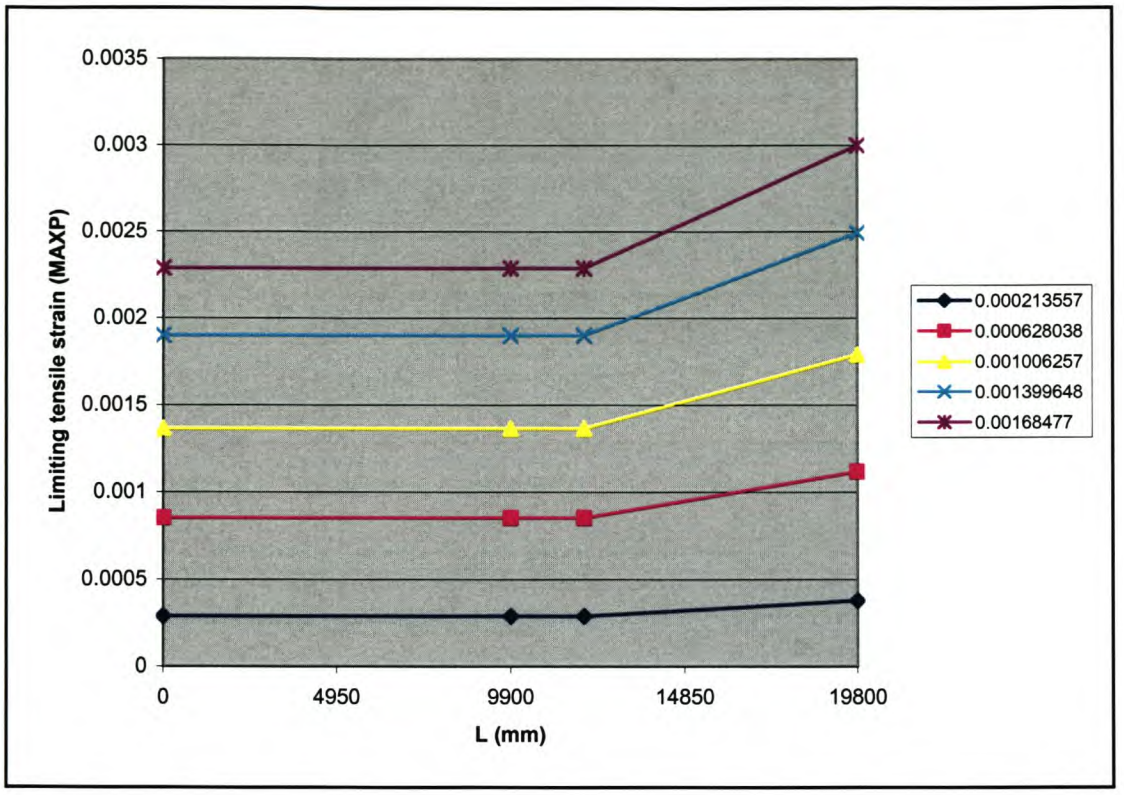

Figure 7.15 Strain ε_{lim} **(MAXP)** versus **L** for various **Δ/L** ratios. (**L/H** = 1).

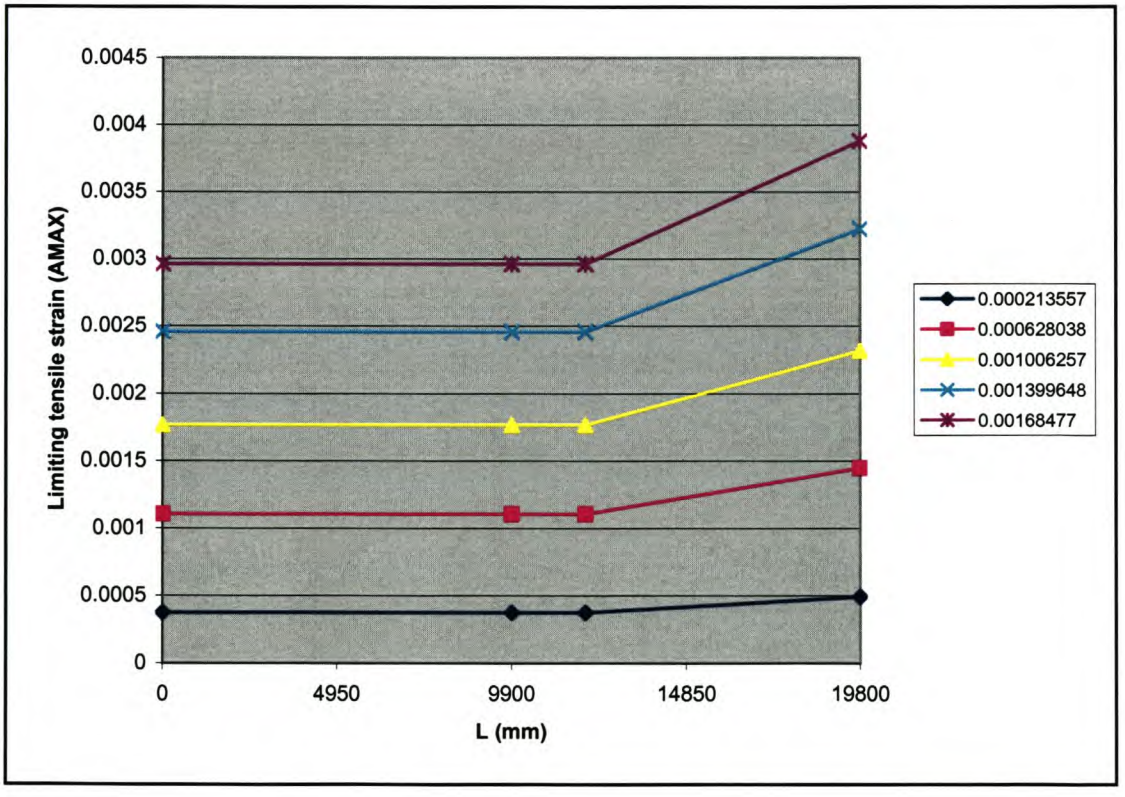

Figure 7.16 Strain ε_{lim} **(AMAX)** versus **L** for various **Δ/L** ratios. (**L/H** = 1).

7.7.2 L/H = 2

Here a single linear relationship between both $\Delta/L:\varepsilon_{bmax}$ and $\Delta/L:\varepsilon_{bmax}$ is presented, representative of all the respective span lengths **L**. Figure 7.17 presents the relationship between $\Delta/L:\varepsilon_{lim}$ for a solid masonry wall of **L/H** equal to 2.

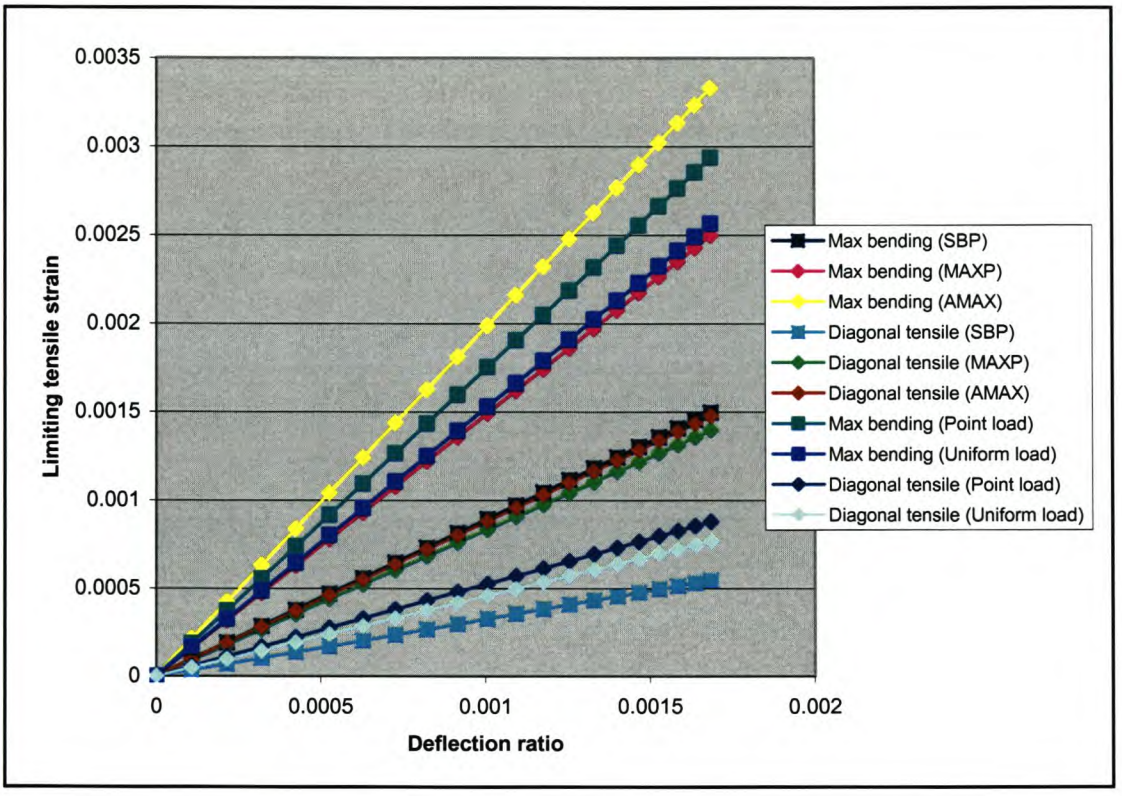

Figure 7.17 Relationship between $\Delta/L:\varepsilon_{lim}$. (**L/H** = 2).

Conclusions pertaining to Figure 7.17 are:

a) Strains ε_{bmax} sampled at position **SBP** are overestimated by the **LTS** for a given Δ/L ratio, whereas ε_d are overestimated to a lesser extent for a given Δ/L ratio.

b) Strains ε_{bmax} sampled at position **MAXP** are slightly overestimated by the **LTS** for a given Δ/L ratio, whereas ε_d are more significantly underestimated for a given Δ/L ratio.

c) Strains ε_{bmax} and ε_d sampled at position **AMAX** are both underestimated by the **LTS** for a given **Δ/L** ratio. The strains ε_{bmax} are underestimated to a lesser extent.

d) The critical strains are ε_{bmax} and are therefore taken to be the limiting tensile strains ε_{lim}.

7.7.3 L/H = 3

Here again a single linear relationship between both **Δ/L**:ε_{bmax} and **Δ/L**:ε_d is presented, that is representative for all the respective span lengths **L**. Figure 7.18 presents the relationship between **Δ/L**:ε_{lim} for solid masonry walls of **L/H** ratio equal to 3.

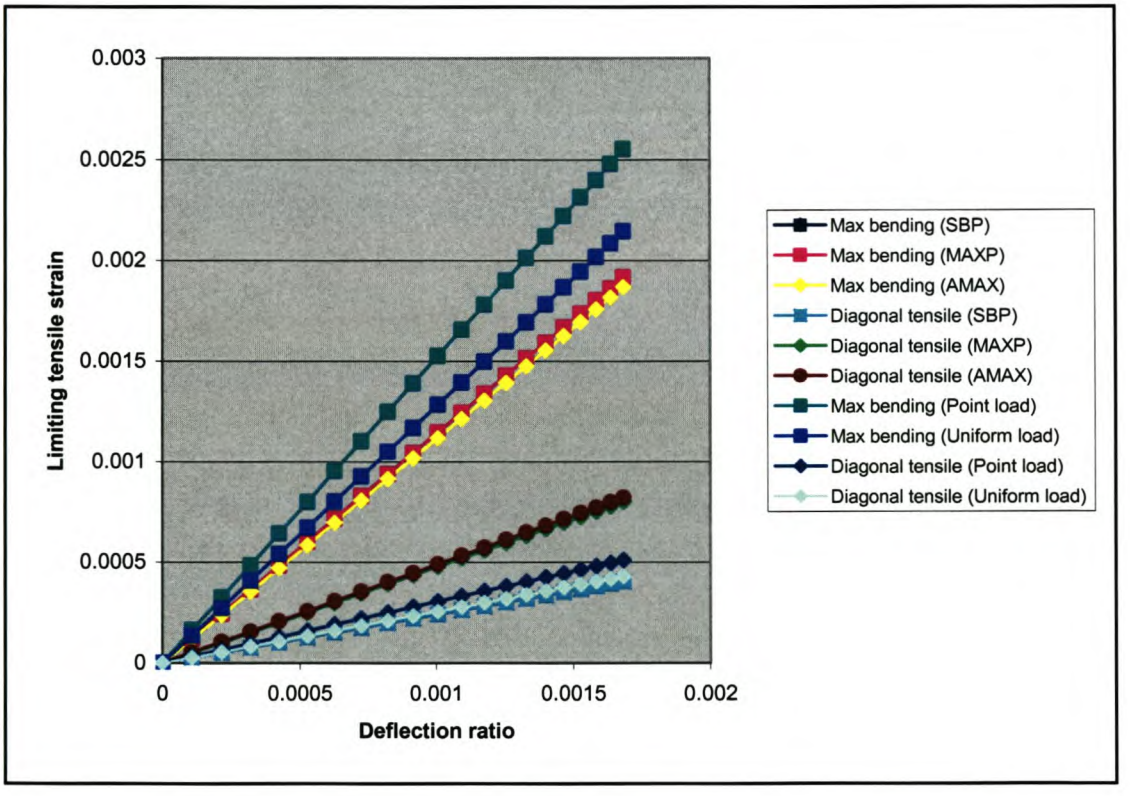

Figure 7.18 The **Δ/L** ratio versus ε_{lim}. (**L/H** = 3).

Conclusions pertaining to Figure 7.18 are:

a) The strains ε_{bmax} sampled at positions **SBP** and **MAXP** are identical to one another, which is evidence that as the **L/H** ratio of a deep beam increases its structural behaviour resembles that of a simply supported elastic beam more closely.

b) The strains ε_{bmax} sampled at position **AMAX** are slightly smaller than those sampled at **SBP** and **MAXP** for a given **Δ/L** ratio. This is due to the fact that the average value of **SBP** or **MAXP** of the respective strains at each respective integration point of a certain element is larger than the peak strain **AMAX** at a single integration point of a certain element.

c) The strains ε_d sampled at positions **MAXP** and **AMAX** are identical to one another.

d) The strains ε_{bmax} sampled at positions **SBP**, **MAXP** and **AMAX** are overestimated by the **LTS** for a given **Δ/L** ratio.

e) The strains ε_d sampled at positions **MAXP** and **AMAX** are underestimated by the **LTS** for a given **Δ/L** ratio.

f) The strains ε_d sampled at position **SBP** conform exactly to those calculated by the **LTS** for a given **Δ/L** ratio.

g) The critical strains are ε_{bmax} and are therefore taken to be the limiting tensile strains ε_{lim}.

7.7.4 L/H = 0.5

As stated earlier, it is concluded that there is no single linear relationship between both **Δ/L**:ε_{bmax} and **Δ/L**:ε_d for solid masonry walls of **L/H** ratio equal to 0.5 that is representative of all possible span lengths **L**. Linear relationships can however be presented for various span lengths **L**.

Figure 7.19 presents the relationship between $\Delta/L:\varepsilon_{bmax}$ sampled at positions **SBP**, **MAXP** and **AMAX**, for deep beams of **L/H** ratio equal to 0.5 and of different span lengths **L**.

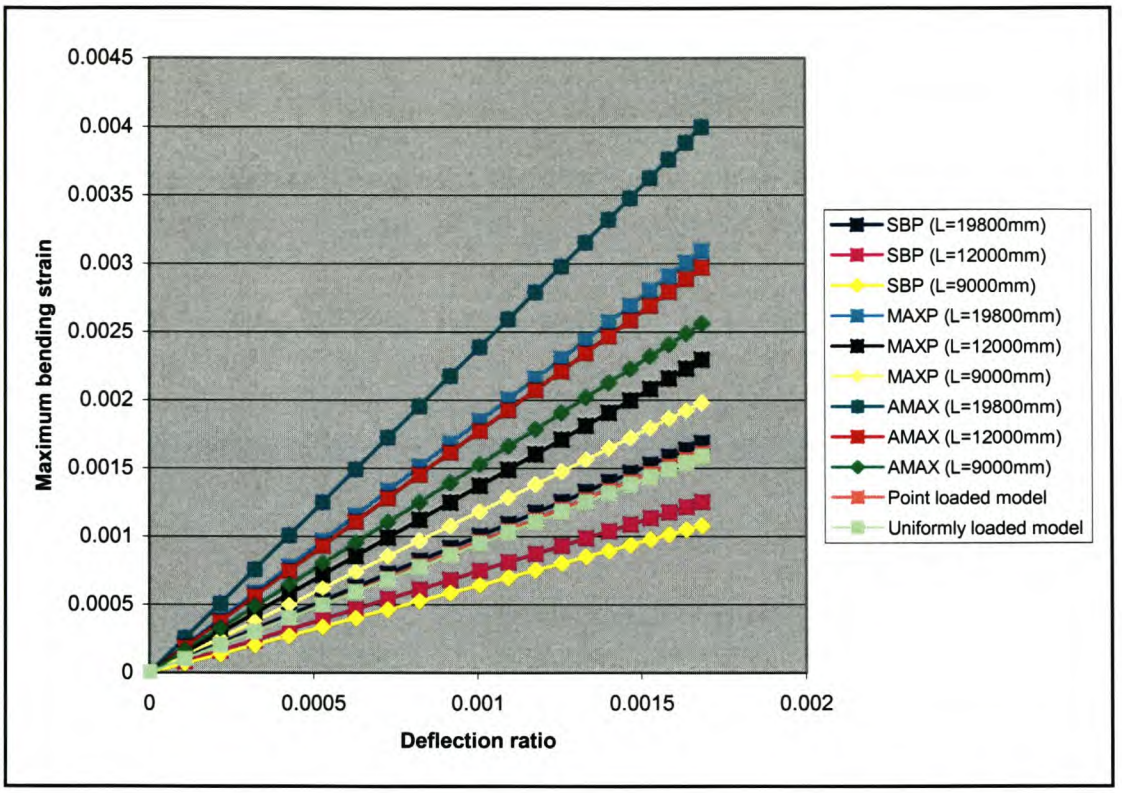

Figure 7.19 Relationship between $\Delta/L:\varepsilon_{bmax}$ for different span lengths **L**. (**L/H** = 0.5).

Conclusions pertaining to Figure 7.19 are:

a) The strains ε_{bmax} sampled at position **SBP** are overestimated by the **LTS** for a given Δ/L ratio and at span lengths **L** smaller than 19800mm. Strains ε_{bmax} sampled at position **SBP** conform closely to those as calculated by the **LTS** for a given Δ/L ratio and a span length **L** equal to 19800mm.

b) The strains ε_{bmax} sampled at position **MAXP** are underestimated by the **LTS** for a given Δ/L ratio and at all the respective span lengths **L**.

c) The strains ε_{bmax} sampled at position **AMAX** are underestimated by the **LTS** for a given Δ/L ratio and at all the respective span lengths **L**.

Figure 7.20 presents the relationship between $\Delta/L:\varepsilon_d$ sampled at positions **SBP**, **MAXP** and **AMAX**, for deep beams of **L/H** ratio equal to 0.5 and of different span lengths **L**.

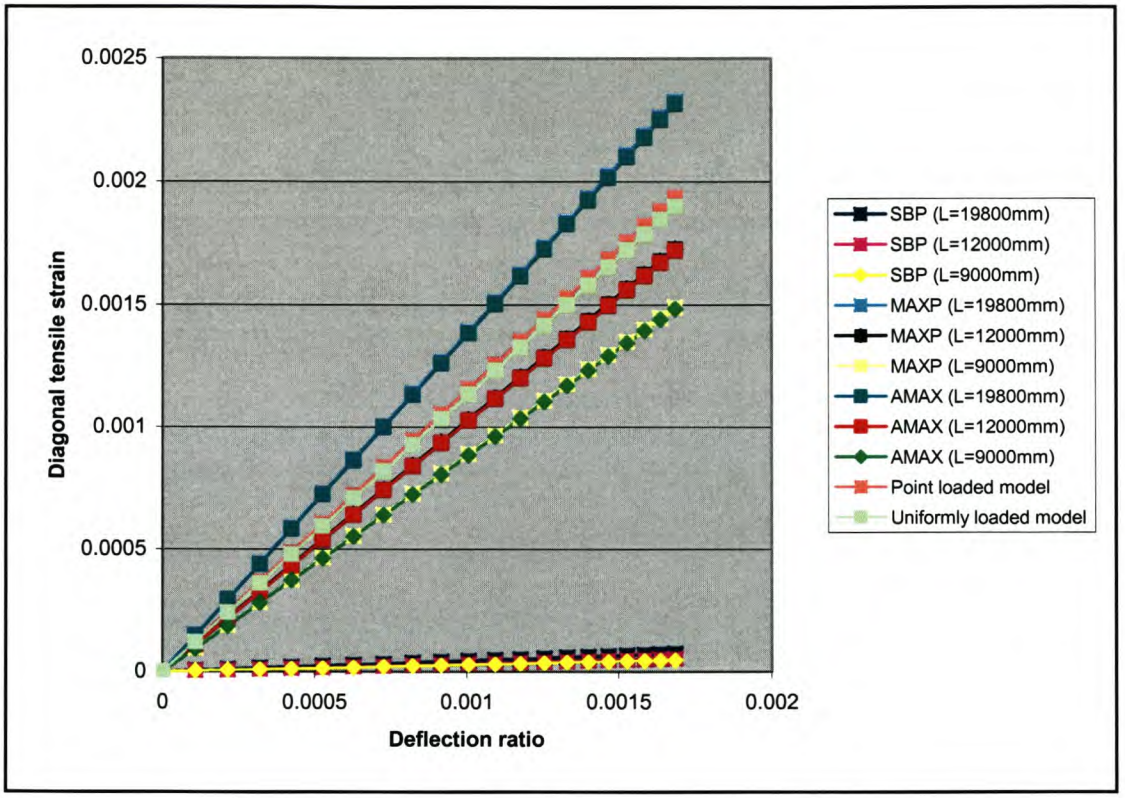

Figure 7.20 Relationship between $\Delta/L:\varepsilon_d$ for different span lengths **L**. (**L/H** = 0.5).

Conclusions pertaining to Figure 7.20 are:

a) The strains ε_d sampled at positions **MAXP** and **AMAX** are identical to one another for a given Δ/L ratio and at all the respective span lengths **L**.

b) The strains ε_d sampled at position **SBP** are overestimated by the **LTS** for a given Δ/L ratio and at all the respective span lengths **L**.

c) The strains ε_d sampled at positions **MAXP** and **AMAX** are overestimated by the **LTS** for a given Δ/L ratio and at span lengths **L** smaller than 12000mm. Strains ε_d sampled at positions **MAXP** and **AMAX** are underestimated by the **LTS** for a given Δ/L ratio and a span length **L** equal to 19800mm.

From Figures 7.19 to 7.20, it is deduced that ε_{bmax} is the critical strain and is therefore taken to be ε_{lim} for solid masonry walls of **L/H** ratio equal to 0.5, irrespective of the span length **L**. Figures 7.21 to 7.23 present the relationship between $\Delta/L:\varepsilon_{lim}$ for an **L/H** ratio of 0.5.

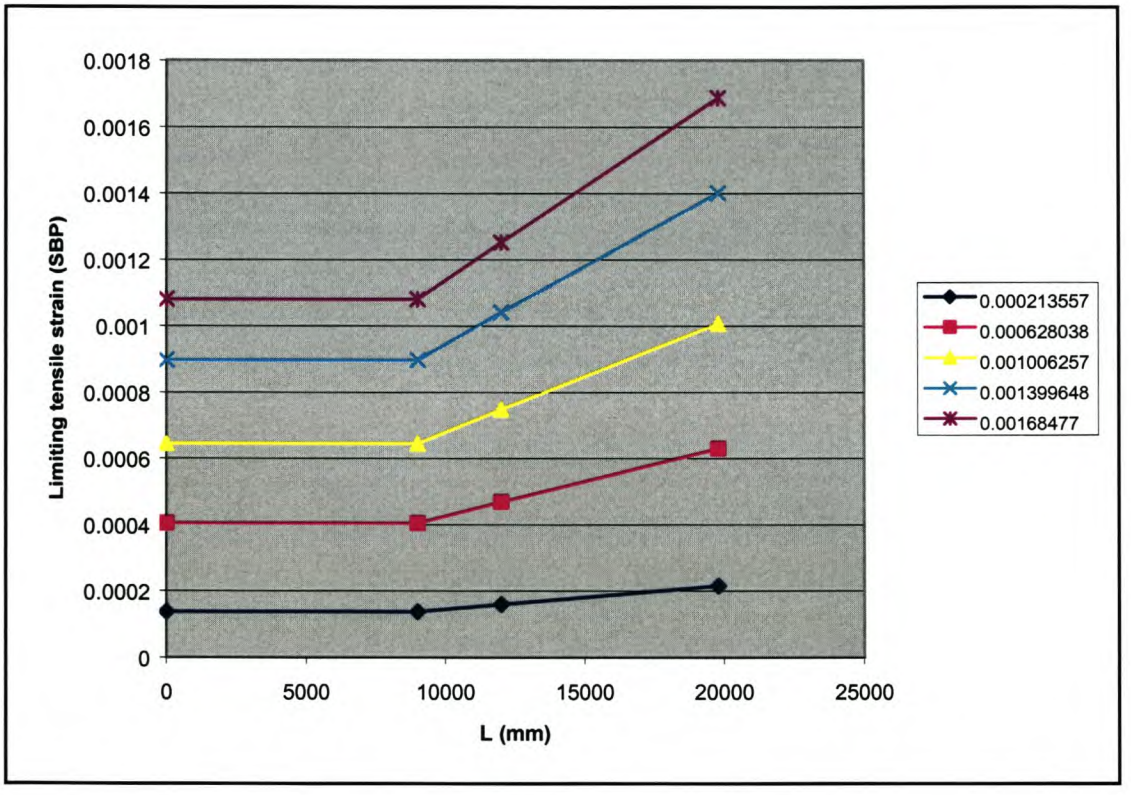

Figure 7.21 The strain ε_{lim} **(SBP)** versus **L** for various **Δ/L** ratios. **L/H** = 0.5.

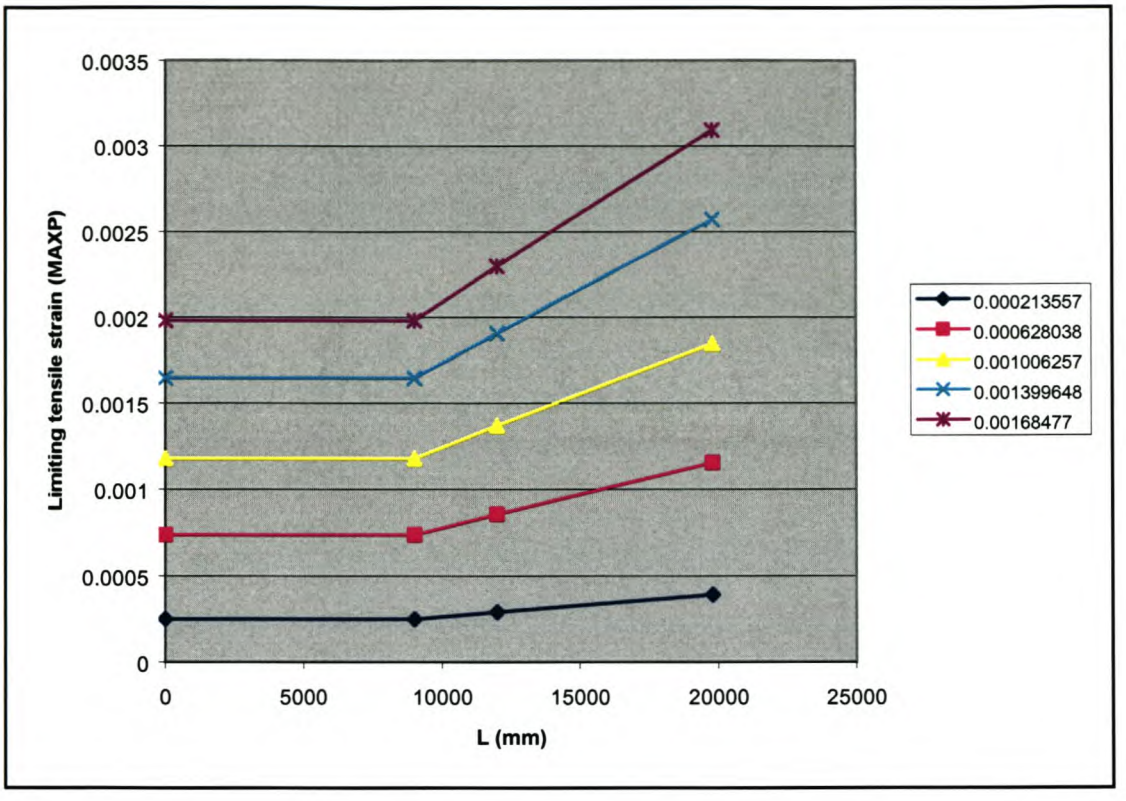

Figure 7.22 The strain ε_{lim} **(MAXP)** versus **L** for various **Δ/L** ratios. **L/H** = 0.5.

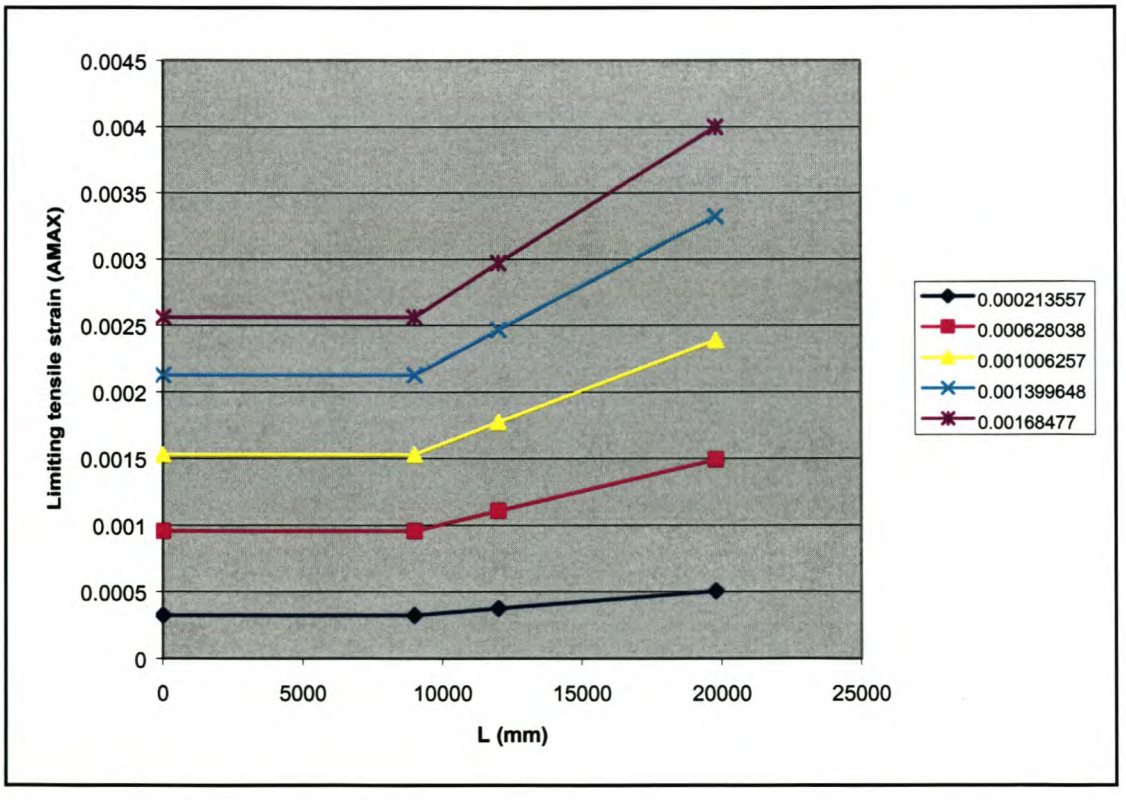

Figure 7.23 The strain ε_{lim} **(AMAX)** versus **L** for various **Δ/L** ratios. **L/H** = 0.5.

7.8 Summary

The results obtained from the linear elastic analyses lead to the conclusion that ε_{bmax} is the critical ε_{lim} in solid masonry walls, irrespective of the wall **L/H** ratio. Table 7.4 tabulates how conservative the **LTS** is with respect to the **P** and **q** models' accuracy in predicting the development of ε_{lim} in solid masonry walls subject to certain **Δ/L**.

L/H	L	SBP	MAXP	AMAX
0.5	> 12000	A	U	U
	< 12000	C	U	U
1.0	> 12000	C	U	U
	< 12000	C	C	U
2.0	All	C	C	U
3.0	All	C	C	C

Table 7.4 Ability of the **LTS** in predicting ε_{lim} in solid masonry walls of different **L/H** ratio.

The abbreviations U, C and A in Table 7.4 denote the following:

U = **LTS** is not conservative with respect to predicting ε_{lim} in solid masonry walls' subject to certain **Δ/L** ratios.

C = **LTS** is conservative with respect to predicting ε_{lim} in solid masonry walls' subject to certain **Δ/L** ratios.

A = **LTS** is accurate with respect to predicting ε_{lim} in solid masonry walls' subject to certain **Δ/L** ratios.

When the variables U and C are colour red, it signifies that the **LTS** very close to predicting the correct magnitudes of ε_{lim}, even though they are not exact.

From Table 7.4 it is clear to see that the **LTS** is unable to accurately predict the magnitude of ε_{lim} in solid masonry walls subject to certain **Δ/L** ratios over the entire spectrum of **L/H** ratios. The **LTS** is only able to conservatively predict the development of ε_{lim} in solid masonry walls of **L/H** ratio 2 and larger, irrespective of the span length **L**. In solid masonry walls of **L/H** ratio equal to 1 and of span lengths

of 12000mm and larger, the **LTS** is able to conservatively predict the development of ε_{lim}. As the magnitude of the **L/H** ratio decreases, the ability of the **LTS** to accurately predict the development of ε_{lim} in solid masonry walls also does.

The reader is reminded, however, that in the **LTS** the mid-span deflections Δ of the simply supported elastic beams are assumed to conform exactly to the sagging zone's maximum relative deflection Δ_{mr}. In reality, however, the wall **Δ/L** ratio is not entirely dependent on the shape of the settlement trough on which it is founded. The solid masonry wall's inherent bending stiffness as well as the wall to soil interaction are expected to play a major role in the final magnitude of the wall **Δ/L** ratio. These factors work towards decreasing the magnitude of the wall **Δ/L** ratio as opposed to the **Δ/L** ratio calculated by the **LTS**. This decreased magnitude of the wall **Δ/L** ratio inevitably decreases the magnitude of ε_{lim} as defined by the respective **Δ/L:ε_{lim}** relationships.

It is therefore necessary to study the relationship between the **Δ/L** ratio, predicted by the settlement trough, and the real **Δ/L** ratio experienced by the solid masonry wall. The next chapter is dedicated into the investigation of this topic.

To conclude, it has also been determined that the structural behaviour of simply supported solid masonry walls of **L/H** ratio 2 and larger, closely represent the structural behaviour of simply supported elastic beams. Solid masonry walls of **L/H** ratio smaller than 2 do not represent the structural behaviour of simply supported elastic beams at all. This is why it is possible to present a single linear relationship between both **Δ/L:ε_{bmax}** and **Δ/L:ε_d** for solid masonry walls of **L/H** ratio 2 and larger, irrespective of the span length **L**. On the other hand, for solid masonry walls of **L/H** ratio smaller than 2, the above relationships are dependent on the wall span length **L**.

Chapter 8

Influence of the soil properties on the deflection ratio

8.1 Introduction

This chapter investigates the effect of the soil properties on the wall **Δ/L** ratio. Two different **Δ/L** ratios are distinguished. The first pertains to the **Δ/L** ratio of the settlement trough **(Δ/L_{st})**, which is calculated with the displacements of the soil, equation (5.11). In reality, however, this **Δ/L** ratio will never realise in the wall, as the wall will bed into the soil, resulting in changing the settlement trough's profile. This bedding-in of the wall is a result of the wall's inherent bending stiffness, the soil stiffness and the soil to wall interaction. The resulting actual **Δ/L** ratio of the wall **(Δ/L_w)**, after the above considerations have been taken into account, is expected to be of a lesser magnitude than that of the Δ/L_{st} ratio. This decrease in **Δ/L** will decrease the expected magnitude of ε_{lim}, which in turn serves to lower the damage category into which the wall is finally classified. The classification of walls into lower damage categories prevents the undertaking of unnecessary mitigating measures. The analyses undertaken in this chapter are referred to as semi-nonlinear analyses because linear material behaviour is considered for the masonry, but the interaction behaviour is considered to be nonlinear as no tensile stresses are permitted. A gap between the soil and the wall will occur if normal tensile stresses develop in the interface.

8.2 Soil to wall interaction

The purpose of this section is to develop way of quantifying the soil to wall interaction.

The effect of the soil on the wall **Δ/L** ratio is dependent on the vertical bearing stiffness of the soil **(K_{soil})**, as well as the vertical stiffness of the wall **(K_{wall})**. A solid masonry wall carries floor loads which are transferred down through the wall and finally into the soil. These floor loads, together with the self-weight of the masonry, exert a pressure on the soil. The bedding of the wall into the soil depends on the size of the wall, the soil properties and the width of the foundation.

The larger the wall, the greater the pressure the wall exerts on the soil. The higher the wall **H** the greater the number of floor loads the wall will be required to carry and the larger the magnitude of the wall span length **L**, the larger each floor load to be carried. Using the **L/H** ratio and the stiffness $\mathbf{K_{wall}}$ to quantify the size of the wall raises the concern of neglecting the dependency of the wall load on the size of the wall itself. This concern, however, can be ignored, as floor loads for load bearing walls in structures of a certain structural class are of the same magnitude. This therefore signifies that different walls of a certain size within a certain type of structure are under the influence of similar loads. Quantification of the load magnitude therefore is deemed to be redundant. Standard floor dimensions as well as floor tributary areas also go toward strengthening the argument of this apparent redundancy. The **L/H** ratio and the stiffness $\mathbf{K_{wall}}$ are therefore seen to be sufficient in quantifying the size of the wall. Note that the above considerations are valid for a typical masonry residential structure with varying floor levels and the load assumptions according to the codes for this case.

The axial stiffness of a structural member is expressed by the following equation:

$$K_{stiffness} = \frac{AE}{l} \tag{8.1}$$

The variables **A**, **E** and **l** are the cross-sectional area, the material Young's modulus of elasticity and the axial length respectively.

The vertical stiffness of the wall is therefore:

$$K_{wall} = \frac{AE}{H} \tag{8.2}$$

Considering the wall as a vertical axial member, its cross-sectional area is expressed as follows:

$$A = bL \tag{8.3}$$

The variable **b** is the width/thickness of the wall, which in this study has been taken to be a constant 300mm. Wider foundations, on which walls are founded in practice, are excluded from the models in this study. The focus is on the walls' structural behaviour independent of the stiffer foundation. The exclusion of the stiffer foundation in the models is conservative with regard to the stress and strain levels in the wall, but also results in a smaller contact area between wall and soil. The smaller the contact area the larger the pressure exerted on the soil. A wall with a width/thickness of 300mm is usually founded on a foundation of width/thickness 600mm, which serves not only to increase the bending stiffness of the wall, but also reduce the pressure on the soil. In order to closely model the true soil to wall interaction, interface elements are inserted between the soil and the wall. This interface is assigned a width/thickness of 600mm. In this way the walls are modelled to transfer their loads to the soil as if founded on a foundation of width/thickness 600mm, but to undergo flexural action independent of the stiffer foundation.

The stiffness of the soil is included in the properties of the interface. Geotechnical engineers are able to provide structural engineers with magnitudes of $\mathbf{K_{soil}}$ directly under the foundations of structures. In this study three different magnitudes of $\mathbf{K_{soil}}$ are considered, soft soil of 10 MN/m^3, medium to stiff soil of 50 MN/m^3 and stiff soil of 80 MN/m^3. The vertical wall stiffness $\mathbf{K_{wall}}$ has the units N/mm. Therefore, in order to express a soil to wall stiffness ratio $\mathbf{K_{soil}/K_{wall}}$, the units of $\mathbf{K_{soil}}$ are converted to N/mm. This is done by multiplying $\mathbf{K_{soil}}$ with the area of the interface between the soil and the wall. The area of the interface between the soil and the wall is expressed by the following equation:

$$A_{int} = jbL \tag{8.4}$$

Where **j** is a factor expressing the thickness/width of the foundation in terms of the thickness/width of the wall. The magnitude of **j** in this study is 2 as the foundation is double the thickness/width of the wall. In this study the soil to wall stiffness ratio is expressed as follows:

$$K_{soil}/K_{wall} = \frac{K_{soil}\,2bLH}{1000bLE}$$

$$K_{soil}/K_{wall} = \frac{K_{soil}H}{500E} \qquad (8.5)$$

Figure 8.1 graphically represents the phenomenon of the soil to wall interaction.

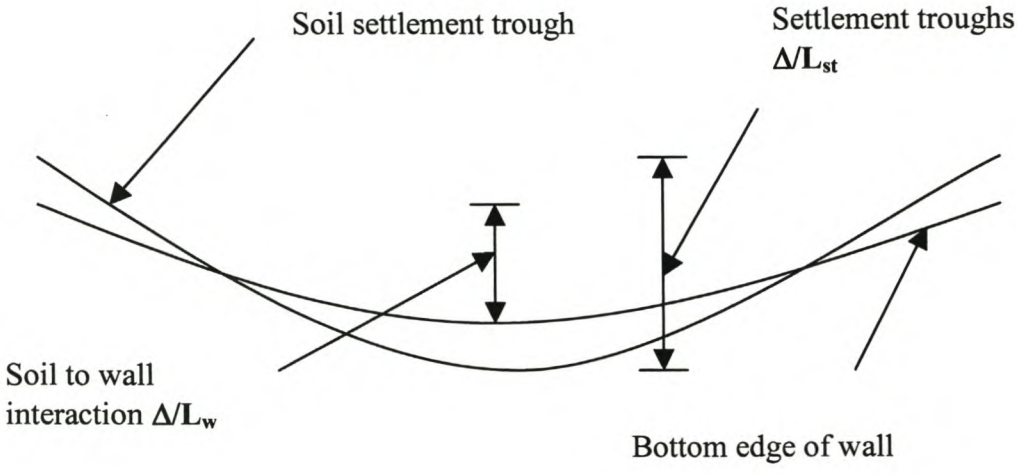

Figure 8.1 Effect of the soil to wall interaction on the **Δ/L** ratios.

Notice how the edges of the wall actually bed into the soil, which serves to lengthen its supports in comparison to the simple supports of the linear elastic models. A gap between the soil and the wall will develop at mid-span if both the walls bending stiffness and yielding tensile strain ε_{yield} are high enough in order for the wall to bridge the gap. The lengthened supports result in the model mimicking the structural configuration of Model 4, Figure 6.2. This lowers the tensile stresses and strains in the wall. Figure 6.9 of chapter 6 depicts this nicely as it compares Model 4's horizontal stress results, along a vertical section at mid-span of a wall, against those of simply supported walls.

The general use of the interaction parameter is defined in DIN 4018 and DIN 4019. This definition was not implemented in this study as it includes a variable concerned with the foundation depth. The walls in this study are investigated independent of foundations. The author's definition of the soil to wall interaction is however also applicable to walls with foundations.

8.3 Loads

The walls are under the influence of three different loads:

- Self-weight of the walls.

- Floor loads at the levels of the respective floors.

- Prescribed displacements of the soil calculated from the tunnel-induced settlement trough.

The finite element program automatically generates the self-weight of the masonry walls. A density of 1800 kg/m³ is used for the masonry as presented in section 5.3. The floor loads are divided into the deadweight of the floors and 50% of the imposed floor loads. The magnitudes of these respective floor loads are as follows:

- Deadweight = 0.7 kN/m² (Timber floors in old masonry structures).

- 50% of imposed load = 0.87 kN/m² (DIN 1055-3)

A typical wall spacing of 7m together with the above floor loads per m^2 are used to calculate the line loads per metre length applied to the walls' floors. A bearing wall in the middle of a residential building is considered so that it is required to carry floor loads from both adjacent sides. Note that line loads are not applied to the top edge of the wall as the roof is considered to be inaccessible. The line loads per metre length are calculated by multiplying the above pressures by the wall spacing. The line loads are as follows:

- Deadweight = 4.9 kN/m (4.9 N/mm)

- 50% of mobile load = 6.1 kN/m (6.1 N/mm)

The total magnitude of the line loads at each floor level is equal to 11 N/mm.

The prescribed displacements are calculated with equation (5.2) considering the wall's original foundation level to be the datum. Therefore, the displacements calculated with equation (5.2) are subtracted by the magnitude of the displacements calculated at the datum level. The prescribed displacements are therefore relative displacements with regard to equation (5.2) and are assigned to the interface element's bottom nodes.

The self-weight of the walls as well as the above floor loads per metre length are applied instantly in the semi-nonlinear analyses. The finite element program suppresses the initial displacements resulting from the instant loads, but stores the stresses and strains in its memory for further development as induced by the prescribed displacements. This is done so that the magnitudes of Δ/L_{st} and Δ/L_w are easily traceable during the running of the analyses. If the initial bearing displacements were not suppressed, the calculation of Δ/L_w would pose difficulties to the analyst. The wall's bottom edge initially displaces evenly due to the uniform pressure of the wall exerted on the soil. Once the prescribed displacements are introduced, however, the wall bottom edge displaces unevenly due to the shifting of the wall's pressure towards the edges. This is due to the soil at mid-span displacing at a faster rate than the soil at the edges, which is as a result of the shape of the sagging zone. If the initial displacements were not suppressed, it would result in them having to be subtracted from the final displacements, before the magnitude of Δ/L_w could be calculated.

8.4 General model outlay

This section describes the structural philosophy behind the models used in this chapter.

Figure 8.2 depicts the general geometry, dimensions and configurations of the supports and loads for the models implemented in the semi-nonlinear analyses. The

number of floors supported by a wall depends on the height of the wall **H** and on the height between floors. A general height of 3m between floors is accepted in this study. The first floor is situated at 500mm above the bottom edge of the wall. The 500mm section is referred to as the pseudo foundation because it is assigned the same thickness as the rest of the wall and because it is situated above the grounds surface.

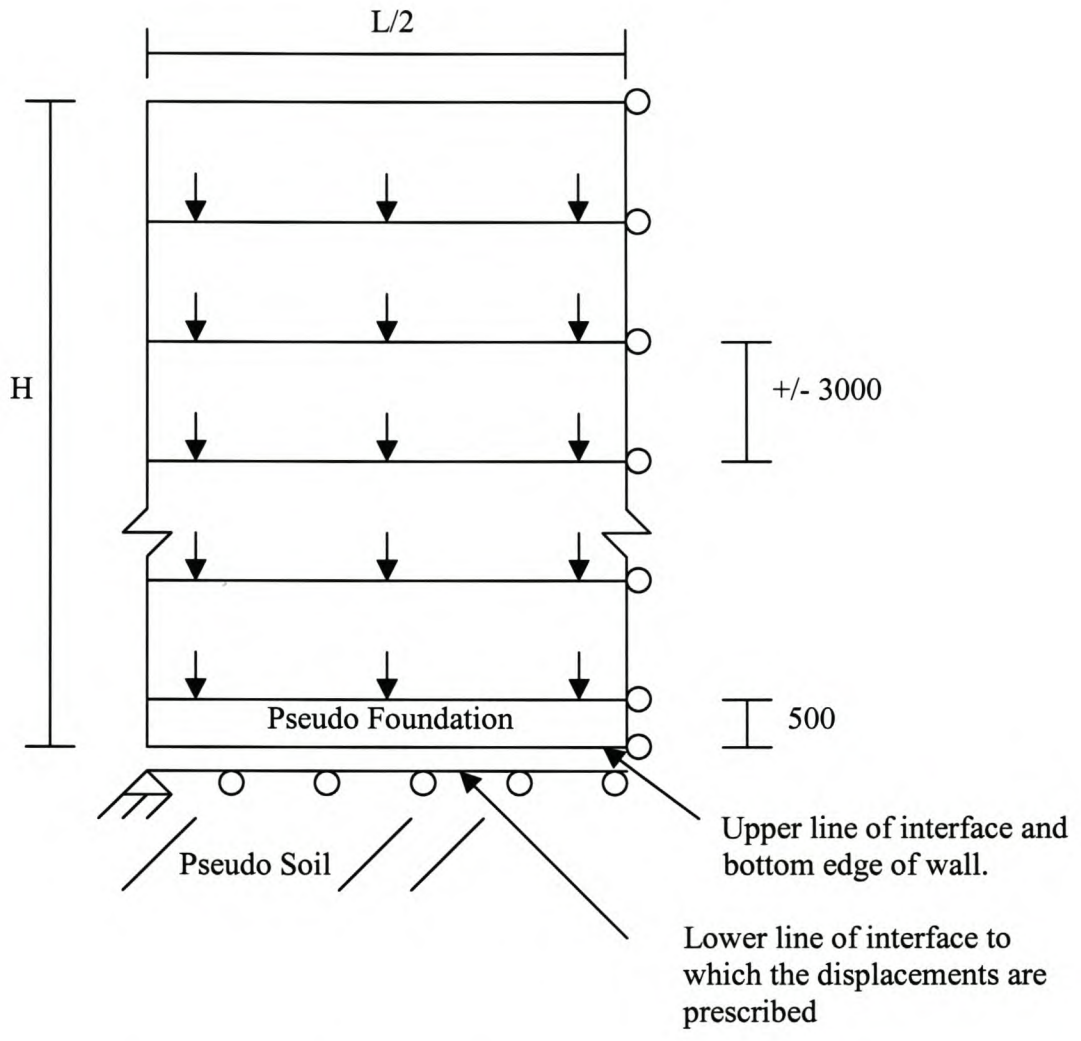

Figure 8.2 Schematisation of the solid masonry wall with soil interaction.

The soil is modelled by the interface with its stiffness properties and therefore not modelled directly. The constraints are applied to the interface lower nodes and to the symmetry axis, as only half the wall is modelled. The bottom left node of the interface is pinned and therefore fixed against translation in both directions. The rest of the nodes at the bottom of the interface are constrained by rollers to facilitate translation

in the horizontal direction. The entire symmetry axis is also constrained by rollers to enforce its translation in the vertical direction only.

8.5 Nonlinear interface

This section describes the mechanism behind the nonlinear interface used to model the soil to wall interaction.

The models implemented in the semi-nonlinear analyses differ from the linear elastic models only in the fact that a nonlinear interface between the wall and the soil is introduced and that the simple column supports are excluded. The nonlinear interfaces allow the wall and the soil to deform independently from one another. The wall bottom edge is not forced to follow the settlement trough movements, but is able to follow its own deformation pattern. Therefore Δ/L_w is able to develop and can be traced in parallel with Δ/L_{st} during the stepped analysis. Relationships between the above two variables can then be plotted for different **L/H** and K_{soil}/K_{wall} ratios.

A nonlinear interface (Van Zijl 2000) is used to model the soil to wall interaction, without actually modelling the soil itself. The parameters of the interface relate the normal stresses σ_n at the integration points of an interface element to the vertical displacement δ_v between the corresponding upper and lower nodes of the interface element, according to Figure 8.3.

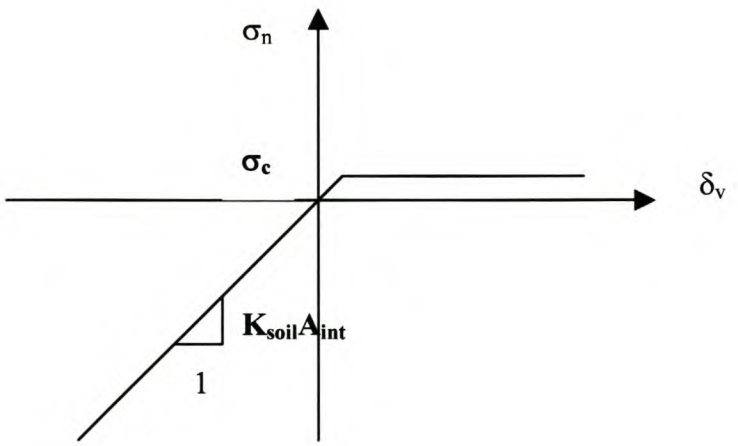

Figure 8.3 Relationship between σ_n and δ_v of the interface elements.

The variable σ_c is a tension limit, or cut-off. Instead of assigning it a magnitude equal to zero to model no-tension in the soil-foundation interface, it is assigned an insignificantly small magnitude to avoid numerical problems. The interface therefore allows gaps between the soil and the wall to develop at positions were normal tensile stresses develop. In the compressive stress region $\mathbf{K_{soil}}$ defines the relationship between the normal compressive stresses at the integration points of an interface element and δ_v between the corresponding upper and lower nodes of the interface element by the following equation:

$$\sigma_n = K_{soil}\delta_n A_{\text{int}} \tag{8.6}$$

The area of the interface is included in equation (8.6) so as to have the units in N/mm).

The walls under consideration in this study experience no soil to wall friction or lateral confinement caused by the existence of adjacent structures. The properties of the interface are therefore modified to model this situation. Figure 8.4 defines the relationship between the absolute value of the shear stress $/\tau_n/$ developed at the integration points of an interface element and the horizontal displacement δ_h between the corresponding upper and lower nodes of the interface element.

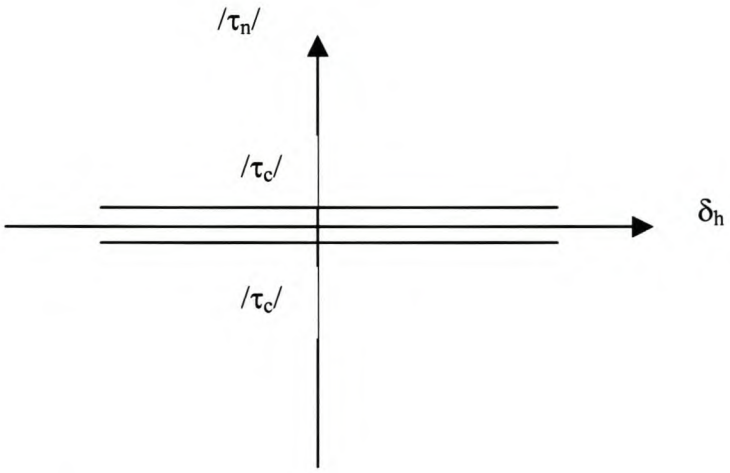

Figure 8.4 Relationship between $/\tau_n/$ and δ_h of the interface elements.

Allowing no shear resistance to develop between the soil and the bottom edge of the wall is a conservative approach with regards to the construction of the relationships between Δ/L_{st} and Δ/L_w. The higher the shear resistance between the soil and the bottom edge of the wall, the lower the prediction of Δ/L_w, and therefore the lower ε_{lim} will be. The shear cut-off $/\tau_c/$ is assigned an insignificantly small magnitude to avoid numerical problems. A zero friction coefficient is considered, as indicated by the horizontal relation between $/\tau_n/$ and δ_h in Figure 8.4.

Figure 8.5 is a graphical representation of a two-dimensional interface element implemented in this study. Figure 8.5 a) represents the topology of the element and 8.5 b), the displacement degrees of freedom. The interface is an element implemented between two lines in a two-dimensional configuration. The element describes a relation between the tractions **t** and the relative displacements $\Delta\gamma$ across the interface. The **h** axis is tangential to the interface. The **n** axis is perpendicular to the interface in the two dimensional plane. The element is based on linear interpolation of the displacement field.

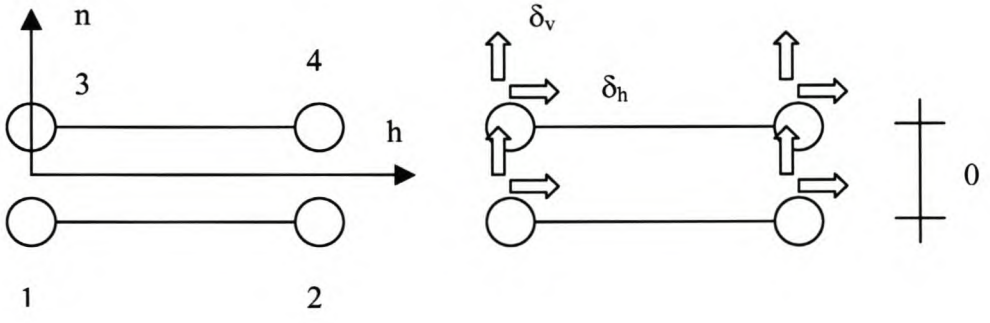

Figure 8.5 Interface, 2+2 nodes, line elements.

a) Topology
b) Displacements

From Figure 8.5 it is seen that the interface elements are assigned heights equal to zero. This is achieved by assigning the same nodal coordinates to the nodal pairs (1,3)

and (2,4). In reality there will be direct contact between the bottom of the wall foundation and the soil itself. This justifies the zero height assigned to the interface elements. The basic variables are the nodal displacements γ, the relative displacements $\Delta\gamma$ and the tractions **t**.

$$\gamma = \begin{Bmatrix} \gamma_n \\ \gamma_h \end{Bmatrix} \tag{8.7}$$

$$\Delta\gamma = \begin{Bmatrix} \Delta\gamma_n \\ \Delta\gamma_h \end{Bmatrix} \tag{8.8}$$

$$t = \begin{Bmatrix} \sigma_n \\ \tau_h \end{Bmatrix} \tag{8.9}$$

8.6 Results

Relationships between Δ/L_{st} and Δ/L_w are calculated from the results of the semi-nonlinear analyses. Table 8.1 tabulates the properties of the models implemented in these analyses with configurations as in Figure 8.2. Figures 8.6 to 8.9 present the above relationships for walls of **L/H** ratio equal to 0.5, 1, 2 and 3 respectively. The legends refer to the K_{soil}/K_{wall} ratio. Note that the curves of different length represent walls of different span length **L**, as tabulated in Table 8.1. Once the magnitude of Δ/L_{st}, the **L/H** ratio of the wall as well as the K_{soil}/K_{wall} ratio have been calculated, the magnitude of Δ/L_w can be read off from one of the above-mentioned figures. The magnitude of Δ/L_w leads to the determination of ε_{lim}, which leads to the damage classification of the wall.

Model	L/H	L (mm)	K_{soil} (MN/m³)	K_{soil}/K_{wall}
H	1	19800	10	0.099
I	1	19800	50	0.495
J	1	19800	80	0.792
K	1	9900	10	0.0495
L	1	9900	50	0.2475
M	1	9900	80	0.396
N	2	19800	10	0.0495
O	2	19800	50	0.2475
P	2	19800	80	0.396
Q	2	9900	10	0.02475
R	2	9900	50	0.12375
S	2	9900	80	0.198
T	3	19800	10	0.033
U	3	19800	50	0.165
V	3	19800	80	0.264
W	3	9900	10	0.0165
X	3	9900	50	0.0825
Y	3	9900	80	0.132
Z	0.5	19800	10	0.198
AA	0.5	19800	50	0.99
AB	0.5	19800	80	1.584
AC	0.5	9900	10	0.099
AD	0.5	9900	50	0.495
AE	0.5	9900	80	0.792

Table 8.1 Semi-nonlinear models.

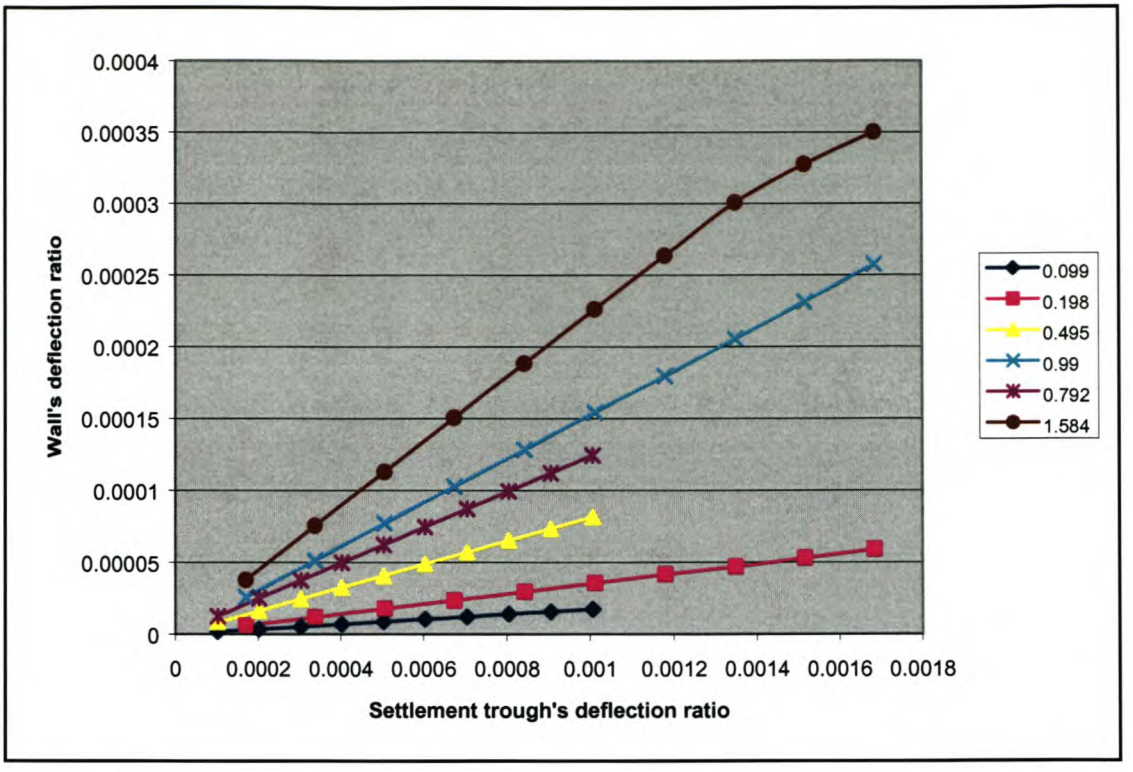

Figure 8.6 Δ/L_{st} versus Δ/L_w for a $L/H = 0.5$. (Legend = K_{soil}/K_{wall})

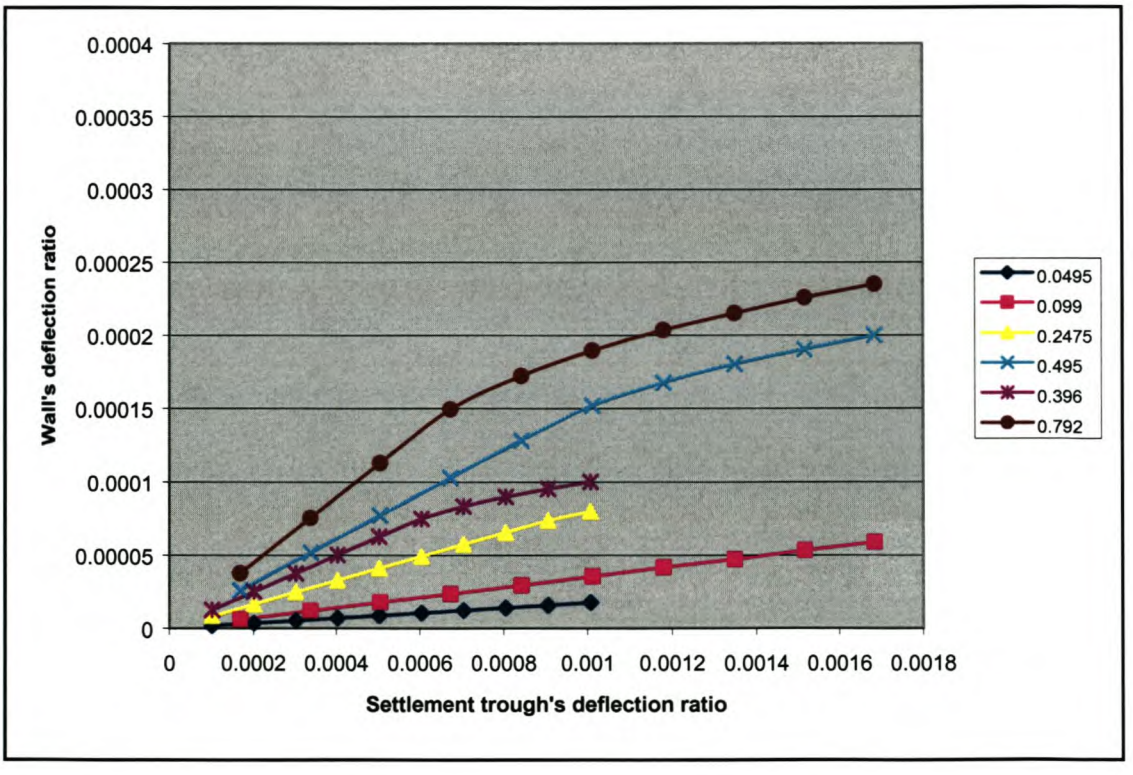

Figure 8.7 Δ/L_{st} versus Δ/L_w for a $L/H = 1$. (Legend = K_{soil}/K_{wall})

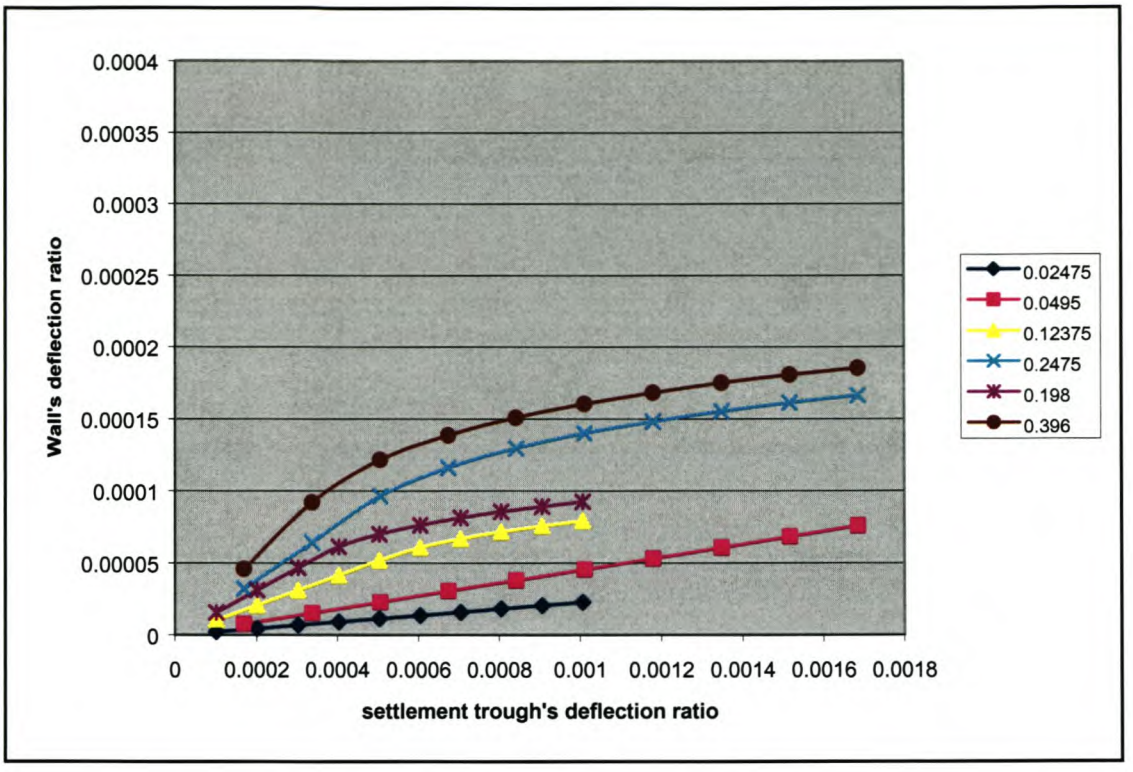

Figure 8.8 Δ/L_{st} versus Δ/L_w for a $L/H = 2$. (Legend = K_{soil}/K_{wall})

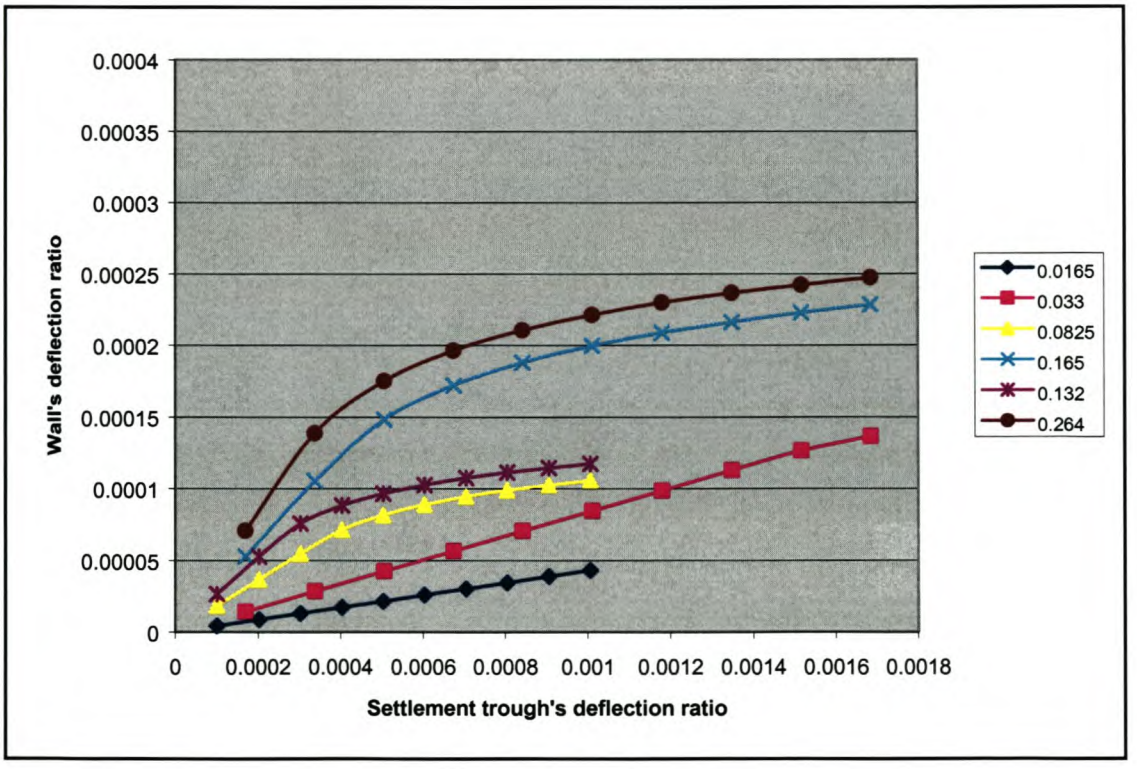

Figure 8.9 Δ/L_{st} versus Δ/L_w for a $L/H = 3$. (Legend = K_{soil}/K_{wall})

The only problem with practically using Figures 8.6 to 8.9 for this purpose is that they only cater for four specific **L/H** ratios. Even though the practical range of **L/H** ratios encountered in practice falls between 0.5 and 3, a more general set of graphs is desired for the purpose of calculating Δ/L_w for all **L/H** ratios in this practical range. In order to design this set of general graphs, certain critical properties of the curves in Figures 8.6 to 8.9 are noted as follows:

a) For a given **L/H** ratio and magnitude of **L**, the limit between the linear and nonlinear region of each curve is defined by a near equal magnitude of Δ/L_w, turning point **(e)**, irrespective of Δ/L_{st}. Notice how curves exhibiting only a linear region have yet to reach the specific magnitude of **e**. See Figures 8.7 to 8.9.

b) Walls of different **L/H** ratio, but equal K_{soil}/K_{wall} ratio do not exhibit the same relationship between Δ/L_{st} and Δ/L_w, irrespective of the magnitude of **L**. Figure 8.10.

c) It is seen that for a given **L/H** ratio, the relationship between the gradient **(m)**, equation (8.10), of the respective curves linear region and the K_{soil}/K_{wall} ratio is independent of the span length **L** of the wall. See Figure 8.11.

d) From Figure 8.7 it can be determined that the distances measured along the vertical axis Δ/L_w, between the turning points of curves (0.792, 0.495) and curves (0.396, 0.2475) are equal. The turning points refer to the points used to define the boundary between each curves linear and nonlinear regions and the fractions in brackets are the K_{soil}/K_{wall} ratios of the respective curves. It is then noted that the division of 0.792 by 0.495 and the division of 0.396 by 0.2475 result in the equal magnitude of 1.6. Similar relationships are detected in Figures 8.8 to 8.9.

Figure 8.10 shows that the relationships between Δ/L_{st}:Δ/L_w for two walls of equal K_{soil}/K_{wall} ratio, but different **L/H** ratio, are not equal.

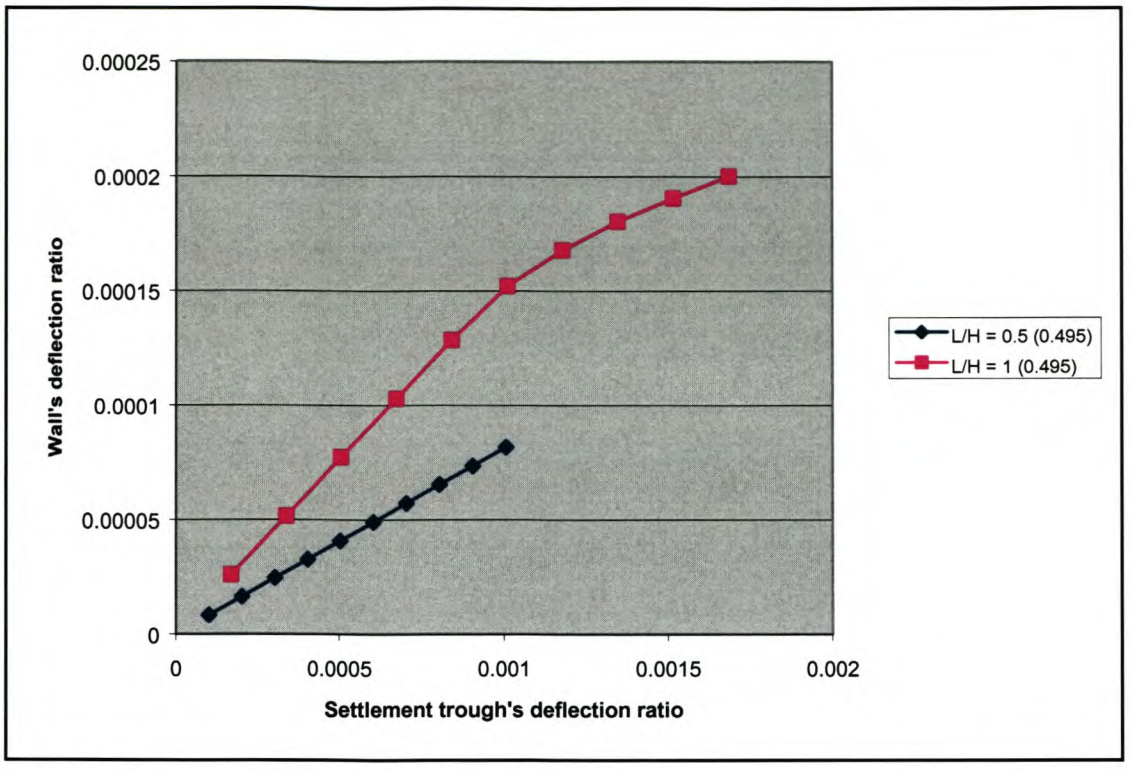

Figure 8.10 Δ/L_{st} versus Δ/L_w for two walls of equal K_{soil}/K_{wall} ratio (0.495), but different **L/H** ratios of 0.5 and 1 respectively.

Figure 8.11 plots the relationship between **m** and the K_{soil}/K_{wall} ratio for various wall **L/H** ratios.

The gradient **m** is defined by the following equation:

$$m = \frac{\Delta/L_w}{\Delta/L_{st}} \tag{8.10}$$

Equation (8.10) is associated with the linear regions of the curves in Figures 8.6 to 8.9. The boundary between the linear and nonlinear regions is defined by the turning point **e**, measured along the vertical axis Δ/L_w.

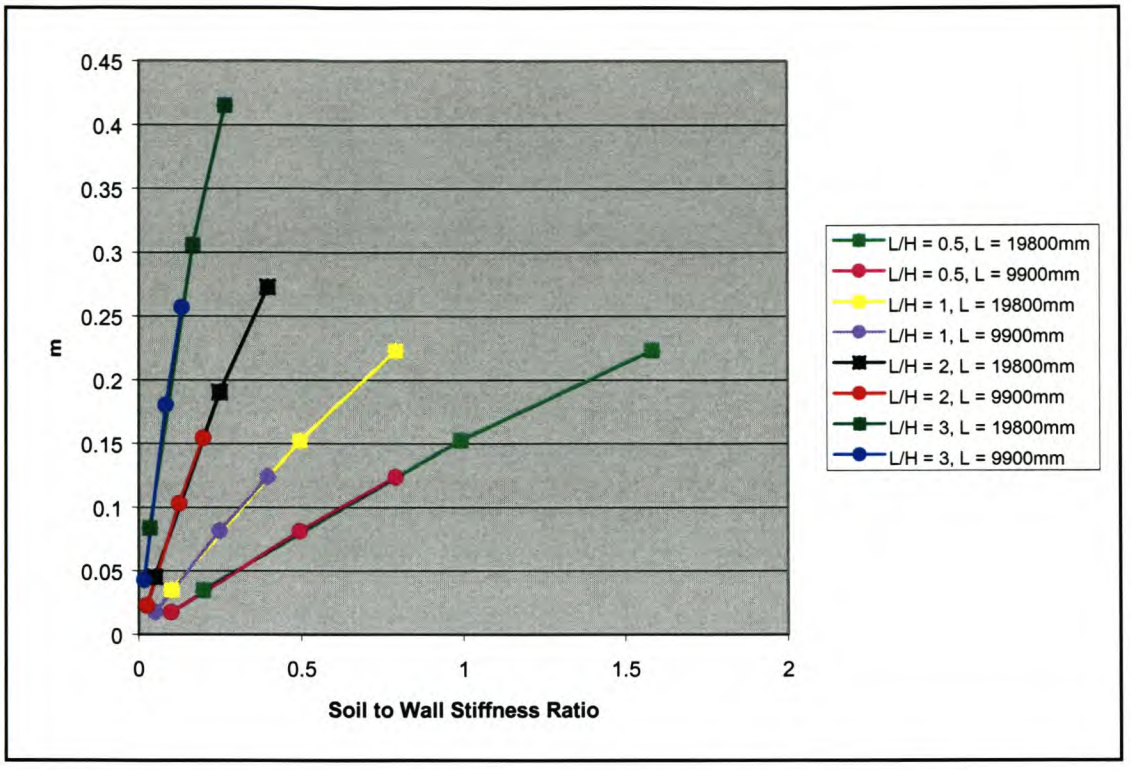

Figure 8.11 **m** versus $\mathbf{K_{soil}/K_{wall}}$ for varying **L/H** ratios and span length's **L**.

It is evident that the relationship between **m** and the $\mathbf{K_{soil}/K_{wall}}$ ratio is only dependent on **L/H**. It is independent of **L**. Walls of different span length **L** founded symmetrically over the sagging zone of a settlement trough experience different progressions of ground displacements due to the change in gradient along the sagging zone. The walls in Figure 8.11 of equal **L/H** ratio, but different span length **L**, are therefore considered as being founded on different green field settlement troughs. This is a very significant point as it leads to the conclusion that the relationships between $\mathbf{\Delta/L_{st}:\Delta/L_w}$, as depicted in Figures 8.6 to 8.9, are independent of a specific green field settlement trough's shape.

The set of graphs that needs to be designed for damage assessment purposes will assist in plotting a curve defining the relationship between $\mathbf{\Delta/L_{st}:\Delta/L_w}$ for a specific wall **L/H** ratio ($0.5 < \mathbf{L/H} < 3$), a specific wall span length **L** and a specific $\mathbf{K_{soil}/K_{wall}}$ ratio.

The first graph in this set is that of Figure 8.12, which presents the relationship between **e** and the wall **L/H** ratio for various wall span length **L**. Magnitudes of **e** for

intermediate values of **L** are obtained by linear interpolation of the results presented in Figure 8.12. The only problem encountered in the construction of this figure is that the magnitudes of **e** with regard to the shorter curves in Figure 8.6 are not directly readable as they are all still in the linear region. The magnitude of **e**, presented in Figure 8.12, at an **L/H** ratio equal to 0.5 and for a span length **L** equal to 9900mm is, however, obtained by taking points a) and d), with regard to Figures 8.6 to 8.9, into account.

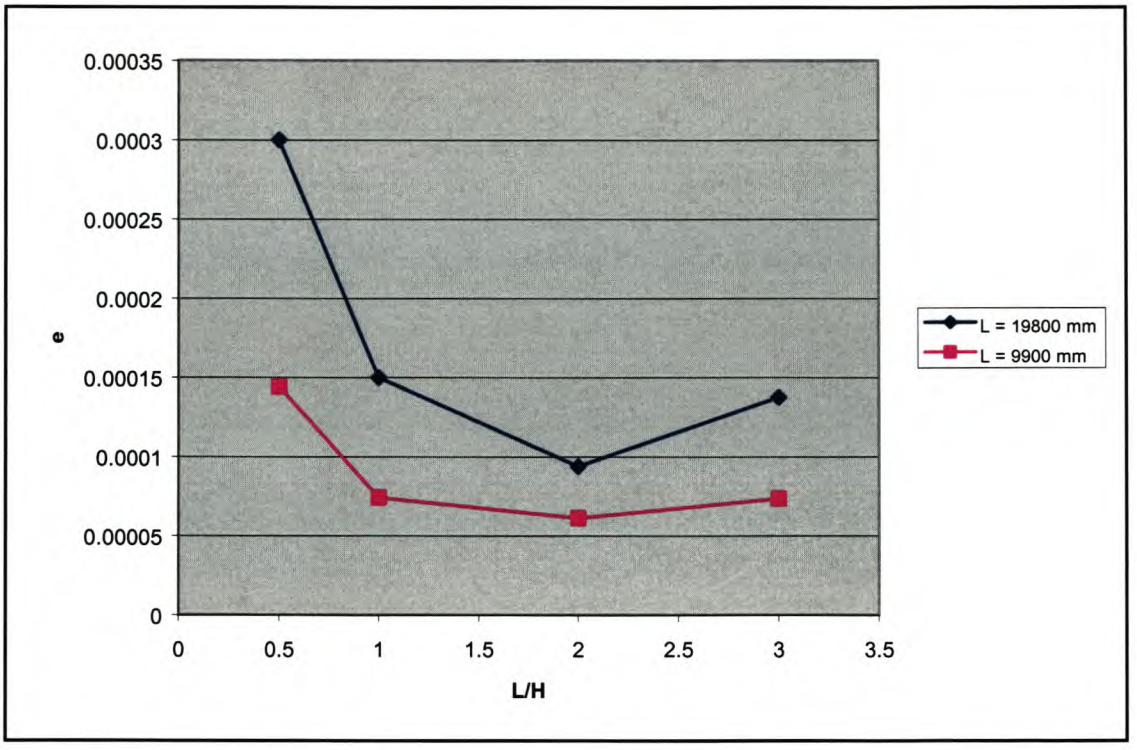

Figure 8.12 **e** versus the **L/H** ratio for various span lengths **L**.

This value of **e** is obtained in the following steps:

a) The linear region of curve (0.99), in Figure 8.6, is extended until it intersected the horizontal line at **e** = 0.0003, which is the turning point as depicted by curve (1.584).

b) The horizontal distance taken along the Δ/L_{st} axis, between these two curves (1.584, 0.99) at the value of **e** = 0.0003, is measured.

c) The linear regions of the curves (0.792, 0.495) are then extended until the horizontal distance between them, measured along the Δ/L_{st} axis, is equal to the horizontal distance, measured along the Δ/L_{st} axis, between the turning points of curves (1.584, 0.99).

d) The division of 1.584 by 0.99 is equal to the division of 0.792 by 0.495 as required by point d) with regards to Figures 8.6 to 8.9.

e) The value of **e** = 0.000144 at which the horizontal Δ/L_{st} distance between curves (0.792, 0.495) matched that between the turning points of curves (1.584, 0.99) is accepted to be the turning point of the shorter curves in Figure 8.6 and is plotted as such in Figure 8.12.

The second graph in the set is Figure 8.13, which plots the relationship between **m** and the **L/H** ratios in the practical range of 0.5 to 3 for different $\mathbf{K_{soil}/K_{wall}}$ ratios. Figure 8.13 is constructed by noticing that in Figure 8.11, for a given **L/H** ratio, the magnitude of the gradient **m** gradually decreases as the $\mathbf{K_{soil}/K_{wall}}$ ratio increases. Figure 8.11 is therefore presented again, as Figure 8.14, by simply linearly extending all the respective curves until a $\mathbf{K_{soil}/K_{wall}}$ ratio of 1.584 is reached. Figure 8.13 is then directly constructed from Figure 8.14. This is seen to be conservative as the gradients **m** predicted by the curves, which are extended will be larger than the actual gradients **m** for the specified $\mathbf{K_{soil}/K_{wall}}$ ratios.

Note that the value of **m** will always be equal to and less than unity as the magnitude of Δ/L_w will never be greater than that of Δ/L_{st}. Figure 8.13 should be used in such a way that the magnitude of **m** is taken as unity at positions where the magnitude of **m** surpassed unity as a result of the modifications performed on Figure 8.11.

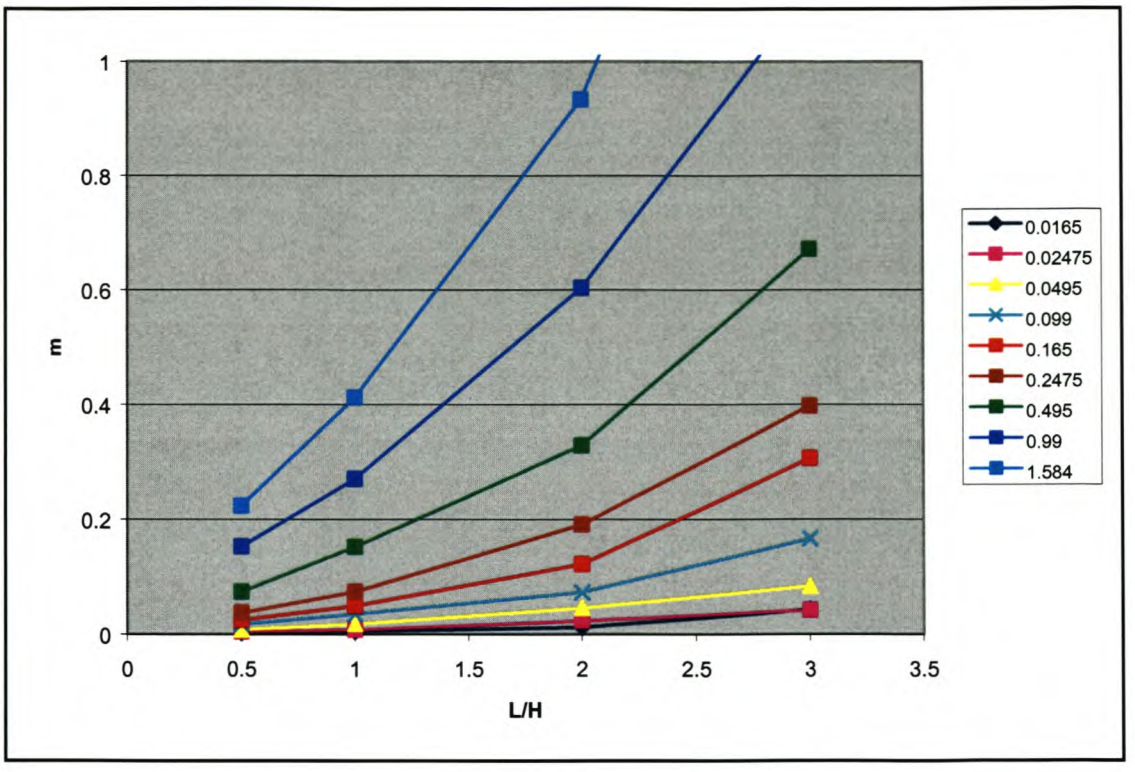

Figure 8.13 **m** versus **L/H** ratio for various $\mathbf{K_{soil}/K_{wall}}$ ratios. (Legend $\mathbf{K_{soil}/K_{wall}}$ ratio).

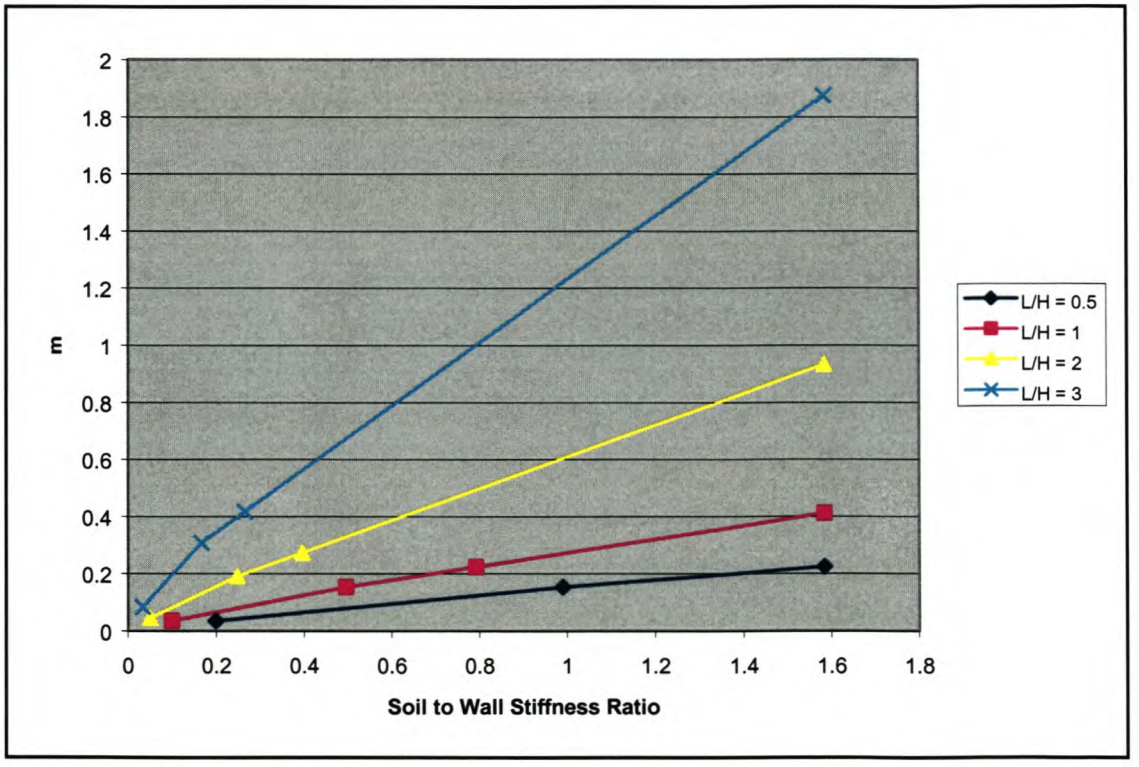

Figure 8.14 Adjusted **m** versus $\mathbf{K_{soil}/K_{wall}}$ for varying **L/H** ratios and span length's **L**.

Figure 8.13 and 8.12 are used in tandem in order to construct the linear region of a curve defining the relationship between Δ/L_{st} and Δ/L_w for a certain **L/H** ratio, a certain span length **L** and a certain K_{soil}/K_{wall} ratio. Once **m** and **e** are calculated from Figures 8.13 and 8.12 respectively, the magnitude of **(f)**, which defines the curves turning point in terms of Δ/L_{st}, is calculated with the following equation:

$$f = \frac{e}{m} \tag{8.11}$$

The magnitude of the predicted Δ/L_{st} ratio obtained from the settlement trough is compared to the magnitude of **f** calculated with equation (8.11). If Δ/L_{st} is smaller than **f**, the following equation is used to determine the specific wall's Δ/L_w:

$$\frac{\Delta}{L_w} = m\left(\frac{\Delta}{L_{st}}\right) \tag{8.12}$$

If, however, Δ/L_{st} is larger than **f** then the nonlinear range between the relationship of Δ/L_w:Δ/L_{st} has been entered. In this region, a third and final graph, Figure 8.15, in the set is needed to describe the relationship between Δ/L_{st}:Δ/L_w for a certain **L/H** ratio, a certain span length **L** and a certain K_{soil}/K_{wall} ratio. Firstly the variables **z** and **w** are defined.

The variable **z** is defined as the difference between the magnitude of Δ/L_w and the magnitude of **e** in the nonlinear region, expressed by the following equation:

$$z = \left(\frac{\Delta}{L_w}\right) - e \tag{8.13}$$

The variable **w** is defined as the difference between the magnitude of Δ/L_{st} and the magnitude of **f** in the nonlinear region, expressed by the following equation:

$$w = \left(\frac{\Delta}{L_{st}}\right) - f \tag{8.14}$$

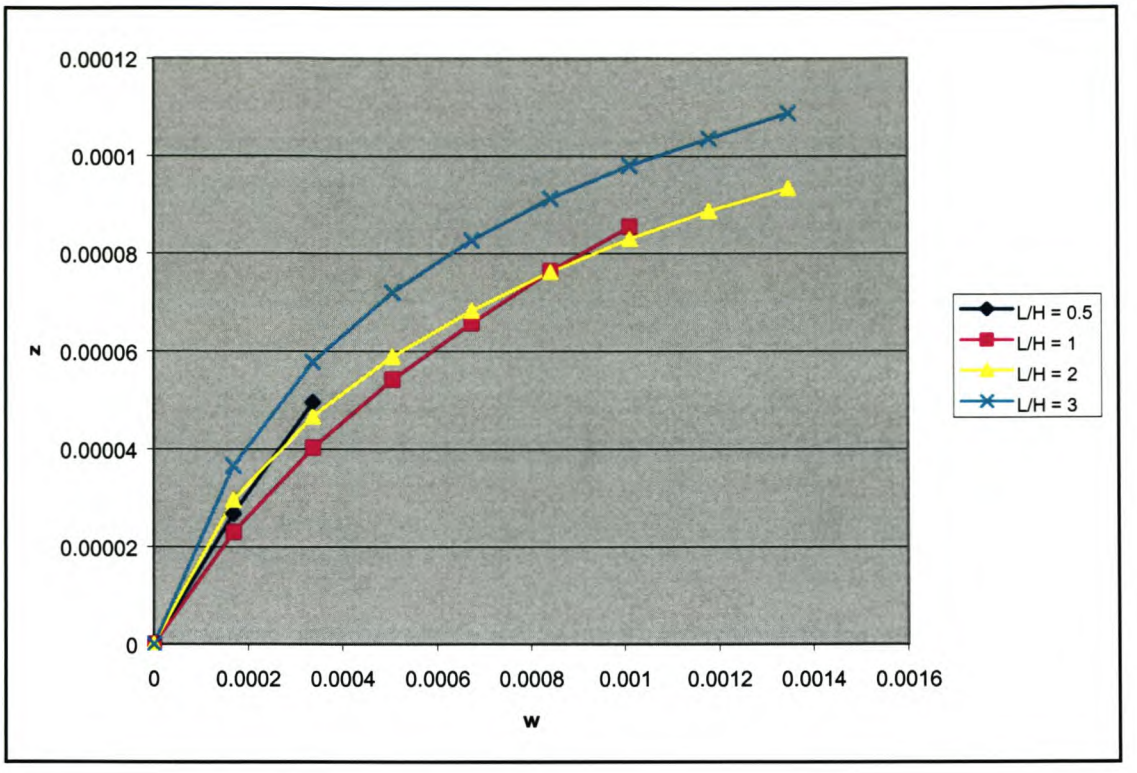

Figure 8.15 **z** versus **w** for various **L/H** ratios.

Figure 8.15 is constructed with the aid of equations (8.13) and (8.14) as well as Figures 8.6 to 8.9. The magnitudes of **z** and **w** are calculated for each of the curves in Figures 8.6 to 8.9, which exhibit a nonlinear region, assuming that the relationship between **z** and **w** is independent of the $\mathbf{K_{soil}/K_{wall}}$ ratio. A relationship between the variables **z** and **w** is presented for various **L/H** ratios, irrespective of the $\mathbf{K_{soil}/K_{wall}}$ ratios, as depicted in Figure 8.15.

Therefore, once it is determined that $\mathbf{\Delta/L_{st}}$ is larger than **f**, equation (8.14) is used to calculate the magnitude of **w** for a certain **L/H** ratio. Figure 8.15 is then used to determine the magnitude of **z**, which is then used to calculate the magnitude of $\mathbf{\Delta/L_w}$ by manipulating equation (8.13) as follows:

$$\frac{\Delta}{L_w} = z + e \tag{8.15}$$

The magnitude of $\mathbf{\Delta/L_w}$ calculated with equation (8.15) is used to calculate the magnitude of $\boldsymbol{\varepsilon_{lim}}$, which leads to the classification of the wall into a specific damage category.

8.7 Summary

This chapter investigated the effect the soil to wall interaction has on the **Δ/L** ratio. As expected, the soil to wall interaction leads to a considerable reduction in the magnitude of the actual **Δ/L** ratio experienced by the wall from the **Δ/L** ratio calculated from the green field settlement trough's shape. Thereby, lower values of ε_{lim}, are predicted, serving to classify solid masonry walls in damage categories lower than those in which they would normally have been classified by using Δ/L_{st}, as is used in the **LTS**.

Relationships between Δ/L_{st}:Δ/L_w can be derived using Figures 8.12, 8.13 and 8.15 for a certain **L/H** ratio, a certain span length **L** and a certain K_{soil}/K_{wall} ratio. Note that the list of variables affecting the categorisation of solid masonry walls into the various damage categories is as follows:

a) The soil to wall interaction determining the magnitude of Δ/L_w., which is dependent on the following variables: **L/H** ratio, span length **L**, K_{soil}/K_{wall} ratio, Δ/L_{st} ratio and material properties of the wall.

b) ε_{lim}, which is dependent on the following variables: Δ/L_w, **L/H** ratio, span length **L** and the material properties of the wall.

The next chapter in this study is dedicated to comparing the **LTS** against the **MLTS** with regard to the damage classification of solid masonry walls symmetrically positioned over the sagging zone of a green field settlement trough. The damage classes implemented are those tabulated in Tables 3.1 and 3.2.

Chapter 9

LTS versus MLTS

9.1 Introduction

This chapter compares the **LTS** with the **MLTS** with regard to the damage classification of solid masonry walls symmetrically positioned over the sagging zone of a green field settlement trough. Section 9.2 defines the example in terms of the walls' dimensions, material properties and the properties of the green field settlement trough. Section 9.3 classifies the respective walls into the different damage categories, tabulated in Tables 3.1 and 3.2, **LTS**. Section 9.4 does the same classification this time using the **MLTS**. Section 9.5 is concerned with comparing the damage categories calculated in sections 9.3 and 9.4.

9.2 Problem

A tunnel, which is to pass directly under a busy city center, is in the process of being designed. The prediction of settlement damage to the surface infrastructure on the route of the tunnel is a major part of the design process. There are large masonry structures founded directly over the tunnels route. The consulting firm responsible for the structural integrity of the surface infrastructure has categorised each of the masonry structures into their critical structural units. Solid masonry walls constitute a large number of these critical structural units. All the walls extend over the entire cross-sectional length of the transverse green field settlement trough induced by the tunnel. The green field settlement trough is defined by the following parameters:

- Depth of the tunnels axis: $\mathbf{z_o} = 22000$ mm.
- Diameter of the tunnel: $\mathbf{D} = 9500$ mm.
- Point of inflection: $\mathbf{i} = 9900$ mm.
- Trough width parameter: $\mathbf{K} = 0.45$.
- Volume loss: $\mathbf{V_l} = 3\%$.

The material properties of the masonry are:

- Young's modulus: **E** = 4000 **MPa**
- Shear modulus: **G** = 1667 **MPa**
- Poisons ratio: ν = 0.2
- Density: ρ = 1800 **kg/m^3**

The consultants are to use the **MLTS** (Author) as well as the **LTS** (Burland and Wroth 1974) to perform the damage categorisation of the various walls into the different damage categories with regard to sagging deformation only.

The following walls are to be categorised:

1a) Wall height: **H** = 39600mm
Soil stiffness: $\mathbf{K_{soil}}$ = 10 MN/m^3

b) Wall height: **H** = 39600mm
Soil stiffness: $\mathbf{K_{soil}}$ = 80 MN/m^3

2a) Wall height: **H** = 6600mm
Soil stiffness: $\mathbf{K_{soil}}$ = 10 MN/m^3

b) Wall height: **H** = 6600mm
Soil stiffness: $\mathbf{K_{soil}}$ = 80 MN/m^3

9.3 Solution: MLTS (Author)

As in the **LTS**, it is assumed that a building can be considered separately either side of a point of inflection. As each wall extends across the entire cross-sectional width of the transverse settlement trough, the span length **L** of the walls symmetrically positioned over the sagging zone is double the distance to the point of inflection, which is 19800mm.

The mid-span deflections Δ of the respective walls are calculated with equation (5.11). Note that this calculation, as represented by equation (9.1), is independent of the respective wall heights **H**.

$$\Delta = \frac{0.31(0.03)(9500)^2}{(0.45)(22000)}\left(1 - e\left(-\left(\frac{(19800/2)^2}{2((0.45)(22000))^2}\right)\right)\right) = 33.36mm \quad (9.1)$$

The Δ/L_{st} ratio of the walls is calculated as follows:

$$\frac{\Delta}{L} = \frac{33.36}{19800} = 1.6848 \times 10^{-3} \quad (9.2)$$

MLTS accounts for the soil to wall interaction by adjusting the magnitude of the Δ/L_{st} ratio. The K_{soil}/K_{wall} ratios for the respective walls are calculated with equation (8.5) as follows:

1a) $$\frac{K_{soil}}{K_{wall}} = \frac{10(39600)}{500(4000)} = 0.198 \quad (9.3)$$

b) $$\frac{K_{soil}}{K_{wall}} = \frac{80(39600)}{500(4000)} = 1.584 \quad (9.4)$$

2a) $$\frac{K_{soil}}{K_{wall}} = \frac{10(6600)}{500(4000)} = 0.033 \quad (9.5)$$

b) $$\frac{K_{soil}}{K_{wall}} = \frac{80(6600)}{500(4000)} = 0.264 \quad (9.6)$$

Figure 8.12 is used to determine the magnitude of the turning point **e** for the respective walls:

1a) 0.0003 (**L/H** = 0.5, **L** = 19800mm).

b) 0.0003 (**L/H** = 0.5, **L** = 19800mm).

2a) 0.0001375 (**L/H** = 3, **L** = 19800mm).

b) 0.0001375 (**L/H** = 3, **L** = 19800mm).

Figure 8.13 is used to determine the magnitude of the linear gradient $(\Delta/L_w)/(\Delta/L_{st})$ **m** for the respective walls:

1a) 0.034924 (**L/H** = 0.5, $\mathbf{K_{soil}/K_{wall}}$ = 0.198).

b) 0.223414 (**L/H** = 0.5, $\mathbf{K_{soil}/K_{wall}}$ = 1.584).

2a) 0.083622 (**L/H** = 3, $\mathbf{K_{soil}/K_{wall}}$ = 0.033).

b) 0.415393 (**L/H** = 3, $\mathbf{K_{soil}/K_{wall}}$ = 0.264).

The magnitude of Δ/L_{st} **f** defined by the above turning points are calculated with equation (8.11) as follows:

1a) $$\frac{\Delta}{L_{st}} = f = \frac{0.0003}{0.034924} = 8.59\times10^{-3} \tag{9.7}$$

b) $$\frac{\Delta}{L_{st}} = f = \frac{0.0003}{0.223414} = 1.3428\times10^{-3} \tag{9.8}$$

2a) $$\frac{\Delta}{L_{st}} = f = \frac{0.0001375}{0.083622} = 1.6443\times10^{-3} \tag{9.9}$$

b) $$\frac{\Delta}{L_{st}} = f = \frac{0.0001375}{0.415393} = 3.3101\times10^{-4} \tag{9.10}$$

The following question then needs to be asked: Is the magnitude of **f** calculated with equations (9.7) to (9.10) for the respective walls smaller or larger than the magnitude of Δ/L_{st} calculated with equation (9.2). The answers are as follows:

1a) Larger.

b) Smaller.

2a) Smaller.

b) Smaller.

If the answer is "larger" then equation (8.12) is used to calculate the magnitude of Δ/L_w for the respective walls as follows:

$$1a)\ \frac{\Delta}{L_w} = 0.034924\left(1.6848\times10^{-3}\right) = 5.884\times10^{-5} \tag{9.11}$$

Therefore, the magnitude of Δ/L_w for wall 1a) falls within the linear region of the Δ/L_{st}:Δ/L_w relationship.

If the answer is "smaller" then equation (8.14) is used to calculate the magnitude of **w**, which is then used in Figure 8.15 to calculate the magnitude of **z**. Equation (5.15) is then used to calculate the magnitude of Δ/L_w. The calculation of **w** is as follows:

$$1b)\ w = 1.6848\times10^{-3} - 1.3428\times10^{-3} = 0.000342 \tag{9.12}$$

$$2a)\ w = 1.6848\times10^{-3} - 1.6443\times10^{-3} = 0.0000405 \tag{9.13}$$

$$b)\ w = 1.6848\times10^{-3} - 3.3101\times10^{-4} = 0.00135379 \tag{9.14}$$

The magnitudes of **w**, calculated with equations (9.12) to (9.14), are used in Figure 8.15 to calculate the magnitudes of **z** as follows:

$$1b)\ z = 0.0000495 \tag{9.15}$$

$$2a)\ z = 9.333\times10^{-6} \tag{9.16}$$

b) $z = 0.0001088$ (9.17)

The magnitudes of **z**, calculated with equations (9.15) to (9.17), are substituted into equation (8.15) to calculate the magnitudes of Δ/L_w:

1b) $\frac{\Delta}{L_w} = 0.0000495 + 0.0003 = 0.0003495$ (9.18)

2a) $\frac{\Delta}{L_w} = 9.333 \times 10^{-6} + 0.0001375 = 0.000146833$ (9.19)

b) $\frac{\Delta}{L_w} = 0.0001088 + 0.0001375 = 0.0002463$ (9.20)

The limiting tensile strains ε_{lim} (chapter 7) calculated according to the magnitudes of the respective Δ/L_w ratios, calculated with equations (9.11), (9.18), (9.19) and (9.20), are tabulated in Table 9.1. Table 9.2 categorises the various walls according to the magnitude of ε_{lim}, calculated with the **MLTS**, into the respective damage categories tabulated in Tables 3.1 and 3.2. The strains coloured in red indicate that they have exceeded the yielding tensile strain ε_{yield} (0.000125) of the masonry.

Number	SBP (ε_{lim})	MAXP (ε_{lim})	AMAX (ε_{lim})	Figure
1a)	0.0000611			7.21
1a)		0.0001087		7.22
1a)			0.000139	7.23
1b)	0.000356			7.21
1b)		0.000674		7.22
1b)			0.000833	7.23
2a)	0.000178	0.000178	0.000178	7.18
2b)	0.000289	0.000289	0.000289	7.18

Table 9.1 ε_{lim} developed in the walls of 1a), b), 2a), b) according to the **MLTS**.

Number	SBP (ε_{lim}) %	MAXP (ε_{lim}) %	AMAX (ε_{lim}) %	Damage Category
1a)	0-0.05			0
1a)		0-0.05		0
1a)			0-0.05	0
1b)	0-0.05			0
1b)		0.05-0.075		1
1b)			0.075-0.15	2
2a)	0-0.05	0-0.05	0-0.05	0
2b)	0-0.05	0-0.05	0-0.05	0

Table 9.2 Damage classification (Table 3.1 and 3.2) of walls according to ε_{lim} calculated with the **MTS**.

9.4 Solution: LTS (Burland and Wroth 1974)

In this approach the buildings are considered separately either side of a point of inflection. The soil to wall interaction is not taken into account in the **LTS**. Therefore, the **Δ/L** ratios of the walls in 1a), b), 2a) and b) are equal to the **Δ/L** ratio calculated with equation (9.2). Table 9.3 tabulates ε_{lim} according to the **q** model calculated with equations (5.16) and (5.17), which calculate ε_{bmax} and ε_d respectively. Table 9.2 categorises the various walls according to ε_{lim}, as calculated with the **LTS**, into the respective damage categories as tabulated in Tables 3.1 and 3.2. Again, the strains colour coded in red indicate that they have surpassed the yielding tensile strain ε_{yield} (0.000125) of the material.

Number	Δ/L	Eq (5.16) ε_{bmax}	Eq (5.17) ε_d	ε_{lim}
1a)	0.0016848	0.001313	0.001575	0.001575
1b)	0.0016848	0.001313	0.001575	0.001575
2a)	0.0016848	0.002407	0.000481	0.002407
2b)	0.0016848	0.002407	0.000481	0.002407

Table 9.3 ε_{lim} developed in the walls of 1a), b), 2a), b) according to the **LTS** (**q** model).

Number	ε_{lim} %	Damage Category
1a)	0.15-0.3	3
1b)	0.15-0.3	3
2a)	0.15-0.3	3
2b)	0.15-0.3	3

Table 9.4 Damage classification (Table 3.1 and 3.2) of walls according to ε_{lim} calculated with the **LTS** (**q** model).

9.5 Damage category classification comparisons

This section compares the damage categories of the respective walls as categorised with the **MLTS** and the **LTS**.

The difference between the **MLTS** and the **LTS** is as follows:

a) The **MLTS** is applicable only to solid masonry walls symmetrically positioned over the sagging zone of a green field settlement trough.

b) The **MLTS** implements $\Delta/L:\varepsilon_{lim}$ relationships calculated with simply supported linear elastic finite element models of solid masonry walls. The existing approach implements $\Delta/L:\varepsilon_{lim}$ relationships based on simple elastic beam theory applied to simply supported elastic beams mimicking the solid masonry walls.

c) The **MLTS** takes the soil to wall interaction into account in the calculation of Δ/L.

As expected, the **MLTS** categorises the respective walls in lower damage categories than the **LTS** does. This is due to the lower Δ/L ratios implemented in the **MLTS** as a result of taking the soil to wall interaction into account. The **LTS** is unable to detect the difference between walls founded, on a soft soil or on a stiff soil. On the other hand the **MLTS** does. The **MLTS** therefore, is an improved model for the prediction of settlement damage to laterally unconfined, solid masonry walls, symmetrically

positioned over the sagging zone of a green field settlement trough with no soil to wall friction.

Table 3.1 defines six categories of damage, numbered 0 to 5 in increasing severity. It is taken that categories 0, 1 and 2 relate to aesthetical damage, 3 and 4 to serviceability damage and 5 relates to damage affecting the stability of the building. This categorisation, however, seems to have been set up for application on a wide variety of different structures and does not cater for the specific walls under investigation in this study. For instance, according to the damage categories tabulated in Table 3.1, the **MLTS** predicts that the walls will only experience aesthetical damage. The **LTS** predicts serviceability damage. Laterally unconfined walls, experiencing levels of strains that surpass their material's yielding tensile strain ε_{yield} will surely experience stability problems. The necessity for structure specific damage categories to be set up is evident. These structure specific damage categories should also make provision for specific support conditions. For instance, a damage classification set up for solid masonry walls can include provisions for laterally unconfined or laterally confined walls with or without the development of soil to wall friction.

As stated in the introduction to this study, it is not intended to justify the damage categories of Tables 3.1 and 3.2, neither is it the intention to set up new damage categories specific to solid masonry walls implementing different support conditions. Seeing that masonry is a brittle material, a masonry wall is considered to experience stability problems if the magnitude of ε_{lim} surpasses the masonry yielding tensile strain ε_{yield}. The **LTS** therefore, predicts stability problems for all four of the walls. The **MLTS**, implementing the **MAXP** criterion predicts stability problems for walls 1b), 2a) and 2b). Wall 1a), on the other hand is predicted to experience no stability problems with the **MLTS** and the **MAXP** criterion. The **MAXP** criterion is used as it is considered the most suitable. The **SBP** and **AMAX** criterions are considered to be upper and lower limits.

The next chapter will determine whether the respective walls experience stability problems or not. Complete nonlinear analyses on the respective walls will be

undertaken for this purpose by allowing the solid masonry walls to crack up if necessary.

Chapter 10

Constitutive nonlinear masonry behaviour

10.1 Introduction

In this chapter the four solid masonry walls discussed in chapter 9 are modelled with finite elements. The models and their loads are as those implemented in chapter 8 of this study. The only difference is that the masonry of the wall is modelled to display nonlinear constitutive material behaviour (van Zijl 2000). After being modelled, the four respective walls are analysed and the results used to judge the ability of both the **LTS** and the **MLTS** in predicting settlement damage to solid masonry walls symmetrically positioned over the sagging zone of a green field settlement trough. The results are used in conjunction with the predictions made in chapter 9 in order to perform the above judgment.

Firstly the nonlinear material model will be discussed before the results of the nonlinear analyses are discussed.

10.2 Material model for nonlinear masonry behaviour (van Zijl 2000)

A brief description is given here of the anisotropic Rankine-Hill model of Van Zijl (2000), which is based on computational continuum plasticity, is used to model the nonlinear behaviour of masonry. The model captures the total load deformational behaviour, from the linear elastic phase, through the peak resistance, to post-peak strength degradation. This is done for both tension and compression, and what is more, loading direction is accounted for. For tension, the strength is limited by a peak value of $\mathbf{f_{tx}}$ in the direction parallel to bed joints, while the lower tensile limit $\mathbf{f_{ty}}$ acts perpendicular to bed joints. In compression, the corresponding limits are $\mathbf{f_{cx}}$ and $\mathbf{f_{cy}}$. The strength limit function in the x and y directions is shown schematically in Figure 10.1, also indicating the uniaxial parameters mentioned above. In Figure 10.1 it can be seen that biaxial strengthening in compression is accounted for.

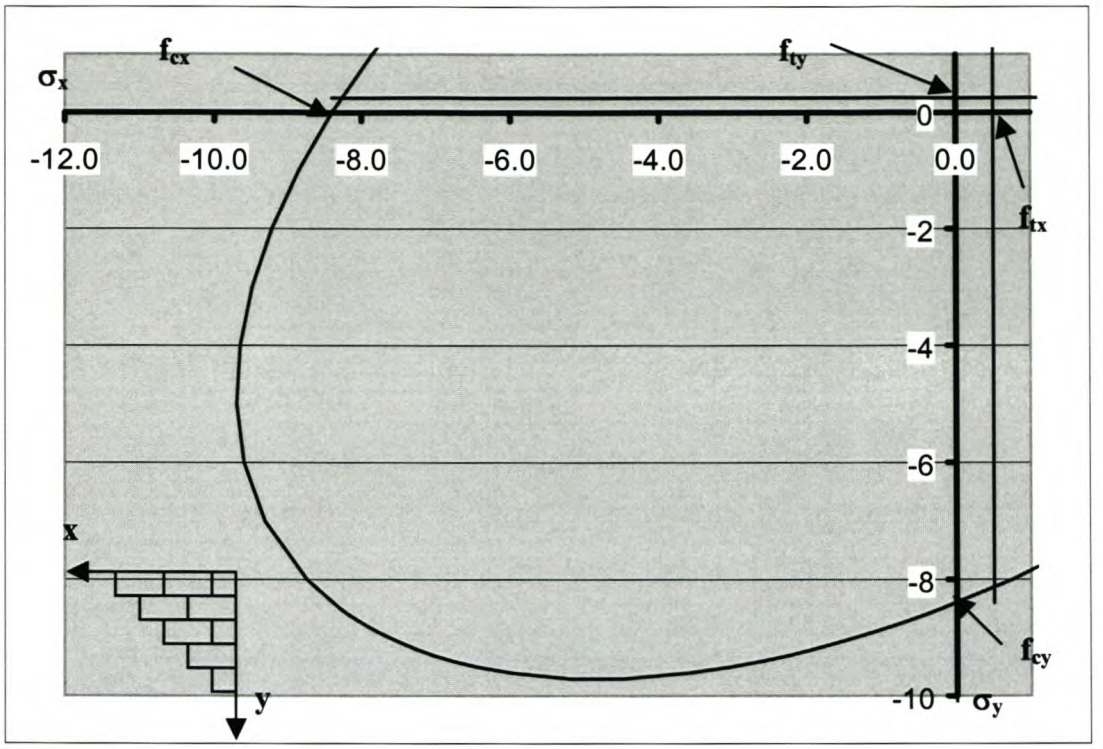

Figure 10.1 Strength limit function: Nonlinear masonry behaviour (van Zijl 2000).

The strength reduction after the respective strains corresponding to the peak stresses in both tension and compression, as well as in both material directions, is governed by fracture energy. For this tension strength degradation parallel and perpendicular to the bed joints, the fracture energies are denoted by $\mathbf{G_{tx}}$ and $\mathbf{G_{ty}}$ respectively, and in compression by $\mathbf{G_{cx}}$ and $\mathbf{G_{cy}}$. Figure 10.2 represents the concept of fracture energy for both tension and compression and depicts its relation to plastic strain $\boldsymbol{\varepsilon_{pl}}$ and stress $\boldsymbol{\sigma}$. The values of all the parameters mentioned above are tabulated in Table 10.1. The stress build-up with increasing strain up to the peak, limiting value, as well as the subsequent softening, or reduced stress with increased strain, is shown in Figures 10.3 for both orthogonal directions respectively.

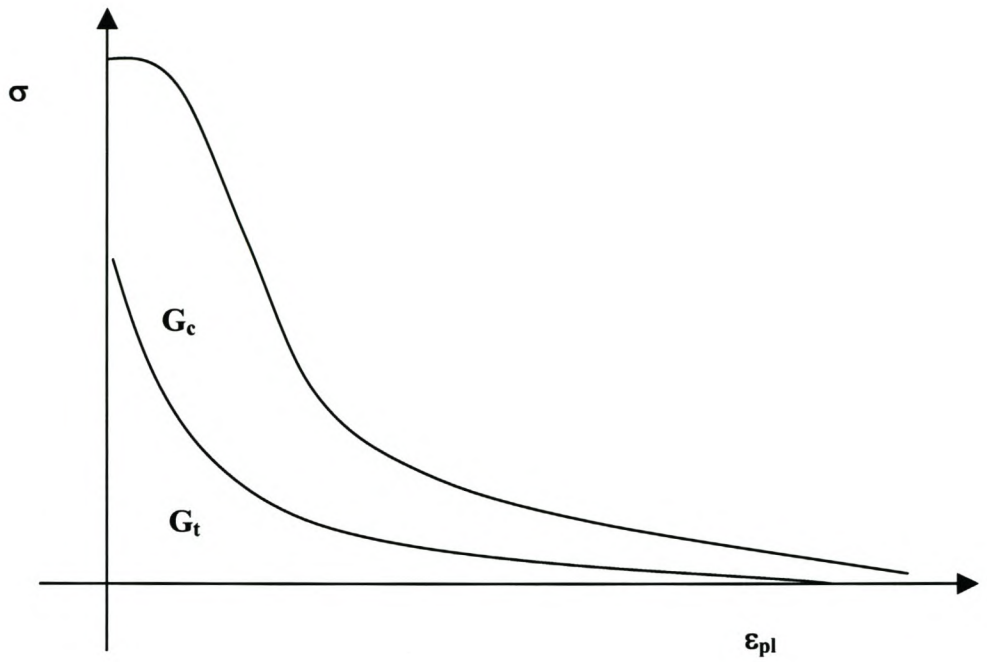

Figure 10.2 Compressive $\mathbf{G_c}$ and tensile $\mathbf{G_t}$ fracture energies.

f_{tx} (MPa)	f_{ty} (MPa)	f_{cx} (MPa)	f_{cy} (MPa)	G_{tx} (N/mm)	G_{ty} (N/mm)	G_{cx} (N/mm)	G_{cy} (N/mm)
0.5	0.25	8.4	8.4	0.03	0.01	20	20

Table 10.1 Material parameters for the masonry nonlinear behaviour, (van Zijl 2000).

The plastic strain ε_{pl} is defined as the total strain ε less the elastic strain ε_{el}, with the following equation:

$$\varepsilon_{pl} = (\varepsilon - \varepsilon_{el})$$

$$\varepsilon_{pl} = \left(\varepsilon - \left(\frac{\sigma}{E}\right)\right) \tag{10.1}$$

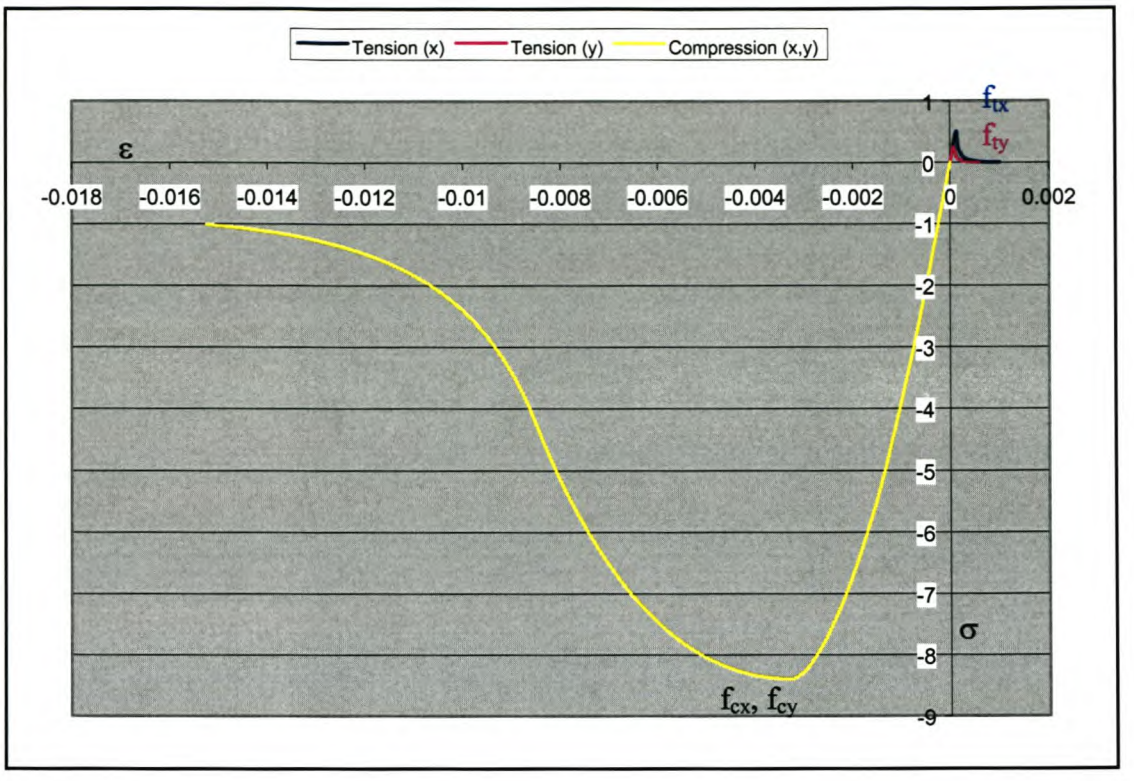

Figure 10.3 Softening and hardening in compression and tension, (x and y direction).

Notice how the masonry tensile behaviour differs in the x and y directions, whereas its compressive behaviour is identical in both directions in this case.

10.3 Results of the nonlinear analyses

Here the results pertaining to the nonlinear analyses of the solid masonry walls are discussed. The four walls under investigation are those presented in chapter 9. The wall Δ/L_{st}:Δ/L_w relationship associated with the nonlinear analysis is compared to the same relationship of equal **L/H** and K_{soil}/K_{wall} ratio, presented in chapter 8. Figures of the walls' maximum principal strain ε_1 contour levels are also presented. These contour level plots highlight the initiation of cracking in the masonry and then depict the point of structural failure.

10.3.1 Wall 1a)

- **L/H** = 0.5.
- $\mathbf{K_{soil}}$ = 10 MN/m³.
- $\mathbf{K_{soil}/K_{wall}}$ = 0.198.

Figure 10.4 compares the Δ/L_{st}:Δ/L_w relationship of wall 1a) associated with linear masonry wall behaviour, (Figure 8.6, chapter 8), and nonlinear masonry wall behaviour (chapter 10).

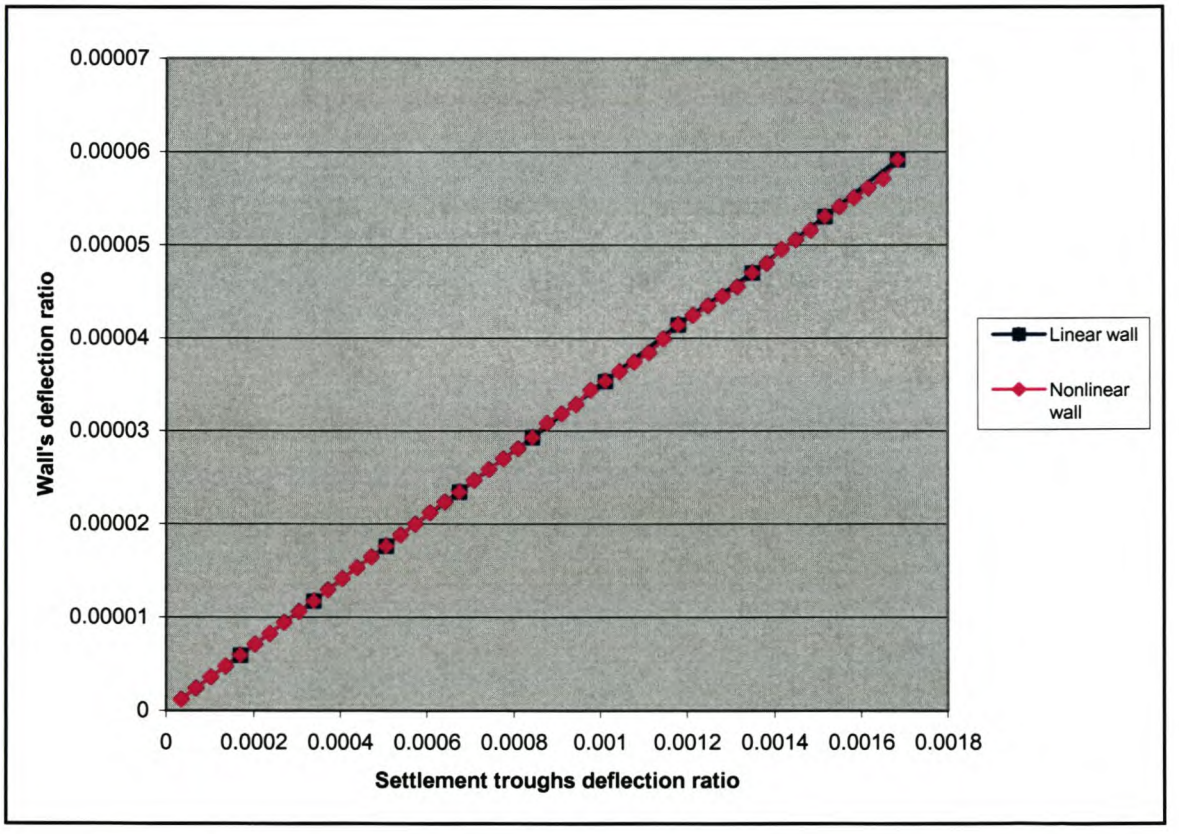

Figure 10.4 Δ/L_{st}:Δ/L_w for both linear and nonlinear masonry wall response. (**L/H** = 0.5, **L** = 19800mm, $\mathbf{K_{soil}}$ = 10 MN/m³).

As seen in Figure 10.4, the relationship corresponding to the linear wall behaviour of the semi-nonlinear models is identical to the relationship corresponding to the nonlinear wall behaviour. The fact that the relationship corresponding to the nonlinear

wall behaviour does not deviate from that of the linear wall behaviour signifies that wall 1a) does not experience any regions of cracking as a result of the ground displacements. The **MLTS** predicted this exact situation with the **MAXP** strain criterion, calculating a ε_{lim} of 0.0001087. This is lower than ε_{yield} of the masonry, which is equal to 0.000125 and therefore the prediction according to **MLTS** is that the wall does not experience regions of cracking and therefore structural failure. The **LTS** on the other hand calculated a ε_{lim} of 0.001575, which predicts that the wall will develop regions of cracking and therefore structural failure. The **LTS** would therefore have resulted in the unnecessary recommendation of mitigating measures for wall 1a), based on the magnitude of ε_{yield}, whereas the **MLTS** would have correctly not recommended any mitigating measures. The inability of the **LTS** to account for the soil to wall interaction is a direct result of the conservatism employed by the **LTS**. Conservatism is a general trait of all engineering processes, but when over conservatism starts causing the implementation of unnecessary mitigating measures that have a negative effect on the economy, the process needs redesigning.

Figure 10.5 presents the contour levels of the maximum principal strains ε_1 associated with wall 1a) at the end of the analysis. The critical maximum principal strains develop at mid-span on the bottom fibre of the wall. The magnitude of strain associated with this region is 0.000112, which is between the magnitudes of ε_{lim} predicted by the **MAXP** and **AMAX** strain criterions of the **MLTS**. The **MAXP** criterion is 0.000108 and the **AMAX** criterion 0.000139. This is a satisfying result as the strain developed in the nonlinear wall falls in between the upper and middle limit strain criterions of the **MLTS**. The reader is reminded that the strain criterions associated with the **MLTS** are obtained by the linear elastic analyses of simply supported solid masonry walls. Walls founded on a deflected soil foundation are not simply supported, but unevenly supported according to Figure 10.6 along their entire bottom edge as a result of the settlement trough's shape. Simply supported solid masonry walls exhibit an arched load path of their loads through their supports into the foundation. The stress distributions are therefore different. Using simply supported solid masonry walls to set up the strain criterions implemented by the **MLTS** is a conservative approach.

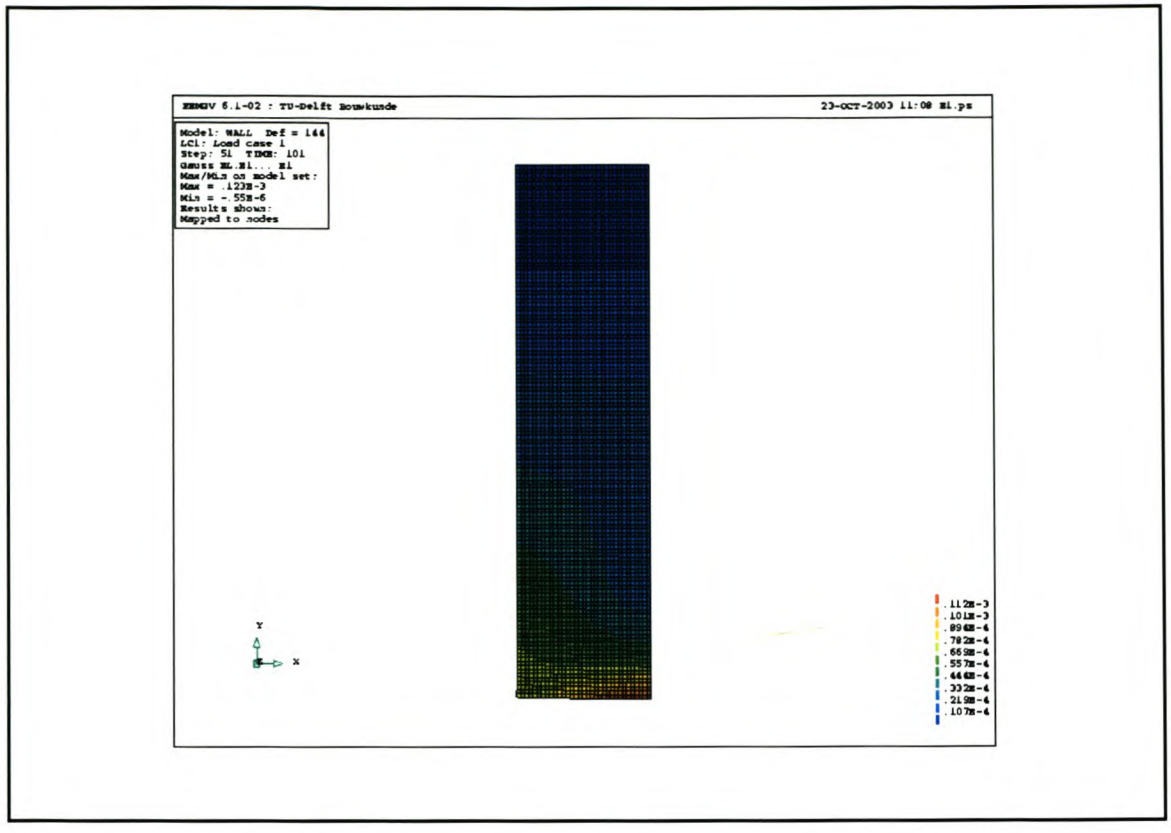

Figure 10.5 ε_1 contour levels: **L/H** = 0.5, **L** = 19800 mm, $\mathbf{K_{soil}}$ = 10 MN/m^3. (Wall 1a)

Figure 10.6 presents the reaction forces on the bottom edge of wall 1a) at the end of the analysis. The reaction forces at the corners of the bottom edge of the wall are larger than those at mid-span. This is due to the fact that the soil at mid-span moves vertically downward at a faster rate than the soil at the corners, as a result of the shape of the settlement trough. The larger reaction forces at the corners signify the increased pressure on the soil foundation at the position of the wall's corners. This causes the bedding of the wall into the soil, which reduces the wall Δ/L ratio from Δ/L_{st} to Δ/L_w. The **MLTS** accounts for this satisfactorily, whereas the **LTS** is unable to predict the difference between the same wall founded on either a soft or a stiff soil foundation.

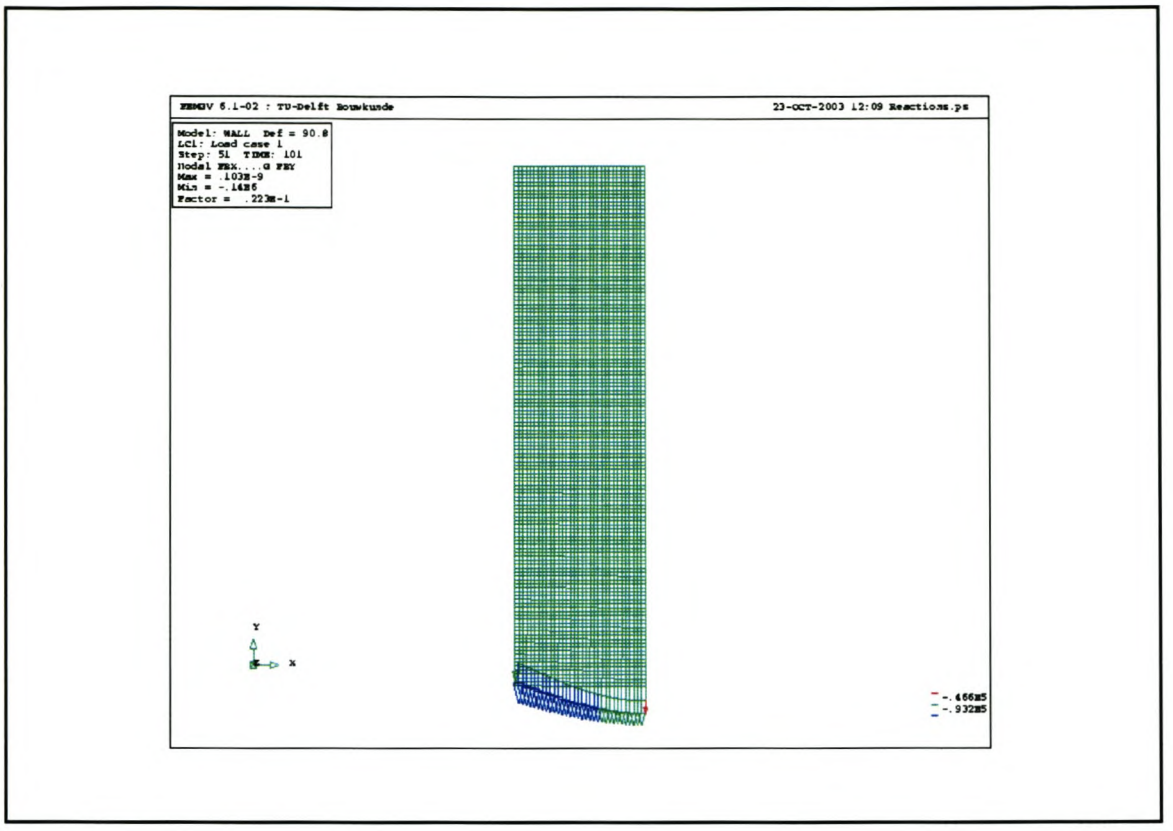

Figure 10.6 Reaction Forces on the bottom edge of wall 1a). (**L/H** = 0.5, **L** = 19800 mm, $\mathbf{K_{soil}}$ = 10 MN/m^3).

10.3.2 Wall 1b)

- **L/H** = 0.5.
- $\mathbf{K_{soil}}$ = 80 MN/m^3.
- $\mathbf{K_{soil}/K_{wall}}$ = 1.584.

Figure 10.7 compares the $\mathbf{\Delta/L_{st}:\Delta/L_w}$ relationship of wall 1b) associated with linear masonry wall behaviour, (Figure 8.6, chapter 8), and nonlinear masonry wall behaviour (chapter 10).

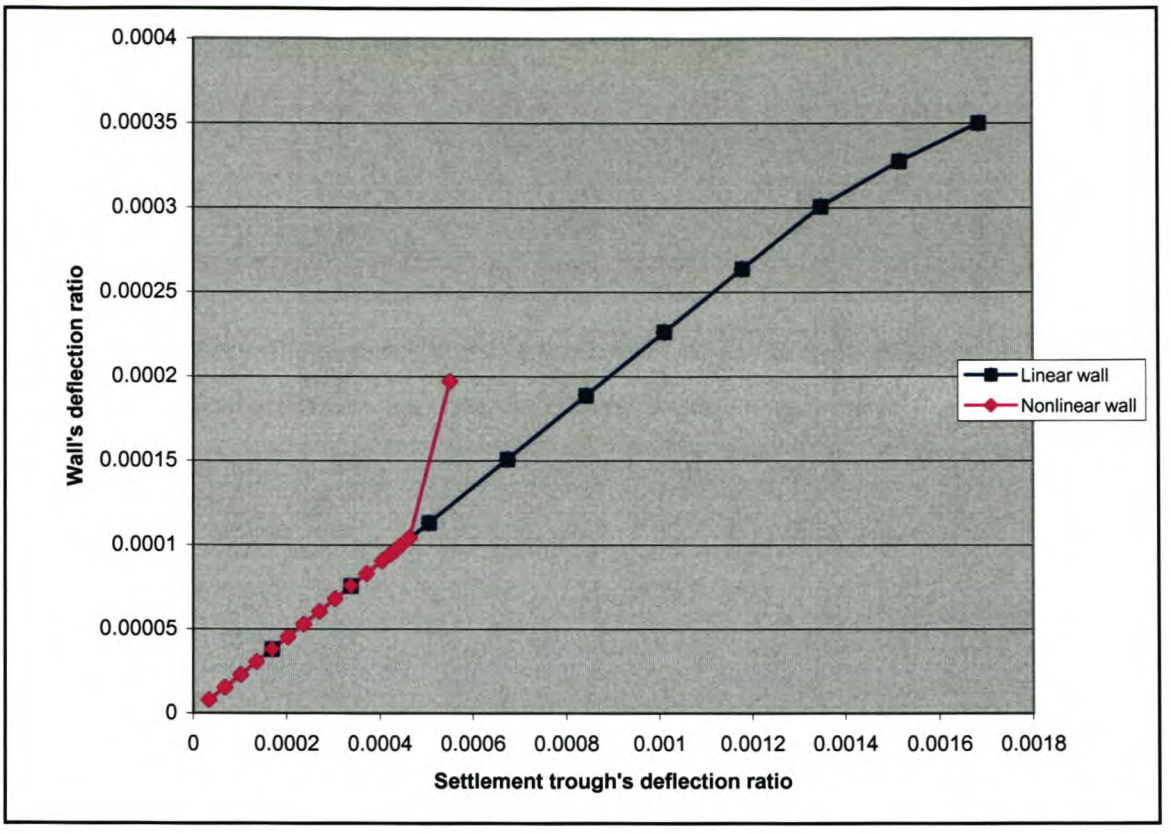

Figure 10.7 Δ/L_{st}:Δ/L_w for both linear and nonlinear masonry wall response. (**L/H** = 0.5, **L** = 19800mm, $\mathbf{K_{soil}}$ = 80 MN/m^3).

As seen in Figure 10.7, the Δ/L_{st}:Δ/L_w relationship associated with the nonlinear wall is identical to that of the linear wall's relationship until regions of cracking start to develop in the wall at the point where the respective relationships start to deviate from one another. The brittle response of the solid masonry wall is depicted by its sudden structural failure with the large increase in the magnitude of Δ/L_w corresponding to a small increase in the magnitude of Δ/L_{st}. The brittle behaviour of the wall at peak load is a difficult issue and beyond the scope of this thesis, Rots (2001) (FramCos proceedings) and Boonpichetvong and Rots (2003) (Euro-C proceedings). Both the **MLTS** and the **LTS** predicted the structural failure of wall 1b). The **MAXP** criterion of the **MLTS** calculated ε_{lim} to be 0.000674 and the **AMAX** criterion 0.000833. The **LTS** calculated ε_{lim} to be 0.001575, which is identical to the prediction for wall1a) not withstanding the fact that both walls are founded on very different soil foundations.

Figure 10.8 presents the contour levels of the maximum principal strains ε_1 associated with the bottom of wall 1b) at the point in the analysis where the material starts developing regions of cracking.

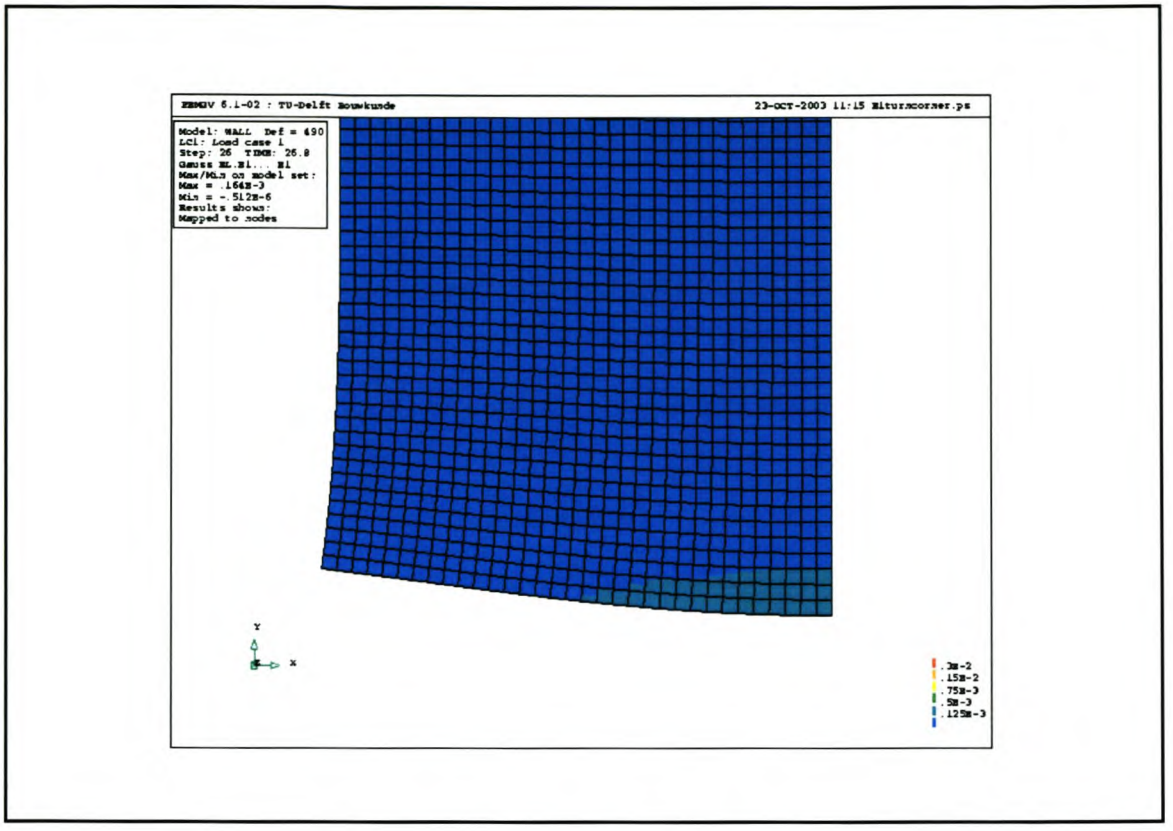

Figure 10.8 ε_1 contour levels: **L/H** = 0.5, **L** = 19800 mm, $\mathbf{K_{soil}}$ = 80 MN/m^3. (Bottom of wall 1b starting to experience tensile cracking).

Notice how the material on the bottom fibre at mid-span starts experiencing regions of cracking first. This is in direct contradiction with the strain distribution of the wall in Figure 7.7, which also has an **L/H** ratio equal to 0.5. In Figure 7.7 the maximum strains develop near the corners of the wall. This was explained in section 10.3.1 with regard to the fact that the wall in Figure 7.7 is simply supported, whereas wall 1b) is not.

Figure 10.9 presents the contour levels of the maximum principal strains ε_1 associated with the bottom of wall 1b) at the point of structural failure. It is seen that the wall develops a sudden crack at mid-span, which propagates vertically up through the wall and results in the wall's structural instability.

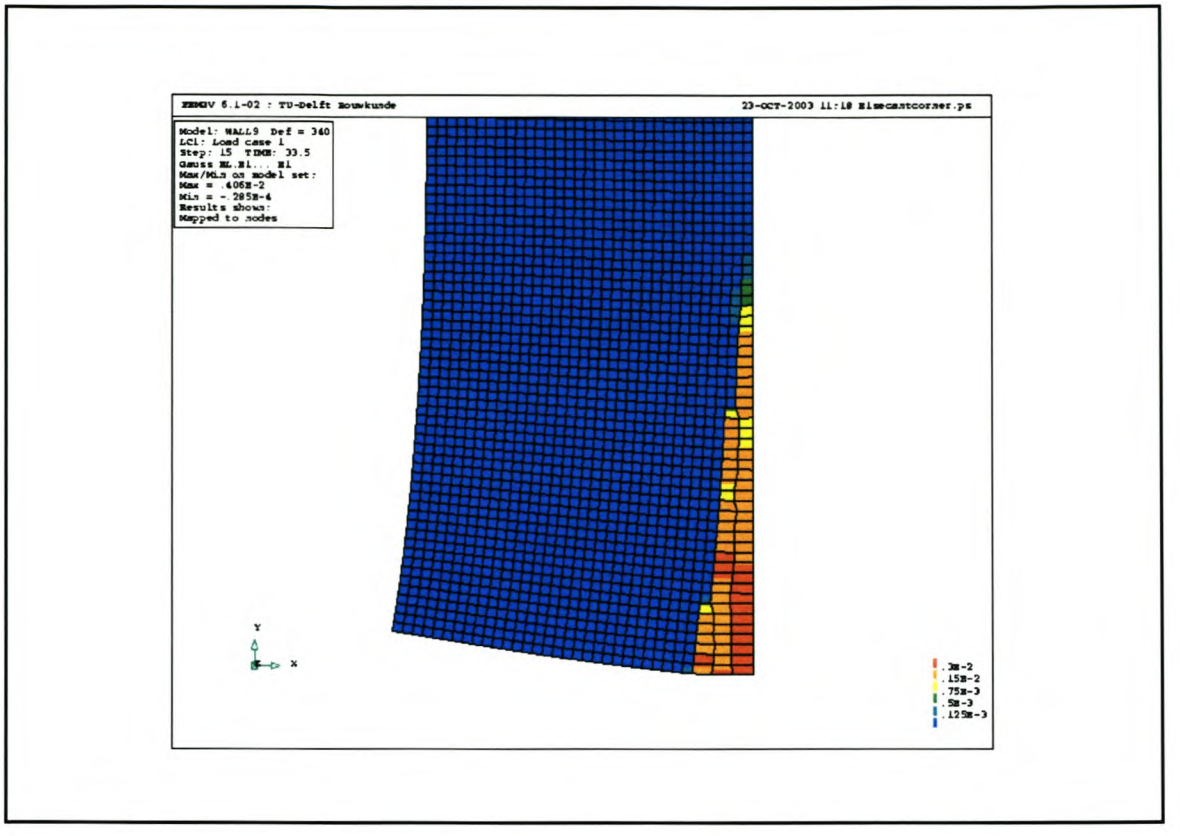

Figure 10.9 ε_1 contour levels: **L/H** = 0.5, **L** = 19800 mm, $\mathbf{K_{soil}}$ = 80 MN/m^3. (Wall 1b at the point of structural failure).

10.3.3 Wall 2a)

- **L/H** = 3.
- $\mathbf{K_{soil}}$ = 10 MN/m^3.
- $\mathbf{K_{soil}/K_{wall}}$ = 0.033.

Both the **MLTS** and the **LTS** predict the structural failure of wall 2a) based on their predictions of ε_{lim}. The **MAXP** and **AMAX** criterions of the **MLTS** calculated ε_{lim} to be 0.000178. The **LTS** calculated ε_{lim} to be 0.002407. Wall 2a) fails in a similar fashion to wall 1b). Initially the linear and nonlinear wall Δ/L_{st}:Δ/L_w relationships correspond closely to one another until regions of cracking start to develop in the wall at mid-span on the bottom fibre. After the development of cracking at mid-span, the

wall failed in a sudden brittle fashion with a crack developing at mid-span and propagating vertically up through the wall, resulting in its structural instability.

Figure 10.10 compares the Δ/L_{st}:Δ/L_w relationship of wall 2a) associated with linear masonry wall behaviour, (Figure 8.9, chapter 8), and nonlinear masonry wall behaviour (chapter 10).

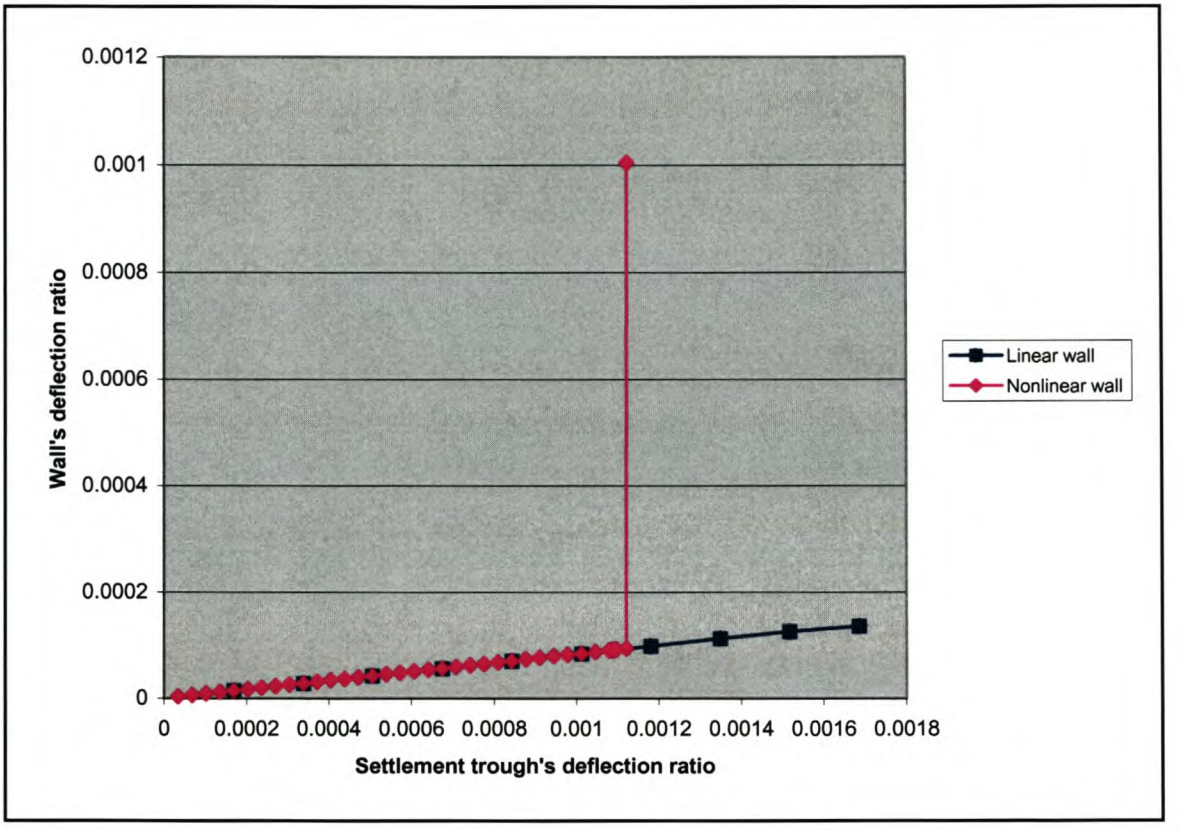

Figure 10.10 Δ/L_{st}:Δ/L_w for both linear and nonlinear masonry wall response. (**L/H** = 3, **L** = 19800mm, K_{soil} = 10 MN/m^3).

It is seen that a wall with an **L/H** ratio equal to 3 fails in a far more brittle fashion than a wall with an **L/H** ratio equal to 0.5 does. A reason for this relates to the fact that the crack at mid-span only needs to propagate over a shorter vertical distance in the wall with an **L/H** ratio of 3 for an equal span length **L**.

10.3.4 Wall 2b)

- **L/H** = 3.

- $\mathbf{K_{soil}} = 80$ MN/m³.

- $\mathbf{K_{soil}/K_{wall}} = 0.264$.

Here again, both the **MLTS** and the **LTS** predict the structural failure of wall 2b) based on their predictions of ε_{lim}. The **MAXP** and **AMAX** criterions of the **MLTS** calculated ε_{lim} to be 0.000289. The **LTS** calculated ε_{lim} to be 0.002407, which is identical to the prediction for wall 2a) not withstanding the fact that both walls are founded on very different soil foundations

Figure 10.11 compares the Δ/L_{st}:Δ/L_w relationship of wall 2b) associated with linear masonry wall behaviour, (Figure 8.9, chapter 8), and nonlinear masonry wall behaviour (chapter 10).

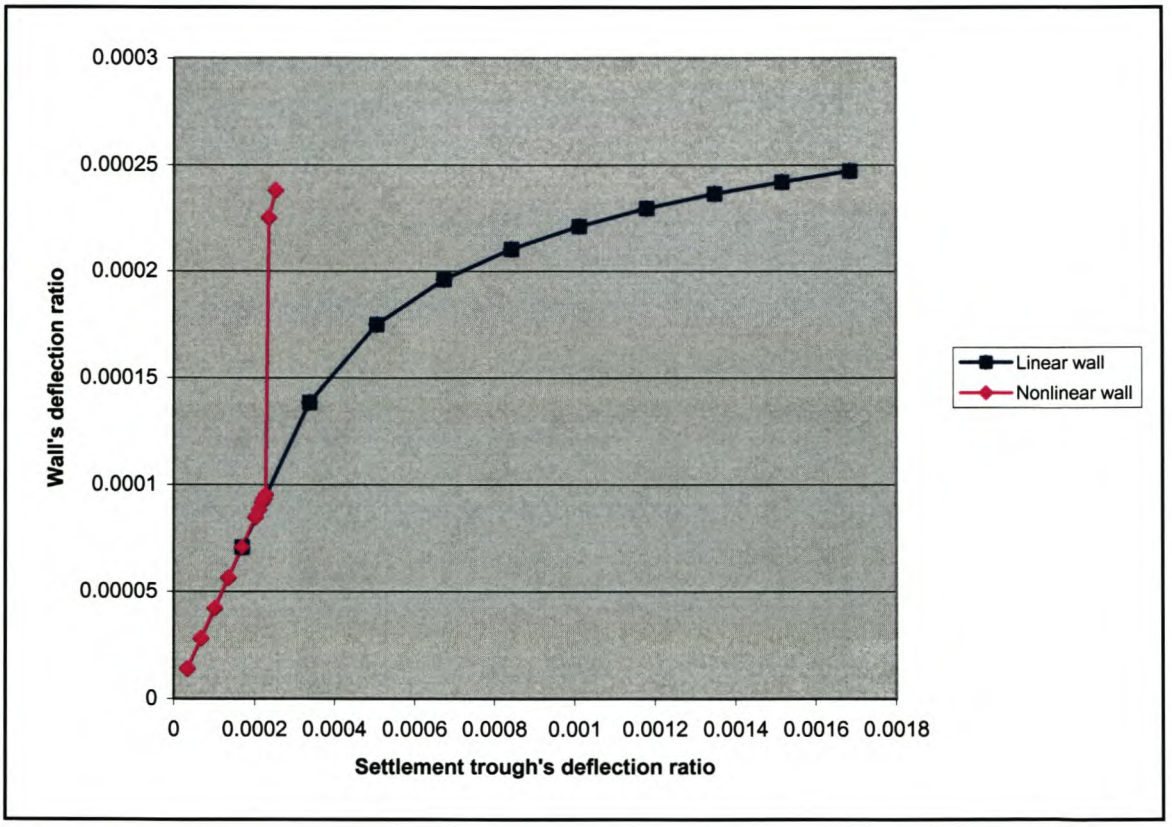

Figure 10.11 Δ/L_{st}:Δ/L_w for both linear and nonlinear masonry wall response. ($\mathbf{L/H} = 3$, $\mathbf{L} = 19800$mm, $\mathbf{K_{soil}} = 80$ MN/m^3).

Wall 2b) fails in a similar fashion to wall 1b) and 2a). Initially the linear and nonlinear wall Δ/L_{st}:Δ/L_w relationships correspond closely to one another until regions of cracking start to develop in the wall at mid-span on the bottom fibre. After the development of cracking at mid-span, the wall failed in a sudden brittle fashion with a crack developing at mid-span and propagating vertically up through the wall resulting in its structural instability.

10.4 Summary

This chapter has highlighted the brittle structural response of a laterally unconfined masonry wall. This brittle response justifies the decision in the summary of chapter 9 to base the settlement damage prediction of the **MLTS** and the **LTS** on the basis of the magnitude of ε_{yield}. It was shown that the **MLTS** was successful in all four predictions, whereas the **LTS** was not. Once the calculated magnitude of ε_{lim} surpasses ε_{yield}, the laterally unconfined solid masonry walls exhibiting no soil to wall friction will experience structural stability problems. Only the solid masonry wall of **L/H** 0.5 exhibited a slight degree of load redistribution as seen in Figures 10.7 and 10.8. As mentioned previously, the basis of the settlement damage prediction for laterally confined solid masonry walls experiencing either the presence of soil to wall friction or not, will be different from that of the laterally unconfined solid masonry walls, as they will be able to redistribute their loads with greater success before their eventual structural failure. This again highlights the need for structure specific damage categories to be set up, with provisions made for specific support conditions.

It has also been shown that the **MLTS** correctly predicts the development of ε_{lim} either side of the materials ε_{yield}. This is a direct result of the ability of the **MLTS** to account for the inherent soil to wall interaction. The **LTS** on the other hand cannot detect the difference between the two same walls founded on different soil foundations. The **LTS** has been shown to be very conservative, which can have a negative effect on the economy if it recommends the undertaking of mitigating effects unnecessarily.

The following chapter is the conclusion to this study as well the definition of future work envisaged for this field of tunnel-induced settlement damage.

Chapter 11

Conclusion

The inevitability of tunneling in urban areas, as a direct result of rapid population growth, has motivated this study. The mechanism of tunneling-induced soil deformations, as well as their effect on the existing surface infrastructure aesthetics, serviceability and structural stability, have been discussed. Economical and time constraints were mentioned as the primary reasons for the necessity of a simple damage assessment approach, limiting tensile strain method **LTS** (Burland and Wroth 1974).

The motivation for this study was to investigate the accuracy of the simple analytical damage assessment approach (Limiting tensile strain method (**LTS**)) against the results of numerical nonlinear analyses of real structures, supported on real soil foundations. The **LTS** is based on calculating the limiting tensile strains ε_{lim} in simply supported elastic beams subject to displacements mimicking a green field settlement trough. These elastic beams are assigned dimensions, span lengths **L** and heights **H**, corresponding to the real structure for which they are predicting settlement damage on the basis of the magnitude of ε_{lim}. Damage classification categories (Tables 3.1 and 3.2) corresponding to the magnitudes of ε_{lim} calculated by the **LTS** are used to predict settlement damage for the real structures.

As stated previously the diversity of structures in a city makes it very difficult for any study to make a general remark on the accuracy of using the **LTS** for the conduction of settlement damage predictions to real structures. For this reason only laterally unconfined, solid masonry walls, symmetrically positioned over the sagging zone of a green field settlement trough with no soil to wall friction, were studied. The material properties of the masonry were presented in section 5.3.

Based on the results of numerical linear elastic analyses of simply supported solid masonry walls, it was concluded that:

- The **LTS** can accurately predict the development of the limiting tensile strain ε_{lim} in the above solid masonry walls for **L/H** ratios 2 and larger.

- The **LTS** is unable to accurately predict the development of ε_{lim} in the above solid masonry walls for **L/H** ratios 2 and smaller.

From the numerical results it was determined that for solid masonry walls of **L/H** ratio 2 and smaller, the magnitude of ε_{lim} is not only dependent on its material properties and **Δ/L** ratio, but also on its span length **L**. For walls of **L/H** ratio 2 and larger the magnitude of ε_{lim} is found to be dependent solely on its material properties and **Δ/L** ratio.

A major downfall of the **LTS** is related to the fact that it is unable to detect the difference in the structural response between the same two walls subject to tunneling-induced settlements founded on soil foundations of different stiffness. The stiffness of a soil foundation plays a major role in the development of the stress and strain distributions in the wall as it defines the magnitude of the wall **Δ/L** ratio. The **LTS** assumes a **Δ/L** ratio mimicking the dimensions of the green field settlement trough. In this study the soil to wall interaction was investigated with numerical analyses conducted on solid masonry wall models implementing a structural interface (van Zijl 2000) to model the soil. Relationships between the **Δ/L** ratio defined by the green field settlement trough and the real wall **Δ/L** ratio were defined for **L/H** ratios in the range of 0.5 to 3 as well as for various $\mathbf{K_{soil}/K_{wall}}$ ratios.

The **MLTS**, the modified version of the **LTS**, differs from the **LTS** as follows:

- The **MLTS** is applicable only to solid masonry walls symmetrically positioned over the sagging zone of a green field settlement trough. Material properties as in section 5.3.

- The **MLTS** implements $\mathbf{\Delta/L:\varepsilon_{lim}}$ relationships calculated with simply supported linear elastic finite element models of solid masonry walls. The **LTS** implements $\mathbf{\Delta/L:\varepsilon_{lim}}$ relationships based on simple elastic beam theory applied to

simply supported elastic beams mimicking the solid masonry walls conforming exactly to the green field settlement trough displacements.

- The **MLTS** takes the soil to wall interaction into account in the calculation of **Δ/L**.

The **MLTS** demonstrated a superiority over the **LTS** in terms of predicting the magnitude of ε_{lim} in laterally unconfined solid masonry walls with no soil to wall friction. This was due to the superiority of the **MLTS** over the **LTS** in terms of:

- An improved representation of the relationship between $\Delta/L:\varepsilon_{lim}$ for solid masonry walls subject to tunneling-induced settlements.

- The ability to account for the soil to wall interaction defined by a K_{soil}/K_{wall} ratio.

The damage classifications as tabulated in Tables 3.1 to 3.2 were deemed insignificant, as they have been designed to serve a broad range of structures and are not accurate in their categorising of the solid masonry walls in this study.

This study has reached the point where the **MLTS** can accurately predict whether the magnitude of ε_{lim} in the above solid masonry walls (Residential structures) of certain span length **L** and **L/H** ratio subject to tunneling-induced settlement and founded on a soil foundation of specific K_{soil}, will surpass the magnitude of ε_{yield}.

The expected future research to follow on from this study is as follows:

- The undertaking of a sensitivity analysis regarding the material properties of masonry. Their effect on the relationship $\Delta/L:\varepsilon_{lim}$ as well as on the soil to wall interaction will be investigated.

- The investigation of various boundary conditions applied to the solid masonry wall models will be undertaken. For instance, the case of laterally confined walls with, as well as without the development of soil to wall friction. Also, the case of

laterally unconfined walls exhibiting the development of soil to wall friction will be studied.

- Development of a range of numerical factors applicable to equations (5.16), (5.17), (5.24) and (5.25). These factors will be dependent on the various variables for example **L**, **L/H**, **Δ/L** as well as the material properties of the wall. This will enable the mentioned equations to be used for the strain calculations in the respective walls instead of the figures in chapter 7.

- The definition of damage category classifications associated with the development of ε_{lim} in solid masonry walls. Sub-categories will be defined to accommodate differing boundary conditions as well as the brittle or ductile nature of the material constituting the wall.

- The definition of a performance function relating to the wall experiencing certain degrees of settlement damage. The performance function will include the concerned variables. The respective statistical distributions of the concerned variables will be obtained so that the reliability of the settlement damage prediction can be calculated.

- Other structural classes will be studied and modifications made to the **LTS** so to enable a more accurate and reliable classification of their expected settlement damage. The other structural classes are for instance, framed concrete buildings, facades, steel structures etc.

References

Burland, J.B. Standing, J.R. Jardine, F.M. (2001) Building response to tunnelling: case studies from construction of the Jubilee Line Extension, London. Volume 1: Projects and methods. London: Telford.

Bares, R. (1971). Tables for the analysis of plates, slabs and diaphragms based on the elastic theory; second edition. Wiesbaden: Bauverlag.

Timoshenko, S. (1931). Strengths of materials Part 1: Elementry theory and problems. London: Macmillan.

Mair, R.J, Taylor, J.N and Burland, L.B. (1996). Prediction of ground movements and assessment of risk of building damage due to bored tunnelling. Geotechnical Aspects of Underground Construction in Soft Ground, Mair and Taylor (eds), (Balkema, Rotterdam), pp. 713-718.

Popov, E.P and T.A.Balan, (1999).Engineering mechanics of solids, second edition. Prentice-Hall, Inc.

R.D.Cook, D.S.Malkus, M.E.Plesha and R.J.Witt, (2002). Concepts and applications of finite element analysis, fourth edition. John Wiley and sons, inc.

van Zijl, G.P.A.G. (2000). Computational Modelling of Masonry Creep and Shrinkage. Meinema BV, Delft.

Boonpichetvong, and Rots, J.G. (2003) Settlement damage modeling of historical buildings. Computational modeling of Concrete Structures, Bićanić et al. (eds) (Swets and Zeitlinger, Lisse), pp.655-665.

Netzel, H.(2003). Review of the tensile strain method for predicting building damage due to ground movements, in (Re)Claiming the Underground Space, Proceedings of ITA World Tunnelling Congress, Amsterdam, the Netherlands, Volume2, pp.997-998. Lisse: Balkema.